

Sodium doping, back interface modification and light trapping in bifacial semi-transparent ultrathin $\text{Cu}(\text{In,Ga})\text{Se}_2$ solar cells

Der Fakultät für Physik
der Universität Duisburg-Essen vorgelegte

Dissertation

zur Erlangung des akademischen Grades eines Doktors der Naturwissenschaft
(Dr. rer. nat.)

Von

Yong Li

Master of Condensed Matter Physics, Shanghai University

geboren am 27.09. 1992

aus Jiangxi, China

Erstgutachter: Prof. Dr. Martina Schmid (Universität Duisburg-Essen)

Zweitgutachter: Prof. Dr. Guanchao Yin (Wuhan University of Technology)

Tag der wissenschaftlichen Aussprache: 12. 09. 2022

Duisburg

To my grandfather Xueting Li and my grandmother Lanying Li, who brought me up and encouraged me to go after my dreams

We all like to congregate at boundary conditions.

Where land meets water.

Where earth meets air.

Where bodies meet mind.

Where space meets time.

We like to be on one side, and look at the other.

- Douglas Adams

Title: Sodium doping, back interface modification and light trapping in bifacial semi-transparent ultrathin Cu(In,Ga)Se₂ solar cells

Table of Contents

Abstract	v
Kurzfassung	vii
Chapter 1 Background and instrumentation	1
1.1 The status of Cu(In, Ga)Se ₂ solar cells on the energy market	1
1.2 General structure and fabrication steps of CIGSe solar cells	4
1.3 Ultrathin Cu(In,Ga)Se ₂ solar cells on Mo back contacts	8
1.4 Cu(In,Ga)Se ₂ solar cells on transparent-conductive-oxides back contacts	9
1.5 Bifacial semi-transparent ultrathin Cu(In,Ga)Se ₂ solar cells	11
1.6 Sodium doping for CIGSe solar cells	12
1.7 Modification of the back interface	14
1.8 Light management in Cu(In,Ga)Se ₂ solar cells	17
1.9 Characterization method, analysis model, and simulation software	21
1.10 Outline of this thesis	31
Chapter 2 Na doping strategies	32
2.1 The requirements of Na doping	33
2.2 Na diffusion, NaF precursor and NaF post-deposition treatment	34
2.3 Comparison of the electrical performance and Na depth distribution	36
2.4 Summary and conclusion	42
Chapter 3 NaF post-deposition treatment	43
3.1 Two scenarios of the NaF post-deposition treatment	44
3.2 Characterization and discussion	45
3.3 SCAPS simulation	56
3.4 Summary and conclusion	60
Chapter 4 Modification of the back interface	61
4.1 Fabrication of the SiO ₂ point-contacts on Mo and ITO substrates	62
4.2 Passivation effects of the back interface by SiO ₂ point-contacts	66
4.3 SCAPS simulation of the back interface	78
4.4 Summary and conclusion	82
Chapter 5 Optimization of front and rear efficiency	83

5.1 Impact of the glass type	84
5.2 Impact of the ITO thickness.....	88
5.3 Impact of the NaF post-deposition treatment dose	96
5.4 Summary and conclusion	100
Chapter 6 Light management	101
6.1 Fabrication of SiO ₂ nanoparticles.....	102
6.2 Front illumination characteristics	103
6.3 Rear illumination characteristics.....	110
6.3 Light trapping mechanism under front and rear illumination	113
6.4 Summary and conclusion	114
Chapter 7 Summary and outlook.....	115
7.1 Summary	115
7.2 Outlook for bifacial semi-transparent ultrathin Cu(In, Ga)Se ₂ solar cells.....	117
Appendix A – Acknowledgement.....	118
Appendix B – Curriculum vitae	120
Experience	120
Publications and conferences	120
Appendix C – Abbreviations and symbols.....	121
References	125

Abstract

Compared to the standard Cu(In,Ga)Se₂ (CIGSe) solar cells with a 2-3 μm thick absorber, ultrathin CIGSe SCs with less than 500 nm absorber thickness have the advantages of high-volume efficiency and less raw materials consumption. However, the reduced thickness of CIGSe causes insufficient light absorption and hinders the achievement of high efficiency for the ultrathin solar cells. Light trapping nanoparticles (NPs) can increase light absorption in solar cells. In addition, if the opaque Mo back contact was replaced with a transparent conductive material, the NPs can trap the light incident from the front and rear side simultaneously, which results in a bifacial semi-transparent ultrathin (BSTUT) CIGSe solar cell. In₂O₃: Sn (ITO) has good conductivity and relative high transparency, which fits the requirements of the back contact for BSTUT CIGSe solar cells. This thesis optimizes the front and rear photovoltaic (PV) performance of the ITO-based BSTUT CIGSe solar cells under three aspects, namely Na doping, back contact interface modification and light management.

Firstly, four different Na doping methods are compared to decide about the optimal strategy for ultrathin CIGSe on ITO substrates. The four methods are Na diffusion from soda-lime glass (SLG), a NaF precursor, NaF post-deposition treatment (PDT), and a NaF precursor combined with PDT. When comparing the PV performance of the samples with different Na incorporation methods, the solar cells with NaF PDT doping exhibit the maximum enhancement compared to the reference (Na-free solar cell). In addition, the NaF PDT dose is optimized in detail and the resulting samples are characterized with multiple methods to explore the working mechanism of NaF PDT and the potential efficiency of BSTUT CIGSe solar cells. The NaF PDT mainly increases the doping density N_A in the CIGSe absorber and enlarges the contact potential difference V_D at the CIGSe/CdS interface. The NaF PDT can also increase the recombination velocity S_b and reduce the effective back barrier $E_{CIGSe/ITO}$ at the CIGSe/ITO interface. Combining those two effects, the NaF PDT levels up the open circuit voltage V_{oc} of the solar cells, even though the short circuit current density j_{sc} is slightly decreased. We also verify this working mechanism of NaF PDT via SCAPS simulation. The average optimal efficiency Eff of the solar cells is 12.1% with 622 mV V_{oc} , 29.6 mA/cm² j_{sc} , and 65.6% fill factor FF .

Secondly, SiO₂ point contacts are integrated at the CIGSe/ITO interface to modify the S_b at the back interface. For comparison, we use Mo back contacts as references for the SiO₂ passivation effects. Consistent with our previous work, the point contacts increase the PV performance of the Mo-based solar cells. However, SiO₂ passivation deteriorates the V_{oc} of our ITO-based ultrathin CIGSe solar cells. SCAPS simulations suggest that the barrier height E_h at the CIGSe/ITO interface decides about the effect of passivation (decreasing S_b) of SiO₂ for the ultrathin CIGSe SCs. According to the simulations, a decreasing S_b increases the effective barrier height $E_{h,e}$ when $E_h > 0.17$ eV (Schottky-like contact), which means passivation is detrimental for the V_{oc} of the ultrathin CIGSe solar cells. The CIGSe/ITO interface is a Schottky-like contact, so the SiO₂ point contacts decrease the performance of the ITO-based BSTUT CIGSe solar cells. On the contrary, a decreasing S_b increases the collection efficiency of photogenerated carriers when $E_h < 0.17$ eV (quasi-Ohmic contact), so passivation benefits the

solar cells. The decreased S_b increases the $E_{h,e}$ slightly, but the overall E_h is small for the solar cells with a quasi-Ohmic contact. The improved collection efficiency of the photogenerated carriers dominates the passivation effects and benefits the Eff of the solar cells. The CIGSe/Mo interface reveals a quasi-Ohmic back contact, so the passivation increases the Eff of Mo-based ultrathin CIGSe SCs.

Thirdly, the front and rear efficiency of BSTUT CIGSe solar cells are optimized using different substrates (SLG and alkali-free pgo glass), ITO thicknesses (100-400 nm) and various NaF PDT doses (0-8 mg). SLG-based solar cells show better front PV performance due to the extra incorporation of Na in the CIGSe co-evaporation process. However, solar cells on pgo glass show higher efficiency under rear illumination because alkali-free glass has a higher transparency than SLG, especially in the long wavelength range. The thicker ITO increases both the front and rear V_{oc} of the solar cells due to the Burstein-Moss shift in the ITO layer, which decreases the valence band offset ΔE_v at the CIGSe/ITO interface. However, the rear Eff is evened for solar cells on different thicknesses of ITO because thicker ITO also induces more severe parasitic absorption and leads to a lower rear j_{sc} . For BSTUT CIGSe solar cells with different NaF PDT doses, the rear PV performance trend is similar to the one under front illumination. The solar cell with the optimal conditions (300 nm ITO, 4 mg NaF PDT) achieves 11.8% front Eff and 6.4% rear Eff .

Fourthly, SiO_2 nanoparticles (NPs) are inserted at the CIGSe/ITO interface to enhance the overall light absorption of BSTUT CIGSe solar cells. The NPs induce waveguide modes and enhance front and rear absorption in the ultrathin CIGSe layer. The NPs also induce jet-like forward scattering, which further increases the collection efficiency of photogenerated carriers under the rear illumination. Compared to the references, the front j_{sc} increases by 4.1-4.4 mA/cm² and the rear j_{sc} by 6.4-7.4 mA/cm² for the BSTUT CIGSe solar cells with SiO_2 NPs. The front and rear V_{oc} gain of the solar cells with NPs can be quantitatively estimated by the relation between j_{sc} and V_{oc} , which means the passivation effects of the SiO_2 NPs are trivial compared to the dominating light trapping effects.

Compared to state-of-the-art Mo-based ultrathin CIGSe solar cells (15%), our BSTUT CIGSe solar cells still have room for performance improvement, especially in V_{oc} . The record V_{oc} is 733 mV for Mo-based and 635 mV for our ITO-based ultrathin CIGSe SCs. For the j_{sc} , however, the record-high j_{sc} is 26.4 mA/cm² for Mo-based and 31.1 mA/cm² (front illumination) for our ITO-based SCs with light trapping SiO_2 NPs, which shows an advantage of the BSTUT CIGSe solar cells. The bifacial Eff is 15.0% from summing up 100% front and 30% rear Eff of our best solar cell, which is close to the 15.2% record of the Mo-based ultrathin CIGSe solar cells. The findings in this thesis can help exploit solar energy with higher efficiency and lower fabrication cost. A summary and outlook will be presented at the end about how the efficiency of BSTUT CIGSe SCs could be further optimized.

Kurzfassung

Im Vergleich zu Standard-Cu(In,Ga)Se₂-(CIGSe-)Solarzellen mit einer Absorberdicke von 2 bis 3 μm bieten ultradünne CIGSe-Solarzellen mit einer Absorberdicke von weniger als 500 nm die Vorteile einer hohen Volumeneffizienz und eines geringeren Rohstoffverbrauchs. Die geringere Dicke des CIGSe führt jedoch zu einer verminderten Lichtabsorption und verhindert das Erreichen hoher Wirkungsgrade der ultradünnen Solarzellen. Nanopartikel (NP), die das Licht einfangen, können die Lichtabsorption in den Solarzellen erhöhen. Wenn der undurchsichtige Mo-Rückkontakt zusätzlich durch ein transparentes, leitfähiges Material ersetzt wird, können die NP gleichzeitig das von der Vorder- und Rückseite einfallende Licht einfangen. Dadurch entsteht eine bifaciale, halbtransparente, ultradünne (engl. bifacial semi-transparent ultrathin, BSTUT) CIGSe-Solarzelle. In₂O₃: Sn (ITO) besitzt eine gute Leitfähigkeit und eine relativ hohe Transparenz, was den Anforderungen an den Rückkontakt für BSTUT CIGSe-Solarzellen entspricht. In dieser Arbeit wird die photovoltaische (PV-) Leistung bezogen auf Vorder- und Rückseitenbeleuchtung der ITO-basierten BSTUT CIGSe-Solarzellen unter drei Gesichtspunkten optimiert: Na-Dotierung, Veränderung der Grenzfläche zum Rückkontakt und Lichtmanagement.

Zunächst werden vier verschiedene Na-Dotierungsmethoden untersucht, um die optimale Strategie für ultradünnes CIGSe auf ITO-Substraten zu finden. Bei den vier Methoden handelt es sich um Na-Diffusion aus Natron-Kalk-Glas (engl. soda-lime glass, SLG), einen NaF-Vorläufer, NaF-Nachbehandlung (engl. post-deposition treatment, PDT) und eine Kombination aus NaF-Vorläufer plus PDT. Beim Vergleich der PV-Leistung der Proben mit verschiedenen Methoden des Na-Eintrags stellen wir fest, dass die Solarzellen mit NaF-PDT-Dotierung die maximale Verbesserung im Vergleich zur Referenz (Na-freie Solarzelle) aufweisen. Anschließend wird die NaF-PDT-Dosis im Detail optimiert und die Proben mit mehreren Methoden charakterisiert, um den Wirkmechanismus des NaF-PDT und die mögliche Effizienz von BSTUT-CIGSe-Solarzellen zu erforschen. NaF-PDT erhöht hauptsächlich die Dotierkonzentration N_A im CIGSe-Absorber und vergrößert die Kontaktpotentialdifferenz V_D an der CIGSe/CdS-Grenzfläche. NaF-PDT kann auch die Rekombinationsgeschwindigkeit S_b erhöhen und die effektive Rückbarriere $E_{\text{CIGSe/ITO}}$ an der CIGSe/ITO-Grenzfläche verringern. Durch die Kombination dieser beiden Effekte erhöht das NaF-PDT die Leerlaufspannung V_{oc} der Solarzellen, obwohl die Kurzschlussstromdichte j_{sc} leicht abnimmt. Dieser Wirkmechanismus des NaF-PDT wird abschließend auch durch SCAPS-Simulationen verifiziert. Der durchschnittliche optimale Wirkungsgrad Eff der Solarzellen beträgt 12,1% mit 622 mV V_{oc} , 29,6 mA/cm² j_{sc} und 65,6% Füllfaktor FF .

Als Zweites werden SiO₂-Punktkontakte an der CIGSe/ITO-Grenzfläche eingefügt, um S_b an der rückseitigen Grenzfläche zu verändern. Zum Vergleich verwenden wir Zellen mit Mo-Rückkontakt als Referenz für die SiO₂-Passivierungseffekte. In Übereinstimmung mit unseren früheren Arbeiten erhöhen die Punktkontakte die PV-Leistung der Mo-basierten Solarzellen. Die SiO₂-Passivierung verschlechtert jedoch die Leistung unserer ultradünnen CIGSe-Solarzellen auf ITO-Basis. SCAPS-Simulationen deuten darauf hin, dass die Barrierehöhe E_h an der CIGSe/ITO-Grenzfläche über die Wirkung der SiO₂-Passivierung (abnehmendes S_b) bei den ultradünnen CIGSe-Solarzellen entscheidet. Den Simulationen zufolge erhöht ein abnehmendes S_b die effektive Barrierehöhe $E_{h,e}$, wenn $E_h > 0,17$ eV (Schottky-ähnlicher Kontakt), was bedeutet, dass die Passivierung für den V_{oc} der ultradünnen CIGSe-Solarzellen nachteilig ist. Die CIGSe/ITO-Grenzfläche ist ein Schottky-ähnlicher Kontakt, so dass die SiO₂-Punktkontakte die Leistung der ITO-basierten BSTUT-CIGSe-Solarzellen verringern. Im Gegensatz dazu erhöht ein abnehmendes S_b die Sammlungseffizienz von photogenerierten Ladungsträgern, wenn $E_h < 0,17$ eV (quasi-Ohmscher Kontakt), so dass die Passivierung den Solarzellen zugutekommt. Das verringerte S_b erhöht $E_{h,e}$ leicht, aber das Gesamt- E_h für Solarzellen mit einem

quasi-ohmschen Kontakt ist gering. Die verbesserte Sammlungseffizienz der photogenerierten Ladungsträgern dominiert die Passivierungseffekte und wirkt sich positiv auf den Wirkungsgrad der Solarzellen aus. Die CIGSe/Mo-Grenzfläche offenbart einen quasi-Ohmschen Rückkontakt, so dass die Passivierung die Effizienz der ultradünnen CIGSe-Solarzellen auf Mo-Rückkontakt erhöht.

Als Drittes wird der vorder- und rückseitige Wirkungsgrad von BSTUT-CIGSe-Solarzellen unter Verwendung verschiedener Substrate (SLG und alkalifreies pgo-Glas), ITO-Dicken (100-400 nm) und NaF-PDT-Dosen (0-8 mg) optimiert. Solarzellen auf SLG-Basis zeigen aufgrund der zusätzlichen Integration von Na in den CIGSe-Co-Verdampfungsprozess eine bessere PV-Leistung bei Beleuchtung von der Vorderseite. Solarzellen auf alkalifreiem (pgo) Glas hingegen zeigen eine höhere Effizienz bei rückseitiger Beleuchtung, da dieses Glas insbesondere im langwelligeren Bereich eine höhere Transparenz als SLG aufweist. Das dickere ITO erhöht sowohl den vorder- als auch den rückseitigen V_{oc} der Solarzellen aufgrund der Burstein-Moss-Verschiebung in der ITO-Schicht, die den Valenzbandversatz ΔE_v an der CIGSe/ITO-Grenzfläche verringert. Allerdings ist die rückseitige Eff bei Solarzellen mit unterschiedlich dicken ITO-Schichten ausgeglichen, da dickeres ITO auch eine stärkere parasitäre Absorption bewirkt und zu einem niedrigeren rückseitigen j_{sc} führt. Bei BSTUT-CIGSe-Solarzellen mit unterschiedlichen NaF-PDT-Dosen ist der Trend der rückseitigen PV-Leistung ähnlich wie bei der Vorderseitenbeleuchtung. Die Solarzelle mit den optimalen Bedingungen (300 nm ITO, 4 mg NaF PDT) erreicht eine vorderseitige Effizienz von 11,8 % und eine rückseitige von 6,4 %.

Zuletzt werden zur Verbesserung der Gesamtlichtabsorption von BSTUT-CIGSe-Solarzellen SiO_2 -Nanopartikel (NP) an der CIGSe/ITO-Grenzfläche eingefügt. Die NP induzieren Wellenleitermoden und verstärken vorder- und rückseitige Absorption in der ultradünnen CIGSe-Schicht. Die NP induzieren auch eine Jet-artige Vorwärtstreue, die weiterhin die Sammlungseffizienz der photogenerierten Ladungsträger bei rückseitiger Beleuchtung erhöht. Im Vergleich zu den Referenzen erhöht sich für die BSTUT-CIGSe-Solarzellen mit SiO_2 -NP der vorderseitige j_{sc} um 4,1-4,4 mA/cm² und der rückseitige j_{sc} um 6,4-7,4 mA/cm². Die vorder- und rückseitige V_{oc} -Verstärkung der Solarzellen mit NP kann quantitativ abgeschätzt werden durch $V_{oc} = (nkT/q) \cdot \ln(j_{sc}/j_0 + 1)$, was bedeutet, dass die Passivierungseffekte der SiO_2 -NP im Vergleich zu den dominierenden Effekten des Lichteinfangs trivial sind.

Im Vergleich zu den aktuellen ultradünnen CIGSe-Solarzellen auf Mo-Basis (15 %) sind unsere BSTUT-CIGSe-Solarzellen noch verbesserungswürdig in der Leistungsfähigkeit, insbesondere was V_{oc} betrifft. Der Rekord- V_{oc} beträgt 733 mV für Mo-basierte und 635 mV für unsere ITO-basierten ultradünnen CIGSe-Solarzellen. Der j_{sc} -Rekord liegt jedoch bei 26,4 mA/cm² für Mo-basierte und 31,1 mA/cm² (Vorderseitenbeleuchtung) für unsere ITO-basierte Solarzellen mit lichteinfangenden SiO_2 -NP, was einen Vorteil der BSTUT-CIGSe-Solarzellen zeigt. Der bifaciale Wirkungsgrad beträgt 15,0 %, wenn wir 100 % Vorderseiten- und 30 % Rückseiten-Effizienz unserer besten Solarzelle aufaddieren, was nahe bei den 15,2 % Rekorderffizienz der ultradünnen CIGSe-Solarzellen auf Mo-Basis liegt. Die Ergebnisse dieser Arbeit können dazu beitragen, die Solarenergie mit höherem Wirkungsgrad und niedrigeren Herstellungskosten zu nutzen. Am Ende werden eine Zusammenfassung und einen Ausblick auf weitere Optimierungsmöglichkeiten von BSTUT-CIGSe-Solarzellen gegeben.

Chapter 1 Background and instrumentation

1.1 The status of Cu(In, Ga)Se₂ solar cells on the energy market

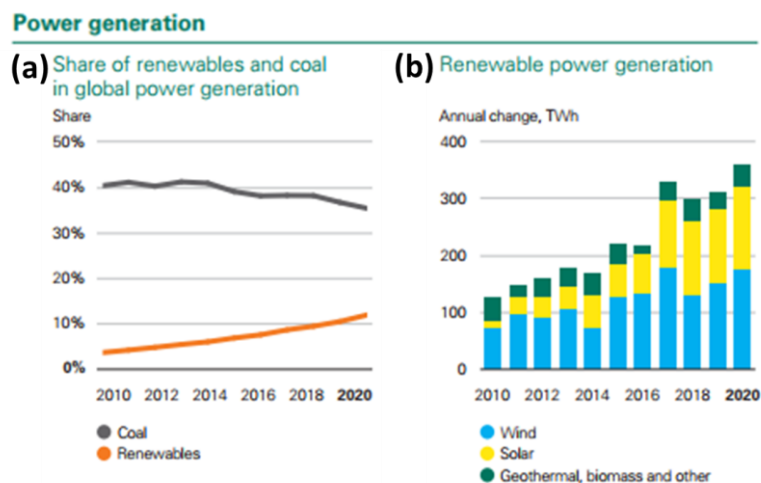


Figure 1-1. Renewable power generation and share of renewables and coal in global power generation. Adapted from reference [1]. Reprint right permitted by BP

According to the latest “Statistical Review of World Energy” from bp [1], renewable energy capacity (including biofuels but excluding hydro) continued to grow steadily. Because of Covid-19 pandemic breakout in 2019, the estimated global energy demand has fallen by 4.5% in 2020, which is the worst recession since 1945. However, the wind and solar capacity increased by a colossal 238 GW (gigawatt, 10^6 kW) – 50% larger than any previous expansion. More specifically, compared to 2019, solar capacity expands by 127 GW, while wind capacity grows by 111 GW. That is encouraging as renewable energy was relatively immune to the worst recession of overall energy demand. Even though the overall power generation fall by 0.9%, the share of renewables increased from 10.3% (in 2019) to 11.7% in 2020 (Figure 1-1 (a)). The capacity also increased. There was a 358 TWh (Terawatt-hours, 10^{12} kWh) increase in renewable power generation in 2020, which was the largest ever (Figure 1-1 (b)). If this increasing momentum holds on, renewables would take the place of coal shortly.

Apart from the increasing capacity and proportion of the energy market, the contribution of renewable energy to environment protection is also becoming more and more significant, especially the electricity powered by photovoltaic (PV) technology. Taking Germany as an example, the electrical energy generated by PV technology shows a tremendous increasing momentum from 2009 on, see Figure 1-2. The contribution can be more intuitively understood when counted as omitted greenhouse gas emissions. In 2020, the PV power plant decreased 35 million tonnes of CO₂ emission [2]. As the proportion of PV energy increases in the coming years, the contribution of omitted CO₂ emissions will also continue to increase.

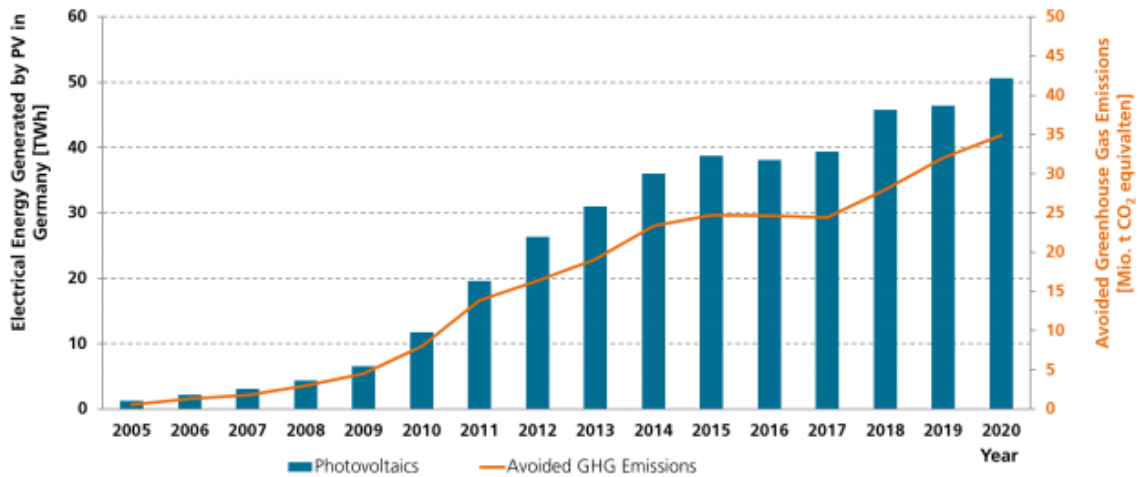


Figure 1-2. Electrical energy generated by PV in Germany and avoided GHG (green-house-gas) emissions [2]. Reprint right permitted by Fraunhofer ISE

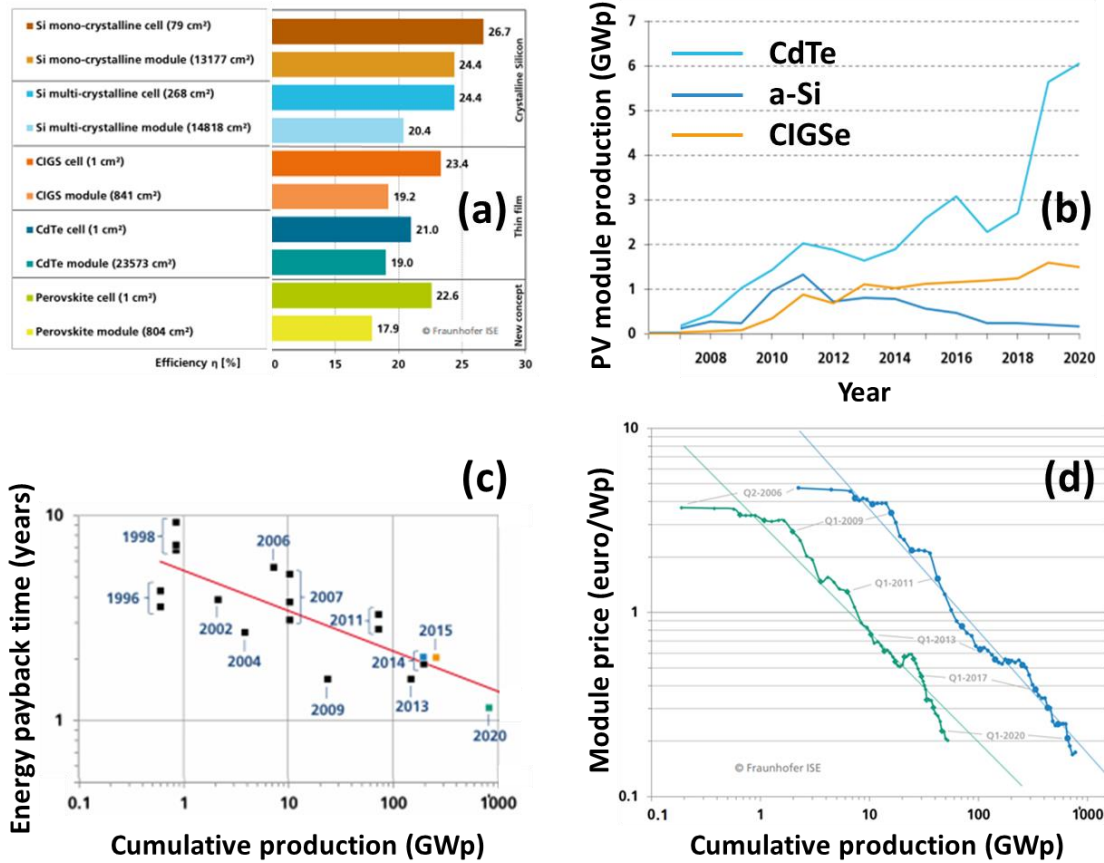


Figure 1-3. (a) Efficiencies of best lab cells versus best lab modules of different materials [3], (b) global annual production of thin film modules [2], (c) learning curve of the energy payback time, and (d) learning curves of the module price (blue circle is c-Si, green diamond is thin film) [2]. Reprint right permitted by BP and Fraunhofer ISE

Electrical energy is critical for a developed society because electricity drives most of the home appliances. Traditional power plants utilize fossil fuels such as coal and oil to generate electricity that emits tons of CO₂ and accelerates global warming. Solar cells, on the other hand, convert solar light into electricity with zero CO₂ emission. In addition, the solar light is abundant and free of charge. Also, employing a photovoltaic roof can minimize energy loss during power transmission. Those advantages of solar cells are critical in addressing crises like fossil energy running out and global warming. The proportion of CIGSe in the energy market is not high for now, but the meanings of research and develop it is undeniable. There is still plenty of room for decreasing the cost of fabrication and increasing the efficiency of the solar cells, which is the strongest motivation for this thesis.

Generally, the status of a product on the market share depends on many factors, such as the cost-performance ratio, brand propaganda, the relation between supply and demand, and consumer preference. In the case of solar panels, the deciding factors include but are not limited to the conversion efficiency, installation price, and payback time of the PV panel. Figure 1-3 (a) compares the best efficiency of laboratory cells and modules of the most common PV species. In the thin film category, compared to the CdTe, the CIGSe solar cells show small advantages of high efficiency in both laboratory cells and modules. Crystalline silicon (c-Si) exhibits the best performance in module efficiency. The high efficiency and economy of scale of the c-Si (including multi-crystal Si and mono-crystal Si) decide its dominant role in the PV market. According to the latest Photovoltaics Report from Fraunhofer ISE, the c-Si took up 95% of the production in 2020 [2]. Even though the thin film solar cells only share 5% of the PV market, the production in 2020 is 7.7 GW (1.5 GW of CIGSe solar cells). Figure 1-3 (b) shows that the module production of CIGSe solar cells has been growing steadily since 2009, and there is a growth momentum in the future.

For the customers, the installation price and payback time of the solar panels are their concerns when choosing PV products. The learning-by-doing framework or learning curves can estimate those two parameters. As the installed solar panels accumulate, the supply chain learns how to become more and more efficient, hence driving the installation costs progressively lower. Figure 1-3 (c) and (d) show the learning curves of the energy payback time (EPBT, for mono-crystal PV rooftop systems installed in southern Europe) and module price (inflation-adjusted, euro/Wp) [2]. As the cumulative production increase, the solar cells' EPBT and price tend to decrease, which is a virtuous cycle for both producer and customers. In the first quarter of 2020, module prices of the c-Si and the thin film are close: both around 0.2 euro/watt, corresponding to 773 GW of c-Si and 52 GW of thin film solar cell. However, for the cumulative production in Figure 1-3 (d), the fitting line shows that the thin film has a much lower module price than the c-Si when reaching the same cumulative production. In real life, the EPBT will also be influenced by the environment of installation, like the geographical location (latitude and weather condition), the maintenance, and the product quality of the PV panel. In short, when installation cost is low enough (comparable to coal cost) and EPBT is fast enough, choosing PV energy over traditional fossil energy will be an easy decision for customers to make in the future.

1.2 General structure and fabrication steps of CIGSe solar cells

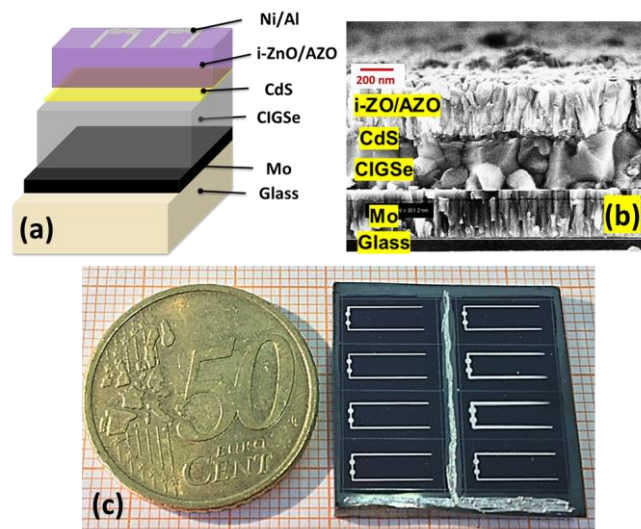


Figure 1-4. (a) General structure of the CIGSe solar cell, (b) cross-section of the solar cell taken with scanning electron microscopy (SEM), and (c) the appearance in real-life

As shown in Figure 1-4 (a) and (b), the general structure of a $\text{Cu}(\text{In,Ga})\text{Se}_2$ (CIGSe) solar cell consists of glass/Mo/CIGSe/CdS/i-ZnO/ZnO:Al(AZO)/Ni/Al. Detailed fabrication conditions and properties for each layer are as follows.

1.2.1 Glass substrate

Generally, soda-lime glass (SLG) is used as substrates for CIGSe solar cells because Na (14% Na_2O) from SLG can diffuse through Mo into the CIGSe during the high-temperature processes and improve the doping level of the semiconductor. The thickness of the SLG is 2mm. In contrast, this thesis also uses alkali-free barium borosilicate glasses (alkali content below 0.3%) to control the Na incorporation precisely for the CIGSe absorber. The alkali-free Coring 7059 glasses (pgo) are purchased from the PGO company and have a thickness of 0.7 mm. Before any usage, we clean all glasses with a standard procedure: 15 min ultrasonic cleaning in acetone, 15 min in isopropanol, and 15 min in deionized water. Then we blow the samples dry with a Ar pistol.

1.2.2 Back contact Mo (or $\text{In}_2\text{O}_3:\text{Sn}$, ITO)

Mo is commonly employed as the back contact because the interfacial MoSe_2 that forms during the CIGSe co-evaporation process can promote an Ohmic or quasi-Ohmic property at CIGSe/Mo interface. We purchase the Mo/glass substrates from Saint Gobain company, which have a 3-4 nm Si_3N_4 barrier between Mo and SLG to block the diffusion of Na. The thickness of Mo is around 350-400 nm.

An alternative, transparent back contact (TCO) material used in this thesis is $\text{In}_2\text{O}_3:\text{Sn}$ (ITO). We deposit ITO on cleaned pgo glasses by sputtering via Kurt J Lesker 75. In a 7.5×10^{-4} mbar argon atmosphere, we use 120 W direct current (DC) sputtering power to fabricate 100-400

nm ITO at a deposition rate of 2.0-2.5 Å/s. We vary the ITO thickness by extending the sputtering time. The substrate temperature uses room temperature for all ITO fabrications. The thickness of ITO is monitored by a calibrated quartz balance built into the chamber and further verified by a DekTak step profiler afterwards. The sheet resistance of the ITO is 10-20 Ω/□, which will drop below 10 Ω/□ after the 3-stage co-evaporation processes.

1.2.3 Absorber Cu(In,Ga)Se₂

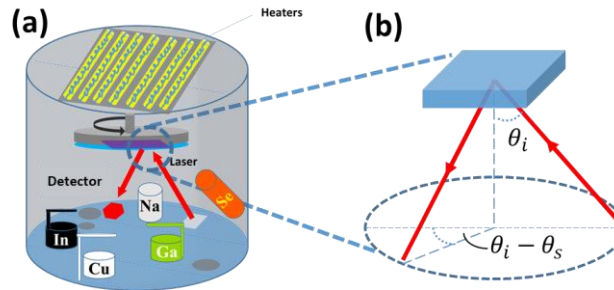


Figure 1-5. (a) Layout of the PVD (physical vapour deposition) chamber for co-evaporation of CIGSe; (b) zenith angles of the LLS (laser light scattering) light path. θ_i is the incident angle, and $\theta_i - \theta_s$ is the scattering light angle

Generally, we fabricate chalcogenide CIGSe with the 3-stage co-evaporation process. In our laboratory, we have adapted a special recipe to achieve good quality CIGSe with an ultrathin thickness (<500 nm) [4, 5]. The detailed mechanism and fabrication processes are as follows:

Figure 1-5 (a) show the layout of the five sources in our PVD (physical vapour deposition) chamber, including Cu, In, Ga, Na, and Se. The red arrows mark the laser light path in Figure 1-5 (b). We employ the laser light scattering (LLS) method to the supervise co-evaporation processes. Generally, the intensity of the light scattered from a film surface depends on the optoelectronic and morphological properties of the film. The scattered light often includes a combination of effects, and a clear assignment is difficult. Therefore, empirical observations rather than analytical evaluations are the basis for applying this method for in-situ monitoring. Nevertheless, we correlate the optical effects to a particular event during film growth, as shown in the next paragraph [6].

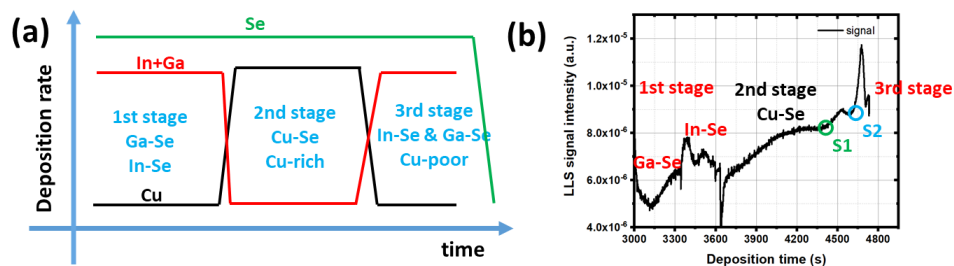


Figure 1-6. (a) Deposition rate of the materials during the 3-stage method and (b) a typical LLS (laser light signal) monitoring record for ultrathin CIGSe absorber. In the first stage of figure (b), Ga-Se is first deposited so we can see a Ga interference. Then followed by the In-Se deposition, which also can be distinguished by the narrower LLS interference

We modify the classic 3-stage method with a lower temperature for the second and third stage to obtain an ideal α phase CIGSe absorber with a chalcopyrite structure [7]. Specifically,

in the first stage, Ga-Se and In-Se are co-evaporated onto the substrates sequentially at a substrate temperature of 410°C. The second stage uses 450°C substrate temperature to deposit Cu-Se. As the content of Cu in the thin film increases, the superstructure chalcopyrite β phase will slowly change to the $\alpha+\beta$ [8]. Compared to the first stage, the increased substrate temperature in the second stage is beneficial for the formation of the α phase. Figure 1-6 (a) shows the deposition rate of each element in the 3-stage co-evaporation and (b) shows the corresponding LLS signal intensity. Usually, the stoichiometry point S1 (marked in green) is hard to distinguish. The S2 (marked blue) is relatively easier to locate as it comes along with a significant increase in LLS intensity. The reason is that when the Cu/(Ga+In) ratio (CGI) in the thin film exceeds 1, the liquid Cu-Se would be floating on the surface of the film, which enhances the reflection of laser light tremendously [9]. At the designed CGI ratio point (usually around 15-20 seconds after S2), we close the Cu source and open Ga/In sources simultaneously until the overall CGI decreases to the 0.85-0.9 range.

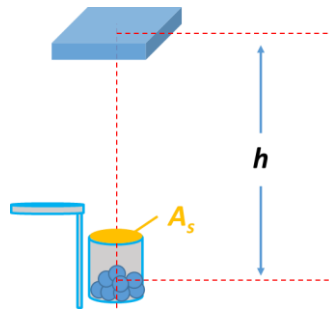


Figure 1-7. Geometry of the evaporation process in the PVD chamber

For the evaporation process, according to the theory of Langmuir-Knudsen, the evaporation rate R_{evp} (g/s) is [10]:

$$R_{evp} = 5.83 \times 10^{-2} A_s \sqrt{\frac{m}{T}} P_e \quad (1-1)$$

A_s is the source area as shown in Figure 1-7 (in cm^2), m is the gram-molecular mass (g/mol), T is the absolute temperature in K, and P_e is the equilibrium vapour pressure in the evaporation source/chamber. Presuming the substrate is right above the source cylinder and horizontal, we can express the deposition velocity v_{dep} as:

$$v_{dep} = \frac{R_{evp}}{\pi N h^2} \quad (1-2)$$

in which N is the density of the material (atoms or grams per cm^3), and h is the perpendicular distance between the source and substrates. In our case, the substrates are not directly on top of the evaporating sources. We should include a tilted angle in the expression above to precisely calculate the velocity. However, A_s and h in our PVD are fixed constants. So, the deposition rate v_{dep} is still proportional to the equilibrium vapour pressure in the evaporation source/chamber P_e after we include a tilted constant (N dependent on the material type, P_e the vacuum of the PVD).

1.2.4 Buffer layer CdS

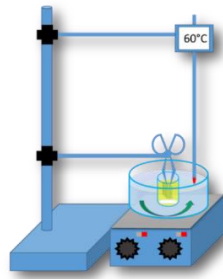
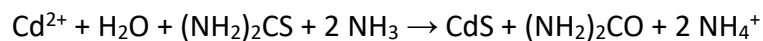


Figure 1-8. Setup for chemical bath deposition

This thesis utilizes cadmium sulphide CdS as a buffer layer to reduce the lattice mismatch between CIGSe and ZnO layers and modify the band alignment. In a Griffin form beaker, we mix 5 ml cadmium acetate in ammonium hydroxide with 3.75 ml thiourea and 41.25 ml water (in total 50 ml), as shown in Figure 1-8. The Griffin form beaker (yellow part) is put into a 60 °C water bath in the flat crystallizer for 8 min. We use an electromagnetic stirrer to ensure the solution is mixed and CdS homogeneously formed on the samples following the formula [100]:



(1-3)

The thickness of the CdS is around 50-80 nm.

1.2.5 Window layers i-ZnO/AZO

In 100sccm argon and 4sccm oxygen flux, we fabricate 80 nm intrinsic ZnO (i-ZnO) by sputtering with 120 W power upon an intrinsic ZnO target. Then we coat 300 nm ZnO: Al by 400 Watt in 100sccm argon flux with an Al-doped ZnO target. After the sputtering, we verify the ZnO thicknesses by the DekTak step profiler. The sheet resistance of the window layers (i-ZnO/AZO together) is around 20-40 Ω/\square . Both ZnO layers use alternative current (AC) sputtering at 6.0 *E-3 mbar pressure with a substrate temperature of 120 °C.

1.2.6 Front grids Ni/Al

We evaporate 10 nm Ni and 2 μm Al as front grids for the CIGSe solar cells to efficiently collect photogenerated carriers and contact with external circuits. The Ni/Al is deposition uses thermal evaporation of metal pellets in tungsten containers.

1.2.7 Completion of the CIGSe solar cells

We have completed CIGSe solar cells after mechanically scribing, as shown in Figure 1-4 (c). We scribe each sample (2.5 cm * 2.5 cm) into eight solar cells (1 cm * 0.5 cm) for further characterization and analysis.

1.3 Ultrathin Cu(In,Ga)Se₂ solar cells on Mo back contacts

Reducing the thickness of CIGSe absorbers is a practical strategy to cut down the consumption of raw materials in the fabrication processes, especially for rare materials indium and gallium. Ultrathin CIGSe (<500 nm) solar cells attract many research interests, as their theoretical efficiency is competitive with the general thickness (2-3 μm) CIGSe under ideal conditions. The most successful CIGSe solar cell was fabricated on Mo so far, so we will review the development of Mo-based CIGSe first and then ITO-based to see how the thickness influences the PV performance of the solar cells.

In state-of-the-art Mo-based CIGSe solar cells, according to Mollica's review in her 2017 thesis [11], j_{sc} clearly shows a decreasing trend when the thickness decreases, even though those results come from different research institutes. From an optical perspective, light absorption in thinned CIGSe is insufficient. Therefore, an anti-reflection layer or light trapping nanoparticles are introduced into Mo-based CIGSe solar cells to enhance light absorption. From an electrical perspective, recombination deteriorates the j_{sc} of solar cells [12]. Passivation layers like Al₂O₃ and SiO₂ can decrease the j_{sc} loss from recombination at the CIGSe/Mo interface. The V_{oc} decreases slightly for the thinned CIGSe solar cells. As an indicator of shunt resistance and series resistance, the FF shows fluctuations due to the different fabrication conditions from group to group. The conversion efficiency Eff shows a decreasing trend for thinner absorbers. However, with proper light management and passivation technologies, we believe Eff of the ultrathin CIGSe will catch up with the general CIGSe shortly.

Since 2016, there is also much outstanding research on Mo-based CIGSe solar cells. To see the direction of the optimization, here we name a few:

- (1) Salomé et al., in 2018, reached 9.7% with 350 nm CIGSe on Mo. They employ an Al₂O₃ passivation layer at CIGSe/Mo back interface [13]. In 2021, they optimized to 11.7% with SiO_x passivation layer at the back interface [14].
- (2) Mansfield et al. from NREL, in 2018, achieved 15.2% with 500 nm CIGSe on Mo by optimizing the Ga notch at the back of the absorber [15]. So far, this is the highest world record of ultrathin CIGSe on Mo-based substrates.
- (3) Nakamura et al. from AIST, in 2019, reached 23.4% Eff with 2000 nm CIGSe on Mo, employing a wider bandgap Cd-free buffer layer [16].
- (4) Schneider et al., in 2020, accomplished 11.8% efficiency with 600 nm CIGSe on Mo. They developed a specially structured back reflector to enhance light absorption [17, 18].
- (5) Gouillart et al., in 2020, marked 13.5% Eff with 510 nm CIGSe on reflective back contact and Al₂O₃ [19].

So far, the highest efficiency of ultrathin CIGSe solar cells on Mo comes from Mansfield et al. [15]. Their V_{oc} reached 733 mV, as high as the 2000 nm CIGSe of 734 mV (of Motoshi Nakamura et al. group). But the j_{sc} is only 26.4 mA/cm², much lower than the 39.6 mA/cm² of

the 2000 nm thick solar cells. As many simulations have predicted, the most promising strategy to improve the efficiency of ultrathin CIGSe solar cells is light management, which will be further reviewed and discussed in the following section 1.4 [20].

1.4 Cu(In,Ga)Se₂ solar cells on transparent-conductive-oxides back contacts

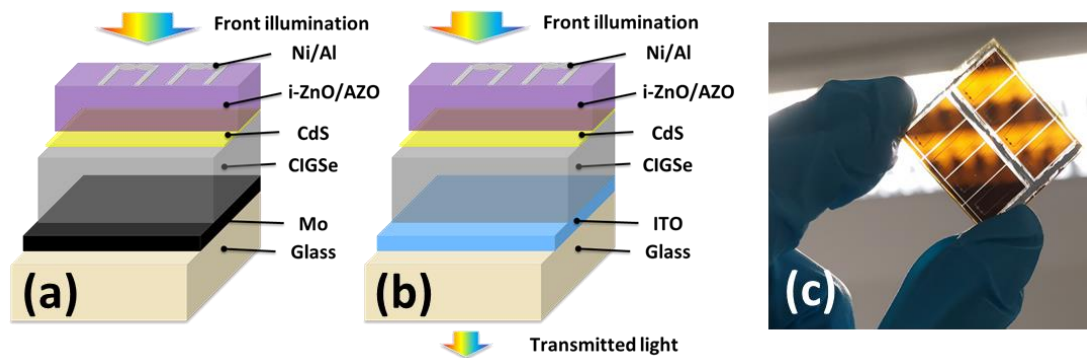


Figure 1-9. From (a) Mo-based to (b) ITO-based CIGSe solar cells, and (c) ITO-based solar cells in real life

In conventional CIGSe solar cells, Mo is chosen as the back contact because the MoSe₂ compound that forms during the CIGSe co-evaporation process can promote a quasi-Ohmic junction between CIGSe and Mo [21]. However, as an opaque metal, Mo induces parasitic light absorption [22] and opaque panels, as shown in Figure 1-9 (a). If we replace Mo with a transparent conductive oxide (TCO) material such as In₂O₃: Sn (ITO) (Figure 1-9 (b)), then part of the front illumination can penetrate through the solar cells to be used further or reflected back into the solar cells (Figure 1-9 (c)). In addition, the solar cells can simultaneously utilize the light from the front and rear sides. According to Yin et al., the reflectivity of the CIGSe/ITO interface is higher than CIGSe/Mo, which can further increase the j_{sc} for ITO-based ultrathin CIGSe solar cells [22]. In short, the TCO back contacts can increase the j_{sc} of ultrathin CIGSe solar cells and enable further exploitation of the transmitted light.

We review the evolution history of CIGSe on TCO back contacts to better understand the challenges and opportunities in TCO-based CIGSe solar cells, as summarized in *Table 1-1*. The earliest replacement of the back contact comes from Nakada et al. in 2004 [23]. He tried many TCOs with different CIGSe thicknesses (2000 nm and 700 nm) and compositions (like CuGaSe₂) and found that the ITO is the best choice. After that, many groups follow this idea to optimize CIGSe thicknesses, TCO material types, and back interfaces (CIGSe/TCOs) to obtain higher efficiency with a thinner absorber. It is worth pointing out that even some of the publications use TCOs as back contacts, but they only focus on the front illumination PV performance and leave out the rear illumination. Among those results, with the ultrathin CIGSe absorber (≤ 500 nm), Park et al. report the highest efficiency of 7.1% under rear illumination and attribute it to the ultrathin glass substrate (200 μ m). Keller et al. [24], Scheer et al. [17, 18] have close high front illumination efficiency with 600 nm CIGSe, and Collin et al. [19, 25, 26] mark the highest front efficiency of 13.5%.

Table 1-1. State-of-the-art CIGSe solar cells on TCO back-contacts. Abbreviations: ITO ($In_2O_3: Sn$), FTO ($In_2O_3: F$), AZO ($ZnO: Al$), IOH ($In_2O_3: H$), AGS (sulfurized AgGa), CIGSSe (Sulphur included CIGSe)

Group/year/reference	Back-contact material	Absorber/thickness/method	Front/rear efficiency (%)	Critical notes
Nakada et al./2004/[23]	ITO	CIGSe/2 μm /3-stage	15.2/-	
	ITO	CIGSe/700 nm/3-stage	12.6/4.9	
	FTO	CIGSe/2 μm /3-stage	13.7/-	
	AZO	CIGSe/2 μm /3-stage	12.8/-	Superstrate configuration and ZnO buffer
	ITO	CGS/1 μm /3-stage	4.0/-	
Negar et al./2016/[27]	AZO	CIGSe/450 nm/single stage	9.2/7.7	With Cu reflector
	FTO	CIGSe/450 nm/single stage	11.4/6.6	With Cu reflector
Park et al./2016/[28]	ITO	CIGSe/230 nm/single stage	5.9/-	Insert 45 nm AGS
Park et al./2019/[29]	ITO	CIGSe/450 nm/single stage	9.4/-	Insert 6 nm WO_x
Park et al./2020/[30]	ITO	CIGSe/500 nm/single stage	10.5/7.1	200 μm glass substrate
Kim et al./2016/[31]	ITO	CIGSSe/250 nm/precursor + selenization	6.5/3.5	Insert amorphous Si layer
Collin et al./2020/[19, 25, 26]	ITO	CIGSe/510 nm/3-stage	13.5/-	With reflective back and Al_2O_3
Scheer et al./2021/[17, 18]	ITO	CIGSe/300 nm/3-stage	8.5/-	
	ITO	CIGSe/550 nm/3-stage	10.9/-	
	ITO	CIGSe/1020 nm/3-stage	11.9/-	
	ITO	CIGSe/600 nm/3-stage	11.8/-	With structured back reflector
Keller et al./2018/[24]	IOH	CIGSe/650 nm/3-stage	11.0/6.0	With 210 nm IOH
Yin et al./2019/[32]	ITO	CIGS/380 nm/3-stage	8.4/-	Back interface passivation with SiO_2
Schmid et al./2017/[33]	ITO	CIGSe/390 nm/3-stage	10.0/-	Optimized the light trapping with nanoparticles along with reflective mirror

According to the literature reviewed above, the main factors that limit the efficiency of TCO-based solar cells include:

- (1) TCO layer (like ITO) may hinder the Na diffusion from the soda-lime glass (SLG) substrates;
- (2) The conductivity of the TCO is damaged after the TCOs go through high-temperature processes like 3-stage co-evaporation of CIGSe;
- (3) There are unexpected compounds (like GaO_x) formed at the CIGSe/TCO interface, which impede the collection of photo-generated carriers.

We must address those three aspects to improve the efficiency of TCO-based CIGSe solar cells, as will be shown in this thesis.

1.5 Bifacial semi-transparent ultrathin $\text{Cu}(\text{In,Ga})\text{Se}_2$ solar cells

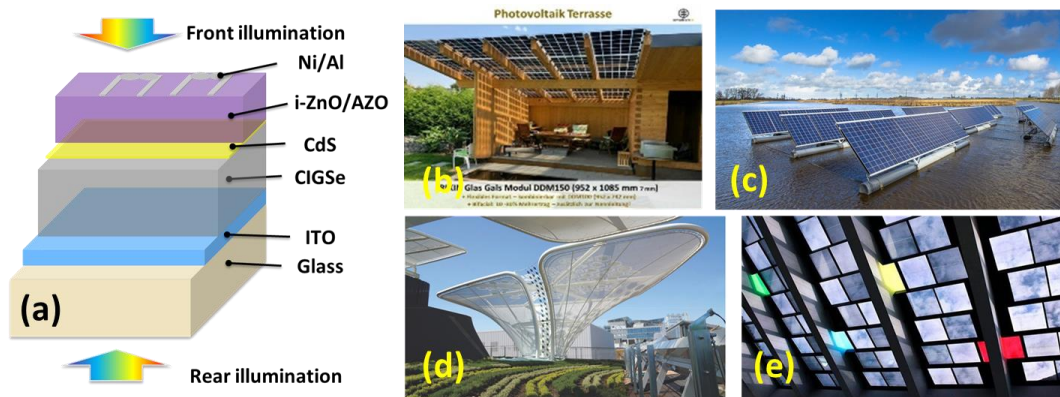


Figure 1-10. (a) The idea of bifacial semi-transparent ultrathin (BSTUT) CIGSe solar cells. Application scenarios: (b) semi-transparent photovoltaic terrace [34], (c) PV installation on water [35], (d) modern architecture [36], (e) semi-transparent photovoltaic window glasses [37].

Lately, bifacial semi-transparent ultrathin (BSTUT) CIGSe solar cells that combine the ultrathin absorber and transparent back contact (TCO) have attracted more and more attention. In that way, BSTUT CIGSe SCs combine the advantages of the ultrathin absorber and TCO back contacts: less raw material consumption in the fabrication processes and both the front and rear illumination can be utilized (Figure 1-10 (a)). In addition, TCO-based ultrathin CIGSe solar cells exhibit transparency in the visible wavelength range. That widens the application scenarios as shown in Figure 1-10: (b) semi-transparent photovoltaic terrace, (c) a photovoltaic system above water that combines with aquaculture, (d) semi-transparent photovoltaic tree and (d) window glasses [34-37]. The semi-transparency of the panels enables compatibility with various architectures and efficiency enhancement since both the front and rear illumination lights can be utilized by the solar cells. Compared to the Si-based modules that dominate the massive photovoltaic power plant, BSTUT solar cells have the advantages of flexibility and light-weight. Therefore, BSTUT is a better fit for building-integrated windows/roofs and vehicle integrated PV (VIPV).

Based on the literature review in section 1.4, we must fulfil three criteria to achieve a successful BSTUT solar cell: (1) ultrathin absorber, (2) transparent back contact, (3) high efficiency. Judging by the state-of-the-art listed in section 1.4, for the CIGSe with ultrathin absorbers, the *Eff* of TCO-based solar cells is approaching the Mo-based solar cells. However, most studies focus on the front efficiency and leave out the rear efficiency optimization. For a successful BSTUT solar cell, the PV properties under rear illumination are as critical as the front ones. In this thesis, chapters 2-4 consider the front PV properties, and chapters 5-6 will characterize the front and rear PV properties. But before that, BSTUT solar cells require a high-quality ultrathin CIGSe. Na doping is unavoidable to obtain a high-quality absorber, as discussed in section 1.6.

1.6 Sodium doping for CIGSe solar cells

1.6.1 History of sodium doping for CIGSe solar cells

Researchers have recognized the importance of Na for CIGSe solar cells since 1993. Hedström et al. found that CIGSe solar cells on soda-lime glass (SLG) are significantly better than on borosilicate glass, sapphire, and alumina substrates [38]. Although the authors could not distinguish if the better PV performance is due to the (112) texturing or the presence of Na, they found a (112) preference in crystalline orientation and a higher Na concentration in the CIGSe on SLG. The authors focused on the presence of the Na, and their later studies showed that with a density of 10^{15} atoms/cm³ in the CIGSe, either the Na is added into the completed CIGSe on Na-free glass or diffused in from the SLG substrates, Na can increase the conductivity of the CIGSe [39]. In 1997, Granate et al. expanded the beneficial range of Na density for the solar cell to 0.005-0.5 at%. The PV performance of the CIGSe will deteriorate if the Na concentration approaches 1.0 at% [40]. Afterwards, most CIGSe solar cells directly employ SLG as substrates.

In 2005, Rudmann et al. brought attention to Na doping when fabricating CIGSe solar cells on flexible polymer foils [41]. They introduced a new Na incorporation method named post-deposition treatment (PDT) and achieved a 14.1% record efficiency on polymer substrates. In 2013, the same group further exploited potassium for the CIGSe PDT process and successfully reached the milestone of 20.4% efficiency for CIGSe solar cells on polyimide [42]. Again, in 2019, they incorporated another alkali element Rb and pushed the record efficiency to 20.8% on flexible substrates [43]. Lately, it is not sodium alone, but all the alkali elements are under severe research in the PV community [44-46]. Adding one type or mixing several types are tried out, which may breed the next breakthrough of the CIGSe solar cells [47]. For now, we focus on sodium alone.

1.6.2 Working mechanism of sodium doping

Researchers have been discussing the mechanism of Na in CIGSe since they discovered its beneficial effects in solar cells. However, they have no uniform conclusion in the PV community so far. But still, the previous theories are helpful before we go further. Here we name a few widely acknowledged effects and some controversial topics of Na doping.

- (1) Na ions can increase the hole concentration of CIGSe [48].
- (2) Na can hinder the intermixing of Ga and In, hence contribute to forming a steeper Ga notch in the CIGSe absorber that can reduce the recombination via field passivation effects [49, 50].
- (3) A Higher Na can induce a smaller grain size of the CIGSe films. Na congregates at the boundary of the CIGSe grains, but the effects of Na congregation are under sharp controversial debate. Nicoara et al. believe that Na can passivate the grain boundary [51], while Daniel Abou-Ras et al. think there is no evidence for the passivation effects of Na [52].

Muzzillo reviews the Na effects on the grain interior, boundary, and interface in reference [53].

Many simulations explore the specific defect types that Na can modify [54, 55]. Some researchers propose that Na can serve as a catalyser and promote the generation of compounds like Mo-Se and Cu-In-Se [56-58]. On top of all those discussions, one clear point is that Na has played a critical role in the history of CIGSe solar cell development. To fabricate a high-efficiency BSTUT CIGSe solar cell, we must handle the Na doping for the ultrathin CIGSe. When using the same method, the depth and quantity of Na incorporated into the ultrathin absorber may be different from the general case of 2 μ m CIGSe thickness.

1.6.3 Sodium doping for bifacial semi-transparent ultrathin CIGSe solar cells

We define a function $\phi(r,t)$ as the density of Na at location r and time t to qualitatively describe the Na depth distribution in the CIGSe. According to Adolf Fick's particle diffusion equation [59]

$$\frac{\partial \phi(r,t)}{\partial t} = D \nabla^2 \phi(r,t) \quad (1-4)$$

D is the diffusion coefficient (in m^2/s). The Na density in CIGSe is sensitive to the Na density gradient and proportional to the diffusion coefficient D . Meanwhile, the diffusion coefficient D in solids at different temperatures is generally found to be well predicted by the Arrhenius equation:

$$D = D_0 \exp\left(-\frac{E_A}{RT}\right) \quad (1-5)$$

D_0 is the maximum diffusion coefficient at infinite temperature, E_A is the activation energy for diffusion, T is the absolute temperature, and R is the universal gas constant [60]. Generally, the material type decides E_A and D_0 , so the temperature is a decisive factor for D in solids. In the case of Na diffusion from SLG, the depth and amount of sodium that diffuses into the CIGSe depends on the substrate temperature and material type of the back contacts. That is why ultrathin CIGSe on Mo and ITO back contacts have different Na incorporated after the same 3-stage co-evaporation.

In BSTUT SCs, to maintain a high conductivity of the ITO back contact, according to Tokio Nakada et al., the maximum substrate temperature should not exceed 520 $^{\circ}\text{C}$ during the 3-stage co-evaporation [23]. However, a lowered temperature for the CIGSe deposition deactivates the inter-diffusion of In-Ga. That leads to inhomogeneity of initial Ga in the precursor, thus resulting in a poor quality of multi-crystal CIGSe [61]. On ITO substrates, an adequate low substrate temperature and sufficient Na doping for the absorber should be satisfied simultaneously to obtain an optimal quality ultrathin CIGSe. For this reason, chapter

2 compares four different Na doping methods for ultrathin CIGSe solar cells. Chapter 3 optimizes the NaF PDT strategy in details to explore the optimal dose and working mechanism.

1.7 Modification of the back interface

1.7.1 The importance of the back interface

The back interface modification has attracted research interests in the PV community because it is critical when collecting photogenerated carriers [12, 62]. As listed in section 1.4, state-of-the-art ultrathin CIGSe solar cells insert a passivation/reflection layer at the back interface, such as Al_2O_3 , SiO_2 , and WO_x . Generally, the generation and separation of photogenerated carriers rely on the CIGSe absorber (including the neutral region and space charge region SCR) [63, 64], and the carrier collection depends on front contact layers (ZnO and Ni/Al) and back contacts. Passivation layers reduce the recombination hence increase the efficiency of collection. The CdS passivates front contact layers well, so we focus more on the back interface here.

On Mo metal substrates, the interfacial MoSe_2 that formed during the CIGSe co-evaporation converts the CIGSe/Mo Schottky into a quasi-Ohmic contact [65]. Generally, the work function of the metal and the electron affinity of the semiconductor decide the barrier height in a Schottky junction. The presence of MoSe_2 diminishes the back barrier height to a trivial degree. The CIGSe/Mo interface is critical for hole collection in a Mo-based CIGSe solar cell. But a detailed and direct investigation is impossible because the formation of the interface takes place during the CIGSe deposition. The interface is not final until the absorber preparation is completed [66]. In the last two decades, the formation conditions of MoSe_2 and its electrical characteristics have drawn tremendous research interest for photovoltaic application [67]. According to Abou-Ras et al., the MoSe_2 formation depends on the crystal orientation of Mo, on the Na concentration (NaF precursor thickness), and on the substrate temperature during the CIGSe co-evaporation [58, 68]. Before him, Kohara et al. also reported that Na diffusion from the SLG during the co-evaporation can promote the MoSe_2 formation and convert the Schottky-type Mo/CIGSe interface into a favourable Ohmic-type contact. Besides, by employing differential quantum efficiency, they calculated the bandgap E_g of MoSe_2 to be 1.41 eV [69]. Furthermore, Rostan and Daniel et al. tried to insert MoSe_2 with an E_g of 1.2 eV on ZnO: Al transparent back-contact and achieved 13.4% conversion efficiency [68, 70]. Because we aim to achieve a successful BSTUT solar cell, the knowledge about back interface modifications on Mo may also apply to the TCO-based solar cells.

In terms of the CIGSe/ITO interface, GaO_x may play the same role as MoSe_2 in Mo-based solar cells [29, 71-75]. Nakada et al. showed that GaO_x is a high resistance interlayer, which will block the carrier collection. Heinemann and Saifullah et al. revealed that Na doping tunes the GaO_x thickness. GaO_x with an optimized thickness can also function as a passivation layer at the CIGSe/ITO interface [29, 72, 74, 76]. Meanwhile, Son et al. proposed that the carriers go through the GaO_x layer by trap-assisted tunnelling. Chantana et al. believe that trap-assisted recombination can convert the CIGSe/ITO interface from a Schottky contact into a quasi-

Ohmic contact. However, Yin et al. proposed that NaF PDT (Post deposition treatment) can increase the defect density hence the recombination velocity to support the carrier transport.[75, 77, 78] Upon all those theories, one clear point is that GaO_x plays a critical role for the CIGSe/ITO interface, but how the working mechanism of GaO_x is still under disputation. As our final goal is to achieve high-efficiency BSTUT solar cells on TCOs, understanding the properties of the back interfaces is critical for modifying CIGSe/TCOs contacts.

1.7.2 Classic transport equations of the Schottky contact

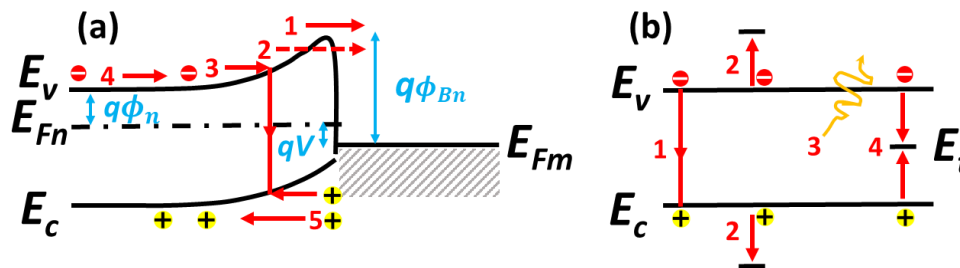


Figure 1-11. (a) Five basic transport processes of a Mott-Schottky contact under forward bias (metal connected to the positive side of the battery, semiconductor n-type): 1) thermionic emission, 2) tunnelling, 3) recombination, 4) diffusion of electrons, 5) diffusion of holes (b) four types of recombination: 1) band-to-band recombination; 2) Auger recombination; 3) radiative recombination and 4) recombination through single level traps (or Shockley-Read-Hall SRH recombination)

We start from the carrier transport mechanism in a basic structure of Schottky contact (semiconductor-metal). Figure 1-11 (a) shows the bandgap diagram between an n-type semiconductor and a metal to exemplify the carrier transport types in a Schottky junction. According to reference [79], which is everything outlines in the following base on, we can classify the process of carriers going through the Schottky barrier into five categories:

- (1) Thermionic emission of electrons over the potential barrier. That is the dominant process for Schottky diodes with a moderate doping level of the semiconductor ($< 10 \text{ E}17 \text{ cm}^{-3}$) operating at moderated temperatures (e.g., 300 K);
- (2) Quantum-mechanical tunnelling of electrons through the barrier, which is a typical process for heavily doped semiconductors and responsible for most Ohmic contacts;
- (3) Recombination in the space charge region;
- (4) Diffusion of electrons in the depletion region;
- (5) Holes injected from the metal that diffuse into the semiconductor (equivalent to recombination in the neutral region).

In practical circumstances, many other factors can influence those transport processes, like edge leakage current due to a high electric field at the junction margin or interface current caused by the trap states at the semiconductor-metal interface. But usually, current-voltage characteristics of the diodes predicted by those five types fit the experimental results well.

Among those five processes, recombination is most relevant to this thesis. Generally, recombination can be further classified into four types, as denoted in Figure 1-11 (b):

- (1) band-to-band recombination;
- (2) Auger recombination;
- (3) radiative recombination;
- (4) recombination via single-level traps (SRH recombination, Shockley-Read-Hall recombination).

In practical experiments, the dominating recombination type in a Schottky junction depends on its fabrication conditions, such as vacuum or air, substrate temperature, surface cleaned or plasma etched. Because under diverse fabrication conditions, the Schottky junction incorporates varying fixed charges, moveable ions, interface compounds, and lattice mismatch. Usually, we can quantitatively characterize the overall recombination current density j_{re} by the expression:

$$j_{re} = \frac{\Delta n}{\tau_n} = \sigma_n v_{th} N_t \Delta n = S_n \Delta n$$

(1-6)

in which Δn is the excess carrier density, τ_n is the lifetime of the minority carriers, σ_n is the electron captures cross-section, v_{th} is the thermal velocity, N_t is the trap state density, and S_n is the recombination velocity. j_{re} is proportional to N_t and S_n , which is the essence of the passivation mechanism: decreasing recombination via diminishing N_t or S_n .

In our case, on Mo back contacts, passivation of the interface has been proved a practical solution to reduce the N_t hence decreasing the interface recombination [13, 73, 80-89]. In most cases, Al_2O_3 , MgF_2 , and SiO_2 dielectric passivation layers benefit the PV performance of CIGSe solar cells. However, according to reference [90], opposite fixed charges may be introduced into the Schottky interface when their fabrication methods are different, even though the interfacial material is the same. In addition, what will happen on the TCO back contacts with passivation layers still need to be verified for our semi-transparent ultrathin CIGSe solar cells, as their carrier transport mechanism may differ from the Mo substrates. Therefore, in chapter 4, we will compare the passivation effects of SiO_2 point contacts on Mo and ITO.

1.8 Light management in Cu(In,Ga)Se₂ solar cells

As wave-particle dualism is the nature of light, optic theories need to adapt to the applying circumstances. For example, we should use wave optics when the objectives are comparable or smaller than the wavelength considered. When dimensions of the considering objects are longer than the wavelength, ray optics are sufficient. Therefore, if the thickness of the CIGSe is 2-3 μm and only uses reflective mirror for light management, ray optics is enough for simulation. However, when the thickness of the absorber is ultrathin (< 500 nm) while the inserted nanoparticles have a dimension in hundreds of nanometres, we should utilise wave optics. We introduce some fundamental ray and wave optics to help understand the light management mechanism in BSTUT CIGSe solar cells.

1.8.1 Ray optics perspective

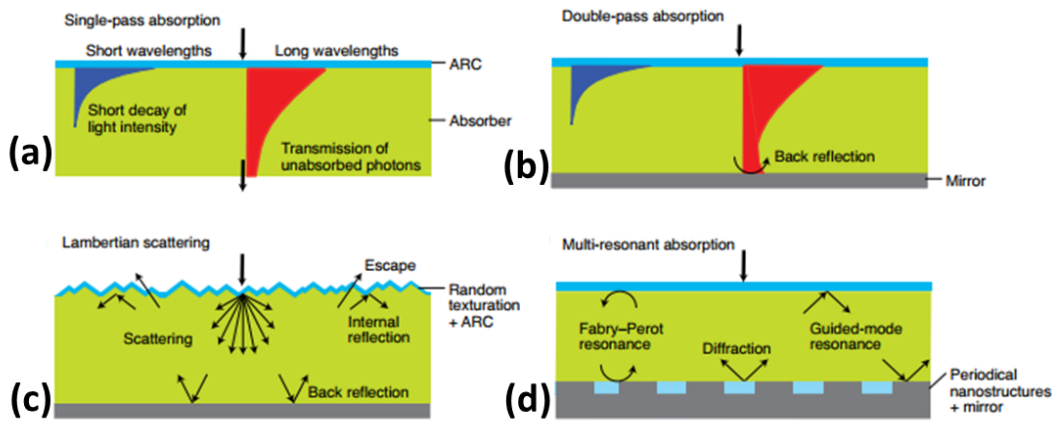


Figure 1-12. Light management types: (a) antireflection coating (ARC), (b) reflective back mirror, (c) random textured surface plus antireflection coating and back mirror, (d) antireflection coating plus periodic nanostructures and back mirror [91]. Reprint right permitted

The intrinsic material properties such as complex refractive index ($n + ik$) and thickness d determine the light absorption in a semiconductor layer. The absorption coefficient $\alpha = 4\pi\kappa/\lambda$ is strongly material- and wavelength-dependent [91]. Light management uses additional coatings, back mirrors, and texturing to affect the light propagation or trap the light in the solar cells. So, we define an optical path enhancement factor F to quantify the light trapping efficiency in a solar cell. The absorption A is a function of α , which is [91]:

$$A = 1 - \exp(-F\alpha d) \quad (1-7)$$

The thickness d of an ultrathin absorber is < 500 nm, while α of CIGSe is empirically considered a constant, so the goal of light management is to increase F hence enhancing A . According to the position within the multi-layered thin film solar cell, the light management layers can be classified into three types [91]:

(1) On top of the solar. For example, the anti-reflection coating (ARC) layer in blue in Figure 1-12 (a), and the diffusely scattering surface with textures (Lambertian) as shown in Figure 1-12 (c);

(2) At the bottom of the solar cell. Back-reflecting layer, as shown in Figure 1-12 (b);

(3) In the middle/interfaces of the solar cell/absorber. Light trapping layer, as shown in Figure 1-12 (d). In this case, when the structures are sufficiently small and the gratings can couple the light to waveguide modes, wave optics should be adapted for simulation.

The theoretical upper limit of F for different light management strategies is different. $F = 1$ represents no additional light management, and a perfect back reflector leads to $F = 2$. Based on the schemes described by Goetzberger and Yablonovitch et al., with random texture on the surface plus ARC and perfect internal reflections in the solar cell, Massiot et al. estimate that the maximum F is as high as 50 [91, 92], which they name as Lambertian scattering. With a periodic light trapping layer at the back interface, however, no general model is available to set the theoretical upper limit of F , even though Wang et al. predict that the F is capable to exceed the Lambertian scattering limit [93]. When nanoscale photonic structures interact with solar photons in a thin film solar cell, the conventional ray optics models break down and wave optics concepts are required to establish new performance limits [94]. In the following section, we will introduce some basic wave optics of resonance modes for further application in the thesis.

1.8.2 Wave optics perspective

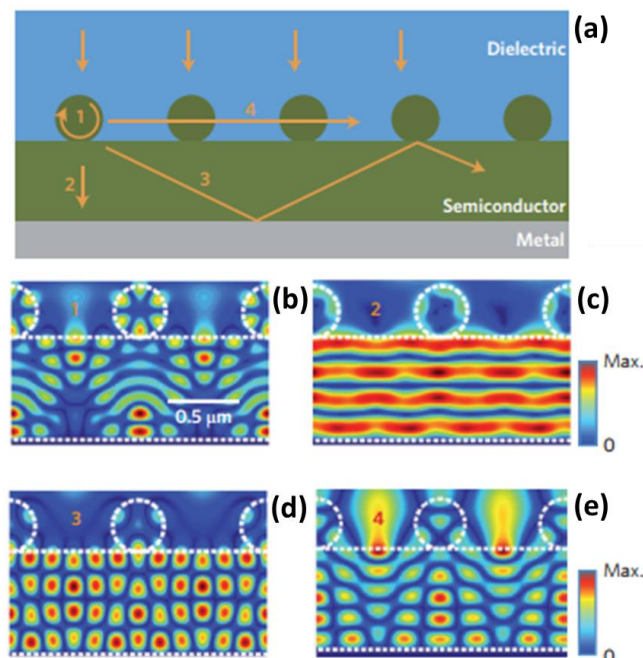


Figure 1-13. Absorption enhancement caused by the excitation of optical resonances in a thin film PV cell. (a) Schematic showing the location of distinct coupling mechanisms. (b)-(e) Electric-field-intensity distribution inside the solar cell for specific illumination conditions as follows: (b) incident wavelength $\lambda=880$ nm, (d) $\lambda=946$ nm, (e) $\lambda=1011$ nm with 0° incident angle; (c) $\lambda=1031$ nm and 28° angle [94]. Reprint right permitted by Dr. Brongersma

Aided by wave optic theory, we can predict light propagation in a multi-layered system by solving Maxwell's equations. The light absorption of each layer in a solar cell can be theoretically simulated. By adjusting the thickness, geometry structure, or (n, k) of the material (refractive index and absorption coefficient), the light absorption in the CIGSe can be optimized, hence achieving the best conversion efficiency for the solar cells. That is the fundamental mechanism of simulation for light management, which is a practical and valuable way of guiding the solar cell design for experiments.

To better explain the light trapping mechanism in wave optics theory, we take a $1\mu\text{m}$ Si-based solar cell as an example to illustrate the wave optics of different modes, as shown in Figure 1-13 [94]. In Figure 1-13 (a), orange arrows mark the propagation direction of the light. The light green circles illustrate a periodic array of c-Si (crystalline silicon) nanowires on top of the c-Si film. Four distinct coupling modes of the optical waves are labelled with 1-4 numbers from the classification of Brongersma et al [94]:

(1) Optical Mie resonances as shown in Figure 1-13 (b). We can see (inside the circles) that the resonances induced by the c-Si nanowires have a hexapolar symmetry. Under the c-Si nanowires, the resonances hybridize with a guided resonance;

(2) Low-quality-factor Fabry-Perot standing-wave resonances, as shown in Figure 1-13 (c). The reflecting top surface and metallic back-reflector confine the light in the solar cell;

(3) Guided resonances as shown in Figure 1-13 (d). The guided resonances have a periodic intensity distribution below and on the surface of the nanowires, which is a typical characteristic of the waveguide modes. Also, it is worth noting that there is a jet-like tail or a focused beam below the nanowires, which is similar to the forward scattering and will be critical to understanding the light trapping effects under rear illumination [22];

(4) Diffracted modes as shown in Figure 1-13 (e). The incident light is redirected into the plane of the nanowires layer. The concentrating field locates between the nano-wires gap.

From the intensity distribution in Figure 1-13, those four modes extend into the underlying semiconductor layer, where the light can be absorbed and utilized to enhance the PV performance of the solar cells.

1.8.3 Light trapping in bifacial semi-transparent ultrathin CIGSe solar cells under front and rear illumination

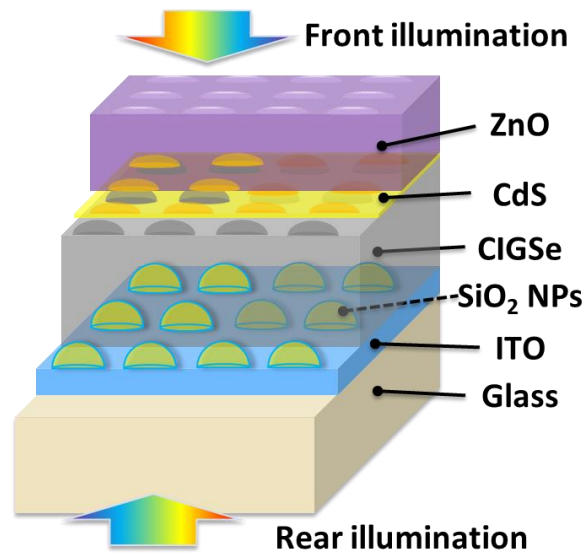


Figure 1-14. Location of the light trapping SiO_2 nano-particles (NPs) in BSTUT CIGSe solar cells

The latest photovoltaic research exploits all light management strategies shown in Figure 1-12 to increase the light absorption in ultrathin CIGSe solar cells. For example, Cho et al. add textured polydimethylsiloxane (PDMS) to the surface of CIGSe solar cells. The solar cells have a 322 nm thick single-stage co-evaporated absorber and ITO ($\text{In}_2\text{O}_3:\text{Sn}$) substrates. Their solar cells reach 10.5% front efficiency and 12.3% average transmittance [95]. Gouillart et al. design a type of reflective back contact made of a multilayer stack (50 nm ZnO: Al/150 nm Ag/30 nm ZnO: Al/100 nm $\text{In}_2\text{O}_3:\text{Sn}$ /3 nm Al_2O_3) that is compatible with 500 °C of CIGSe deposition and achieve 13.5% efficiency with 510 nm CIGSe [19]. Yin et al. employ SiO_2 nanoparticles fabricated by SCIL (substrate conformal imprint lithography) method and obtain 10% efficiency with 390 nm CIGSe [33]. Highly reflective metals like Au and Ag have also been compared and introduced in a superstrate configuration to enhance the j_{sc} to a different degree [25, 26, 96].

However, most research is limited to front-light trapping. For a successful BSTUT CIGSe solar cell, the efficiency under rear illumination shown in Figure 1-14 is equally important as the front efficiency. Therefore, chapters 5 and 6 optimize the rear and front PV performance of the BSTUT CIGSe solar cells together. From a simulation perspective, light trapping via periodic nanoparticles is a promising method to boost the front and rear j_{sc} of BSTUT CIGSe solar cells. Yin et al. theoretically predict that the rear j_{sc} can be enhanced by 4 mA/cm^2 if the optimal light trapping nanoparticles were inserted at CIGSe/ITO interfaces and a reflection mirror added on the AZO layer. Chapter 6 mainly explores the light trapping effects of SiO_2 nanoparticles in BSTUT CIGSe solar cells to verify this prediction.

1.9 Characterization method, analysis model, and simulation software

1.9.1 Current-voltage (IV) and temperature dependent current-voltage (IVT) characteristics

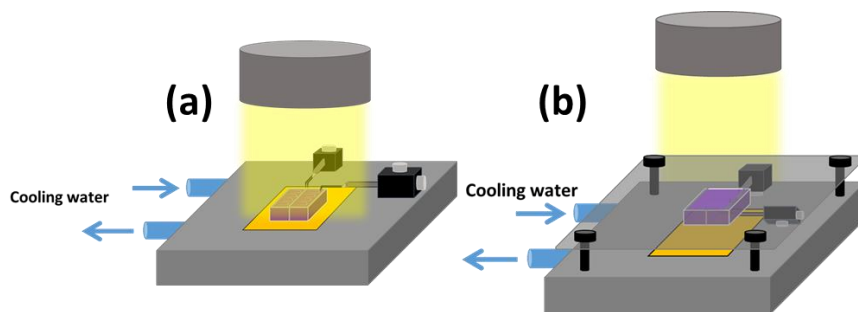


Figure 1-15. Schematic of the bifacial IV measurement setup. (a) front illumination and (b) rear illumination

Current-voltage (IV) characteristics are a fundamental but effective method for evaluating the performance of the solar cells. Figure 1-15 shows a setup for front and rear illumination IV measurements to characterize the PV properties of BSTUT solar cells, in which (a) is for front illumination while (b) for rear illumination. The AAA solar simulator uses a xenon and a helium lamp to simulate the solar spectrum under air mass 1.5 (AM1.5) conditions. The sample holder is a water-cooled plate made of brass, to keep a constant temperature of 25 °C. Also, the brass can reflect part of the transmitted light into the BSTUT solar cell, which results in a higher j_{sc} and probable higher V_{oc} for the testing sample. When the measuring sample has certain transparency, we should put a black cloth or paper between the brass plate and the testing solar cell to avoid reflection.

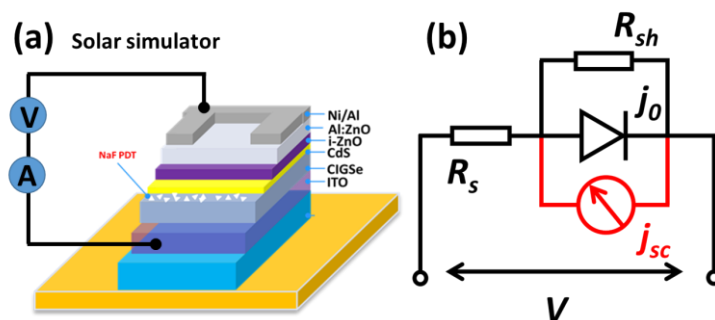


Figure 1-16. (a) schematic figure of IV (current voltage) measurements and (b) equivalent circuit of the classic one diode model

Thoroughly understanding the IV characteristics of an ultrathin CIGSe solar cell can be challenging, as a solar cell has so many layers. Yet, the information we can learn from the IV curve is valuable for evaluating and optimizing the efficiency of solar cells. As denoted in Figure 1-16 (b), this thesis processes IV curves with the classic one diode model to simplify the analysis processes. R_s and R_{sh} correspond to series and shunt resistance of the diode, respectively. j_0 is the dark saturation current density, while j_{sc} is the short circuit current density of the diode. V is the bias voltage imposed on the solar cell. According to the Shockley diode equation [97]:

$$j = j_0 \exp\left(\frac{q}{nkT}(V - R_s j)\right) + \frac{V}{R_{sh}} - j_{sc} \quad (1-8)$$

in which j is the overall current density flowing through the device, n is the ideality factor of the diode, k is the Boltzman constant, and T is the absolute temperature. The dark saturation current density j_0 is:

$$j_0 = j_{00} \exp\left(\frac{-\Phi_b}{nkT}\right) \quad (1-9)$$

where j_{00} is the prefactor of the dark current that depends on the dominating recombination mechanism in the device, and Φ_b is the barrier height of the diode. Combining equations (1-8) and (1-9), we obtain the open circuit voltage V_{oc} at $j = 0$:

$$V_{oc} = \frac{\Phi_b}{q} - \frac{nkT}{q} \ln\left(\frac{j_{00}}{j_{sc}}\right) \quad (1-10)$$

By which we can deduce Φ_b via extrapolating T to 0. According to Hegedus et al., when $T \rightarrow 0$, $V_{oc} \rightarrow E_g/q$, where E_g is the bandgap of the primary light-absorbing layer [97]. If the dominant recombination occurs in the absorber layer, then $\Phi_b = E_g$. When a back contact diode with a barrier height E_h is in series connection with the main diode, and the back diode has an opposite direction to the main diode, then we should modify the expression of Φ_b [33]:

$$\Phi_b = E_g - E_h \quad (1-11)$$

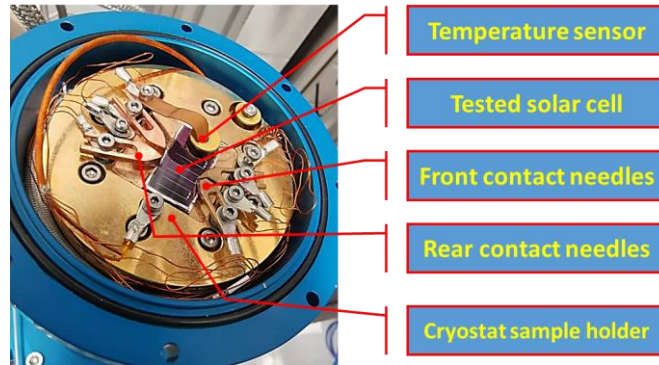


Figure 1-17. The cryostat used for temperature dependent current-voltage (IVT) measurements

This formula is helpful when interpolating the temperature-dependent current-voltage (IVT) characteristics of the BSTUT solar cells. Figure 1-17 displays the setup used for IVT measurements. It consists of a cryostat that uses a closed-loop liquid He cooling system and a set of contacting needles for low temperature IV measurements.

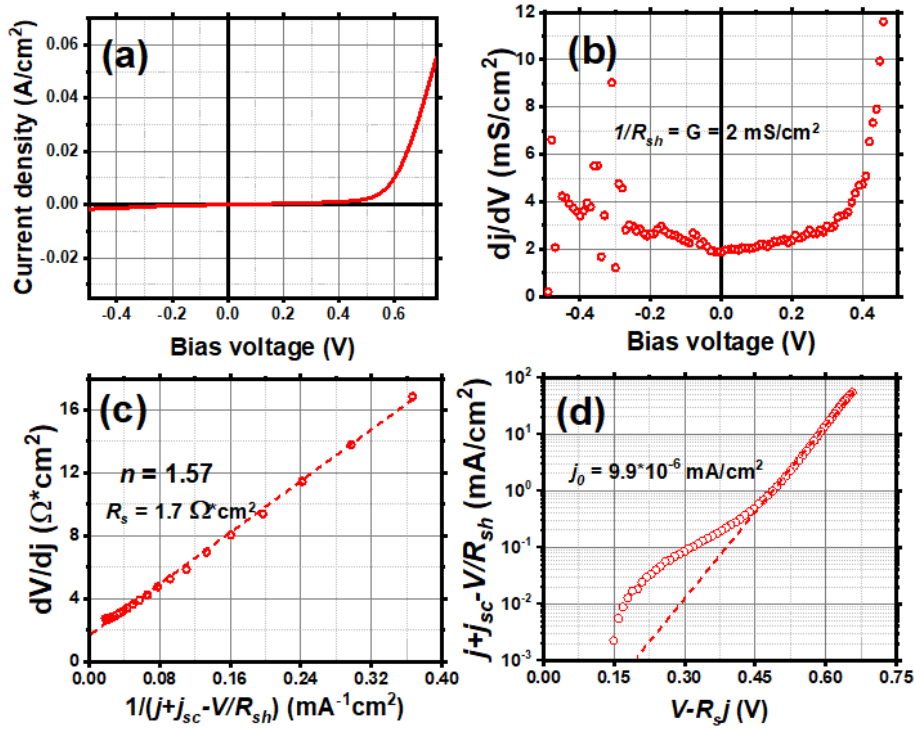


Figure 1-18. Hegedus method for diode parameter extraction from the dark IV characteristics of a well-behaved ultrathin CIGSe solar cell on Mo. (a) standard IV curve in dark condition, (b) Shunt conductance G , (c) Series characterization for R_s and n , (d) $\ln(j+j_{sc}-V/R_{sh})$ with fit used to extrapolate j_0

We extract the PV performance of solar cells from the IV characteristics under AM1.5 illumination. Here we focus more on the diode parameters extraction from the light or dark IV curves, as the software can extract PV parameters generally. The dark IV curves are measured by turning off the solar simulator. Two methods are available for diode parameter extraction based on the one diode model. Method one can be referred to as the Hegedus method, as it is recommended by Hegedus et al. The Hegedus method includes four successive plots, as shown in Figure 1-18 [97]:

(a) A standard rectifying IV curve under dark conditions. The V_{oc} , j_{sc} , FF , and E_{ff} usually can be extracted or derived from the light illuminated IV curve (not shown here).

(b) A plot of the derivative dj/dV against V . By this figure, we can determine the shunt conductance G_{sh} which equals the reciprocal of the shunt resistance R_{sh} . G_{sh} is usually taken near j_{sc} or in the reverse bias region where the diode term in equation (1-8) becomes negligible.

(c) Also, from equation (1-8), the derivative of the voltage equals the resistance $r(j)$:

$$r(j) \equiv \frac{dV}{dj} = R_s + \frac{nkT}{q} (j + j_{sc})^{-1}$$

(1-12)

A correction should be made to the abscissa $(j + j_{sc})^{-1}$ when the R_{sh} is not negligible, as shown in Figure 1-18 (c) of $(j + j_{sc} - V/R_{sh})^{-1}$. Then the intercept with the ordinate is R_s while the slope is nkT/q (thermal kT/q equal to 0.0259 eV at room temperature).

(d) A semi-logarithmic plot of $(j + j_{sc} - V/R_{sh})$ against $(V - R_s j)$ using the R_s obtained from the plot (c):

$$\ln \left(j + j_{sc} - \frac{V}{R_{sh}} \right) = \frac{q}{nkT} (V - R_s j) + \ln (j_0)$$

(1-13)

From equation (1-13), the intercept is j_0 of the diode.

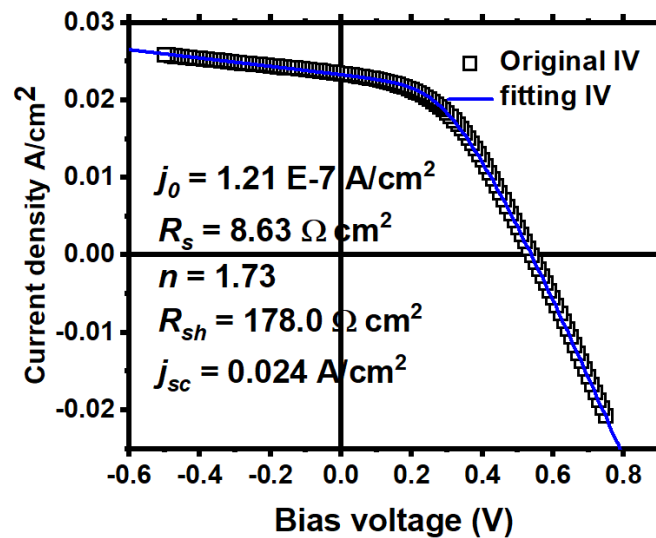


Figure 1-19. Example fitting curve of the experimental IV result (open squares) by the nonlinear implicit diode equation

Now we move on to the second extraction method. The Hegedus method gives accurate and reliable diode parameters. However, the analysis procedure requires plotting and extrapolating, which is time-consuming. Because we need to analyse lots of solar cell samples, here we introduce another faster method with the aid of e.g. Origin software. This method is called the nonlinear regression method. The algorithm of the nonlinear regression method starts by defining a function f to calculate the deviation between the experimental current density j and the one diode model current:

$$f = j + j_0 \left(\exp \left(\frac{q(V + jR_s)}{nkT} - 1 \right) \right) + \frac{V + jR_s}{R_{sh}} - j_{sc}$$

(1-14)

R_{sh} is the differential result at 0 bias, R_s is the differential result at the V_{oc} bias point, and j_{sc} is the crossing point of IV curves with the y-axis. By adjusting j_0 and n , Origin can find the minimum value of f , which is the closest fitting of the IV curve. An exemplary fitting curve in comparison to the experimental IV result is shown in Figure 1-19.

1.9.2 Capacitance voltage (CV) characteristics

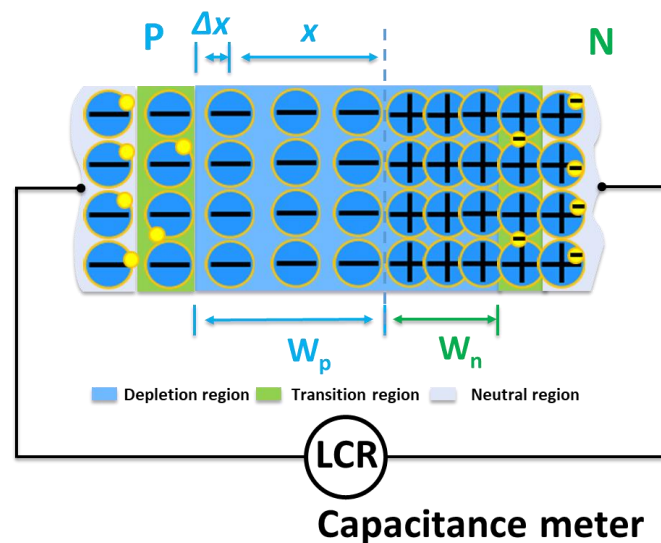


Figure 1-20. (a) schematic diagram of a pn junction. W_p and W_n indicate the width of SCR (space charge region) in the p-type and n-type semiconductor respectively, LCR is the capacitance meter

Like IV measurements, capacitance spectroscopy of the solar cells contains valuable information about the device, such as built-in electric field, doping density, and defects state density [98]. Typically used capacitance spectroscopy methods include capacitance-voltage (CV) measurements, drive-level capacitance profiling (DLCP), and admittance spectroscopy (AS) [99]. Those three capacitance spectroscopies use very different measuring approaches. CV measures the capacitance as a function of varied bias voltage, and DLCP changes the amplitude of the testing signal (AC voltage) superposed on the bias voltage (DC voltage), while AS measures the capacitance with different stimulating frequencies. Consequently, the mechanisms differ from one another. Here we focus on the simple and widely used CV method, which will be referred to and used frequently in the following chapters [100]. The interpretation of CV data relies on the analysing model. For comparison, here we introduce two models to extract critical parameters of the device, such as doping level, built-in electric field, and space charge region width.

The first model is the most classic model developed by Kimerling in 1974 [101]. Presume there is a one-sided pn^+ junction as shown in Figure 1-20, the space charge region (SCR) is free of mobile carriers, and the width of SCR in the n-type semiconductor W_n is smaller compared to W_p . The majority of carriers in the neutral region distribute in a semi-Gaussian shape. In the transition region, the Debye tail of majority carriers extends into the SCR from the neutral region. In this case, according to Gauss's law:

$$\Delta E = \frac{\Delta V}{x} = \frac{q}{\epsilon_r \epsilon_0} N_{cv}(x) \Delta x$$

(1-15)

x is the distance marked in Figure 1-20, Δx is the differential variable, and ΔE is the electrical field flux. ΔV is the change of externally added bias, and ϵ_r and ϵ_0 are the dielectric constants

of the semiconductor and vacuum, respectively. q is the elemental charge, and $N_{cv}(x)$ is the fixed charge concentration. Rearranging the orders, we get:

$$N_{cv}(x) = \frac{\epsilon_r \epsilon_0}{q} \frac{\Delta V}{x \Delta x} \quad (1-16)$$

According to the parallel plate capacitance approximation, we have $x = \epsilon_r \epsilon_0 / C$ and $\Delta x = \epsilon_r \epsilon_0 \Delta C / C^2$. Substitute those two variations, and we have:

$$N_{cv}(x) = \frac{C^3}{q \epsilon_r \epsilon_0} \frac{\Delta V}{\Delta C} \quad (1-17)$$

By adjusting the bias voltage applied to the solar cell device, the variation x can scan through the whole SCR, so we obtain the N_{cv} distribution in the SCR, as shown in Figure 1-21 (a). Define the same bias voltage for all solar cells, such as 0 V. Then, we can locate a capacitance value and the equivalent parallel plate capacitor width (W_p) according to $x = \epsilon_r \epsilon_0 / C$. In that way, we can compare the width W_p in different solar cells. Sometimes people also compare the minimum value of N_{cv} in solar cells. Generally, the minimum N_{cv} is close to the N_{cv} point at 0 V bias.

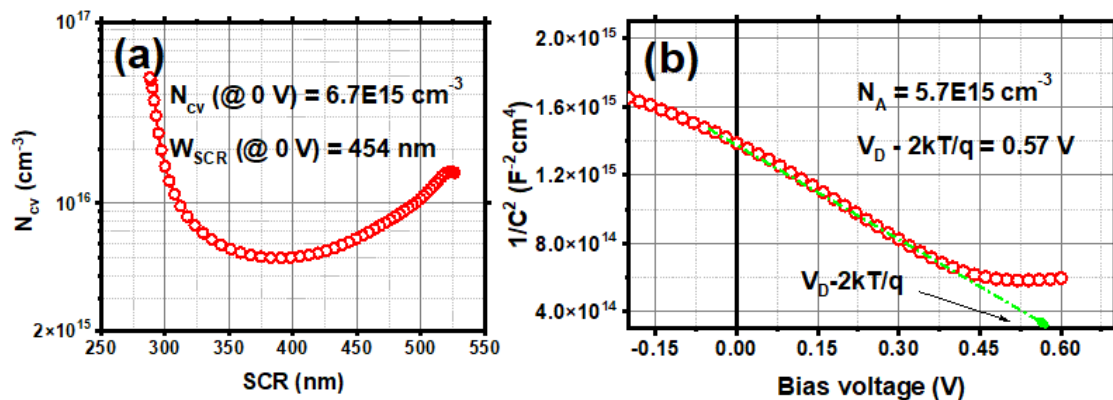


Figure 1-21. (a) carrier density N_{cv} distribution in the space charge region based on Kimerling's model and (b) Mott-Schottky plot for the same sample to extract the doping density N_A and the potential difference between the pn^+ junction

The second model also uses a one-sided abrupt pn^+ junction approximation. Because it was applied in the Mott-Schottky junction at the first place, we refer to it as the Mott-Schottky model. From the Poisson equations, we obtain [79]:

$$W_p + W_n = \sqrt{\left(V_D - \frac{2kT}{q}\right) \left(\frac{2\epsilon_r \epsilon_0}{q}\right) \left(\frac{N_A + N_D}{N_A N_D}\right)} \quad (1-18)$$

V_D is the potential difference at the pn⁺ junction, N_A is the acceptor doping density in the p-type semiconductor, and N_D is the donor density on the n-type side. The overall device has to be neutral, so we have:

$$W_p N_A = W_n N_D \quad (1-19)$$

W_n can be neglected if N_D is two or three orders of magnitude higher than N_A . In the pn⁺ junction, we can simplify equation (1-18) to:

$$W_p = \sqrt{\frac{2\epsilon_r \epsilon_0}{q N_A} \left(V_D - \frac{2kT}{q} \right)} \quad (1-20)$$

When a voltage V is applied to the pn⁺ junction, V_D should be replaced by $(V_D - V)$ in equation (1-20). The depletion region capacitance per unit area is $C_D = (\epsilon_r^* \epsilon_0)/W_p$, so the capacitance per unit area of a one-sided abrupt pn⁺ junction is given by:

$$C_D = \frac{\epsilon_r \epsilon_0}{W_p} = \sqrt{\frac{q \epsilon_r \epsilon_0 N_A}{2}} \left(V_D - V - \frac{2kT}{q} \right)^{-\frac{1}{2}} \quad (1-21)$$

Therefore, rearranging the above equation leads to:

$$\frac{1}{C_D^2} = \frac{2}{q \epsilon_r \epsilon_0 N_A} \left(V_D - V - \frac{2kT}{q} \right) \quad (1-22)$$

$$\frac{d(1/C_D^2)}{dV} = -\frac{2}{q \epsilon_r \epsilon_0 N_A} \quad (1-23)$$

With equations (1-22) and (1-23), by plotting $1/C^2$ versus V , the slope gives the doping concentration N_A , and the extrapolation of $1/C^2$ to 0 gives $(V_D - 2kT/q)$, as shown in Figure 1-21 (b).

The application and interpretation of capacitance spectroscopy are still under severe development [102, 103]. The information contained in the capacitance is still to be extracted and discovered. Our TCO-based ultrathin CIGSe solar cells show good rectifying IV properties, so we assume the one diode model is valid for relative comparison. But we should be cautious that models have limits when interpreting CV results in experiments. With different models, measurement conditions (dark or light), and testing setups (frequency, signal amplitudes), CV may give different results. The used models and measurement conditions should be the same for a valid comparison.

1.9.3 Quantum efficiency characteristics

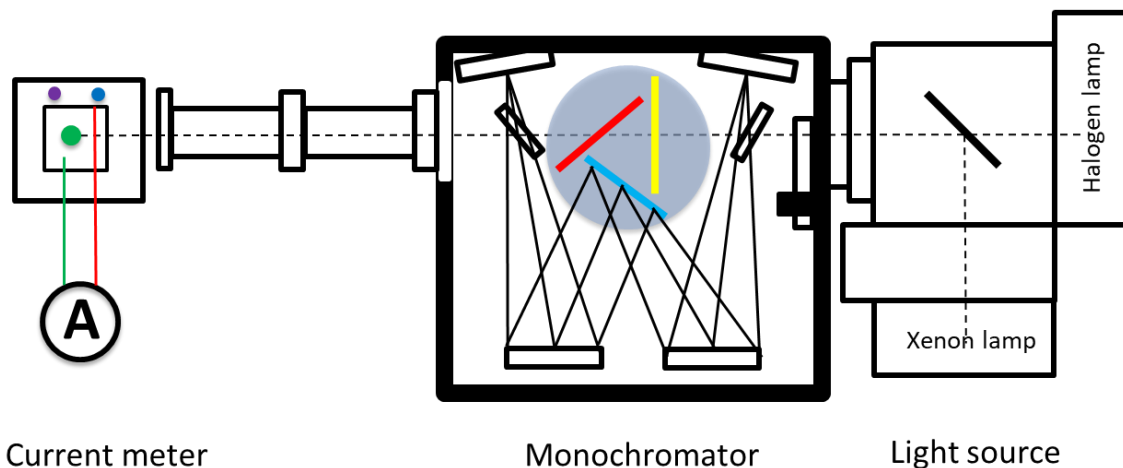


Figure 1-22. Schematic diagram of external quantum efficiency (EQE) measurement setup

The definition of external quantum efficiency (EQE) for a solar cell is the ratio of the number of collected carriers over the number of incident photons for a given energy (wavelength). Therefore, by folding the EQE with the number of photons in the AM1.5 solar spectrum $\varphi(\lambda)$ and integrating it over the absorption range, we obtain an equivalent current density j_{EQE} :

$$j_{EQE} = q \int_{\lambda_1}^{\lambda_2} EQE(\lambda) \varphi_{ph}^{AM1.5}(\lambda) d\lambda$$

(1-24)

where q is the elemental charge, λ is the wavelength, $\varphi(\lambda)$ is the number of photons of the corresponding wavelength, (λ_1, λ_2) is the wavelength range 300-1350 nm of the solar spectrum at AM1.5. We chose the 300-1350 nm wavelength range because it covers the absorption range of CIGSe solar cells. The bandgap E_g of our CIGSe is around 1.14 eV, so the cut-off edge of EQE is at the 1080-1090 nm wavelength range. In that way, we can cross-check the j_{EQE} results with the j_{sc} measured by IV. IV measurements need to count the testing area of solar cells, while EQE is a dimensionless ratio independent of the sample area.

Figure 1-22 illustrates the schematic diagram of our EQE setup. It uses two light sources to simulate the solar spectrum and a set of mirrors/lenses to make the light beam monochromatic. The sample holder can rotate to measure the front and rear EQE of BSTUT CIGSe solar cells. The purple dot on the sample holder is a Ge reference, and the blue dot is a Si reference solar cell for calibration. The green dot is the incident light spot on the testing sample.

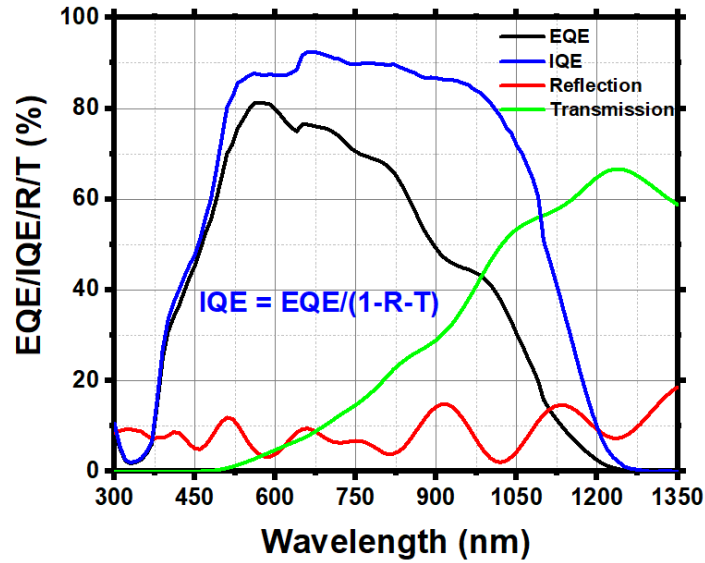


Figure 1-23. Aligning the EQE with the T/R (transmission/reflection). IQE stands for the internal quantum efficiency

EQE is a powerful tool when locating the origin of photocurrent losses in a solar cell, especially when we align the EQE with transmission/reflection (T/R) characteristics of the same sample. For a semi-transparent solar cell, we can see through it, as shown in Figure 1-9 (c). In this case, the transmitted light can be explicitly quantified and compared with reflected light, as displayed in Figure 1-23. Compared to the reflected light, the transmitted light is higher in the long-wavelength range (green line), while reflection is higher in the short wavelength range (red line). Generally, we calculate the internal quantum efficiency (IQE) by $IQE = EQE / (1 - R)$. In our case, the transmitted light is comparable to the reflection (or even higher). Therefore, for a valid comparison of our IQE, the formula needs to be modified to:

$$IQE = \frac{EQE}{1 - R - T}$$

(1-25)

The differences in shape and cut-off wavelengths are related to the absorber bandgap E_g . The shape and magnitude at short wavelengths are related to the device structure and parasitic absorption in the window layers.

1.9.4 Transmission and reflection characteristics



Figure 1-24. Lambda 1050

Figure 1-24 (a) shows LAMBDA 1050 from PerkinElmer company used for transmission and reflection (T/R) measurements. Its light sources and detectors cover the UV/VIS/NIR spectrum (ultraviolet/visible/near-infrared spectrum, 250-2500 nm). It uses an integrating sphere to measure total T/R characteristics of the solar cells.

1.9.5 X-ray fluorescence and glow discharge optical emission spectroscopy

We use a SPECTRO XEPOS with XRF Analyzer Pro to detect the thickness, Cu/(Ga+In) (CGI) and Ga/(Ga+In) (GGI) ratio of our CIGSe absorber. XRF is short for X-ray fluorescence. The SPECTRO XEPOS uses an X-ray as an excitation light source and the resulting fluorescence spectroscopy for empirical analysis of the sample. Because of this, calibration of the analysis model is critical to obtaining accurate content information.

We employ a GDA 659 HR from SPECTRUMA ANALYTIC GMBH company for determining the depth distribution of the elemental components in our solar cells. GD-OES is short for glow discharge optical emission spectroscopy. By bombardment of the surface with Ar atoms, the sample is removed layer by layer. The removed atoms pass into the plasma by diffusion. We can distinguish and record the elements in the testing sample by those removed atoms' emission spectroscopy. .

1.9.6 SCAPS simulations

We utilize SCAPS-1D (a solar cell capacitance simulator) to simulate the ultrathin CIGSe solar cell device to assist in understanding and interpreting experimental results [104]. SCAPS-1D can calculate the electrical properties of a one-dimension multi-layered device. It finds numerical solutions to the system of three coupled differential equations constituting the basic semiconductor equations: Poisson equation and continuity equations for both electrons and holes. It can export IV (current-voltage), CV (capacitance-voltage), C-f (capacitance-frequency), and QE (quantum-efficiency) results of the defined solar cell under illuminated and dark conditions. We will list the simulation settings for each layer in the corresponding chapters.

1.9.7 RefDex simulations

We use RefDex to simulate the optical properties of the multi-layered structures (solar cells or SiO₂/ITO/Glass), such as absorption in each layer and overall T/R of the devices. RefDex uses the transfer matrix method to simulate the light propagation in the multi-layered system [105]. RefDex needs film thickness and complex refractive index ($n + ik$) of every layer in the system to calculate the T/R and absorption. RefDex can also extract ($n + ik$) of the target layer using the overall T/R and ($n + ik$) of other layers in the system.

1.10 Outline of this thesis

Based on the background described previously, the outline of this thesis is: Chapter 2 chooses the optimal Na doping method for ultrathin CIGSe solar cells on ITO substrates. Chapter 3 optimizes the NaF PDT dose in detail and characterizes the samples with multiple techniques to explore the working mechanism of NaF PDT doping. Chapter 4 passivates the back interface with SiO₂ point-contacts to reduce recombination velocity S_b at the back interfaces. Then in chapter 5, we optimize the front and rear efficiency of BSTUT CIGSe solar cells. We compare the front/rear PV performance of ultrathin CIGSe solar cells on different glass types, ITO thicknesses, and NaF PDT doses. Chapter 6 inserts SiO₂ nanoparticles (NPs) to enhance the front and rear light absorption in BSTUT solar cells. Chapter 7 gives a summary and outlook.

Chapter 2 Na doping strategies

On Mo back contacts, Na doping has been proven beneficial for enhancing the PV performance of CIGSe solar cells, either by diffusion from soda-lime glass (SLG), NaF precursor, or post-deposition treatment (PDT) [106, 107]. On the degenerated semiconductor ITO, however, it is reported that ITO would impede the Na diffusion from the SLG substrate [74, 75]. Yet, a transparent back contact is one of the basic requirements for bifacial semi-transparent ultrathin CIGSe solar cells. Therefore, finding an adequate Na doping strategy for ITO-based ultrathin absorbers is essential to achieving a high-efficiency BSTUT CIGSe solar cell.

This chapter compares different Na doping methods for ultrathin CIGSe on ITO substrates. We fabricate ultrathin CIGSe solar cells on alkali-free barium boron-silicate glasses (pgo glass) as reference samples. Then, we compare Na diffusion doping from SLG substrates with the reference. Also, on pgo glasses, we try NaF precursor, NaF PDT, and NaF precursor combined with PDT doping for ultrathin CIGSe absorbers. By comparing the corresponding IV, CV, and GD-OES characteristics, with the aid of literature research, we make certain deductions for deciding the optimal Na doping strategy in our ITO-based ultrathin CIGSe solar cells.

2.1 The requirements of Na doping

Firstly, the Na density in the CIGSe should be in the range of 0.005-0.5 at%. On the one hand, higher than 1.0 at% of Na shall meet the risks of absorber delamination and PV performance deterioration. On the other hand, if the Na density is too low, the CIGSe will suffer from bad quality. Available Na doping methods include diffusion from SLG substrate, NaF precursor, and NaF PDT. For the diffusion doping, SLG substrates will serve as Na sources, and the substrate temperature should be sufficiently high to motivate the Na diffusion process. According to equation (1-4), the depth and density of Na that diffuses into the CIGSe depend on the substrate temperature. Given the ultrathin thickness of our CIGSe, we have to adjust the NaF dose for precursor/PDT accordingly to achieve ideal Na density.

Secondly, the Na doping step should not damage other layers or introduce undesirable interfacial compounds (such as GaO_x) into the solar cell. Specifically, a substrate temperature higher than 520 °C will destroy the high conductivity of the ITO layer [23]. This requirement limits the maxim amount of Na that can diffuse into the absorber from SLG. Therefore, we fix the highest substrate temperature at 450 °C for the 3-stage co-evaporation to meet this requirement [7]. We will use other Na doping methods (NaF precursor or PDT) if the incorporated Na amount is insufficient.

Meeting those requirements, this chapter compares four Na doping methods to decide the optimal Na doping strategy for ITO-based ultrathin CIGSe solar cells. We will introduce those strategies and compare the PV performance of the corresponding solar cells. We also use diode parameters extracted from dark IV, Na depth distribution measured via GD-OES, and W_{SCR}/N_{CV} calculated from CV measurements to help understand the Na doping mechanisms.

2.2 Na diffusion, NaF precursor and NaF post-deposition treatment

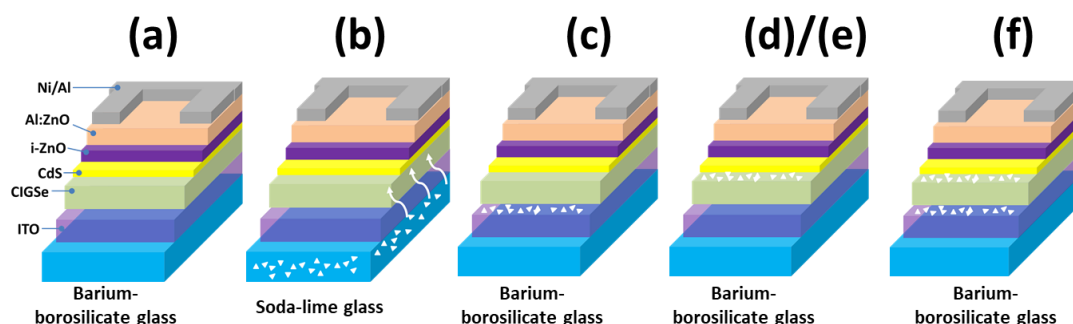


Figure 2-1. Four Na doping strategies: (a) Na-free reference sample on barium-borosilicate glass substrate; (b) diffusion of Na from the soda lime glass substrate; (c) NaF precursor doping with 2 mg NaF precursor evaporated onto the Na-free substrate before CIGSe; (d) and (e) PDT post-deposition treatment (PDT) doping using 2 and 4 mg NaF, respectively; (f) 2 mg precursor plus 2 mg PDT doping

As shown in Figure 2-1, we compare four Na doping methods for ultrathin CIGSe absorbers:

- (a) Reference sample, no Na doping, alkali-free barium-borosilicate glass substrate;
- (b) Diffusion from SLG. SLG has 14% Na₂O that may diffuse through the ITO layer into the CIGSe absorber;
- (c) NaF precursor doping. We evaporate NaF precursor onto ITO substrates before we co-evaporate the ultrathin CIGSe absorber;
- (d)-(e) NaF post-deposition treatment doping. After the 3-stage co-evaporation, we evaporate 2 or 4 mg NaF salt onto the ultrathin absorber;
- (f) NaF precursor plus NaF PDT. In this case, we evaporate a NaF precursor onto ITO substrates before the CIGSe co-evaporation. After the absorber deposition finishes, we conduct the NaF PDT process again.

The PV performance of CIGSe solar cells is directly related to the amount/thickness of incorporated Na. To precisely control the Na incorporation amount, samples (a) and (c)-(f) use Na-free barium-borosilicate (pgo) glasses, while sample (b) uses SLG substrate. In this way, the amount of incorporated Na in sample (b) depends on the substrate temperature T during the 3-stage co-evaporation process (according to the diffusion equations (1-4) and (1-5)). For samples (c)-(f), the amount of Na depends on the NaF precursor/PDT dose. To ensure the comparability of ultrathin absorbers, the CIGSe layer of all those samples comes from the same co-evaporation batch. The thickness of the CIGSe layer is 431 nm, CGI is 0.89, and GGI is 0.33. Before loading samples (c) and (f) into the PVD, we deposit a 2 mg NaF precursor on the ITO back contacts. After the ultrathin CIGSe co-evaporation process, we perform the PDT for samples (d)-(f) by putting them back into the PVD chamber with 2 mg NaF powder.

For the optimal NaF dose/thickness, according to Rudmann et al., 20-40 nm thick NaF is the beneficial range for the PDT-processed CIGSe solar cells (2 μ m CIGSe on polymer substrates or SLG with a Na barrier). Usually, 30 nm is used in their cases [41, 49, 106, 108, 109]. They lower the substrate temperature to 400 °C for the NaF PDT processes and evaporate the NaF in the presence of Se vapour [43]. It might be more accurate to name their NaF PDT method

'4-stage method', as the NaF PDT follows the 3-stage co-evaporation. The PDT process lasts 20 minutes to allow the Na to diffuse into the CIGSe absorber.

In our case, we adapt the NaF thickness to the ultrathin CIGSe to obtain the desired Na density in absorbers. Given that 30 nm NaF is needed for 2000 nm CIGSe, our 500 nm CIGSe requires 7.5 nm thick NaF. Such a thin thickness is difficult to measure directly. Therefore, we presume that the weight of evaporated NaF salt is proportional to NaF thickness. In that way, we evaluate the NaF thickness by measuring NaF powder weight before loading it into the PVD chamber. According to our calibration, 2 mg NaF powder corresponds to 3.4 nm thickness when NaF source temperature is 900 °C while substrate temperature is 360 °C. Therefore, sample (c) use 2 mg NaF precursor (4 mg NaF cause delamination of the CIGSe), and samples (d) and (e) used 2 and 4 mg NaF PDT, respectively. Sample (f) used 2 mg precursor plus 2 mg PDT. The ratio between NaF thickness and weight may be different from machine to machine, as the evaporation rate v_{evp} is proportional to the equilibrium pressure inside the chamber P_e (according to equations (1-1)

and (1-2)). P_e depends on the volume of chamber V and the amount of source material N (according to the ideal gas equation: $P_e = NRT/V$, N the amount of substance, R the ideal gas constant, T the temperature and V the volume of the PVD chamber). Generally, the V is different from group to group.

2.3 Comparison of the electrical performance and Na depth distribution

Table 2-1. The photovoltaic (PV) parameters V_{oc} , j_{sc} , FF, Eff, series resistance R_s , shunt resistance R_{sh} , diode ideal factor n , dark saturation current density j_0 , space charge region width at 0 bias voltage, and carrier density N_{cv} of the best solar cells. The PV parameters (V_{oc} , j_{sc} , FF, Eff) are extracted from IV curves measured under AM1.5 solar simulator conditions. The diode parameters (R_s , R_{sh} , n and j_0) are fitted through the model introduced in section 1.9.1 (method 2), and W_{SCR} and N_{cv} are deduced based on the L.C. Kimerling's model introduced in section 1.9.2

Sample	Na doping method	V_{oc} (mV)	j_{sc} (mA/cm ²)	FF (%)	Eff (%)	R_s (Ω cm ²)	R_{sh} (Ω cm ²)	n	j_0 (E-6 A/cm ²)	W_{SCR} (nm)	N_{cv} (E15 cm ⁻³)
A	None	540	23.4	44.1	5.6	8.6	178.0	1.73	0.121	491	2.31
B	Diffusion	534	27.0	57.6	8.3	2.5	264.5	2.09	1.20	465	13.5
C	2 mg precursor	463	18.4	28.8	2.5	0.3	37.8	3.17	17.7	107	412
D	2 mg PDT	542	27.6	58.9	8.8	1.1	159.1	1.41	0.842	370	8.08
E	4 mg PDT	621	26.1	63.9	10.3	0.8	114.4	2.06	0.868	274	11.3
F	2 mg precursor + 2 mg PDT	363	16.4	32.7	2.0	1.5	29.1	2.66	23.6	141	669

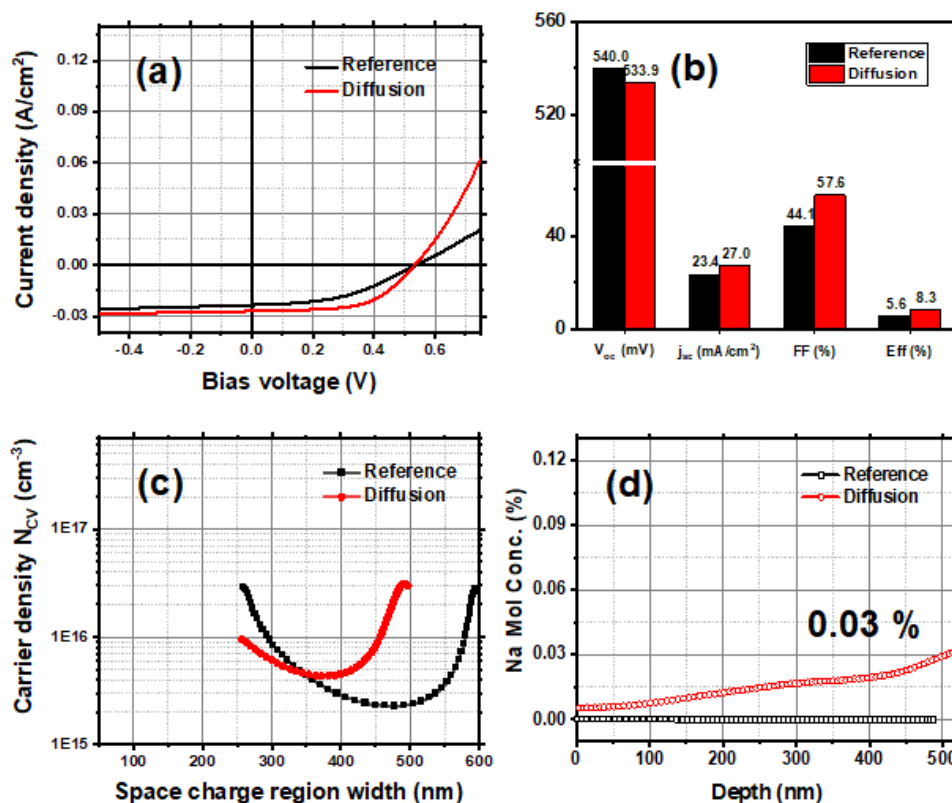


Figure 2-2. Comparison of sample B with the reference A in (a) current-voltage characteristics, (b) PV parameters, (c) carrier density N_{cv} distribution vs SCR (space charge region) width and (d) Na depth distribution in the absorber

Table 2-1 summarizes the best electric performance of solar cells with different Na doping methods. We compare the corresponding IV, CV, and GD-OES with the reference sample to help understand the differences induced by Na incorporation methods.

As shown in Figure 2-2 (b), compared to the reference sample A, sample B with Na diffusion from SLG has a lower V_{oc} but a higher j_{sc} and FF , so its Eff increases from 5.6 to 8.3%. Better PV performance of sample B implies Na can penetrate the ITO layer and enter the CIGSe, even though we use a relatively low substrate (450 °C) for the co-evaporation process. In addition, it proves the importance of Na incorporation for a high-quality CIGSe absorber. According to reference [100], a decreased V_{oc} along with an increased j_{sc} is because of the grain boundary (GB). The shrink GB limits the recombination of photogenerated carriers at zero bias, so the j_{sc} of the solar cell increases. The diode current at forwarding bias is large, so the V_{oc} of the solar cell decreases [100]. In short, the Na diffusion influences the GB (or high defect zone) distribution, hence deciding the PV performance of the solar cells. Generally, Na incorporation by PDT increase the V_{oc} of the solar cells. In our case, the Na diffusion from SLG decreases the V_{oc} . That is because the Na incorporation method is also critical for the performance of the solar cells. The kinetic of the compound (Cu-In-Ga-Se) formation might be different for NaF precursor and PDT/SLG diffusion. Figure 2-2 (c) shows that sample B has a narrower SCR. Taking the values at zero-volt bias, the N_{cv} of sample B is almost one magnitude higher than sample A. The SCR width of sample B is also narrower than sample A, as listed in Table 2-1. In conclusion, Na diffusion from SLG increases N_{cv} in the CIGSe layer and induces a narrower SCR width for the ultrathin CIGSe solar cell.

Compared to the reference, sample B shows lower R_s but higher R_{sh} . That attributes to the change in absorber conductivity σ , as the CIGSe layer is the only variation between sample B and the reference. According to Rudmann et al., Na (diffusing from SLG into CIGSe) increases the CIGSe conductivity σ because N_{cv} increases with the Na incorporation ($\sigma = q * N_{cv} * \mu_p$, in which q is the elemental charge, N_{cv} the carrier density of the p-type semiconductor, μ_p the mobility of the p-type semiconductor) [108]. However, the increased N_{cv} also induces higher recombination in the device. According to equation (1-6), recombination is proportional to the trap state density (equivalent to the N_{cv} here). The increased recombination for sample B is verified by the higher diode ideality factor n and dark saturation current density j_0 , as shown in Table 2-1.

Figure 2-2 (d) shows that Na content in the Na-free reference is below the detection range of GD-OES. The Na content in sample B is higher than in sample A at all depths. The Na density in sample B slopes up to the CIGSe/ITO interface and peaks at around 0.03% close to the ITO layer.

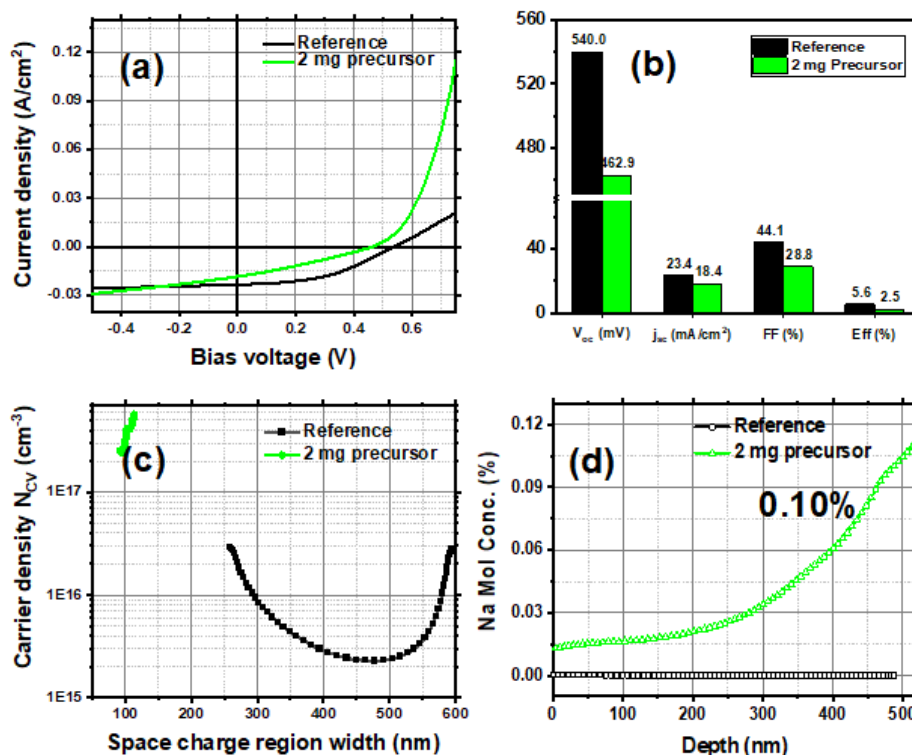


Figure 2-3. Comparison of sample C with the reference A in (a) current-voltage characteristics, (b) PV parameters, (c) carrier density N_{cv} distribution vs SCR (space charge region) width and (d) Na depth distribution in the absorber

Figure 2-3 (a) and (b) compare IV curves and PV parameters of sample C with the reference, revealing an overall deteriorated PV performance after 2 mg NaF precursor doping. That is against the results in references [108], even though our NaF dose/thickness is in their recommendation range. The GD-OES results shown in Figure 2-3 (d) confirm that the maximum Na density is 0.10 % at the back contact, which is still in the recommended 0.005~0.5% range. One possible reason is that Rudmann et al. use Mo back contacts layer while we use ITO. Therefore, the NaF precursor may influence the interfacial compound (MoSe_2 at the CIGSe/Mo interface [58], GaO_x at the CIGSe/ITO interface [74].) differently hence leading to the deterioration of ITO-based solar cells. Another possibility is that Rudmann et al. use 2 μm CIGSe, and our CIGSe is around 500 nm. Even though we have reduced the NaF dose/thickness proportionally, it might be that CIGSe with ultrathin thickness is more sensitive to NaF doping. Therefore, further detailed optimization is required before we can draw solid conclusions. With those considerations, we have tried 0, 2, 4, and 8 mg NaF precursors on both Mo and ITO back contacts. On Mo, the CIGSe peels off during the CBD process when the NaF precursor is 8 mg; on ITO, however, the CIGSe peels off when the NaF is 4 mg. When the NaF dose is lower than 2 mg, experiments are difficult to manoeuvre, as the weighting process of NaF powder induces higher error in such a small weight range. The point is that ultrathin CIGSe solar cells on ITO are more sensitive (or less tolerant) to the NaF precursor than on Mo back contacts.

Figure 2-3 (c) shows that the carriers of sample C congregate in a very narrow region close to the CdS side. At zero bias, the SCR width is only 107 nm while the N_{cv} is as high as $4.12 \text{ E}17 \text{ cm}^{-3}$, two magnitudes bigger than the reference sample. That is consistent with the GD-OES

result that Na goes into the CIGSe and tunes the N_{cv} distribution in the SCR like in sample B. Yet, the amount of Na incorporated by NaF precursor is much higher than from SLG diffusion, as sample C shows a three times higher Na density than sample B at the CIGSe/ITO interface. The R_s of sample C decreases to 0.3Ω due to the increased CIGSe conductivity. However, the R_{sh} of sample C decreases to 37.8Ω , which may be because of unexpected shunting dots or pinholes induced by the overdosing of NaF. The ideality factor n increases to 3.2, exceeding the defined range of 1-2. According to reference [100], n bigger than the limiting value for Shockley-Read-Hall (SRH) recombination of 2 is due to the gradually saturated recombination with increasing electric forward bias. In our case, recombination in the SCR may be limited, as the SCR width is narrower. Consequently, the j_0 of sample C increases to 1.8 E-5 A/cm^2 , two magnitudes higher than the reference.

In short, the NaF precursor has effectively increased the carrier density N_{cv} in the CIGSe layer. However, 2 mg NaF precursor doping deteriorates the PV performance of ultrathin CIGSe solar cells. The main reason might be that the ITO-based CIGSe have a different Na incorporation mechanism from the Mo-based, thus a lower NaF tolerance dose for our ITO-based ultrathin CIGSe solar cells.

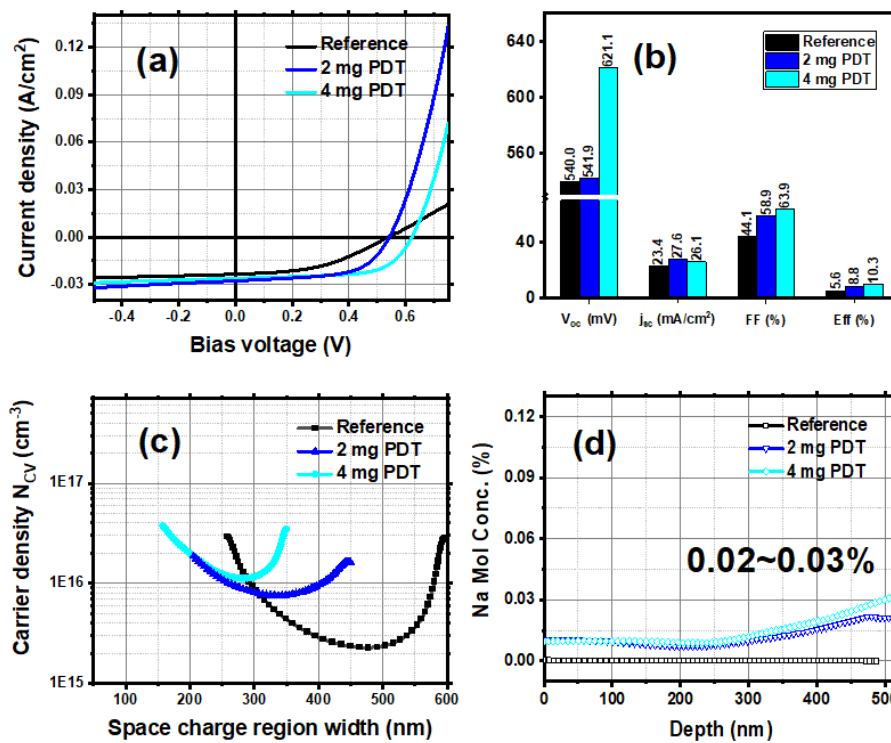


Figure 2-4. Comparison of sample D/E with the reference A in (a) current-voltage characteristics, (b) PV parameters, (c) carrier density N_{cv} distribution vs SCR (space charge region) width and (d) Na depth distribution in the absorber

In Figure 2-4 (a) and (b), samples D and E show an enhancement in PV performance after NaF PDT. The V_{oc} , FF, and Eff show a continuous increase along with the NaF dose. The V_{oc} increase can be attributed to the strengthened built-in electric field V_D , as the N_{cv} increases to 8.1 E15 and 1.1 E16 cm^{-3} for samples D and E, respectively. According to the formula [79]:

$$V_D = d_{SCR}^2 \frac{q}{2\epsilon_r \epsilon_0} \frac{N_A N_D}{N_A + N_D} \quad (2-1)$$

in which q is the electron charge, N_D is the donor concentration of the n-type side. In our case, the n-type side corresponds to the CdS/i-ZnO/AZO layers. ϵ_r and ϵ_0 are the relative dielectric constant and vacuum dielectric constant, respectively. N_A is the acceptor carrier density. For a rough estimation, if we set N_D to $1 \text{ E}16 \text{ cm}^{-3}$, ϵ_r and ϵ_0 to 13.6 and 1, respectively [110], insert the values for SCR width and N_{cv} of samples A, D, and E into the equation (2-1), then we find a V_D increase from 0.5 to 0.6 and further to 0.7 V. Another quantitative method to estimate the V_{oc} increase induced by N_{cv} changes follows equation [111]:

$$V_{oc} = \frac{kT}{q} \ln \left[\frac{(N_A + \Delta n) \Delta n}{n_i^2} \right] \quad (2-2)$$

kT/q is the thermal voltage, Δn is the excess carrier density, and n_i is the intrinsic carrier density (generally decided by temperature). Firstly, set N_A to $2.3 \text{ E}15 \text{ cm}^{-3}$ for the reference sample A (from CV measurement), T to 298 K, and n_i to constant $8.6 \text{ E}9 \text{ cm}^{-3}$ (corresponding to 298 K), then, adjusting Δn to fit the V_{oc} of 540 mV, we obtain Δn is $4.3 \text{ E}13 \text{ cm}^{-3}$. The Δn is mainly depending on the illumination intensity or the absorption degree in CIGSe, so we can also use this value for samples D and E. When inserting the N_{cv} of $8.1 \text{ E}15$ for sample D, the calculated V_{oc} is 572 mV, higher than the experimental 542 mV. When putting in N_{cv} $1.1 \text{ E}16$ of sample E, the calculated V_{oc} is 580 mV, lower than the measured 621 mV. This deviation implies the NaF PDT doping not only tunes the N_{cv} in the SCR but also brings extra effects like diminishing/enhancing the Schottky barrier height at the CIGSe/ITO interface. Chapter 5 will quantitatively analyse this V_{oc} increase.

Compared to the reference, R_s and R_{sh} of samples D and E show a consistent decrease with the NaF doping dose. That can also be attributed to the increased conductivity and deteriorated shunting property in the CIGSe layer. Interestingly, the Na shows a higher concentration at CIGSe/ITO interfaces, even though the PDT process comes after the CIGSe co-evaporation. That may also fundamentally change the Na working mechanism in CIGSe absorbers. The Na incorporated by diffusion from SLG or NaF precursor joins the formation of Ga-Se and In-Se phases during the 3-stage co-evaporation, which may facilitate internal ternary compounds like Ga-Se-Na or In-Se-Na. For NaF PDT doping, the chalcogenide CIGSe formation is finished when the Na diffuses into the CIGSe absorber. That is why people find more Na congregation at CIGSe grain boundaries but less in the grains of CIGSe [51]. The Na density is 0.02% for sample D and 0.03% for sample E, close to sample B of 0.03% but much lower than sample C of 0.1%. From this perspective, the optimal Na density for BSTUT CIGSe solar cells on ITO is more likely close to 0.02~0.03% at the CIGSe/ITO interface.

The j_0 of samples D and E is at the same level/magnitude. It indicates that the recombination degree is similar in those two cells. Also, the j_0 of samples D and E is higher than the reference because their N_{cv} increases after Na doping. The n of sample D is 1.41, lower than the

reference of 1.73. Sample E shows a 2.06 ideality factor because of the narrowed SCR and saturated recombination mechanism similar to sample C [100].

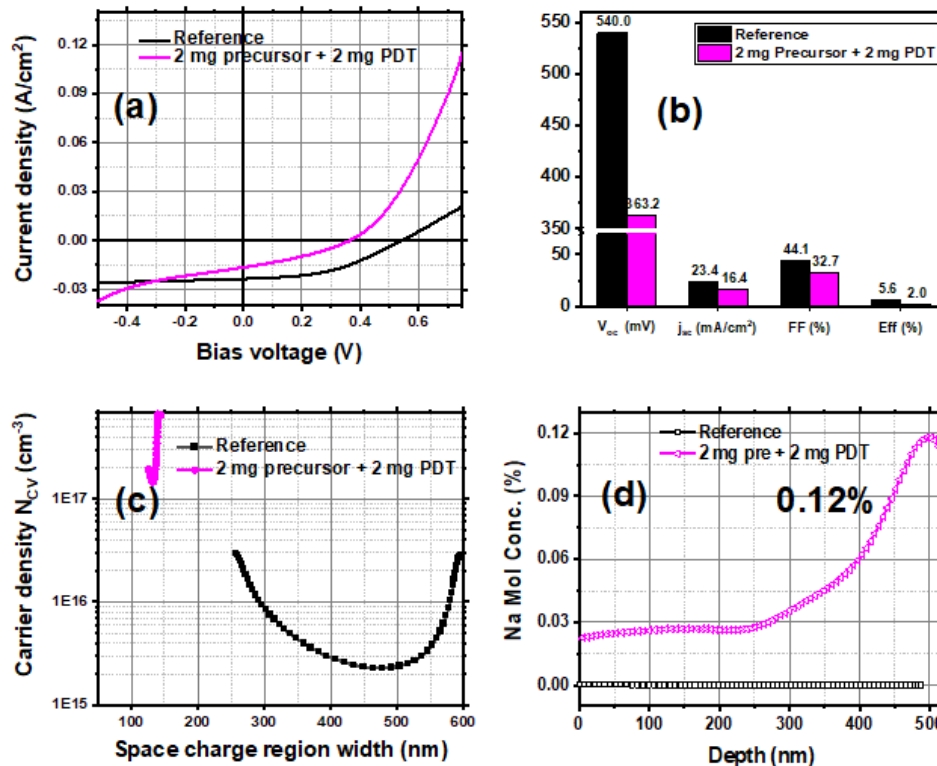


Figure 2-5. Comparison of sample F with the reference A in (a) current-voltage characteristics, (b) PV parameters, (c) carrier density N_{cv} distribution vs SCR (space charge region) width and (d) Na depth distribution in the absorber

The PV parameters of solar cells with NaF precursor plus NaF PDT (sample F) show a dramatic drop of efficiency to 2.0%. Sample F has the lowest R_{sh} among all samples. It also has the highest j_0 , N_{cv} and the maximum Na density at the CIGSe/ITO interface. The origin of PV performance deterioration is similar in samples F and C. Meanwhile, compared to sample C, sample F shows a higher FF, wider SCR width, and a lower ideality factor n . It implies that the NaF PDT process modifies the properties of the CIGSe (such as passivating the grain boundary [51]) after the Na incorporation from the NaF precursor. The 0.12% Na content at CIGSe/ITO interface is also slightly higher than sample C of 0.1%, which is quantitatively equal to 0.02% of sample D plus 0.1% of sample C.

Until now, we do not know why NaF precursor doping behaves so differently from NaF PDT. One possible reason is the timing of Na incorporation for those two methods. The Na is incorporated into the absorber during the CIGSe co-evaporation for NaF precursor and SLG diffusion doping. In that way, Na can influence the interdiffusion of Ga and In, hence the Ga grading in the CIGSe. According to reference [108], the morphology of chalcopyrite CIGSe changes with Na incorporation, such as peaks in XRD (X-ray diffraction) and grain size under SEM. In short, the Na incorporation changes the CIGSe growth process. For the PDT process, the Na comes after CIGSe co-evaporation. In that way, when Na diffuses into the absorber, the CIGSe morphology formation has already finished, so the Na can only diffuse into the grain boundary [45]. In addition, for the NaF PDT, overdosed NaF will be washed away in the

following step of CBD for the CdS layer, thus showing a higher tolerance in the NaF dose than the NaF precursor.

2.4 Summary and conclusion

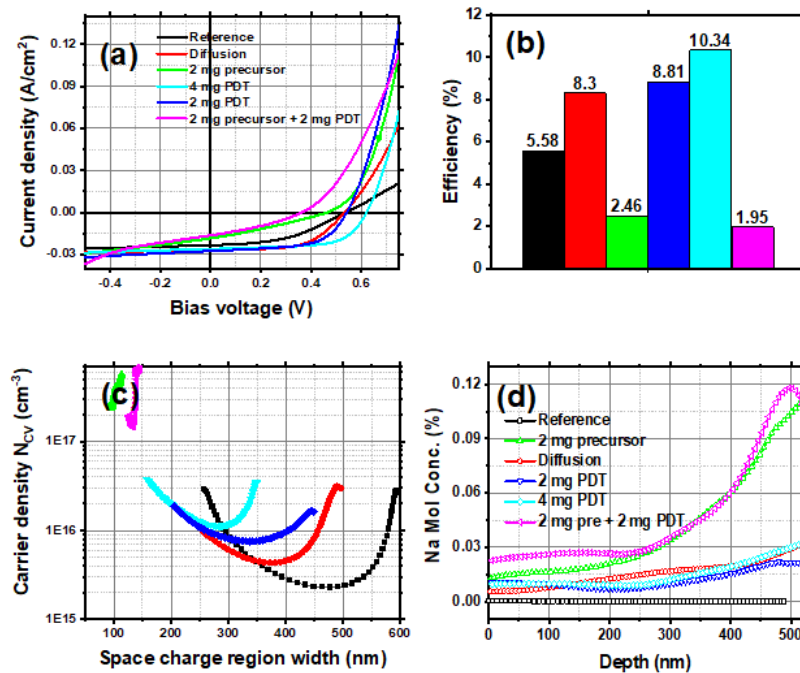


Figure 2-6. Comparison of all samples in (a) current-voltage characteristics, (b) efficiency, (c) carrier density N_{cv} distribution vs SCR (space charge region) width and (d) Na depth distribution in the absorber

In summary, through the explicit comparison of the PV performance, diode parameters, N_{cv} distribution, and GD-OES, we figure out:

- (1) The Na doping method can tune the carrier density N_{cv} distribution in the ultrathin CIGSe solar cells;
- (2) The solar cell with 2 mg NaF precursor plus 2 mg NaF PDT doping shows the highest Na density and carrier density N_{cv} but the worst PV performance;
- (3) The solar cells with Na diffusion from SLG and 2 mg NaF PDT show similar N_{cv} and PV performance, but 4 mg PDT reveals the highest efficiency of 10.3% (Figure 2-6 (b)). NaF PDT is the most controllable Na doping strategy among the four Na incorporation methods. It has the highest tolerance for NaF dose.

Chapter 3 NaF post-deposition treatment

Based on the explicit comparison of different methods for Na doping, we find that NaF post-deposition treatment (PDT) is the optimal Na doping strategy for ITO-based ultrathin CIGSe solar cells. NaF PDT doping has the following advantages.

- (1) The lowered substrate temperature (450 °C) maintains a good conductivity of the ITO layer, as all samples show fair conversion efficiency. Na can diffuse through ITO into the CIGSe absorber from soda-lime glass substrates. This adequate high temperature is critical because the temperature plays a decisive role in the Na diffusion process, no matter whether the Na source is SLG substrates or additional NaF salt;
- (2) The PDT process is conducted after the 3-stage co-evaporation, which means the formation of CIGSe morphology and a possible interfacial layer GaO_x at the CIGSe/ITO interface have already finished when the Na is incorporated.
- (3) The following step of CBD can wash away extra NaF salt. That provides a higher dose tolerance for the NaF PDT than the other Na doping methods. That also addresses the peel-off problem caused by overdosing NaF in the precursor method.

This chapter focus on the working mechanism of NaF PDT doping in ITO-based ultrathin CIGSe solar cells. We will detail the optimization of the NaF PDT doping using 0-8 mg NaF to cover the thickness range of 0-13.6 nm. We do not use an equal step but an equal ratio for the NaF weight (0, 2, 4, and 8 mg), anticipating Na density in the CIGSe has a magnitude change. So, the PV performance of solar cells can show more clear differences. We employ IV, CV, IVT, photoluminescence (PL) mapping, and GD-OES to deepen the understanding of the NaF PDT working mechanism. We use characterization conditions/models introduced in section 1.9. We also utilize a 519 nm laser with 5 mW power as an excitation light source during the PL mapping. Our cryostat cools down the samples to 80-85 K to reduce the thermal emission interferences. In addition, we employ SCAPS simulations to verify the experimental deductions.

3.1 Two scenarios of the NaF post-deposition treatment

Similar to chapter 2, samples in this chapter use barium-borosilicate glass 7059 to control the Na incorporation precisely. After the standard cleaning procedures, 300 nm ITO is deposited for all substrates. The fabrication of other layers in the ultrathin CIGSe solar cells uses general conditions introduced in section 1.2. For the NaF PDT process, there are two scenarios:

(1) The first one can be referred to as ‘sequential PDT’. We load the weighted NaF powder into the PVD with the other source materials (Cu, Ga, In and Se). In that way, the NaF PDT step can be performed right after the 3-stage co-evaporation, as Rudmann et al. have done [108]. The advantage of this scenario is that the vacuum in the chamber is maintained for the PDT processes. When the 3-stage co-evaporation is finished, we only need to lower the substrate temperature to 360 °C, open the NaF shutter and heat the NaF source to 900 °C to evaporate NaF. The disadvantage, however, is that the CGI/GGI depth distributions and the thickness of the ultrathin CIGSe may have tiny differences from batch to batch for different NaF doses.

(2) We can refer to the second scenario as ‘vacuum-break PDT’. After the 3-stage co-evaporation is finished, eight samples of ultrathin CIGSe absorbers (from one batch) are taken out of the PVD and divided into four groups. Then each group of absorbers is again inserted into the PVD along with the weighted NaF powder. The samples are then heated up to 360 °C again for the NaF PDT process. In that way, we diminish the differences in CGI, GGI, and thickness between different samples. The disadvantage of this scenario is that the CIGSe absorbers have to go twice through heating up and cooling down: once for CIGSe co-evaporation and once for NaF PDT, which may introduce other variations that are not known yet.

Considering the delicacy of ultrathin CIGSe absorbers and that NaF dose for PDT is the only variation we want to optimize at this stage, this chapter uses the ‘vacuum-break PDT’ scenario. Specifically, we take 0, 2, 4, and 8 mg NaF powder for the PDT process, and we will refer to them as NaF_0, NaF_2, NaF_4, and NaF_8, respectively. For all NaF PDT processes, we wait 20 minutes after the NaF source is heated up to 900 °C to ensure all the NaF evaporated. The thickness, CGI, and GGI of the batch found here to be 491 nm, 0.87, and 0.31.

3.2 Characterization and discussion

3.2.1 Current-voltage and capacitance-voltage characteristics

Table 3-1. PV parameters (averaged over at least 6 cells for each sample), minimum carrier density N_{cv} in the SCR, width of the SCR W_{SCR} at zero bias voltage, acceptor doping density N_A , and potential difference V_D of ultrathin CIGSe solar cells with different NaF PDT dose

Sample name	NaF PDT dose (mg)	V_{oc} (mV)	j_{sc} (mA/cm ²)	FF (%)	Eff (%)	N_{cv} minimum (E15/cm ³)	W_{SCR} @ 0 Volt (nm)	N_A (E15/cm ³)	V_D (mV)
NaF_0	0	510.0 ± 13.2	30.4 ± 1.0	54.8 ± 4.0	8.5 ± 1.0	1.88	588	2.19	533
NaF_2	2	620.0 ± 2.2	29.6 ± 0.7	64.9 ± 1.4	11.9 ± 0.4	6.40	380	6.91	691
NaF_4	4	622.1 ± 5.5	29.6 ± 0.7	65.6 ± 3.0	12.1 ± 0.7	7.15	369	7.95	716
NaF_8	8	635.6 ± 4.3	29.2 ± 0.3	63.1 ± 4.1	11.7 ± 0.7	9.56	318	11.62	749

Table 3-1 summarizes averaged PV parameters of the ITO-based ultrathin CIGSe solar cells with 0-8 mg NaF PDT doses (at least six out of eight cells included for each sample). We notice a continuous increase in the open circuit voltage V_{oc} . Compared to the reference sample NaF_0, NaF_2 shows an increase of 110 mV (21.5% increase). It implies that Na has been effectively doped into the ultrathin CIGSe layer by the sequential NaF PDT scenario. In addition, it highlights the importance of Na doping, especially for V_{oc} of ultrathin CIGSe solar cells [33, 112]. The V_{oc} of NaF_4 continues to increase and peaks at 636 mV of NaF_8, which shows a positive influence of the higher NaF dose. However, the j_{sc} illustrates a decreasing trend as the NaF dose increase. The decrease between NaF_2 and NaF_0 is 0.8 mA/cm², corresponding to 2.6% relative. 2.6% is minor compared to 21.5% of V_{oc} increase, but it implies that NaF PDT also harms the ultrathin CIGSe solar cells. The fill factor FF shows a more complicated change when the NaF dose increases: firstly, it rises and then decreases. The FF indicates a trade-off between V_{oc} increase and j_{sc} decrease for a higher NaF dose, and the optimal NaF dose lies in the range of 2-8 mg. Overall, the conversion efficiency Eff peaks at NaF_4 with 12.1%.

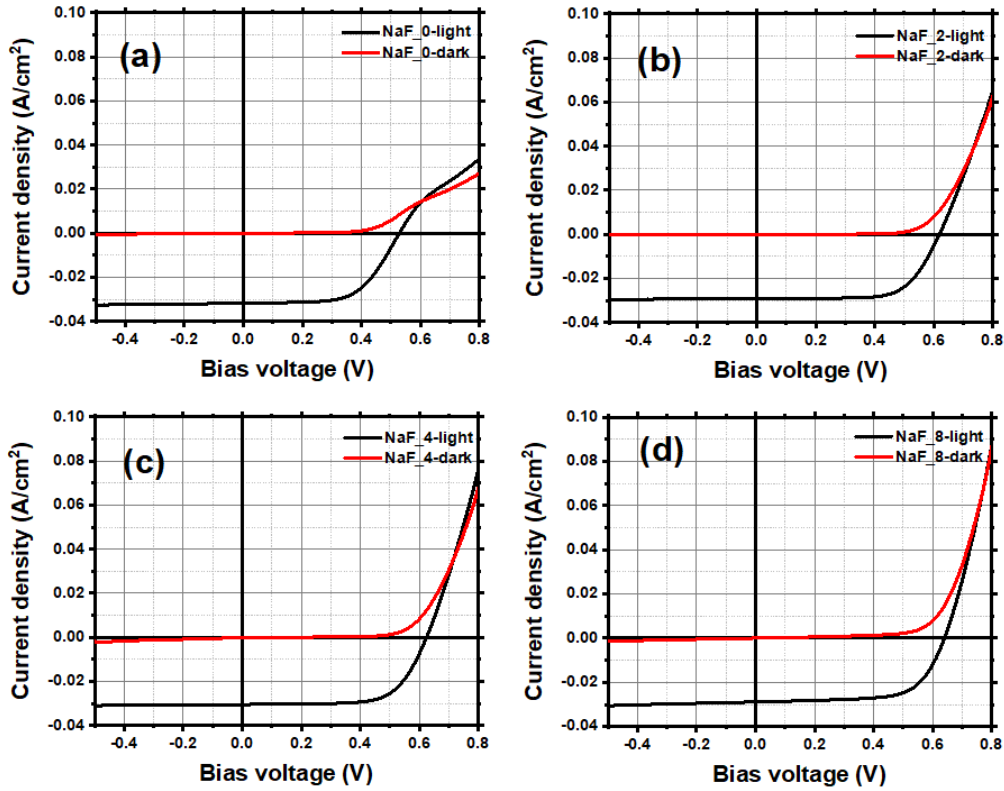


Figure 3-1. IV characteristics of the best ultrathin CIGSe solar cells with 0 mg (NaF_0), 2 mg (NaF_2), 4 mg (NaF_4) and 8 mg (NaF_8) NaF PDT dose under dark and illuminated condition

Figure 3-1 displays the current-voltage characteristics of the best solar cells. In the first quadrant of Figure 3-1 (a), the current curves of NaF_0 display bending in both dark and illuminated conditions. Generally, people refer to it as a roll-over phenomenon or S-shaped IV curves. However, the roll-over disappears in the NaF PDT processed samples, as shown in Figure 3-1 (b)-(d). According to Saive, the roll-over phenomenon is a frequently occurring hurdle in silicon heterojunctions and thin film solar cells, which is attributed to the mismatch between the energy levels of the absorber and the charge extraction layers, leading to a barrier to charge extraction [113]. In our case, there is an energy level mismatch between CIGSe and ITO layer. This thesis will refer to CIGSe/ITO as the back contact. In general, to describe the mismatch of energy levels in an ideal Schottky junction under zero bias, the barrier height for electrons E_{h0} is [79]:

$$qE_{h0} = W_{ITO} - \chi_{CIGSe} \quad (3-1)$$

in which W_{ITO} is the work function of the ITO layer, and χ_{CIGSe} is the electron affinity of the CIGSe layer. The Na diffusion into CIGSe bulk might increase the χ_{CIGSe} and diminish the energy level mismatch at the CIGSe/ITO back-contact.

In practical situations, however, E_{h0} will also be influenced by the interface state density D_{it} or an extra interfacial compound. According to Abou-Ras et al., on Mo back-contact, the formation of the MoSe₂ layer can diminish the effective barrier height, hence converting the CIGSe/Mo interface from a Schottky to an Ohmic or quasi-Ohmic contact [58, 68]. On ITO back

contacts, Saifullah et al., Son et al. and Heinemann et al. suggest that the GaO_x layer plays a similar role as MoSe₂ [72, 74, 75]. In our case, the fundamental mechanism of how NaF PDT diminishes the actual barrier height E_h between CIGSe and the ITO layer will need further discussion. Judging by the removed roll-over effects in IV curves, the NaF PDT process must have diminished the E_h at the CIGSe/ITO interface.

In Figure 3-1 (a)-(d), the dark IV curve is crossed with the light IV for all samples, commonly known as the cross-over effect. According to Niemegeers et al., the cross-over effect originates from deep acceptor states in the extra layer between CdS and CIGSe, for which he coined the phrase ‘ordered defect compound’ (ODC) layer [110]. The deep acceptor state density is in the order of 10^{18} cm^{-3} , and the cross-over is a property of the CIGSe absorber material, thus independent of the properties of the buffer layer. To quantitatively evaluate the cross-over degree, we define a current density value j_{cross} corresponding to the crossing point of dark and light IV curves. The higher j_{cross} , the smaller the degree of the cross-over effect. As the NaF dose increases, the corresponding j_{cross} is 15, 35, 35, and 60 mA/cm² for NaF_0, NaF_2, NaF_4, and NaF_8, respectively. The increasing j_{cross} may imply that the defect state density in the ODC layer decreases when the PDT dose increases. For NaF_0, it is worth noting that the cross-over comes along with the roll-over effect. Again, according to Niemegeers et al., in this case, the cross-over may be due to minority carrier recombination at the back-contact junction. Further details can be found in references [114] and [100].

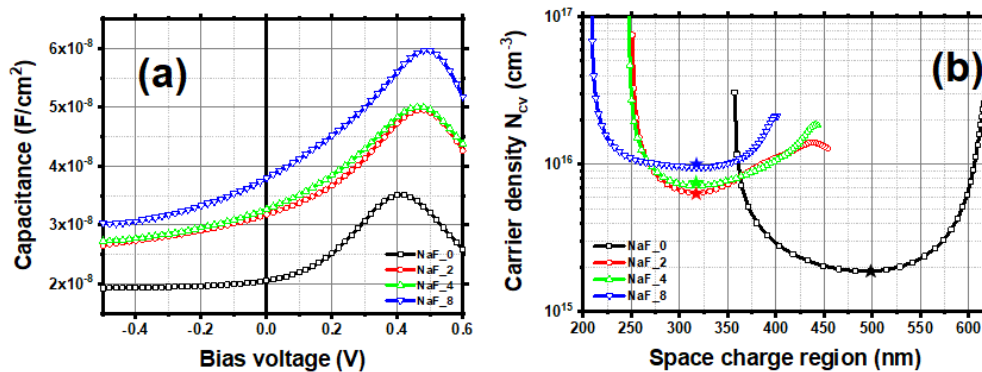


Figure 3-2. (a) CV characteristics of representative CIGSe solar cells with 0-8 mg NaF PDT and (b) carrier density N_{cv} distribution in the SCR

Figure 3-2 (a) compares capacitance-voltage characteristics of representative solar cells, and Table 3-1 summarizes the extracted CV results. Via Kimerling’s model introduced in section 1.9.2, we calculate the carrier density N_{cv} and space charge region width W_{SCR} at zero-volt bias in the solar cells. We measure the CV characteristics in dark conditions to avoid the influences of photogenerated carriers.

Firstly, in Figure 3-2 (a), we notice that the capacitance increases as the NaF PDT dose increases. According to the approximation of a parallel plate capacitor, we have

$$C = \frac{Q}{d} \tag{3-2}$$

where C is the capacitance of the parallel plate capacitor, Q is the total charge, and d is the distance between the plates. If we treat the solar cell as a parallel plate capacitor (as shown in Figure 1-20), Q corresponds to N_{cv} times the volume, and d corresponds to W_{SCR} . In our case, a higher capacitance suggests a higher N_{cv} or a narrower W_{SCR} for the NaF PDT-processed samples.

Secondly, based on Kimerling's model, Figure 3-2 (b) illustrates the N_{cv} distribution in the SCR of the solar cells. NaF_0 has the widest SCR and the lowest N_{cv} value. The NaF PDT-processed samples show a continuously increasing N_{cv} and a decreasing W_{SCR} , as summarized in *Table 3-1*. That is consistent with our previous deductions under the approximation of a parallel plate capacitor. We should be careful when interpreting the CV results because Kimerlings' model is based on a one-sided abrupt PN^+ assumption and considers only one parallel plate capacitor. Kimerlings' model does not fit if other interfacial effects (such as fixed charges or moveable ions) or more than one capacitor are involved in the solar cells. For example, NaF_0 shows an SCR width of 588 nm, which is wider than the thickness of the CIGSe layer (491 nm). Therefore, NaF_0 may have an extra back-contact diode or other interfacial effects that make it deviate from the one-diode PN^+ approximation. In other words, those CV results come from relative measurements, which means they are only comparable to each other, but the absolute values may deviate from the objective facts. To ensure the comparability of our CV results, the conditions for measurements and models for N_{cv} extraction are the same for all samples, so we believe those results are still reliable.

Thirdly, to crosscheck the results extracted by Kimerling's model, we also employ the Mott-Schottky model to extract the acceptor doping density N_A and the potential difference V_D in the solar cells, as summarized in *Table 3-1* [97]. N_A shows a consistently increasing trend with N_{cv} . NaF_0 has an N_A of $2.2 \text{ E}15 \text{ cm}^{-3}$, slightly lower than the commonly estimated $5.5 \text{ E}15 \text{ cm}^{-3}$ [110] due to a lack of Na incorporation in the CIGSe layer. For NaF_2 ($6.9 \text{ E}15 \text{ cm}^{-3}$) and NaF_4 ($8.0 \text{ E}15 \text{ cm}^{-3}$), N_A is slightly above $5.5 \text{ E}15 \text{ cm}^{-3}$, which means the Na has been incorporated into the CIGSe effectively. Furthermore, the N_A of NaF_8 continues to increase to $11.6 \text{ E}15 \text{ cm}^{-3}$, which is one order of magnitude higher than for NaF_0. As for V_D , NaF_0 has 533 mV, close to its V_{oc} of 510 mV. NaF_2 ($V_D = 691 \text{ mV}$) shows an increase of 158 mV in V_D , which is close to the V_{oc} boost from 510 mV (NaF_0) to 620 mV (NaF_2). It implies that the tremendous V_{oc} gain of NaF PDT is due to the V_D increase in the SCR. The V_D continues to increase for NaF_4 ($V_D = 716 \text{ mV}$) and NaF_8 ($V_D = 749 \text{ mV}$), but the increased momentum slows down, like the V_{oc} gain in the solar cells.

Combining the above CV and IV analysis, we find the NaF PDT increases the acceptor doping density N_A effectively, thus narrowing down the SCR and enhancing the contact potential difference V_D . That contributes to the main gain in V_{oc} that boost the *Eff* of ITO-based ultrathin CIGSe solar cells.

3.2.2 Temperature dependent current-voltage characteristics

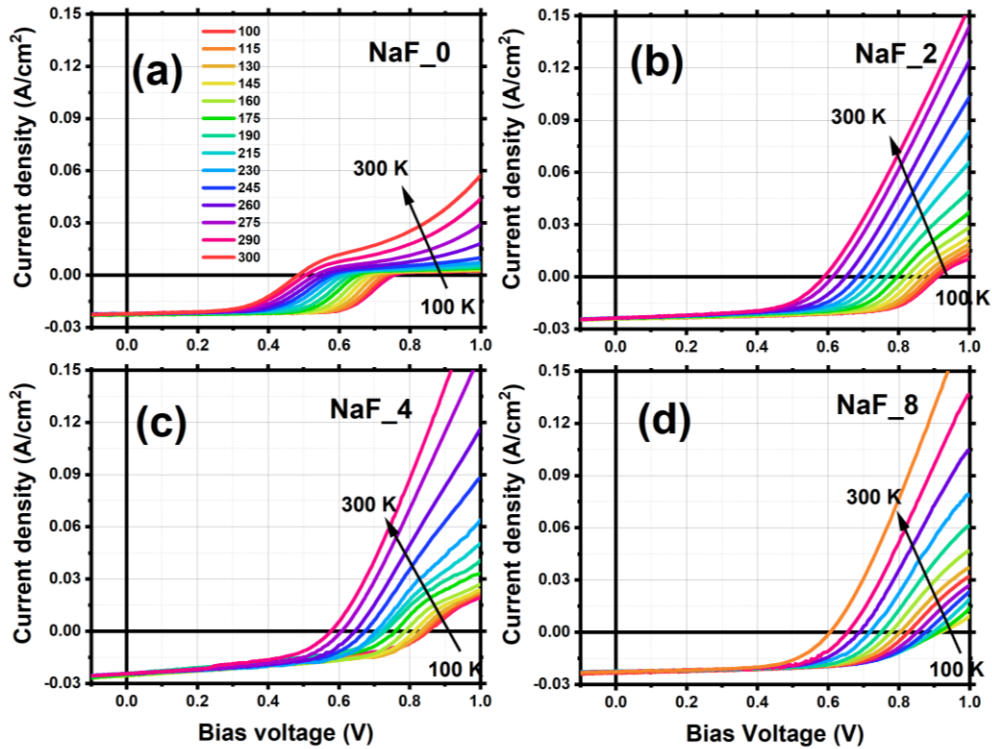


Figure 3-3. Temperature dependent current-voltage characteristics of the representative CIGSe solar cells with (a) 0, (b) 2, (c) 4, and (d) 8 mg NaF PDT

As shown in Figure 3-3, we perform temperature-dependent current-voltage (IVT) measurements in the 100-300 K range to further understand how the NaF PDT improves the V_{oc} of ITO-based ultrathin CIGSe solar cells. We notice that the roll-over effect has a temperature dependency. The roll-over effect appears in the entire 100-300 K range for NaF_0 and in the low-temperature range of 100-190 K only for NaF_2 and NaF_4. The temperature-dependency of the roll-over effect also occurs in Mo-based CIGSe solar cells [115], which attributes to the second junction at CIGSe/Mo back interface. The second junction can reasonably explain the roll-over effect at room temperature, but it cannot answer why roll-over only appears at low temperatures for NaF_2 and NaF_6. For simplicity, we can call this phenomenon a temperature-dependent roll-over effect (TD-ROE). In short, TD-ROE means the second junction at the back interface only shows up at low temperature and vanishes at room temperature. The second diode only influences the IV curves at low temperatures and will need further discussion.

According to Green, the thermal energy of electrons is lower at a lower temperature, fewer electrons can jump into the conduction band, and fewer defect states are activated in the semiconductor. Because of this, solar cells have a wider bandgap E_g show a higher V_{oc} at low temperatures [116]. In reference [117], the NaF PDT correlates to the N1 signal in admittance spectroscopy and the TD-ROE. N1 is a type of defect states close to the conduction band minimum E_c , and details are in references [118] and [102]. Therefore, it is reasonable to interpret the TD-ROE in this way: the NaF PDT moves the peak position of N1 closer to the E_c . For example, from 0.3 eV to 0.1 eV in reference [117]. If N1 is closer to the E_c , there is a higher possibility for defect states to become activated (charge and discharge). At room temperature,

the N1 defects are active due to thermal motion, so the doping density is relatively high in CIGSe. The back barrier height E_h of the second junction decreases when the CIGSe doping density is high, so the IV curves have no roll-over. On the contrary, at low temperatures (such as 100 K for NaF_2), the N1 states are “frozen”, the CIGSe carrier density is low, and the E_h is high, so the IV curves show a roll-over effect. The closer the N1 to E_c , the lower the temperature needed to freeze the N1 and see the IV curves roll-over [119].

In our case, the N1 of NaF_0 is relatively far away from E_c , which has a low possibility of being activated by thermal motion. At room temperature, the N1 is frozen, so the CIGSe carrier density is low while the E_h is high, and we can see the roll-over affects its IV curves. N1 states in NaF_2 are closer to E_c , so the thermal motion has a higher chance when activating the N1. At room temperature, the N1 is active because of the thermal energy, the carrier density is high, so the E_h is relatively low and the IV curves exhibit no roll-over. When the temperature is below 240 K, the thermal energy is not enough to activate the N1, and the roll-over effects appear. For NaF_4, the N1 is closer to E_c than NaF_2 and easier to ionize (hard to freeze), so the roll-over slowly appears in the IV curves when the temperature is below 220 K. NaF_8 shows no roll-over effect above 100 K because its N1 is very close to its E_c and makes it impossible to freeze those defective states. In summary, the NaF PDT moves the N1 closer to the E_c , thus needing a lower temperature to freeze those defect states. The higher the NaF dose, the lower the temperature for the roll-over effect in *Figure 3-3*.

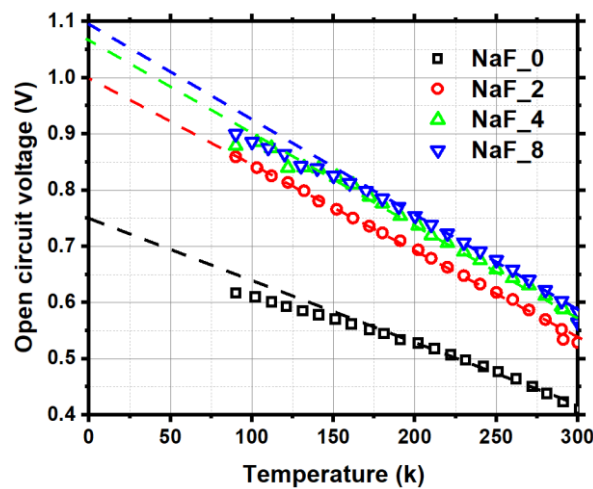


Figure 3-4. V_{oc} dependent on temperature for ultrathin CIGSe solar cells with different NaF dose

According to equation (1-11), we can evaluate the back-barrier height E_h (for holes) from temperature-dependent IV measurements. As plotted in *Figure 3-4*, V_{oc} against temperature T is extracted and linearly extended to intersect with the y-axis. The barrier height of the diodes Φ_b is 0.75 eV, 1.00 eV, 1.10 eV, and 1.12 eV for NaF_0, NaF_2, NaF_4, and NaF_8, respectively. The Φ_b increases with the NaF PDT dose is attributed to the E_h decrease at the CIGSe/ITO back interface: as the CIGSe absorbers come from the same batch, the band gap E_g is the same for all samples, while $\Phi_b = E_g - E_h$. Meanwhile, dotted lines of the linear fitting are parallel, which means the $(nkT/q) \cdot \ln(j_{00}/j_{sc})$ values are equal. It implies that the recombination mechanism is the same for ultrathin CIGSe solar cells with different NaF doses.

It is worth mentioning that IVT characterizes the whole device, so the Φ_b variation reflects the overall potential change in the solar cell, including SCR and back-contact interface. The potential difference V_D in SCR is critical for photogenerated carrier separation, and E_h at the CIGSe/ITO interface is vital for carrier collection. At room temperature, the maximum $V_{oc, max}$ should be:

$$V_{oc, Max} = V_D - \frac{E_h}{q} \quad (3-3)$$

Under ideal conditions, when the temperature is down to 0 K, V_D is replaced by E_g , as the bandgap is the only limit for V_{oc} then [116]. Chapter 5 will give a further quantitative analysis of potential changes in the SCR and back interface.

In summary, via the IVT characterization, we learn that NaF PDT may have changed the location of the N1 defects in the CIGSe, hence inducing the temperature-dependent roll-over effects in the NaF_2 and NaF_4. Judging by the increased Φ_b of solar cells with higher NaF doses, the NaF PDT also diminishes the barrier height E_h at the CIGSe/ITO interface.

3.2.3 Photoluminescence mapping characteristics

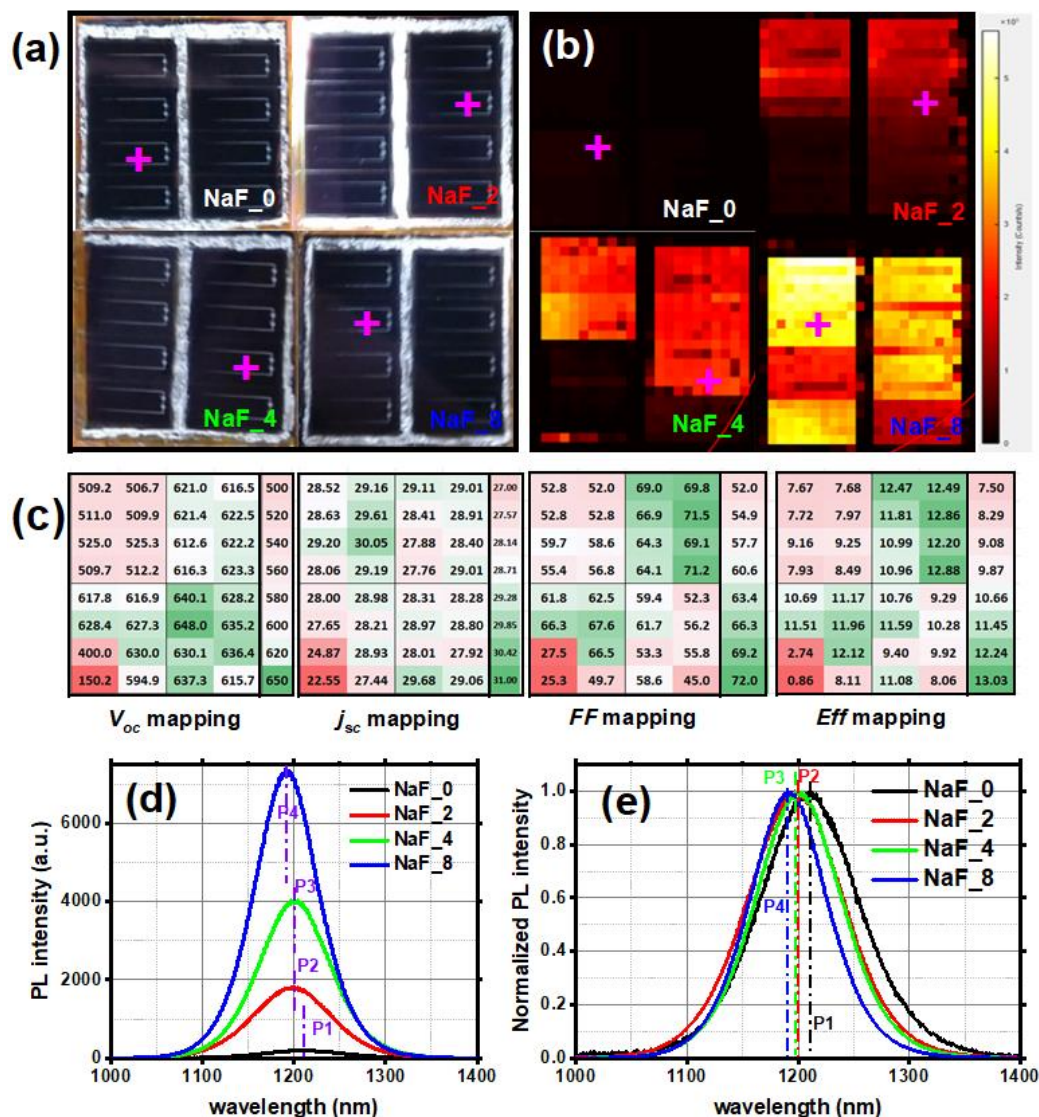


Figure 3-5. Photoluminescence mapping of the semi-transparent ultrathin CIGSe solar cells with 0-8 mg NaF PDT dose. (a) layout of the samples in the cryostat; (b) PL counts intensity mapping; (c) mapping of PV parameters V_{oc} (mV), j_{sc} (mA/cm²), FF (%) and Eff (%). The bar at the right side of each PV parameter represents the corresponding color scale; (d) PL intensity extracted from the pink crosshair marked spots in (a) and (b); (e) normalized PL intensity of the peaks from (d)

We carry out photoluminescence (PL) mappings at 80-85 K to gain insights into the recombination in ITO-based ultrathin CIGSe solar cells. The exciting light source is a 519 nm laser, which works at 5 mW power. Figure 3-5 (a) illustrates the layout of testing samples in the cryostat when measuring the PL mappings. All samples are loaded into the cryostat together to ensure the comparability of PL illuminating intensity.

Figure 3-5 (b) shows that solar cells with a higher NaF doping dose display a higher PL brightness. NaF_0 displays a dark image because its illumination counts (or contrast) are too low. Figure 3-5 (c) exhibits the V_{oc} , j_{sc} , FF , and Eff mappings to compare with the corresponding PL intensity. In each sample, the cells with dimmer PL intensity correlate to a lower Eff , such as the bottom left cells in the samples NaF_2 and NaF_4.

Table 3-2, FWHM (full width half maximum) value, corresponding energy value of the PL peak wavelengths, PL intensity and PV parameters of the corresponding solar cells for the measured in Figure 35 (d)

Sample name	FWHM (meV)	Peak Energy (eV)	PL intensity (Counts)	V_{oc} (mV)	j_{sc} (mA/cm ²)	FF (%)	Eff (%)
NaF_0	96	1.027	200	525	29.2	59.7	9.16
NaF_2	88	1.035	1700	622	28.9	71.5	12.86
NaF_4	78	1.038	4000	630	28.9	66.5	12.12
NaF_8	72	1.043	7000	648	29.0	61.7	11.59

In Figure 3-5 (a) and (b), we label representative cells with pink crosshairs to compare the PL spectra of ultrathin solar cells with different NaF doses. Figure 3-5 (d) displays the corresponding PL spectra, and Figure 3-5 (e) illustrate the normalized PL intensity in ratio to better locate the shift in peak wavelengths. Table 3-2 summarizes the full-width half maximum (FWHM), peak energy (according to $E = hc/\lambda = 1240/\lambda$, where h is Planck's constant, c is the speed of light, E is the photon energy, PL intensity, and PV parameters of the corresponding solar cells. For ultrathin CIGSe solar cells with a higher NaF dose, the PL peak exhibits a narrower FWHM, a higher PL peak energy (corresponding to bandgap), and a higher PL intensity.

Firstly, a broad PL emission (FWHM) is typical for Cu-poor CIGSe polycrystalline solar cells due to an unavoidable band tail [13]. Specifically, NaF_0 shows a wide FWHM of 96 meV, which consistently decreases to 88, 78, and 72 meV for NaF_2, NaF_4, and NaF_8. Therefore, the narrowed FWHM implies that NaF PDT narrows the radiative band tails in ultrathin CIGSe. That is consistent with our previous argument for the TD-ROE: a higher dose of NaF PDT moves the N1 defect states closer to the E_c of CIGSe hence the band tails are also narrowed. Secondly, as the NaF dose increases, the peak energy of PL enlarges from 1.027 to 1.043 eV for NaF_0 to NaF_8. Those peaks may originate from In_{Cu} donor defects, as the gap between the In_{Cu} energy level and the valence band maximum E_v of the CIGSe is 1.033 eV [54, 120]. In addition, Wei et al. predict that Na doping in $CuInSe_2$ would eliminate In_{Cu} defects, thus increasing the effective hole density [55]. In short, the increased peak energy of PL is caused by the widened energy gap between In_{Cu} and E_v as the NaF PDT process eliminates part of In_{Cu} defects. Thirdly, compared to the Na-free reference NaF_0, the PL intensity of NaF_2 increases by one order of magnitude. The PL intensity of NaF_4 and NaF_8 continues to increase with a less pronounced increment. According to Ledinek et al., a higher PL intensity can be attributed to the increase of the carrier density, as the radiative recombination is proportional to the carrier density [121]. From this perspective, the increasing PL intensity confirms the N_{cv} and N_A extracted from CV measurements.

3.2.4 Depth distribution of Cu, Ga and Na in the absorber

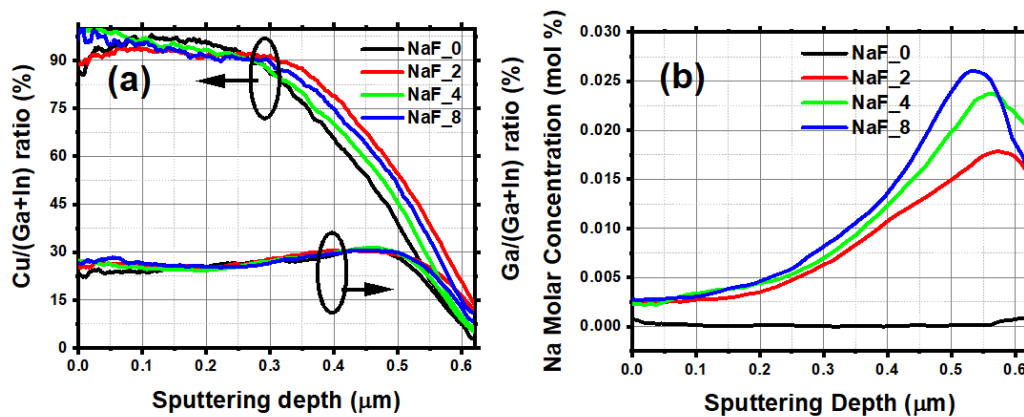


Figure 3-6. (a) Depth distribution of Cu/(Ga+In) and Ga/(Ga+In) ratio and (b) depth distribution of Na in the ultrathin CIGSe absorber; 0 represents the CdS interface

The depth distribution of the Ga/(Ga+In) (GGI) ratio plays a critical role in deciding the bandgap E_g gradient in CIGSe absorbers. Figure 3-6 (a) presents the depth distribution of Cu/(Ga+In) (CGI) and GGI. The GGI ratios of those four samples are overlapping, while CGI shows a similar slope towards the back interface. The main reason behind the similarity of depth distribution is that those CIGSe absorbers come from the same co-evaporation batch, as we use the vacuum break PDT scenario described in section 3.1. The similarity in Ga gradient and Cu distribution is consistent with observations from the reference [122]. From this perspective, NaF PDT does not change the composition of CIGSe but rather passivates the grain boundaries formed during the 3-stage co-evaporation, thus increasing N_A in the CIGSe bulk [51]. According to Mansfield et al. [15], on Mo back-contacts, the ultrathin CIGSe can achieve 733 mV V_{oc} by optimizing the Ga gradient (called the Ga bandgap notch), basically equal to 734 mV of 2μm thick CIGSe solar cells [16]. Consequently, in terms of Ga grading, the V_{oc} of our ITO-based ultrathin CIGSe solar cells still has room for optimization, as the maximum V_{oc} achieved via NaF PDT is only 648 mV.

Figure 3-6 (b) displays the depth distribution of Na in CIGSe absorbers. Consistent with the results in chapter 2, NaF_0 shows almost no Na signal, while NaF_2-NaF_8 reveal a consistently increasing Na density inside the CIGSe. Furthermore, the Na is congregating at the CIGSe/ITO interface, which is surprising as the NaF PDT comes from the front side. The high Na density close to the CIGSe/ITO interface may influence the back barrier height E_b , as discussed in section 3.2.2. In the bulk of CIGSe, the Na concentration of the NaF PDT-doped samples is higher than the reference NaF_0. It implies that the NaF PDT has also modified the CIGSe bulk properties, such as N_A .

In conclusion, GD-OES analysis confirms that Na is incorporated into the CIGSe effectively via NaF PDT doping. Na shows the distribution in CIGSe bulk and a congregation close to the CIGSe/ITO interface. That assures the NaF PDT influences CIGSe bulk and the CIGSe/ITO back interface.

3.2.5 High-resolution transmission electron microscopy characteristics

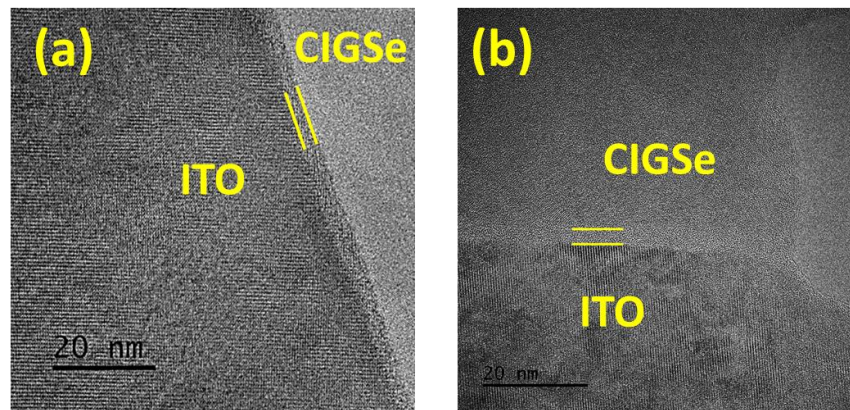


Figure 3-7. HRTEM of the interfacial layer at the CIGSe/ITO back-interface. (a) NaF_2 and (b) NaF_8

We employ high-resolution transmission electron microscopy (HRTEM) to see the surface morphology of the CIGSe/ITO back interfaces. This is a cooperation work with Dr. Sophie Meuret and Cecile Marcelot from CEMES (Toulouse). The research leading to these results has received funding from the European Union Horizon 2020 research and innovation programme under grant agreement No. 823717 – ESTEEM3.

For an immediate comparison, we chose NaF_2 and NaF_8 as representative samples and mechanically thinned them into CIGSe lamellae. Figure 3-7 shows HRTEM photo of those two lamellae. Between CIGSe and ITO layer, we can observe a transition region with different textures, as indicated by the yellow lines. According to references [71, 74, 123], we refer to this region as the GaO_x layer. Based on the HRTEM estimation, the thickness of the GaO_x is 4-7 nm for NaF_2 and 1-5 nm for NaF_8. The GaO_x thickness depends on the locations in the lamellae, while a general difference between NaF_2 and NaF_8 is hard to summarize. Also, the homogeneity of GaO_x thickness is hard to distinguish. Overall, HRTEM confirms the GaO_x existence. It may have been formed similar to MoSe_2 between CIGSe and Mo.

As reviewed in section 1.7, the properties of the GaO_x layer are difficult to clear because the GaO_x formation takes place during the CIGSe deposition. Judging from the IV, CV, and IVT characteristics, the E_h at the CIGSe/ITO interface plays a critical role in the PV performance of ITO-based ultrathin CIGSe solar cells. From a material perspective, the properties of GaO_x (such as thickness, bandgap, conductivity, and work function) decide the E_h directly. Therefore, the NaF PDT process must have tuned the properties of GaO_x . Because ITO is an n-type degenerated semiconductor, while CIGSe is a p-type semiconductor, the GaO_x must have modified the bandgap mismatch at the CIGSe/ITO interface. Given the complexity of the CIGSe/ITO back interface, chapter 4 will focus on comparing the similarities and differences between CIGSe/Mo and the CIGSe/ITO interface.

3.3 SCAPS simulation

According to the device and material characterizations illustrated in section 3.2, we can summarize the working mechanism of NaF PDT in two aspects:

- (1) Increased acceptor doping density N_A of the CIGSe layer, hence improved V_{oc} of the solar cells;
- (2) Diminished back barrier height E_h at the CIGSe/ITO interface, thus removed roll-over effect in the IV curves at room temperature.

This section employs SCAPS simulation to verify those two points and to reproduce the experimental observations [124]. Table 3-3 lists the settings of each layer, which mainly refer to the generally accepted model from reference [110]. We adjust part of the parameters to fit our experiment conditions as follows: for the CIGSe layer, the thickness is reduced to 500 nm, and the bandgap E_g increases to 1.25 eV; for the CdS layer, the thickness is 80 nm, and the bandgap is 2.45 eV; for the i-ZnO layer, the shallow doping density increases to 5 E18 cm⁻³. For the other settings, such as layer structure and interfacial properties, we use the default settings in SCAPS [125, 126]. It is worth noting that the parameter settings are not fully optimized here, as our goal is to reproduce the PV performance trend of ultrathin CIGSe solar cells that depends on N_A and E_h .

Table 3-3. parameter settings of SCAPS simulation. ODC represents the ordered defect compound layer

Layer	CIGSe	ODC	CdS	i-ZnO
Thickness (nm)	500	15	80	80
Bandgap E_g (eV)	1.25	1.45	2.45	3.4
Electron affinity (eV)	4.5	4.5	4.45	4.55
Dielectric permittivity (relative)	10	10	10	10
Effective density of states (conduction band) N_c (cm ⁻³)	2 E18	2 E18	2 E18	4 E18
Effective density of states (valence band) N_v (cm ⁻³)	2 E18	2 E18	1.5 E19	9 E18
Electron thermal velocity (cm s ⁻¹)	1 E7	1 E7	1 E7	1 E7
Hole thermal velocity (cm s ⁻¹)	1 E7	1 E7	1 E7	1 E7
Electron mobility m_n (cm ² V ⁻¹ s ⁻¹)	50	1	50	50
Hole mobility m_p (cm ² V ⁻¹ s ⁻¹)	20	1	20	20
Shallow doping type and density (cm ⁻³)	p-type, density varies from 1-15 E15	p-type, 1 E13	n-type, 1 E16	n-type, 5 E18
Defect type and density (cm ⁻³)	Neutral 1 E18	Neutral 1 E17	-	-

3.3.1 Acceptor doping density

Table 3-4. Comparison of PV parameters and carrier density between simulation and experiments

Simulation results					
	N_A (E15 cm ⁻³)	V_{oc} (mV)	j_{sc} (mA/cm ⁻²)	FF (%)	Eff (%)
	1	549	28.3	53.3	8.3
	5	596	30.1	65.6	11.8
	8	609	29.9	65.6	11.9
	10	616	29.6	65.0	11.9
	15	635	29.0	62.9	11.6
Experimental results					
	N_A (E15 cm ⁻³)	V_{oc} (V)	j_{sc} (mA/cm ⁻²)	FF (%)	Eff (%)
NaF_0	2.2	510 ± 13	30.4 ± 1.0	54.8 ± 4.0	8.5 ± 1.0
NaF_2	6.9	620 ± 2	29.6 ± 0.7	64.9 ± 1.4	11.9 ± 0.4
NaF_4	7.9	622 ± 6	29.6 ± 0.7	65.6 ± 3.0	12.1 ± 0.7
NaF_8	11.6	636 ± 4	29.2 ± 0.3	63.1 ± 4.1	11.7 ± 0.7

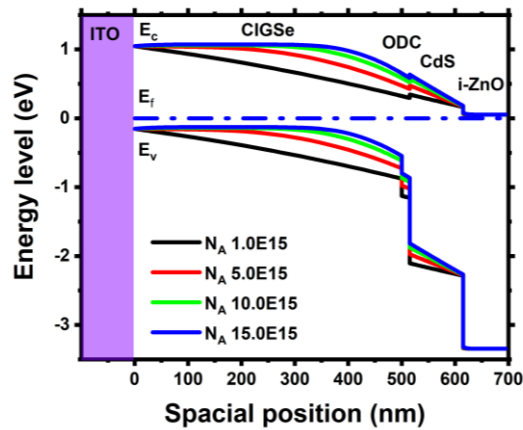


Figure 3-8. Energy band diagram (under dark condition) of the ultrathin CIGSe solar cells with different acceptor doping density N_A

Table 3-4 summarizes the PV parameters of the solar cells from simulations and experiments. In SCAPS simulations, we vary N_A in the 1-15 E15 cm⁻³ range to see the PV performance of the ultrathin CIGSe solar cells. We extract the N_A from the experimental results of four representative samples via the Mott-Schottky model.

For a higher N_A , the V_{oc} shows an increasing trend in simulation, which is consistent with the experimental results. The reason is a strengthened potential difference V_D in the SCR for a higher N_A . Under ideal conditions, equation (2-1) can estimate V_D in the SCR of a PN⁺ junction [78]. Figure 3-8 illustrates the bandgap diagram of ultrathin CIGSe solar cells under an equilibrium state (in dark conditions and with no bias voltage applied). The bending energy level in the CIGSe layer corresponds to the SCR of solar cells, which graphically demonstrates that a higher N_A induces a narrower SCR. Based on the calculation in reference [78], V_D depends on W_{SCR} (the width of the SCR) and N_A , and an increased N_A increases V_D , thus enhancing the V_{oc} of ultrathin CIGSe solar cells.

For j_{sc} and FF , however, a more sophisticated trend can be seen in the simulation results: first, it increases with N_A and then decreases slightly. The experimental FF shows a consistent trend with the simulation results. However, the experimental j_{sc} shows an overall decreasing trend. For a higher N_A , the j_{sc} of ultrathin CIGSe solar cells decreases. The reason is that the recombination loss of photogenerated carriers increases. A narrower SCR means a wider neutral region, hence a higher possibility for recombination in the CIGSe bulk. The simulated and experimental Eff exhibit the same trend: first increasing with N_A and then slightly decreasing. It implies that there exists an optimal N_A for the CIGSe absorbers, which can balance the stronger V_D (thus higher V_{oc}) and a lowered j_{sc} (induced by higher recombination) in ultrathin CIGSe solar cells.

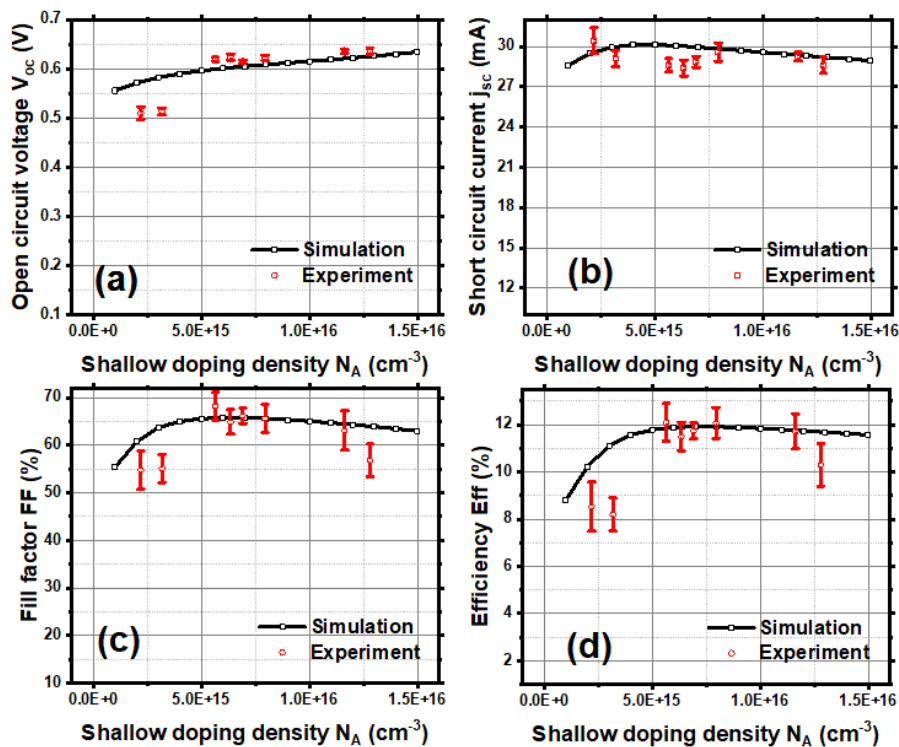


Figure 3-9. PV parameters alignment between the simulation and the experiments. Black squares are SCAPS simulation data, and red circles are the experimental results. For experimental results, N_A used to compare with the simulation results is extracted from Mott-Schottkey plots

Figure 3-9 compares the PV parameters of simulations and experiments to align the fitting graphically. SCAPS simulations use smaller N_A steps, and experiment results include eight samples from one batch co-evaporation. We can see simulations and experimental results display a consistent trend. We observe that more than one batch of CIGSe solar cells reveals the same PV performance trend in experiments (not shown here). Therefore, it is reasonable to conclude that a higher N_A enhances V_D , hence the V_{oc} of ultrathin CIGSe solar cells after NaF PDT.

3.3.2 Back-contact barrier

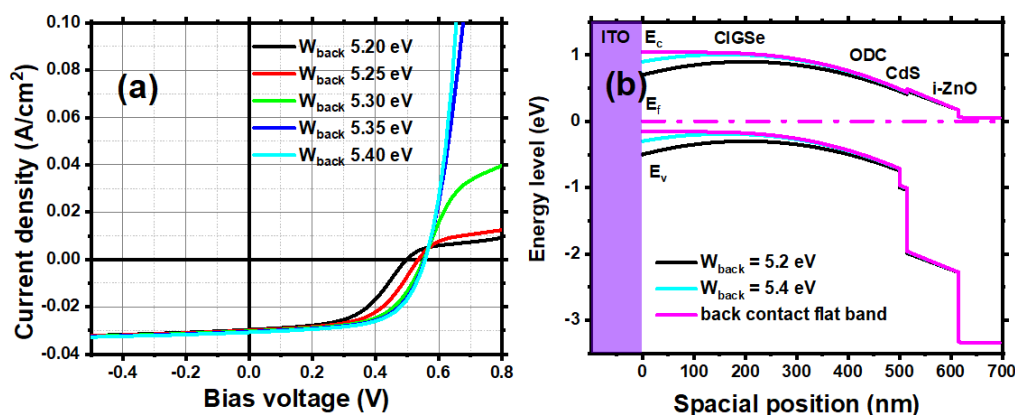


Figure 3-10. (a) SCAPS simulated IV results of ultrathin CIGSe solar cell with different work function W_{back} of the back-contact

Now we move on to simulating the roll-over effect in the IV curves. According to equation (3-1) $q^*E_h = W_{back} - \chi_{CIGSe}$, we can reproduce the changes in E_h by varying the work function of back-contact W_{back} or the electron affinity χ_{CIGS} of the CIGSe layer. We chose to change W_{back} when simulating the back barrier height changes in E_{h0} at the CIGSe/ITO interface, as the variation of χ_{CIGS} may induce additional effects at CIGSe/CdS interface. In SCAPS, the barrier E_h corresponds to the majority carriers, which are holes in CIGSe. The N_A in CIGSe was set at the general doping level of $5.5 \text{ E}15 \text{ cm}^{-3}$ [110], and Table 3-3 lists the settings of other layers in the ultrathin CIGSe solar cells.

Figure 3-10 (a) presents IV curves of the simulated solar cells with W_{back} in the 5.2-5.4 eV range. In reality, the work function of ITO W_{ITO} depends on its fabricating procedure and varies between 4.10-5.53 eV [127]. When W_{back} increases from 5.30 to 5.35 eV, the roll-over effect in IV curves disappears. The roll-over effect is sensitive to the work function. Also, it implies that E_h has a turning point E_{hT} . When $E_h < E_{hT}$, E_h increases with W_{back} . When $E_h \geq E_{hT}$, the roll-over effect in IV curves disappears, and E_h does not change with W_{back} increase. Figure 3-10 (b) exemplifies the bandgap diagram when $W_{back} = 5.2 \text{ eV}$ (black), $W_{back} = 5.4 \text{ eV}$ (cyan), and flat band ($W_{back} = 5.52 \text{ eV}$) (pink) in equilibrium states. A lower W_{back} induces a band bending at the CIGSe/ITO interface, which forms a double-banded bandgap in the solar cell, as Kim et al. predict [31]. This double-banded bandgap means that a lower W_{back} induces a back-contact diode into the solar cell. It has an opposite direction to the main PN junction at CIGSe/CdS. However, when W_{back} slowly increases, the bandgap bending at the CIGSe/ITO interface is gradually flattened until it reaches the flat band condition.

In summary, SCAPS simulations verify that adjusting E_h at the back contact can tune/diminish the roll-over effect in IV curves of ultrathin CIGSe solar cells. Changing W_{back} can tune the E_h , and when $E_h \geq E_{hT}$, the roll-over effect disappears in IV curves.

3.4 Summary and conclusion

This chapter optimizes the NaF PDT dose for the ultrathin CIGSe absorber on ITO substrates. We achieve a maximum efficiency of 12.9% for ITO-based ultrathin CIGSe solar cells [78]. Based on the CV analysis, NaF PDT can effectively tune the distribution and number of N_{cv} in the SCR. Combining IV and CV characterizations, it is deduced that the NaF PDT mainly increases acceptor doping density N_A in the bulk of CIGSe and diminishes the barrier E_h for holes at the CIGSe/ITO interface, hence improving the V_{oc} of the solar cells. The temperature-dependent roll-over effects imply that the NaF PDT changes the location/depth of N1 defect states. Also, the PL intensity increase confirms that the NaF PDT process increases N_A in the solar cells. GD-OES results reveal that the NaF PDT step does not change the Ga or Cu ratio in-depth distribution. The Na has been effectively doped into the absorber and shows an aggregation approaching the CIGSe/ITO interface. That supports our claim that the NaF PDT improves N_A in the CIGSe bulk and diminishes E_h at the CIGSe/ITO interface. For verification, we simulate the influences of an increasing N_A in SCAPS to fit the experiment PV results. We also reproduce the roll-over effect in the simulated IV curves to verify that the NaF PDT has diminished E_h at the CIGSe/ITO interface.

In summary, the influences of NaF PDT mainly have two aspects:

- (1) Increased acceptor doping density N_A in the bulk of CIGSe from 2.2 to 11.6 E15 cm⁻³;
- (2) Reduced back-barrier E_h at the CIGSe/ITO interface.

Combining those two effects, the optimized ultrathin CIGSe solar cells with 8 mg NaF PDT have a V_{oc} of 635 mV on ITO substrates.

Chapter 4 Modification of the back interface

According to equation (1-11), bandgap E_g of the CIGSe layer and back-barrier height E_h at the CIGSe/ITO interface decide the barrier height Φ_b of CIGSe solar cells. Therefore, E_h is critical for the open circuit voltage V_{oc} of the solar cells. Similarly, the recombination velocity S_b of the photogenerated carriers at the back interfaces also influences the PV performance of the ultrathin CIGSe solar cells. Based on Kotipalli et al.'s simulations, inserting a 2 nm rear-passivation layer can reduce the back S_b and improve the Eff of the Mo-based ultrathin CIGSe solar cells [12]. In the experiments, materials such as Al_2O_3 , MgF_2 [81], SiO [90], and gallium oxide Ga_2O_3 [73] can diminish the S_b hence improving the solar cell efficiency. S_b affects the recombination processes described in equation (1-6), and E_h influences the thermionic emission (or diffusion) process. E_h and S_b characterize different mechanisms of carrier transport in the same junction. Even though recombination and thermionic emission (or diffusion) are independent mechanisms, S_b and E_h are not independent of each other. If we define an effective barrier height $E_{h,e}$ to quantify the blocking effect of the junction for the passing current, according to reference [79], the $E_{h,e}$ decrease with S_b increases. In the latest simulation research [128], a higher back S_b is favourable for the ultrathin CIGSe solar cells with a Schottky back-contact because higher S_b diminishes $E_{h,e}$ hence releasing the blocking effects of the Schottky back-contact for the passing current.

Given the importance of back interfaces, clearing passivation/recombination properties at the back contacts is critical before inserting nanoparticles in the bifacial semi-transparent ultrathin solar cells (BSTUT SCs) for light and carrier management. In this chapter, we first introduce the fabrication processes of SiO_2 point-contacts on Mo and ITO ($In_2O_3: Sn$) substrates. The passivation effects of SiO_2 point-contacts for Mo-based solar cells have been proved beneficial in our previous work [112]. Here Mo-based solar cells are working as reference to guarantee we fabricate the SiO_2 properly. We compare the characteristics (IV, CV, IVT, EQE/IQE, PL, and GD-OES) of the solar cells deposited on Mo and ITO back-contacts with/without passivation. Then the deductions from those characterizations will be verified by SCAPS simulation theoretically.

4.1 Fabrication of the SiO₂ point-contacts on Mo and ITO substrates

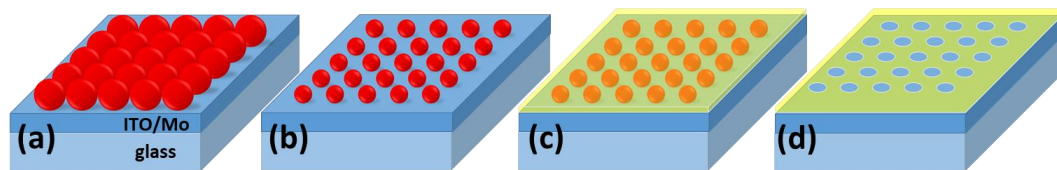


Figure 4-1. Fabrication steps of the SiO₂ point-contact: (a) deposition of the PS (polystyrene) spheres on the substrate surface; (b) plasma etching of the PS spheres; (c) deposition of SiO₂; (d) removing of the PS spheres

We use nanosphere lithography (NL) method to prepare SiO₂ point-contact nanostructures. Using polystyrene (PS) nanospheres as masks, the NL method has demonstrated its feasibility and applicability to deposit SiO₂ in reference [112]. Figure 4-1 shows the preparation steps of the SiO₂ point-contacts:

(a) Firstly, we mix the PS spheres purchased from microparticles GmbH (the product type is PS-R-KM391) with solution A in a volume ratio of 1:1. The solution A contains 10 μ l H₂SO₄ (98%) and 1 ml ethanol (with 1 vol. % styrene). In the second step, we disperse the diluted PS spheres on the deionized water surface to form a closely-packed monolayer in a petri dish. After 10 minutes, we shake the petri dish gently so that the PS monolayer can re-crystallize since there are still many line defects and point defects after the first dispersion. After the re-crystallization, we slide Mo/glass and ITO/glass substrates to the bottom of the petri dish beneath the PS spheres. After sucking out the water with a pipette, the PS spheres are transferred onto Mo and ITO substrates, as illustrated in Figure 4-1 (a);

(b) The samples are then put into Femto (from Diener electronic) for reaction plasma etching to reduce the diameter of the PS spheres. The Femto uses a pressure of 0.2 mbar with 99.99% O₂ and a power of 240 Watt. The diameter of PS reduces in the plasma etching process. We use three etching times: 15 mins, 22 mins, and 30 mins. For simplicity, we refer to the corresponding samples as Mo-15, Mo-22, and Mo-30 (or ITO-15, ITO-22, and ITO-30);

(c) The SiO is thermally evaporated in an O₂ atmosphere in a PVD to form a 50 nm (and 200 nm) SiO₂ layer on Mo and ITO substrates. During SiO evaporation, the substrates use room temperature, and a calibrated quartz balance monitors the deposition rate. For simplicity, we refer to the substrates without SiO₂ as Mo_0 (or ITO_0) and with 50 nm SiO₂ as Mo_50 (or ITO_50);

(d) After the SiO₂ deposition, we remove the PS masks via supersonic bath with toluene and deionized water for 20 minutes. The blue openings in Figure 4-1 (d) represent the point-contact that allows CIGSe to contact with ITO or Mo, and the yellow parts stand for the SiO₂.

For the solar cells presented in this section, the thickness of ITO layer is 300 nm, and the NaF used for PDT is 2 mg. The thickness, Cu/(Ga+In) and Ga/(Ga+In) ratio of CIGSe are 50 nm, 0.80, and 0.31 for the first batch sample (50 nm SiO₂), and 451 nm, 0.82, and 0.34 for the second batch (200 nm SiO₂), respectively. The other layers (CdS and i-ZnO/AZO/Ni/Al) were deposited according to the same recipes described in the first chapter and have a thickness of 60 nm/80 nm/300 nm/10 nm/2000 nm correspondingly.

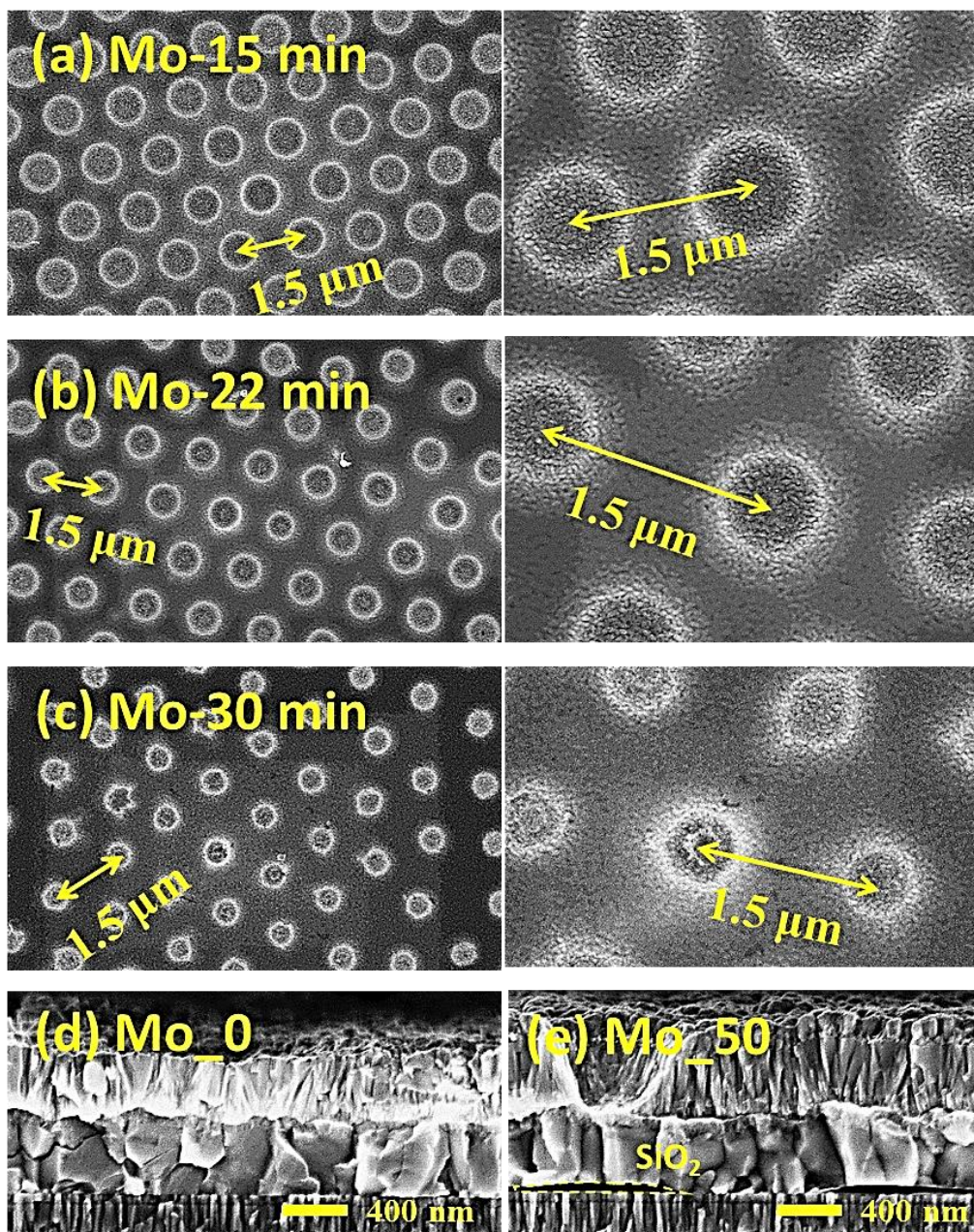


Figure 4-2. SiO_2 point-contact on Mo substrates with plasma etching of PS spheres for (a) 15 minutes; (b) 22 minutes; (c) 30 minutes. (d) cross-section SEM of Mo without SiO_2 and (e) Mo with 22 minutes of etching. The thickness of SiO_2 is 50 nm

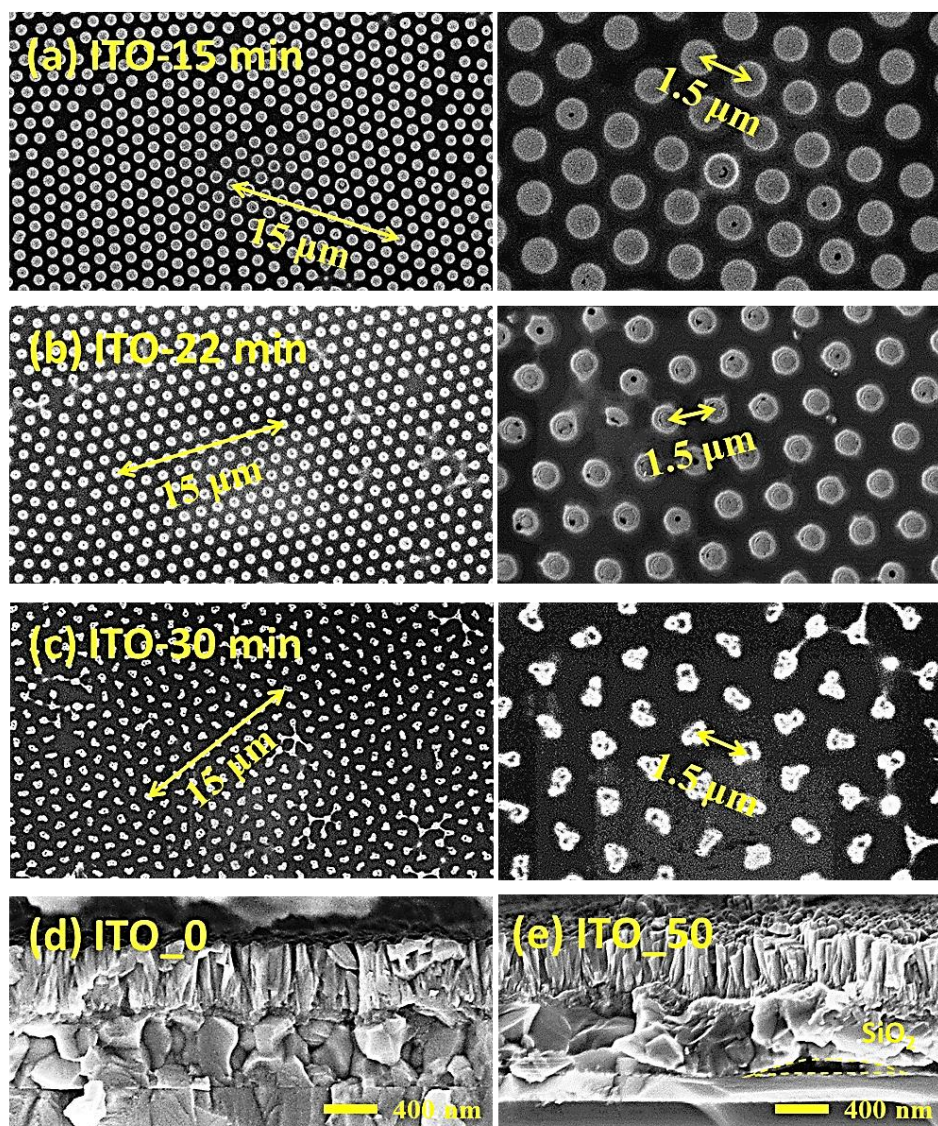


Figure 4-3. SiO_2 point-contact on ITO substrates with plasma etching of PS spheres for (a) 15 minutes; (b) 22 minutes; (c) 30 minutes. (d) cross-section SEM of ITO without SiO_2 and (e) ITO with 22 minutes of etching. The thickness of SiO_2 is 50 nm

After the NL process, we take scanning electron microscopy (SEM) pictures to check the surface morphology of Mo and ITO passivated by SiO_2 point-contacts. Figure 4-2 (a)-(c) and Figure 4-3 (a)-(c) show the top-view of SiO_2 point-contacts on Mo and ITO substrates. As the yellow arrows mark, the pitch of all contact circles is $1.5 \mu\text{m}$, equal to the diameter of PS spheres. The diameter of contact circles is also estimated based on SEM measurements. It is 1000 nm for 15 minutes of etching, 790 nm for 22 mins, and 450 nm for 30 mins, respectively. Therefore, the contact ratio between CIGSe and ITO (or Mo) is 40%, 25% and 8% for 15, 22 and 30 min, as listed in Table 4-1.

In Figure 4-2 (a)-(c), we can observe texture in grain shapes on the Mo-based samples, especially at the circle edges. The reason is that 50 nm SiO_2 is relatively thin compared to the surface grain size of Mo. Because of shadowing effect of the PS spheres, the circle edges are not sharp but sloped. The cross-section SEM picture in Figure 4-2 (e) verifies that SiO_2 has a dome shape instead of a rectangular shape. On ITO back-contacts, however, we can recognize no texture. This is due to the fact that sputtered-ITO has a smooth surface. In Figure 4-3 (c),

the edge of point-contacts is not circular but more like a dumbbell or a three-balls-congregation shape. The reason is that residua adhered to the PS spheres after the plasma etching process. During the SiO₂ co-evaporation process, those residua also have a shadowing effect, so the point-contacts lose their circular shape. The Mo-based samples have no residua problem, as the point-contacts maintain their circular shapes in Figure 4-3 (c). Compared to ITO substrates, Mo substrates have a higher conductivity and coarser surface, which might have influenced the plasma etching process and distribution of residua. In the following characterizations and discussions, we focus more on ITO-22 and Mo-22, whose point-contacts have a circular shape.

Figure 4-2 (d)-(e) present the cross-section SEM of Mo_0 and Mo_50, and Figure 4-3 (d)-(e) show ITO_0 and ITO_50. In the CIGSe layers, we find no obvious differences (such as grain size) in morphology between references and SiO₂ passivated samples. On the reference, window layers display erecting grains. On passivated samples Mo_50 and ITO_50, ZnO layers show sector columns due to their conformal growth on the SiO₂ point-contacts. That may bring extra interdiffusion effects in the CIGSe layer during the 3-stage co-evaporation process, as the glowing discharge optical emission spectroscopy (GD-OES) characteristics part will discuss.

In summary, we have fabricated SiO₂ point-contacts with 8%, 25% and 40% contact ratios via changing the etching time of PS spheres. SiO₂ point-contacts and other layers of the solar cells have grown conformally on ITO and Mo substrates without hollows or delamination. That is the basis for further analysis and characterizations of the solar cells.

4.2 Passivation effects of the back interface by SiO₂ point-contacts

4.2.1 Current-voltage and capacitance-voltage characteristics of the solar cells

Table 4-1. PV parameters of the ultrathin CIGSe solar cells with different back-contact. Explanation of abbreviations: Mo-x means the ultrathin CIGSe solar cells are fabricated on Mo substrates, ITO-x means the samples are ITO-based. The suffixes 'x' represent the etching time, and 'x' stands for the SiO₂ thickness

Sample ID	SiO ₂ thickness (nm)	Plasma etching time (min)	Contact area ratio (%)	V _{oc} (mV)	j _{sc} (mA/cm ²)	FF (%)	Eff (%)	R _s (Ωcm ²)	R _{sh} (Ωcm ²)	Referred to as
Mo-0	0	0	100	609±6	25.3±1.0	61.8±4.4	9.5±0.6	6.1	244	Mo_0
Mo-15	50	15	40	606±4	26.4±1.4	67.9±1.6	10.9±0.4			
Mo-22	50	22	25	609±5	28.2±2.2	64.5±2.3	11.1±0.9	5.3	531	Mo_50
Mo-30	50	30	8	608±5	27.5±1.0	62.0±1.6	10.4±0.3			
ITO-0	0	0	100	597±3	26.6±1.1	59.9±3.6	9.5±0.4	11.2	336	ITO_0
ITO-15	50	15	40	580±5	26.7±1.1	58.0±2.0	9.0±0.3			
ITO-22	50	22	25	574±7	26.9±1.2	58.0±1.7	9.0±0.2	11.3	508	ITO_50
ITO-30	50	30	8	466±20	13.3±3.6	19.6±2.3	1.2±0.5			
Mo-0	0	0	100	613±7	25.1±0.4	65.6±2.7	10.1±0.6			
Mo-15	200	15	40	632±18	25.8±0.2	69.9±2.9	11.4±0.8			
Mo-22	200	22	25	637±8	25.5±0.5	66.6±4.8	10.8±1.0	3.5	1077	Mo_200
Mo-30	200	30	8	646±8	26.2±0.3	67.0±5.6	11.3±1.1			
ITO-0	0	0	100	603±6	27.9±0.4	58.0±2.1	9.8±0.5			
ITO-15	200	15	40	517±14	29.2±0.4	50.0±1.9	7.6±0.5			
ITO-22	200	22	25	473±29	28.4±0.6	35.7±2.3	4.8±0.5	28.1	4527	ITO_200
ITO-30	200	30	8	-	-	-	-	-	-	-

Table 4-1 lists geometry-related parameters (etching time of the PS spheres and contact ratio between CIGSe and ITO or Mo), average PV parameters (open circuit voltage V_{oc} , short circuit current density j_{sc} , fill factor FF , and conversion efficiency Eff), and resistances of the representative solar cells.

According to Table 4-1, 50 nm SiO₂ point-contacts enhance j_{sc} , FF and Eff of the Mo-based ultrathin CIGSe solar cells, which is consistent with our previous results in reference [112]. Optically, SiO₂ point-contacts reduce the Mo parasitic light absorption and increase the light reflection from CIGSe/Mo interface, which contributes 1.1-2.9 mA/cm² gain in j_{sc} . Electrically, SiO₂ restrains the recombination at CIGSe/Mo back interfaces, hence improving the FF of passivated solar cells [112]. V_{oc} shows slight variations from sample to sample, with an amplitude of 1-3 mV in the averaged values. Two reasons are responsible: Firstly, these samples reveal a steep back Ga grading (as shown in section 4.2.5). It repels photogenerated electrons from the back contact and thus restrains the back recombination, which acts similarly to passivation. Because of this, back interface passivation will bring a reduced beneficial effect on ultrathin cells with a high Ga grading. Secondly, we co-evaporate the

absorbers at a relatively low temperature (450 °C maximum), so the interfacial MoSe_x may not have formed well. That will decrease the V_{oc} of our solar cells. Under combined actions of these two factors, the V_{oc} remains stable after back interface passivation for ultrathin CIGSe solar cells on Mo.

When the thickness of the SiO₂ layer of the point-contacts increases to 200 nm, on Mo all PV parameters of the passivated samples exhibit an enhancement. The average V_{oc} of the passivated solar cells is enhanced by 19-33 mV compared to the reference. A prime reason is that the SiO₂ influences the interdiffusion between Ga-Se and In-Se, as will be confirmed later by GD-OES measurements. When the SiO₂ point-contacts have a thickness of 200 nm that is comparable to the CIGSe thickness of 451 nm, the surface terrain of SiO₂ point-contacts can promote the Ga-In interdiffusion process hence mitigating the Ga grading in solar cells. The average j_{sc} is also increased by 0.4-1.1 mA/cm² because SiO₂ suppresses the recombination at CIGSe/Mo and enhances the reflection from the CIGSe/SiO₂/Mo interface. Overall, all the SiO₂ passivated solar cells on Mo show higher Eff than their reference samples.

However, SiO₂ passivated solar cells manifest a deteriorated efficiency on the ITO back-contacts. When the thickness of SiO₂ point-contacts is 50 nm, the average V_{oc} drops from 597 to 466 mV as the etching time increases. FF also decreases from 59.9% to 19.6%, even though the j_{sc} manifests a 0.1-0.3 mA/cm² increase. When the SiO₂ thickness increases to 200 nm, the decreasing trend in efficiency remains the same. The average j_{sc} shows a 0.5-1.3 mA/cm² increase, revealing an enhanced collection efficiency of photogenerated carriers. R_{sh} of the diodes increases on Mo and ITO because SiO₂ point-contacts restrain the leakage current at the solar cell edges where mechanically scribed. But the reason why the FF increases on Mo whilst it decreases on ITO requires further characterizations and discussion. Given the major difference is the back-contact materials, the contradictory passivation effects are attributed to their different passivation properties.

The SiO₂ point-contacts influence the PV performance of ultrathin CIGSe solar cells differently on Mo and ITO substrates. The reason involves recombination velocity S_b at the back interface. According to the latest findings in SCAPS simulation, an increased S_b is beneficial for the ultrathin CIGSe solar cells with a Schottky back-contact [128]. In our case, the passivated solar cells on ITO show deteriorated Eff because they have a Schottky back-contact, as the SiO₂ point-contacts decrease the S_b according to equation (1-6).

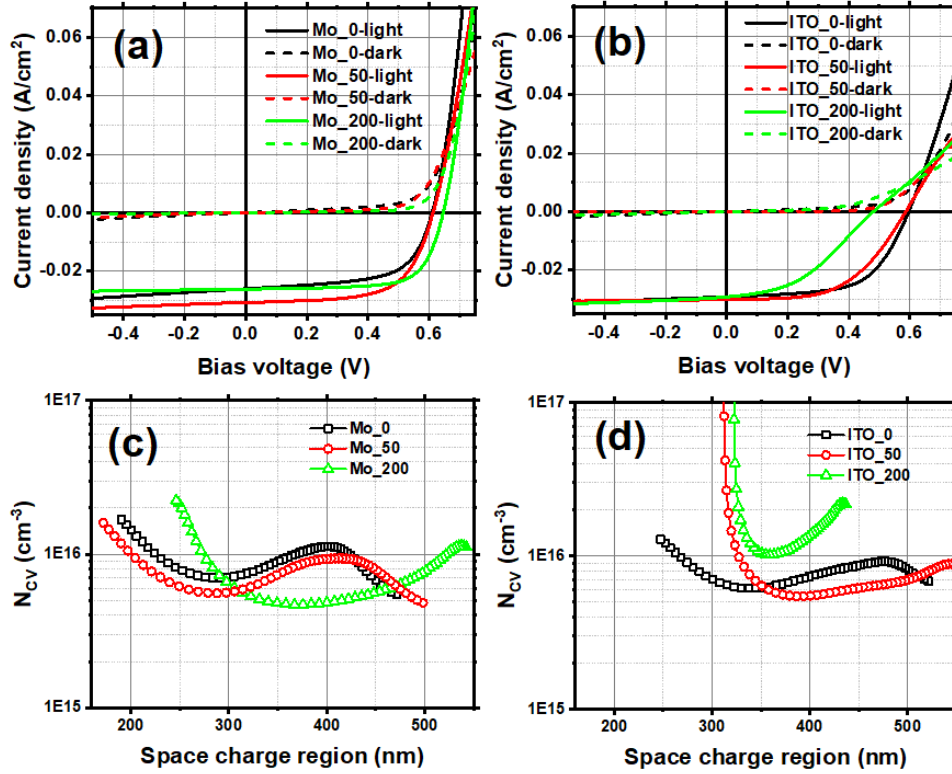


Figure 4-4. (a) and (b) show the representative IV characteristics of Mo_0 - Mo_200 and ITO_0 - ITO_200 under dark and light illumination. (c) and (d) give the corresponding carrier density N_{cv} distributions in the space charge region

Figure 4-4 (a) and (b) demonstrate the representative IV curves of ultrathin CIGSe solar cells on Mo and ITO with/without point-contacts under light and dark conditions. Two characteristics worth mentioning here. The first is the cross-over effect between dark and light IV curves, which attributes to the ordered defect compound ODC layer at the CdS/CIGSe interface [110]. We can recognize the cross-over effect on both substrates, so the SiO₂ passivation does not change the ODC layer on both Mo and ITO back-contacts. The second character in those IV curves is the roll-over effect. The roll-over effect is an indicator that there are extra barriers in the diodes. On Mo substrates, we observe no roll-over effect in all IV curves, which implies the CIGSe/Mo interface shows no blocking at room temperature. But on ITO back-contacts, both ITO_50 and ITO_200 show restrained IV curves in the first quadrant, indicating an extra barrier occurs at the CIGSe/ITO interfaces. The additional back-barrier blocks the collection of photo-generated carriers, hence decreasing V_{oc} of the solar cells. In the first quadrant, the bending degree of ITO_200 is more severe than for ITO_50, which indicates that ITO_200 has a higher back barrier.

Figure 4-4 (c) and (d) compare carrier density N_{cv} distributions in the space charge region (SCR). The insertion of SiO₂ on Mo substrates induces minor changes in the N_{cv} distribution. Under 0 bias voltage, Mo_0 has an N_{cv} of 9.1 E15 cm⁻³ and SCR width of 387 nm. For Mo_50, N_{cv} = 1.1 E16 cm⁻³ and W_{SCR} = 387 nm. For Mo_200, N_{cv} decreases to 5.1 E15 cm⁻³, which is against the fact that passivated solar cells should have a higher V_{oc} [12]. The reason might be that the single-sided PN⁺ approximation (described in section 1.9.2) does not fit here. For solar cells on ITO, however, ITO_200 has the highest N_{cv} but the lowest V_{oc} , contradicting the general trend found in chapter 3. Kimerling's model does not fit the passivated solar cells on ITO

substrates because there is a back-barrier at the CIGSe/ITO interface. Therefore, we should be careful when interpreting the CV data here. In summary, judging by those room temperature IV/CV characteristics, there is an extra back-barrier in the SiO₂ passivated solar cells on ITO, but none (or trivial) in Mo-based ultrathin CIGSe solar cells.

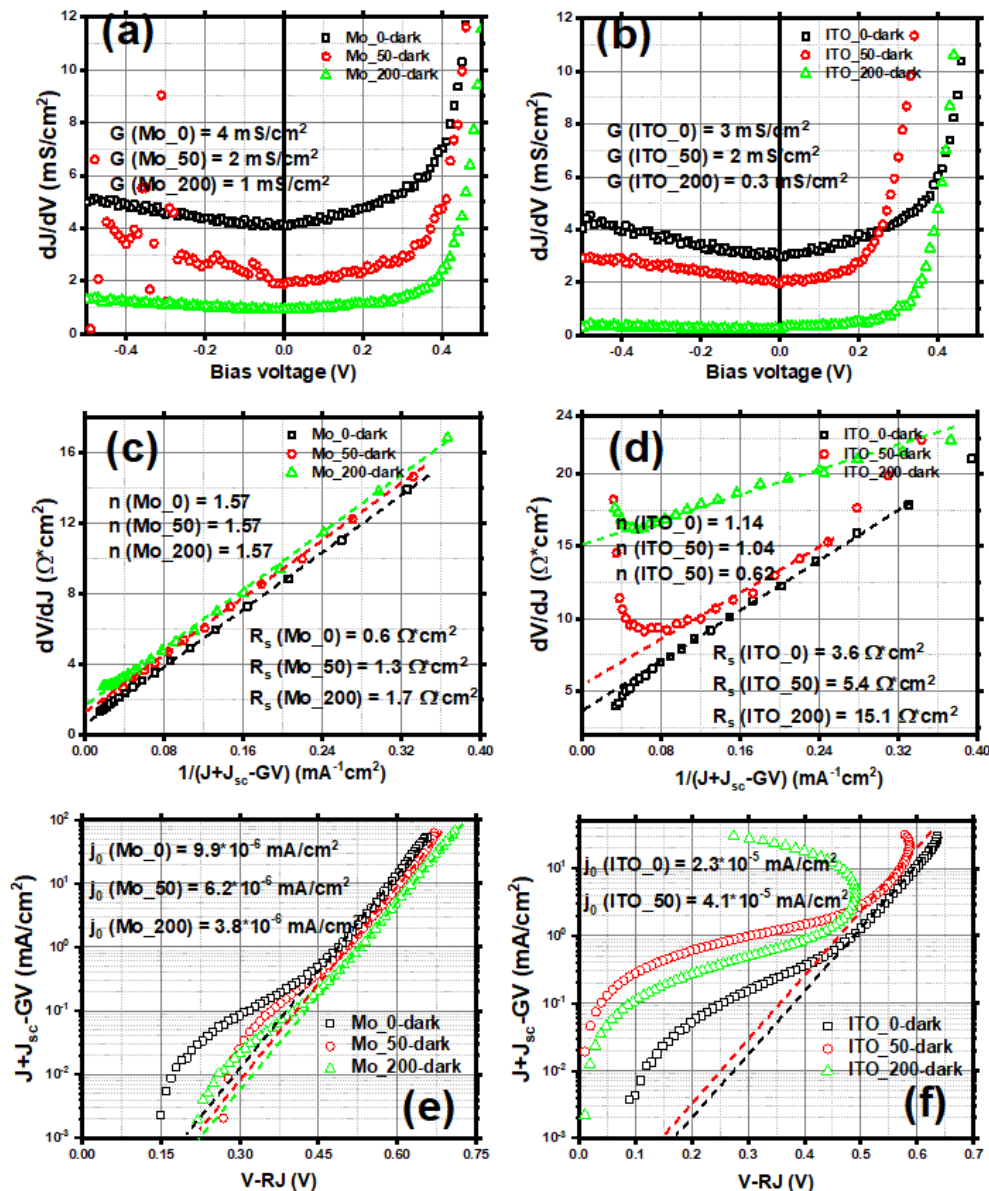


Figure 4-5. Extraction of diode parameters from the dark IV curves for cells on Mo or ITO, based on the model introduced in section 1.9.1.: (a) and (b) shunt resistance $R_{sh}=1/G$, (c) and (d) series resistance R_s , (e) and (f) dark saturation current density j_0 extracted as interception with the ordinate from the semi logarithmic plot of $\ln(j + j_{sc} - GV)$ with linear fit

In Figure 4-5, we extract the diode parameters (including shunt resistance $R_{sh} = 1/G$ where G is the shunt conductance, series resistance R_s , diode ideality factor n , and dark saturation current density j_0) by the Hegedus method to estimate the passivation effects of SiO₂ point-contacts. Mo_50 displays a lower G than Mo_0, and Mo_200 has the lowest G among Mo-based samples. The reason might be that SiO₂ suppresses the leakage current at the edges of scribed sub-cells. The n of Mo_0 is 1.57, close to 1.5 of the 2000 nm-thick CIGSe solar cells in reference [97]. Mo_50 and Mo_200 show the same value of 1.57. We expect the passivated

samples have a Due to the decreased recombination at CIGSe/Mo interface, a lower n for the passivated samples might have been expected. However, as the point-contact passivation does not change n of the diodes, the dominating recombination is not at CIGSe/Mo but CIGSe/CdS and in the bulk of CIGSe. The R_s of Mo_50 increases to 1.3 from 0.6 Ω/cm^2 of Mo_0, and Mo_200 continues to increase to 1.7 Ω/cm^2 . Because SiO_2 is a dielectric material, it has a lower conductivity than the other layers of semiconductor/metal materials, so overall the conductivity of the solar cells decreases after the insertion of point-contacts. The j_0 decreases from 9.9 E-6 mA/cm^2 to 3.8 E-6 mA/cm^2 , which means the recombination at CIGSe/Mo is decreased by the SiO_2 . That also implies j_0 is more sensitive to interfacial recombination than n . Presume an ultrathin CIGSe solar cell has the main junction at CIGSe/CdS in a series connection with a back-contact junction at CIGSe/Mo, and the dark j_0 of those two junctions is different in quantity, it is the smaller dark j_0 in those two junctions that decides the overall dark j_0 for the solar cell. From this perspective, a decrease of the overall dark j_0 reflects that the SiO_2 point-contact passivation diminishes the recombination at the CIGSe/Mo junction.

On ITO substrates, the G of ITO_50 decreases to 2 from 3 mS/cm^2 for ITO_0 and ITO_200 decreases to 0.3 mS/cm^2 , showing a consistent trend with the Mo-based solar cells. The R_s increases from 3.6 to 15.1 Ω/cm^2 . However, the n of ITO_50 decreases to 1.04 from 1.14 for ITO_0 and ITO_200 to 0.62. Such a low n is not realistic. In Figure 4-5 (d), fitting curves of sn show deviation in ITO_50 and ITO_200, which implies the ITO-based solar cells do not fit the one-diode model. For the j_0 of ITO_200, fitting is invalid in Figure 4-5 (f). The linear fitting range cannot cover two magnitudes of y-axis. That indicates the passivated solar cells on ITO do not fit the one-diode model in Hegedus method anymore. In short, with SiO_2 point-contacts, the increased R_{sh} and R_s are consistent with our previous IV analysis. However, the Hegedus method fails to fit the n and j_0 , indicating a second junction or extra barrier in the passivated solar cells on ITO.

In summary, SiO_2 point-contacts have increased R_{sh} and R_s similarly on Mo and ITO substrates due to the isolating properties of SiO_2 material. When extracting n and j_0 , the passivated solar cells on Mo show linear fittings, while the ITO-based samples illustrate deviation from linear fitting. It implies the passivated ITO-based solar cells have a higher back-barrier at the CIGSe/ITO interface. Given the fact that ITO is a degenerated semiconductor or quasi-metal and Mo is a metal, we conclude that differences at the back interfaces are the origins of the contradictory passivation effects on Mo and ITO.

4.2.2 Temperature dependent current-voltage characteristics of the solar cells

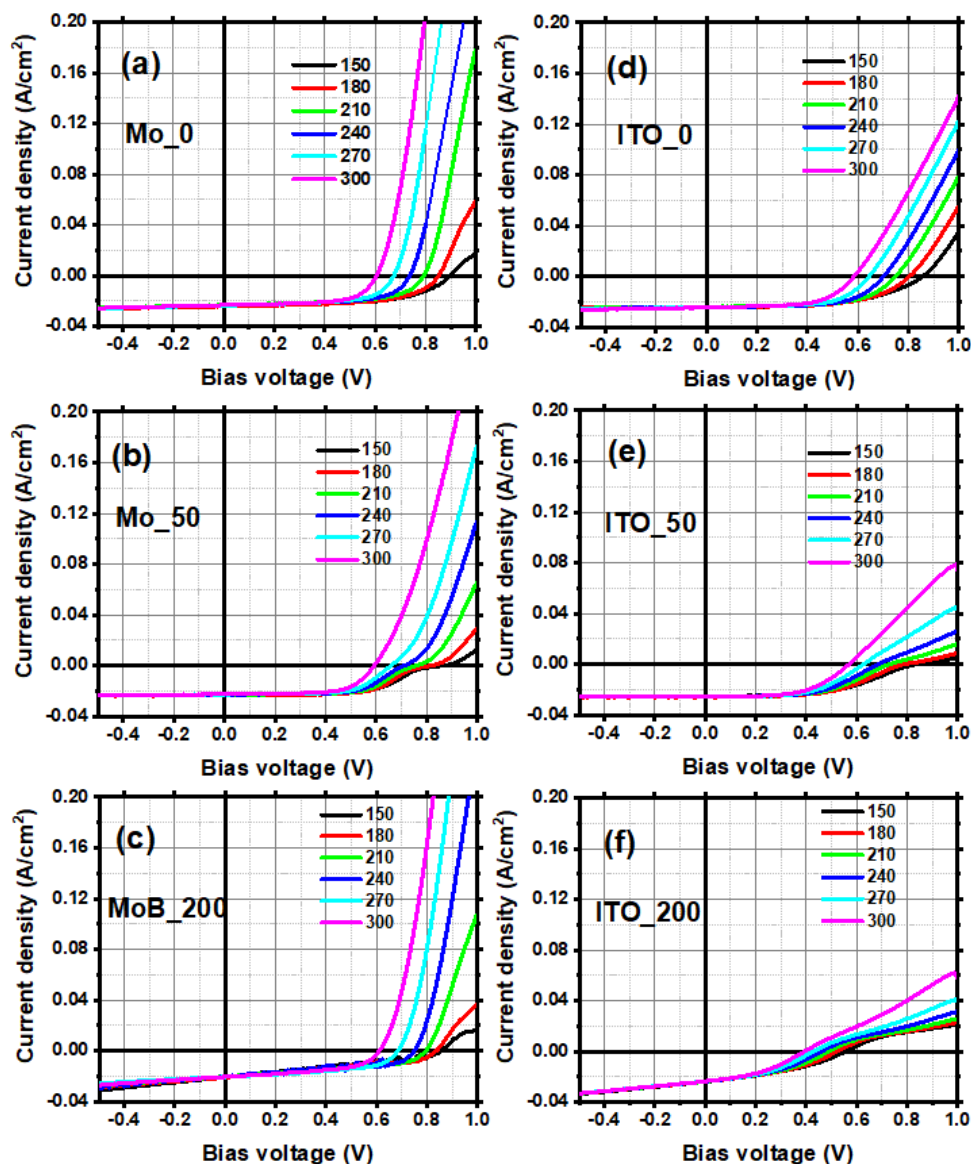


Figure 4-6. Temperature-dependent IV characteristics of the ultrathin CIGSe solar cells under 100 mW/cm^2 illumination

As illustrated in Figure 4-6, temperature-dependent IV characteristics (IVT) of the solar cells are measured under 100 mW/cm^2 illumination in the 150-300 K range to investigate the properties of the back-barrier for holes E_h . Here we refer to the E_h at the CIGSe/ITO interface as $E_{\text{CIGSe/ITO}}$ and at the CIGSe/Mo interface as $E_{\text{CIGSe/Mo}}$. Mo-based solar cells manifest a temperature-dependent roll-over effect (TD-ROE). We can define a temperature point T_r when the roll-over effect shows up. The T_r of Mo_0 is 180 K, as shown in Figure 4-6 (a). When the temperature is equal to or below 180 K, for photogenerated holes close to the CIGSe/Mo interface, their thermal kinetic energy is not enough to surpass the potential energy $E_{\text{CIGSe/Mo}}$ [100, 113]. Therefore, the barrier blocks the moving of those holes towards the Mo side, and the roll-over effect shows up. The T_r of Mo_50 increases to 240 K, which indicates that the kinetic energy of the holes is too low to cross the $E_{\text{CIGSe/Mo}}$ at and below 240 K. The reason is that the $E_{\text{CIGSe/Mo}}$ of Mo_50 has been increased by SiO_2 passivation, as a decreased S_b leads to

a higher effective barrier. In short, a higher effective $E_{\text{CIGSe}/\text{Mo}}$ at the back interface induces a higher T_r for the solar cells. However, when the thickness of SiO_2 point-contacts increases to 200 nm, the T_r of Mo_200 decreases to 180 K. That may be because a mitigated Ga gradient reduces the field passivation effect in the Mo_200. The Ga gradient is critical for the barrier height Φ_b of solar cell devices [16]. According to reference [112], when the SiO_2 thickness is above 150 nm, the Ga gradient decreases as the interdiffusion between Ga and In is active. In conclusion, SiO_2 point-contacts increase the effective $E_{\text{CIGSe}/\text{Mo}}$, but Ga grading in the absorber reduces the effective $E_{\text{CIGSe}/\text{Mo}}$. Those two factors cancel each other hence the T_r of Mo_200 decreases to 180 K.

On ITO substrates, no roll-over effect can be seen in the 150–300 K range for ITO_0, as displayed in Figure 4-6 (d). ITO_0 shows a roll-over IV when the temperature decreases to 130 K, which means the $E_{\text{CIGSe}/\text{ITO}}$ is nonzero, just a lower T_r is required to see it. ITO_50 has a T_r of 270 K, and ITO_200 shows roll-over IV at room temperature (300 K). Unlike on Mo substrates, SiO_2 point-contacts increase the effective barrier height $E_{\text{CIGSe}/\text{ITO}}$ at the CIGSe/ITO interface consistently. T_r of the passivated solar cells on ITO is generally higher than on Mo substrates, and when the SiO_2 thickness increases, the T_r shows different trends on Mo and ITO. That implies $E_{\text{CIGSe}/\text{ITO}}$ is higher than $E_{\text{CIGSe}/\text{Mo}}$, and the back interfaces are passivated differently by SiO_2 point-contacts.

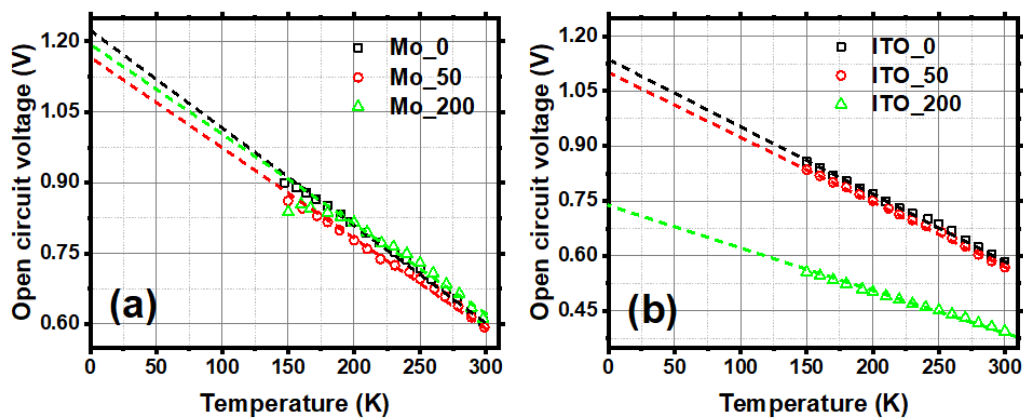


Figure 4-7. The extracted V_{oc} from the temperature dependent IV characteristics

Figure 4-7 represents V_{oc} versus temperature ($V_{oc}-T$) to quantify the changes in the back-barrier height E_b . According to equation (1-10), we can extract the barrier height of the solar cells Φ_b by extrapolating the temperature to 0 K [85]. For clearance, here we also specify Φ_b by $\Phi_{\text{CIGSe}/\text{Mo}}$ and $\Phi_{\text{CIGSe}/\text{ITO}}$ to refer to the Φ_b in Mo-based and ITO-based solar cells.

Firstly, $\Phi_{\text{CIGSe}/\text{Mo}}$ of Mo_0 is 1.22 eV, and 1.16 eV for Mo_50. Compared to the reference sample Mo_0, SiO_2 introduces 0.06 eV equivalent barrier height $\Phi_{\text{CIGSe}/\text{Mo}}$ into the back interface of Mo_50. For Mo_200, the y-axis intercept of the V_{oc} linear fitting is 1.19 eV. The linear fitting of Mo_200 is bent in the low-temperature range because the V_{oc} decreases when the temperature approaches 150 K. That is an overall result of a mitigated Ga gradient and an increased $\Phi_{\text{CIGSe}/\text{Mo}}$. If the linear fitting is limited in the low-temperature range (150-250 K) [85], $\Phi_{\text{CIGSe}/\text{Mo}}$ of Mo_200 is lower than Mo_50. In some literature, linear fittings of $V_{oc}-T$ are separated into high-temperature range and low-temperature range, even though the

boundary between high and low-temperature is unclear. According to (1-11), $\Phi_{\text{CIGSe/Mo}}$ of Mo_200 is higher than Mo_50 and Mo_0 in the 150-250 K range.

Secondly, on ITO substrates, $\Phi_{\text{CIGSe/ITO}}$ is 1.13 eV for ITO_0, 1.10 eV for ITO_50, and 0.75 eV for ITO_200. Therefore, the $E_{\text{CIGSe/ITO}}$ increases 0.03 eV for 50 nm SiO₂ and 0.38 eV for 200 nm SiO₂ point contact. In summary, Φ_b of the solar cells decreases after SiO₂ insertion on both substrates. Therefore, the E_h at CIGSe/Mo and CIGSe/ITO also increase by different degrees.

4.2.3 Photoluminescence characteristics of the solar cells

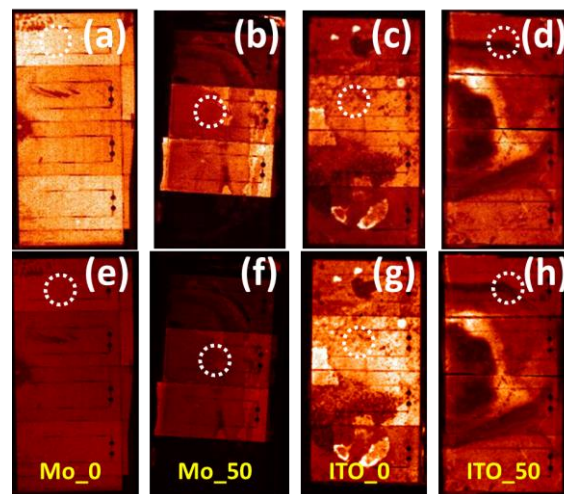


Figure 4-8. Photoluminescence mapping of the solar cells with and without SiO₂ passivation. Each column is the same sample. The white circles mark the cells that are characterized with EQE later

As shown in Figure 4-8, we test photoluminescence (PL) mappings of the completed solar cells to investigate radiative recombination in the devices. The wavelength of the exciting laser is 650 nm, and an InGaAs detector detects photoluminescence intensity from the samples in the 0-2200 nm wavelength range. Here we focus on references (Mo_0 and ITO_0) and representative solar cells with 50 nm SiO₂ point-contacts passivation (Mo_50 and ITO_50) to simplify the comparison.

Figure 4-8 (a)-(d) use auto contrast to obtain the best resolution for each sample. On Mo_0, we can observe Ni/Al finger contacts and some scratches. On ITO_0, two cells in the middle illustrate brighter PL intensity than the top and bottom cells. We can also localize some bright spots on ITO_0. The bright spot at the bottom of Figure 4-8 (c) shows a circular shape. That is thermal conductive glue used to attach the sample back to the cryostat for cooling. Because ITO-based solar cells are semi-transparent, especially in the long-wavelength range, the detector can receive PL signals from the back side of the solar cells. In Figure 4-8 (b) and (d) of Mo_50 and ITO_50, we recognize water stains around sample corners, which come from the SiO₂ fabrication processes. This is just for clarification and not the features we are interested in.

Figure 4-8 (e)-(h) use fixed contrast for an instant comparison between different samples. On both substrates, the SiO₂ passivated samples display dimmer PL than the reference samples.

According to equation (1-6), recombination is proportional to the density of the traps N_t . Therefore, the weak PL intensity implies that SiO_2 point-contacts diminish the recombination velocity S_b in the passivated samples. Those PL mapping results are consistent with observations in section 3.2.3, where a higher PDT dose induces higher recombination (the higher carrier density) hence a brighter PL image.

4.2.4 External and internal quantum efficiency of the solar cells

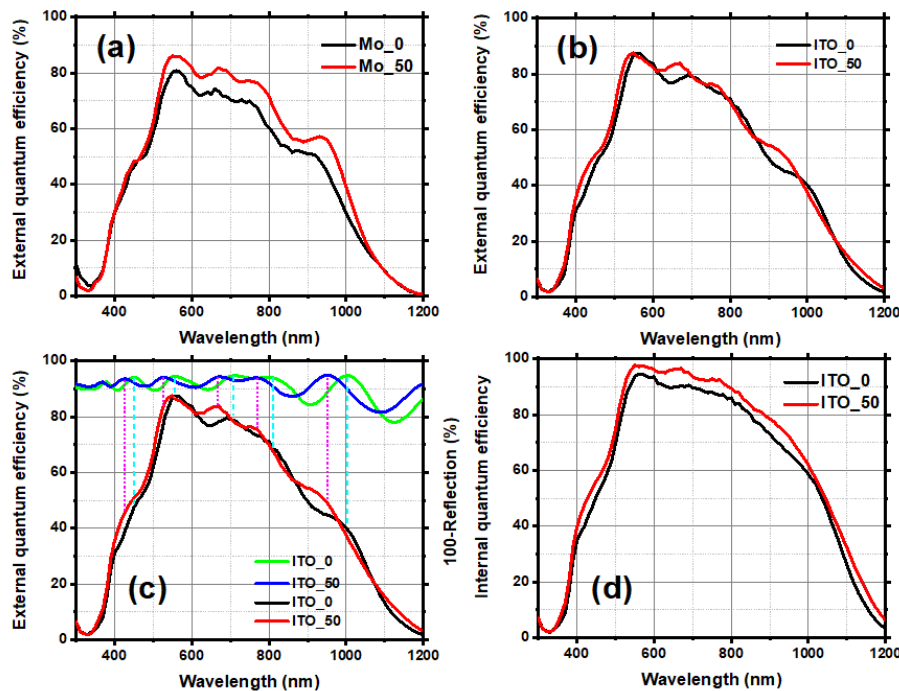


Figure 4-9. External quantum efficiency (EQE) of (a) Mo_0 and Mo_50 and (b) ITO_0 and ITO_50. (c) EQE and 100-R% (100-Reflection) of ITO_0 and ITO_50. (d) Internal quantum efficiency (IQE) of ITO_0 and ITO_50 calculated by equation (1-25)

Figure 4-9 shows quantum efficiency characteristics of the ultrathin CIGSe solar cells with and without SiO_2 point-contacts to demonstrate mechanisms of the j_{sc} gain after passivation. As illustrated in Figure 4-9 (a), SiO_2 increases the external quantum efficiency EQE of Mo_50 in the middle wavelength range, which implies the passivation enhances the lifetime of photogenerated carriers in the devices [129]. On ITO substrates, the EQE curves of ITO_50 and ITO_0 cross with each other, which makes it hard to draw a clear conclusion. When comparing EQE and 100-R% of ITO_0 and ITO_50, we find their peak wavelengths align with each other, as shown in Figure 4-9 (c). Therefore, optical reflection/transmission induces the crossing EQE curves of ITO_0 and ITO_50. We calculate the internal quantum efficiency (IQE) of the cells on ITO to isolate the optical disturbance of R/T, as exhibited in Figure 4-9 (d). The IQE of ITO_50 is higher than of ITO_0 in the 300-1200 nm wavelength range. That implies SiO_2 point-contacts have diminished recombination of photogenerated carriers in the ITO-based solar cells as well [100].

Table 4-2. Short circuit current density of the corresponding cells (marked with white dot circles in Figure 4-8) and the equivalent current density j_{EQE}

	j_{sc} (mA/cm ²)	j_{EQE} (mA/cm ²)
Mo_0	24.9	23.9
Mo_50	27.2	26.5
ITO_0	26.6	26.4
ITO_50	26.9	27.2

Table 4-2 lists j_{sc} extracted from IV characteristics and equivalent current j_{EQE} integrated via equation (1-24). Compared to the references, j_{EQE} of the SiO₂ passivated solar cells show a consistent trend with the j_{sc} extracted from IV characteristics. In conclusion, by comparing PL mappings and quantum efficiency, it is cross-checked that the SiO₂ passivation has diminished recombination in the solar cells on both substrates.

4.2.5 Interdiffusion of Ga-Se and In-Se in the CIGSe absorber

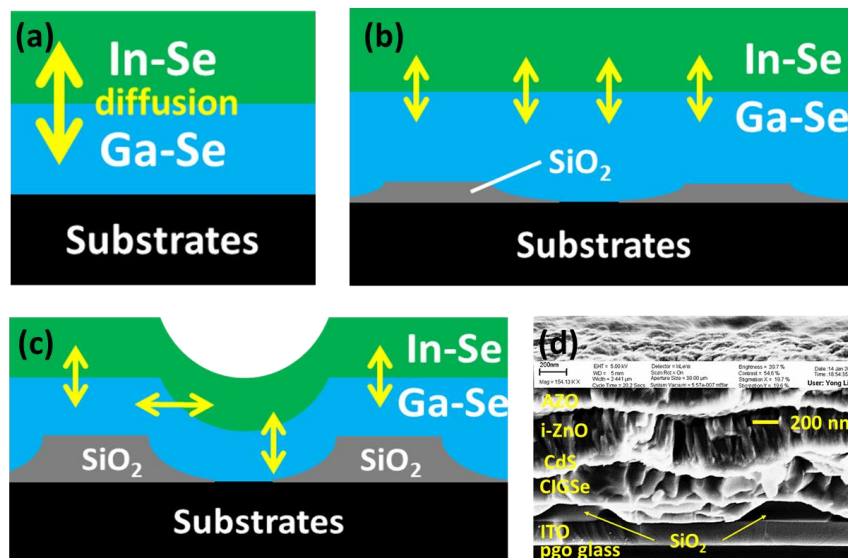


Figure 4-10. Ga-Se and In-Se interdiffusion on the substrates with (a) flat surface, or (b) SiO₂ point-contacts with a relative thin thickness, or (c) SiO₂ with a thick thickness. (d) cross-section SEM of ITO_200

During the CIGSe 3-stage co-evaporation, interdiffusion between Ga-Se and In-Se plays a critical role in deciding the Ga gradient and hence the bandgap gradient in the absorber [15]. Roughness of the substrate surface can influence the interdiffusion process. Dependent on the thickness of the SiO₂ point-contacts, the interdiffusion process in CIGSe can be differentiated in three mechanisms, as Figure 4-10 (a)-(c) sketches:

(1) When the substrates have a flat surface, the interdiffusion mainly happens in the vertical direction, as illustrated in Figure 4-10 (a);

(2) When the SiO₂ point-contacts have a relatively thin thickness, as shown in Figure 4-10 (b), the dominating interdiffusion also happens in the vertical direction;

(3) The interdiffusion process will happen in vertical and horizontal direction during the 3-stage co-evaporation (Figure 4-10 (c)) when the thickness of the SiO₂ is comparable to the ultrathin CIGSe absorber, and the Ga-Se layer grows conformally on the surface. The contact area between the SiO₂ passivated surface and evaporated materials will also increase as the solar cells have a planar structure. Therefore, the contact area between Ga-Se and In-Se will also increase, hence promoting interdiffusion of Ga and In. However, the specific thickness of the SiO₂ that is required to trigger this interdiffusion mechanism is not known. According to Yin's estimation in reference [112], 50 nm is enough to promote the interdiffusion of Ga-In. Depth distribution of the Ga gradient characterized by GD-OES can help verify this assumption.

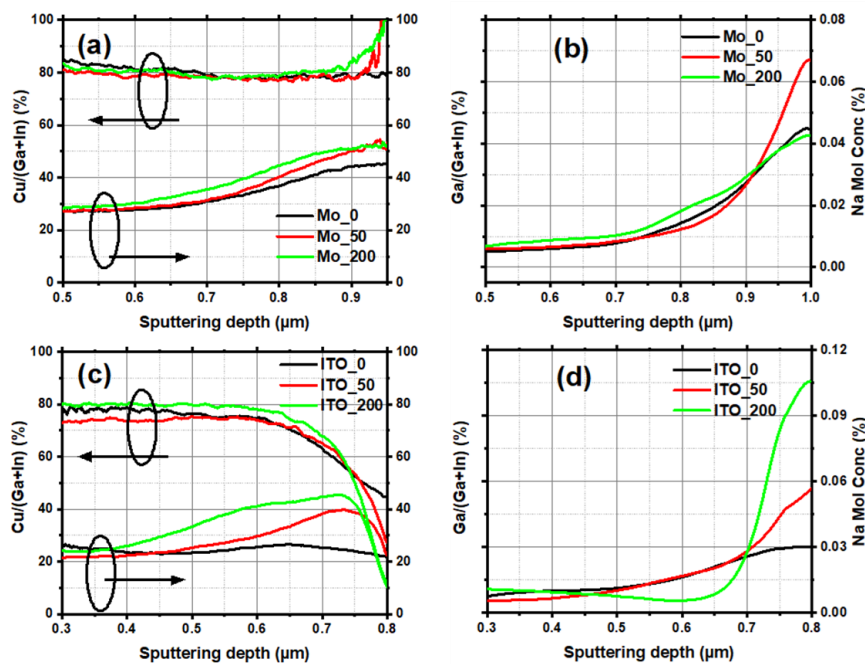


Figure 4-11. CGI, GGI and Na depth distribution in the ultrathin CIGSe absorber

The results from glow discharge emission spectroscopy (GD-OES) characterization in Figure 4-11 reveal the depth distribution of Cu/(Ga+In) (CGI), Ga/(Ga+In) (GGI), and Na in the absorbers. Compared to reference Mo₀, Mo₅₀ shows a higher GGI on the back. That implies the second interdiffusion mechanism applies to Mo₅₀. Because 50 nm SiO₂ is too thin, it will not significantly enlarge the contact area between the passivated substrates and CIGSe thin film. Therefore, when CIGSe grows conformally on the substrates, the Ga ratio in the shallow dents (blue parts in Figure 4-11 (d)) of Mo₅₀ is higher than in Mo₀. For Mo₂₀₀, GGI in the middle of CIGSe is higher than for the other two samples, which implies the third interdiffusion mechanism applies to Mo₂₀₀. Due to the increased interdiffusion increases between Ga-Se and In-Se in horizontal direction, Mo₂₀₀ shows the lowest Ga gradient among the Mo-based samples. It confirms the deductions from the previous IVT analysis: with 200 nm SiO₂ point-contact passivation, the field passivation effect caused by the Ga gradient decreases in the solar cells. The CGI confirms that those ultrathin CIGSe absorbers are Cu poor at the CIGSe/CdS interface. The SiO₂ also influences the Na distribution, as shown in Figure

4-11 (b). Compared to Mo_0, Mo_50 manifests a higher Na density at CIGSe/Mo interface. Mo_200 shows a lower but wider Na distribution in the absorber. Interestingly, the Na density seems proportional to GGI in the CIGSe. But no direct relevance is known between the solubility of Na in CIGSe and the Ga ratio.

On ITO substrates, however, ITO_0 displays a flat GGI. The reason is that In from the In₂O₃:Sn (ITO) layer interferes the In signal from the CIGSe layer. During GD-OES measurements, the sputtered cave is not flat at the bottom but sloping in a 'W' shape. Therefore, the detected Ga/(Ga+In) ratio decreases as In in the denominator increases abnormally. ITO_50 exhibits a higher hump approaching the back side because the SiO₂ point-contacts partially block the In signal from ITO layer. Similar to Mo_200, ITO_200 has a broader and flatter Ga distribution than the other two ITO-based samples. The reason is that SiO₂ point-contacts enhance the interdiffusion between Ga-Se and In-Se. Figure 4-11 (d) illustrates that the Na concentration at the back interface consistently increases with SiO₂ thickness. However, there is no correlation between Na density at the CIGSe/ITO interface and the PV performance of the solar cells.

In summary, when the thickness of SiO₂ point-contacts is 50 nm, Ga grading in the CIGSe is increased on Mo and ITO substrates. When the SiO₂ thickness is 200 nm, Ga grading in the CIGSe decreases because the Ga-In interdiffusion increases in the horizontal direction.

4.3 SCAPS simulation of the back interface

Based on previous characterizations, SiO₂ point-contacts decrease the back recombination in ultrathin CIGSe solar cells on both Mo and ITO substrates. A general experience is that back interface passivation is beneficial for the efficiency of CIGSe solar cells [12]. However, our experimental results have shown that reduced back recombination is advantageous for Mo-based solar cells only but detrimental for ITO-based ones. According to the latest findings in simulation, a passivated back interface can be adverse if the solar cells have a Schottky back-contact [128]. Our $V_{oc}-T$ linear fittings indicate $E_{CIGSe/ITO}$ is higher than $E_{CIGSe/Mo}$. The back barrier height E_h may decide the role of passivation effects in ultrathin CIGSe solar cells, as E_h is relatively high in Schottky but low for Ohmic back-contacts. From this perspective, a passivated back interface is favourable for ultrathin CIGSe solar cells only when their back-contacts are Ohmic (or quasi-Ohmic) contacts with a relatively low E_h . A decreased back recombination is detrimental when the back-contacts are Schottky-like with a relatively high E_h . Naturally, there is a turning point in the E_h values, which we define as E_t : when $E_h < E_t$, back passivation is beneficial for the solar cells; when $E_h > E_t$, the passivation is detrimental. Therefore, we will verify the following two points via SCAPS simulations:

- (1) When $E_h = 0$ eV at the back-contact (Ohmic contact), a reduced recombination velocity S_b is beneficial for the efficiency of ultrathin CIGSe solar cells. When $E_h = 0.2$ eV (Schottky contact), a decreased S_b deteriorates the PV performance of the solar cells;
- (2) If we increase E_h values continuously, there should be a turning point E_t . In the $E_h < E_t$ region, passivation is desirable. And in the $E_h > E_t$ region, recombination is desirable.

According to equation (1-6), we vary $S_n = \sigma_n * v_{th} * N_t$ at the back interface to simulate the passivation effects of SiO₂ point-contacts because the trap density N_t shall be decreased after passivation. We use S_b to represent the S_n at the back interfaces. Table 4-3 lists layer settings for the SCAPS simulations presented in this section [130].

Table 4-3. Model parameters in SCAPS simulation of the structure back contact/CIGSe/ODC/CdS/i-ZnO/AZO, whereby ODC stands for ordered-defect-compound, AZO for ZnO:Al and i-ZnO for intrinsic ZnO. VB DOS: Density of states in the valence band, CB DOS: Density of states in the conduction band, A: acceptor, D: donor [130]

Layer Parameter	Symbol (Unit)	Back Contact	CIGSe	ODC	CdS	i-ZnO	AZO
Thickness	d (nm)	-	485	15	50	80	300
Bandgap	E_g (eV)	-	1.10	1.45	2.45	3.4	3.5
Electron affinity	χ (eV)	-	4.5	4.5	4.45	4.55	4.65
Relative permittivity	ϵ_r	-	13.6	13.6	10	9	9
VB DOS	N_v (cm^{-3})	-	4.12E18	2E18	1.5E19	9E18	9E18
CB DOS	N_c (cm^{-3})	-	7.96E17	2E18	2E18	4E18	4E18
Doping	N_A, N_D (cm^{-3})	-	8E15 (A)	5E16 (D)	5E17 (D)	1E18 (D)	1E20 (D)
Electron mobility	μ_n ($cm^2V^{-1}s^{-1}$)	-	100	1	100	100	100
Hole mobility	μ_p ($cm^2V^{-1}s^{-1}$)	-	25	1	25	25	25
Thermal velocity	v_{th} (cm/s)	-	1E7	1E7	1E7	1E7	1E7
Defect density	N_T (cm^{-3})	-	1E13	1E13	2E17	2E16	2E16
Electron capture cross-section	σ_e (cm^2)	-	5E-13	5E-13	1E-13	1E-12	1E-12
Hole capture cross-section	σ_h (cm^2)	-	5E-15	5E-15	1E-13	1E-12	1E-12
Back interface recombination velocity	S_b (cm/s)	variable	-	-	-	-	-
Barrier height for holes	E_h (eV)	variable	-	-	-	-	-

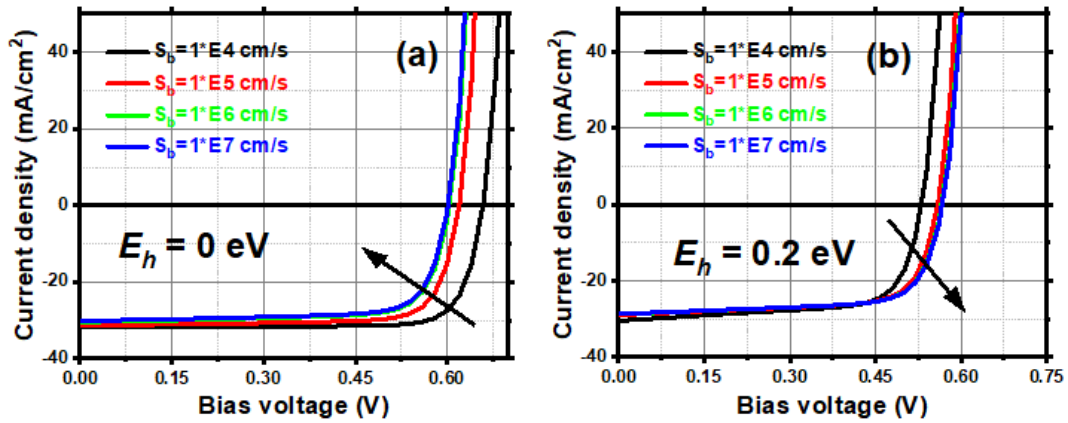


Figure 4-12. Simulated IV curves of solar cells with (a) $E_h = 0$ eV and (b) $E_h = 0.2$ eV at the back for varied recombination velocity S_b . The black arrows mark the direction of increasing S_b

Figure 4-12 displays light IV curves from SCAPS simulations of the ultrathin CIGSe solar cells. $E_h = 0$ eV simulates a solar cell having an Ohmic back-contact, and $E_h = 0.2$ eV stands for a solar cell on a Schottky back-contact. The maximum $S_b = 1 \text{ E}7$ cm/s represents no passivation effect at the back interface, so photogenerated carriers recombine with the room temperature thermal velocity. The minimum $S_b = 1 \text{ E}3$ cm/s simulates back recombination being diminished to a low degree by SiO_2 point-contact passivation. Figure 4-12 (a) demonstrates that the PV performance of the solar cells deteriorates with increasing S_b on Ohmic back-contacts. It verifies that passivation is favourable for the CIGSe solar cells with an Ohmic back-contact. On Schottky back-contacts, however, the PV performance of the solar cells exhibits an enhancement in V_{oc} when S_b increases, see Figure 4-12 (b). In this case, passivation is detrimental.

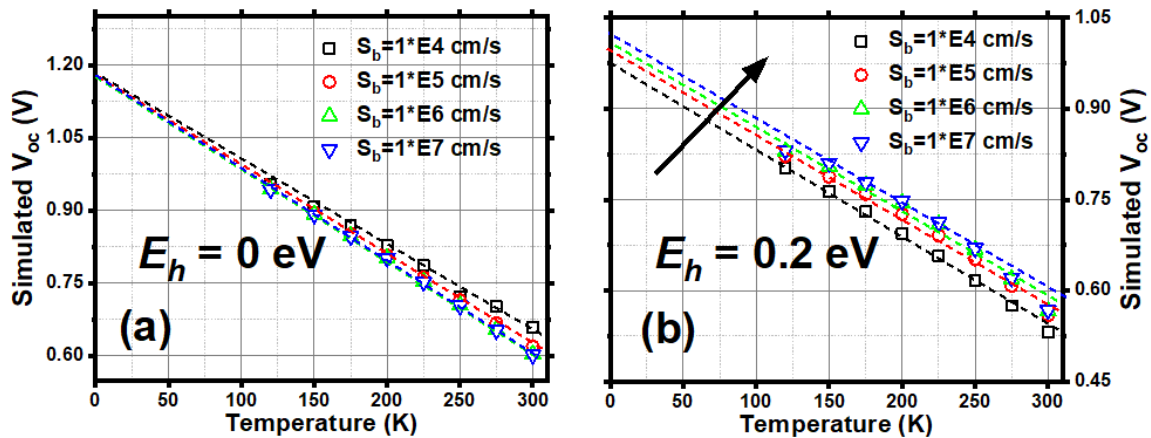


Figure 4-13. SCAPS simulated temperature-dependent V_{oc} at varied S_b for (a) $E_h = 0$ eV and (b) $E_h = 0.2$ eV back-contact. Arrows indicate the direction of increasing S_b

Figure 4-13 shows the V_{oc} dependance on the temperature T to extract the diode barrier height Φ_b of the solar cells with different E_h and S_b . On Ohmic back-contacts, Φ_b is 1.20 eV, 0.1 eV higher than the bandgap E_g (1.1 eV) of the ultrathin CIGSe layer. The reason is that we introduced an ordered defect compound (ODC) layer between CIGSe and CdS in our model.

The ODC layer has an E_g of 1.45 eV. We also notice Φ_b is independent of the S_b change in Figure 4-13 (a). That implies back recombination has little influence on the ultrathin CIGSe solar cells with an Ohmic back-contact at low temperature.

On Schottky back-contacts, Φ_b of the solar cell with $S_b = 1 \text{ E4 cm/s}$ is 1.00 eV, which is 0.2 eV lower than on Ohmic contacts. The reason is that E_g and E_h decide the Φ_b according to equation (1-11). However, Φ_b of the solar cells increases when S_b increases in the Schottky back-contacts. It implies that a higher back recombination diminishes the effective barrier at the back interface. Comparing Figure 4-7 (from experiments) with Figure 4-13 (from simulations), both CIGSe/Mo and CIGSe/ITO interfaces are inclined to have Schottky-like back contact. In practical experiments, the situation is more complicated than in ideal simulations. For example, SCAPS simulations do not consider Ga grading in the absorber. Here we are not aiming for a perfect fitting between experiments and simulation results but focus on the evolution trend of Φ_b that depends on S_b and E_h at the back-contacts.

In summary, SCAPS simulations have verified that E_h can fundamentally change the effect of back passivation for ultrathin CIGSe solar cells. That explains that SiO_2 point-contact passivation is detrimental for the PV performance of solar cells on ITO but beneficial for ultrathin CIGSe solar cells on Mo substrates.

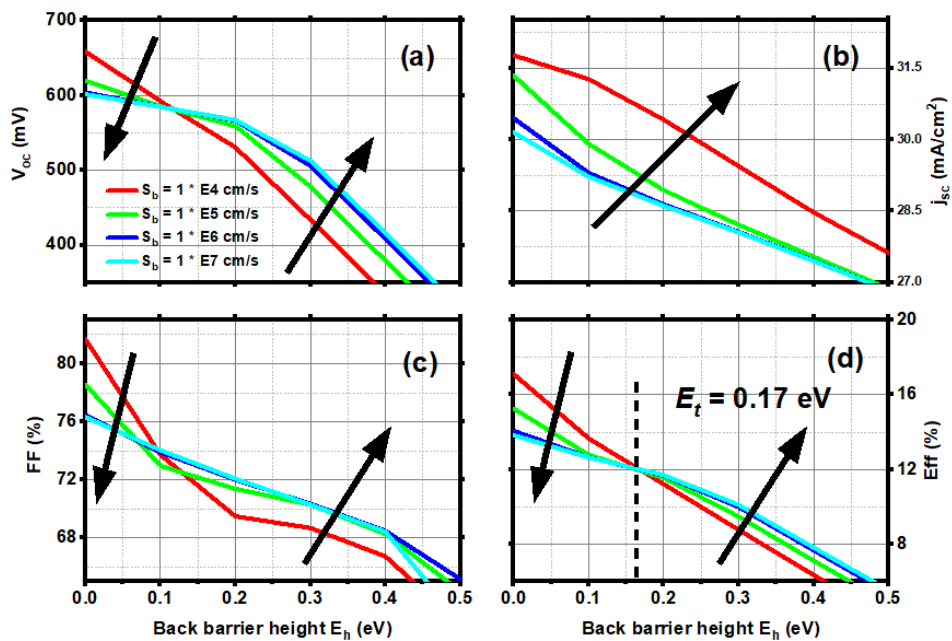


Figure 4-14. Simulated PV parameters of the solar cells depending on the back potential barrier height E_h and on the recombination velocity S_b

Now we increase E_h continuously in simulations to find the turning point E_t of the back barrier height. Figure 4-14 reveals the PV performance of the ultrathin CIGSe solar cells with a varied E_h at the back-contacts. For each E_h value, S_b varies in the range from $1 \text{ E4} - 1 \text{ E7 cm/s}$. In Figure 4-14 (a), V_{oc} of the solar cells shows a turning point at 0.12 eV. The black arrows indicate V_{oc} decreases for $E_h < 0.12$ eV and increases for $E_h > 0.12$ eV when S_b increases. Figure 4-14 (b) shows j_{sc} of the solar cells decreases with increasing S_b , and this decreasing trend is independent of E_h values. Back interface recombination always deteriorates j_{sc} of the ultrathin

CIGSe solar cells. The turning point in FF is 0.1 eV, as shown in Figure 4-14 (c). Overall, Eff of the ultrathin CIGSe solar cells shows a turning point at 0.17 eV, as the dotted line denotes in Figure 4-14 (d). In conclusion, a higher S_b decreases solar cell efficiency when E_h is lower than 0.17 eV, thus back interface passivation is beneficial for PV performance of the ultrathin CIGSe solar cells. On the contrary, a higher S_b increases Eff of the solar cells when E_h is higher than 0.17 eV, so back passivation is detrimental to the solar cell performance.

4.4 Summary and conclusion

Through systematically characterizing the passivation effects of SiO_2 point-contacts on Mo and ITO, we find out that SiO_2 decreases back recombination on both substrates. ITO-based CIGSe solar cells have a higher back barrier height for holes E_h than Mo-based ones at the back-contacts. The E_h region decides that passivation is beneficial for Mo-based but detrimental for ITO-based ultrathin CIGSe solar cells. SCAPS simulations verify that a higher S_b deteriorates the PV performance of solar cells with $E_h < 0.17$ eV (Ohmic contact). On the contrary, a higher S_b improves the PV performance of ultrathin CIGSe solar cells with $E_h > 0.17$ eV (Schottky contact) at the back-contact. Back-contacts with a relatively low E_h are crucial for the V_{oc} of the ultrathin CIGSe solar cells. Besides, barrier height E_h at the back-contacts decides passivation effects for the ultrathin CIGSe solar cells. In conclusion, passivation at back interfaces is not desirable for the solar cells with a Schottky back-contact.

Chapter 5 Optimization of front and rear efficiency

The unique advantage of bifacial semi-transparent ultrathin (BSTUT) CIGSe solar cells (SCs) is that they can exploit illumination from front and rear. However, most research on the TCO-based CIGSe solar cells focuses only on front illumination. In this chapter, we will optimize the efficiency of BSTUT CIGSe solar cells under both front and rear.

Geometrically, the rear illumination light goes through glass and ITO before reaching CIGSe. Therefore, reflection from the back surface and at interfaces, parasitic absorption in ITO and glass, as well as the back barrier height E_b at the CIGSe/ITO interface are critical for the rear efficiency of BSTUT CIGSe solar cells. This chapter concentrates on the following three items:

- (1) The glass types. We will compare the rear transmission/reflection (T/R) characteristics of 300 nm ITO on soda-lime glass (SLG) and on alkali-free barium boron-silicate glass (pgo glass). We characterize and discuss the front and rear PV performance of the samples on SLG and pgo glasses to decide which is the better type for BSTUT CIGSe SCs;
- (2) The thickness of ITO. We quantify parasitic absorption in the back-contact layer (ITO) to decide about the optimal ITO thickness for BSTUT CIGSe SCs;
- (3) The NaF PDT dose. We will compare the front and rear PV performance of BSTUT CIGSe solar cells with 0-8 mg NaF used in the PDT process.

5.1 Impact of the glass type

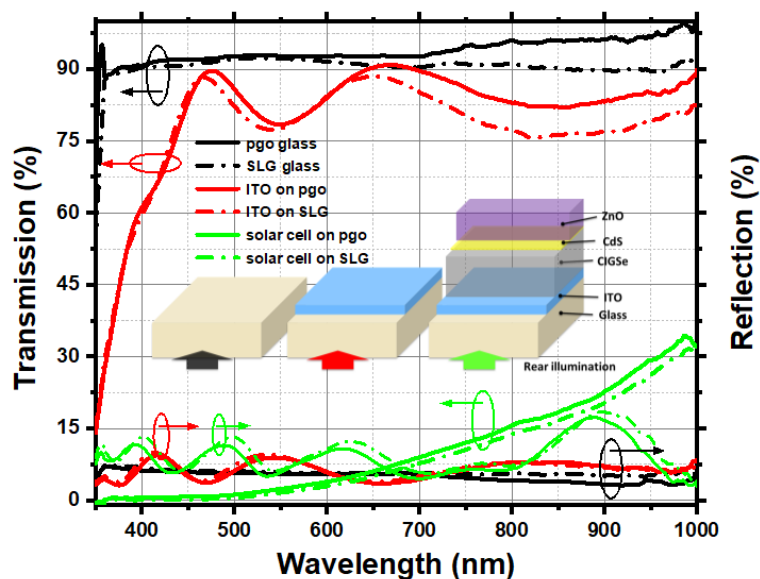


Figure 5-1. Rear transmission and reflection (T/R) of the bare glasses (black lines), 300 nm ITO on the glasses (red lines), and the completed solar cells (green lines). Solid lines are corresponding to pgo glass and dash-dotted lines to SLG

Firstly, we compare the transmission/reflection (T/R) of pgo glass and SLG. The pgo glass (solid lines) exhibits higher T and lower average R than SLG (dash-dotted lines) in the wavelength range of 600-1000 nm, as the black lines show in Figure 5-1. It indicates that SLG has higher parasitic absorption than pgo glass (not shown here). There are two possible reasons for the higher parasitic absorption of SLG. The first possibility is that SLG is thicker than pgo glass, as the thickness of pgo glass is 0.7 mm, and SLG is 2 mm. The second is their difference in alkali content because pgo glass has less than 0.3% alkali elements, and SLG has 14% of Na_2O . Given absorption coefficient k in glasses is relatively low, the second possibility is more likely in real life. Then we compare the rear T/R of 300 nm ITO on the glasses, compare the red curves in Figure 5-1. On both glasses, we can see two interference peaks at 460 and 650 nm in the transmission curves, which can be attributed to Fabry-Perot interferences in the thin film system. We can also observe Fabry-Perot interferences in the reflection curves in the 350-650 nm wavelength range. In the wavelength range of 650-1000 nm, ITO on pgo glass shows a higher transmission than on SLG because pgo glass has lower parasitic absorption than SLG. Lastly, we compare the rear transmission of completed solar cells, see the green curves in Figure 5-1. Both green lines show transparency above 30% at 1000 nm, revealing the insufficient light absorption in ultrathin CIGSe absorbers. The solid green line being higher than the dash-dotted line means ultrathin CIGSe solar cells on pgo glass have better transparency than on SLG, especially in the long wavelength range.

In summary, the samples (including glass, ITO/glass, and completed solar cells) on pgo glass exhibit higher transmission than on SLG, which is attributed to the higher parasitic absorption of SLG. Better transparency is critical for successful BSTUT CIGSe solar cells because it brings more room for light management.

Table 5-1. PV parameters and doping density N_A of ultrathin CIGSe solar cells on SLG and pgo glass. The suffix 'R' means rear illumination PV performance of the solar cells

Sample name	ITO thickness (nm)	V_{oc} (mV)	j_{sc} (mA/cm ²)	FF (%)	Eff (%)	N_A (cm ⁻³)
SLG-300	300	607±16	27.7±0.4	64.3±10.4	10.8±1.9	4.04 E15
pgo-300	300	587±11	28.7±0.3	57.8±2.8	9.7±0.7	4.12 E15
SLG-300R	300	571±10	16.6±1.4	59.6±2.2	5.7±0.7	
pgo-300R	300	546±8	18.5±0.9	57.3±2.3	5.8±0.6	

We load the substrates made of ITO/SLG and ITO/pgo into the PVD for the same batch of CIGSe co-evaporation to minimize the differences such as CGI, GGI, and thickness of the absorbers. For the PDT process, we use 2 mg NaF with the first scenario described in section 3.1. Following the 3-stage co-evaporation, we evaporate the NaF sequentially without breaking the vacuum in the PVD chamber. In that way, we can avoid a low-quality absorber caused by insufficient Na doping to the pgo-based CIGSe. However, NaF PDT plus Na diffusion from SLG may deteriorate the CIGSe quality on SLG; as chapter 2 manifests, Na from SLG can diffuse through ITO into the absorber. For the batch of absorbers shown in this section, XRF indicates that CGI, GGI, and thickness are 0.90, 0.34, and 453 nm, respectively. Table 5-1 summarizes the PV parameters and N_A of BSTUT CIGSe SCs on the corresponding glasses. SLG-300 is the abbreviation for the solar cell on SLG glasses with 300 nm ITO, and pgo-300 stands for the same on pgo glass. The suffix R means we measure PV parameters of the samples under rear illumination.

Compared to pgo-300, SLG-300 exhibits a higher front V_{oc} . There are two potential reasons. Firstly, it is the thickness of the glass. According to reference [30], the glass thickness affects the growth process of the polycrystalline CIGSe thermodynamically. The CIGSe grain size that grows on different glass thicknesses will be different, which will be a decisive point for the final CIGSe morphology. In our case, SLG is 2 mm thick, and pgo glass is 0.7 mm. We characterize two representative samples with cross-sectional SEM to verify whether the grain size has been influenced by the glass thickness, see Figure 5-2 (a) and (b). Judging from these SEM pictures, the grain size is similar on SLG and pgo glasses, which indicates the glass thickness is not the culprit of the V_{oc} difference.

The second possibility that may cause the V_{oc} difference is the Na incorporation methodology and quantity. The SLG has 14% Na₂O, while the pgo has an alkali content lower than 0.3%. As concluded in chapter 2, the Na in SLG can diffuse into the CIGSe. Na incorporation during the 3-stage co-evaporation might influence the interdiffusion of Ga-In hence the Ga gradient in the absorber [108]. Quantitatively, even though 2 mg NaF PDT is employed upon the CIGSe on both glass types, the overall Na concentration in the absorber might be different.

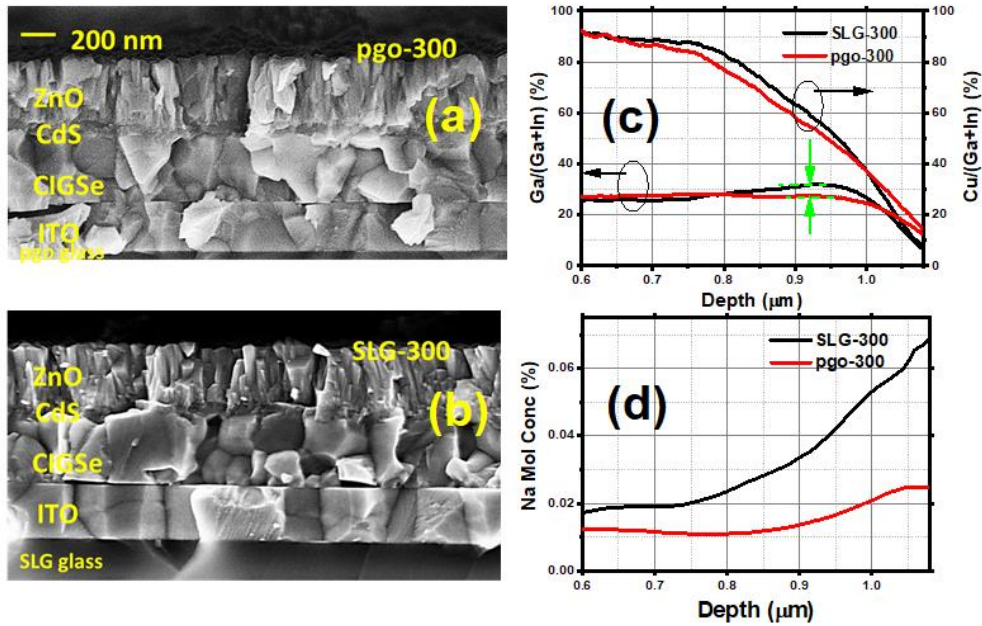


Figure 5-2. Cross-section SEM picture of (a) pgo-300 and (b) SLG-300, (c) depth distribution of Ga/(Ga+In) and Cu/(Ga+In) in the CIGSe, and (d) Na Molar concentration in the absorber

Figure 5-2 (c) displays the Cu/(Ga+In) (CGI) and Ga/(Ga+In) (GGI) ratio in the absorber obtained by GD-OES measurements to compare their depth distribution. As marked by the green arrows, the pgo-300 (red line) shows a flatter GGI than SLG-300 (black line), which implies the SLG-300 has a higher Ga gradient approaching the ITO side. Empirically, on Mo substrates, the Ga gradient plays a critical role in both general 2 μm CIGSe and ultrathin CIGSe (< 500 nm) according to [15, 131]. The Ga gradient can forge a sloping bandgap as a higher Ga content induces a wider bandgap of the CIGSe [132], thus decreasing the recombination in the CIGSe bulk and enhancing the V_{oc} via electric field effect passivation. Therefore, it is reasonable to attribute the 20 mV higher V_{oc} of SLG-300 to the Ga gradient in the absorber. Also, the collection efficiency of the photogenerated carriers is increased by the field effect passivation, so SLG-300 exhibits a higher FF than pgo-300. It is worth mentioning that the back recombination is helpful for the collection of photogenerated carriers, as concluded in chapter 4. Yet, we still believe bulk recombination in the CIGSe is detrimental to the ultrathin solar cells because the bulk recombination only decreases the lifetime and collection efficiency of the minority carriers from the solar cells. Figure 5-2 (d) reveals Na concentration in the CIGSe. Consistent with the results obtained in section 2.3, pgo-300 has 0.025% Na close to the back interface, while SLG-300 has 0.068%, slightly higher than 0.032% from SLG diffusion plus 0.025% from NaF PDT. However, their doping concentration N_A shows approximately equal values as extracted in Table 5-1, which implies the V_{oc} difference is because of the Ga back gradient in CIGSe instead of the doping level in the absorber.

The lower j_{sc} of SLG-300 compared to pgo-300 is also a consequence of stronger field-effect passivation in SLG-300. We often observe a higher V_{oc} but lower j_{sc} resulting from the Ga back grading or bandgap engineering (graded E_g) in CIGSe solar cells [133-136]. According to reference [137], “the losses in j_{sc} approximately equal to the reduced absorption in the CdS/CIGSe junction”. In our case, the width of the SCR is close to the thickness of the ultrathin

absorber, as Figure 3-8 graphically illustrates that the width of the SCR (bending part of the bandgap) takes half of the absorber thickness when the N_A is $5 \times 10^{15} \text{ cm}^{-3}$. That means the CdS/CIGSe junction extends deep into the ultrathin CIGSe layer, as the N_A is $4 \times 10^{15} \text{ cm}^{-3}$ here. Judging from the lower j_{sc} , the higher Ga gradient of SLG-300 induces a lower absorption at the back side of the ultrathin CIGSe absorber. The pgo-300 has a relative flat GGI, which is favourable in terms of photon absorption for the ultrathin CIGSe solar cells. Compared to pgo-300, SLG-300 has higher front Eff because the extra Na diffusion from SLG induces a higher back Ga gradient in the CIGSe layer.

Compared to the front illumination, all the rear PV parameters decrease for the same sample, especially the j_{sc} drops by 35-40%. Compared to pgo-300R, SLG-300R is still higher in V_{oc} and FF . However, the j_{sc} of pgo-300R (18.5 mA/cm^2) surpasses SLG-300R (16.6 mA/cm^2) by 1.9 mA/cm^2 , which makes its rear Eff higher than SLG-300R. This is because 300 nm ITO on pgo glass provides higher transmission to the absorber enabling higher absorption and hence current generation, as illustrated in Figure 5-1.

In conclusion, the front PV performance of BSTUT CIGSe solar cells on SLG outperforms the one on pgo glass because the Na diffusion from SLG promotes a higher back Ga gradient in the absorber. However, the rear PV performance of the devices is better on pgo glass because 300 nm ITO on pgo glass has higher transmission than on SLG. Given the delicacies of Na diffusion into the ultrathin absorber, we employ the pgo glasses only in the following experiments to precisely control the Na incorporation into the CIGSe.

5.2 Impact of the ITO thickness

5.2.1 Transmission and Burstein-Moss shift

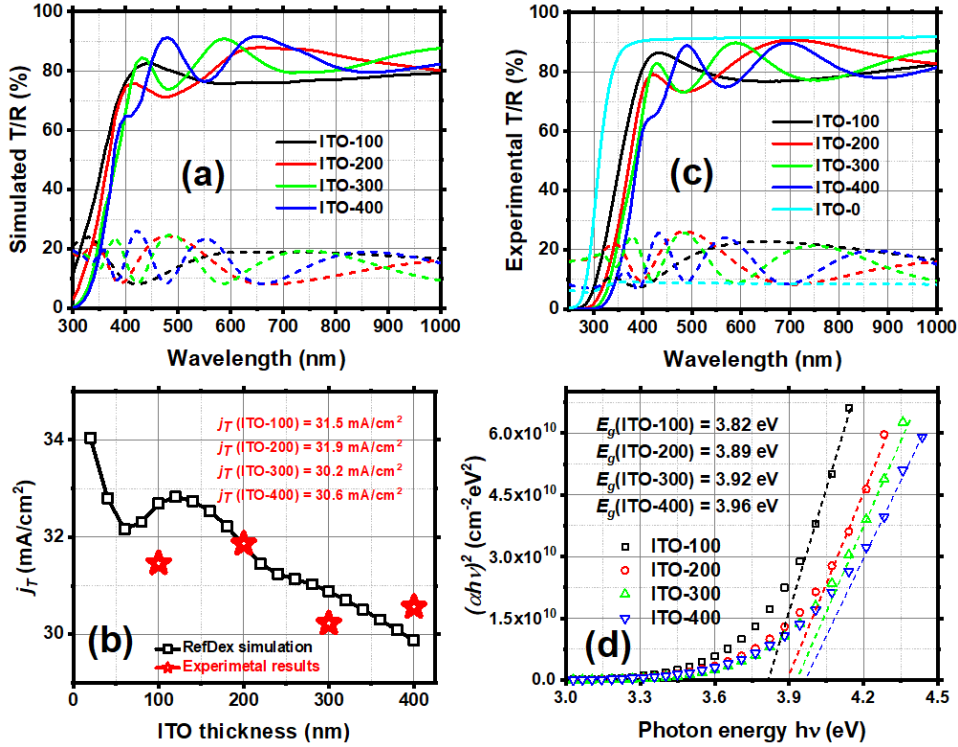


Figure 5-3. (a) Simulated and (c) experimentally measured transmission (solid lines) and reflection (short dashed lines) of ITO/glass with 100, 200, 300 and 400 nm thick ITO. ITO-0 in (c) represents the bare glass. Light illumination comes from the rear side (glass side). (b) equivalent transmission current j_T converted from the transmission of ITO/glass by equation (1). Open squares use simulated transmission results, whilst red stars relate to experimental transmission data. (d) Derivation of the optical bandgap E_g of 100-400 nm ITO on glass

Transparency of the back-contact layer ITO on glass is critical for the rear efficiency of BSTUT CIGSe SCs. Under ideal conditions, if refractive index n and extinction coefficient k of the ITO and glass remain constants when the thickness of ITO increases, the transmission of ITO/glass will decrease because the parasitic absorption in the ITO layer will increase. There are many other factors such as changing (n,k) of the ITO with its thickness and Fabry-Perot interferences in the multi-layered system. Here we focus on the influence of Fabry-Perot interferences first. When the ITO thickness increases, corresponding wavelengths of the peaks and valleys in the transmission/reflection (T/R) shift because of Fabry-Perot interferences (result of multiply reflections). Given photons of different wavelengths contain different energy in the solar spectrum, we define an equivalent transmission current j_T to quantify the transmission for varying ITO thickness:

$$j_T = \int_{350}^{1000} n(\lambda) * T(\lambda) * e * d\lambda$$

(5-1)

$n(\lambda)$ is the number of photons at the corresponding wavelength in the AM1.5 solar spectrum, $T(\lambda)$ is the transmission of the ITO/glass, e is the elementary charge, and λ is the wavelength.

Here, we integrate λ in the wavelength range of 350-1000 nm, which is enough to cover the absorption range of CIGSe solar cells.

Figure 5-3 (a) illustrates the simulated T/R of ITO/glass with 100-400 nm ITO (ITO-100 to ITO-400) via RefDex [105]. For the T/R simulations, the used (n,k) of the ITO layer is extracted from 200 nm ITO on pgo glass by RefDex in the reverse calculation and assumed to be fixed. In Figure 5-3 (a), we notice ITO-100 displays one peak at 420 nm, ITO-200 has two at 400 and 650 nm, ITO-300 has two at 430 and 580 nm, and ITO-400 has three at 400, 470, and 650 nm. The number of the peaks increases with ITO thickness, and the corresponding wavelengths shift due to Fabry-Perot interferences in the thin-film system. Here we only present the T/R of ITO-100 to ITO-400 with a 100 nm increment step. When the ITO thickness step is detailed to 20 nm (i.e., ITO-20, ITO-40, etc.), we obtain the j_T dependent on ITO thickness, as shown in Figure 5-3 (b). As we expect a thicker ITO induces severe parasitic absorption, the j_T curve generally decreases with ITO thickness. The j_T also exhibits an interference due to Fabry-Perot interferences, and the peak at around 120 nm implies the optimum ITO thickness compromises parasitic absorption and reflection loss.

Experimentally, we coat 100, 200, 300, and 400 nm ITO onto glass substrates, and their rear illumination T/R is measured as shown in Figure 5-3 (c). Based on the experimental transmission, we extract the j_T for each ITO thickness via equation (5-1) and mark the results with red stars in Figure 5-3 (b). ITO-200 shows an 0.4 mA/cm² enhancement in j_T compared to ITO-100, which equals to the difference of 0.4 mA/cm² between ITO-400 and ITO-300. The maximum difference lies between 100 and 200 nm ITO on one side and 300 and 400 nm ITO on the other side. It experimentally accounts for 1.3 mA/cm² on average. That is close to the 2.0 mA/cm² difference expected from RefDex simulations.

The electrical properties of the ITO layer also depend on its thickness. According to Kim et al., the optical band gap E_g , the polycrystalline size, and the donor carrier density N_D of the ITO thin film increase with its thickness because of the Burstein-Moss (B-M) shift [138]. For the dependency of E_g on the ITO thickness, Figure 5-3 (d) illustrates the extraction processes and results. As a direct band gap semiconductor, we extract the optical band gap E_g of ITO by the formula:

$$(\alpha h\nu)^2 \propto (h\nu - E_g)$$

(5-2)

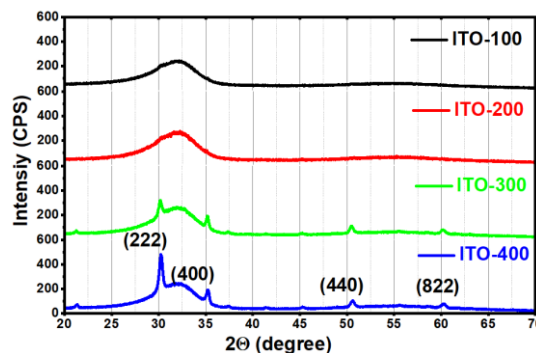


Figure 5-4. XRD (X-ray diffraction) pattern of ITO-100 to ITO-400

$h\nu$ is the photon energy, and α is the absorption coefficient. When the linear fitting line to $(\alpha h\nu)^2$ plotted vs $h\nu$ and intersects with the x-axis, the left side of equation (5-1) equals zero, and we have $h\nu = E_g$. We extract the absorption coefficient α via the formula:

$$T = (1 - R)\exp(-\alpha d) \quad (5-3)$$

T and R are the transmission and reflection, and d is the ITO thickness. As a result we find, that when the ITO thickness increases from 100 to 400 nm, the E_g widens from 3.82 eV to 3.96 eV. Generally, a wider E_g in the window or back-contact layers causes less parasitic absorption, which is beneficial for the BSTUT SCs.

We perform X-ray diffraction measurements to crosscheck the B-M shift observed from T/R , see Figure 5-4. The peak at 30 degrees becomes more and more prominent when the ITO thickness increases. According to reference [138], the enhanced diffraction peaks correlate to the crystal orientation (as marked in the brackets), and thicker ITO has a preferential orientation in the (222) direction because of the B-M shift.

In conclusion, we experimentally have verified that a higher ITO thickness induces a higher parasitic absorption, which is consistent with the RefDex simulations. The optical E_g of the thicker ITO, however, becomes wider because of the B-M shift. Compared to ITO-100, ITO-400 is 0.14 eV wider in the optical E_g . Judging from j_T that does not consider the E_g changes, ITO-400 exhibits a 1.3 mA/cm² higher parasitic absorption than ITO-100.

5.2.2 Front and rear photovoltaic performance of the BSTUT CIGSe solar cells

Table 5-2. Front and rear photovoltaic performance of the BSTUT CIGSe SCs on 100-400 nm ITO. Carrier density N_A , space charge region (SCR) width, and built-in electric field V_D are derived from CV measurements under dark condition. Shunt resistance R_{sh} , series resistance R_s , and ideality factor n are extracted from dark IV curves. The appendix “-R” (e.g. ITO-100R) means illumination from the rear side

Sample name	ITO thickness (nm)	V_{oc} (mV)	j_{sc} (mA/cm ²)	FF (%)	Eff (%)	SCR width (nm)	N_A (E15 cm ⁻³)	V_D (mV)	R_{sh} (Ω cm ²)	R_s (Ω cm ²)	n
ITO-100	100	573±9	29.5±0.6	54.9±2.8	9.3±0.6	450	5.62	770	499	6.3	1.37
ITO-200	200	610±9	28.8±0.6	55.6±1.8	9.8±0.4	408	8.53	950	127	4.9	1.52
ITO-300	300	606±6	28.7±0.9	59.0±3.2	10.3±0.7	408	7.13	790	215	3.6	1.49
ITO-400	400	621±7	28.6±0.6	60.7±4.2	10.8±1.0	397	7.35	770	477	3.9	3.20
ITO-100R	100	558±9	22.7±1.1	51.3±3.2	6.5±0.6						
ITO-200R	200	579±11	22.2±0.9	49.8±4.3	6.4±0.6						
ITO-300R	300	581±2	21.1±2.0	53.0±0.7	6.5±0.6						
ITO-400R	400	596±17	21.4±0.8	51.8±5.6	6.6±1.1						

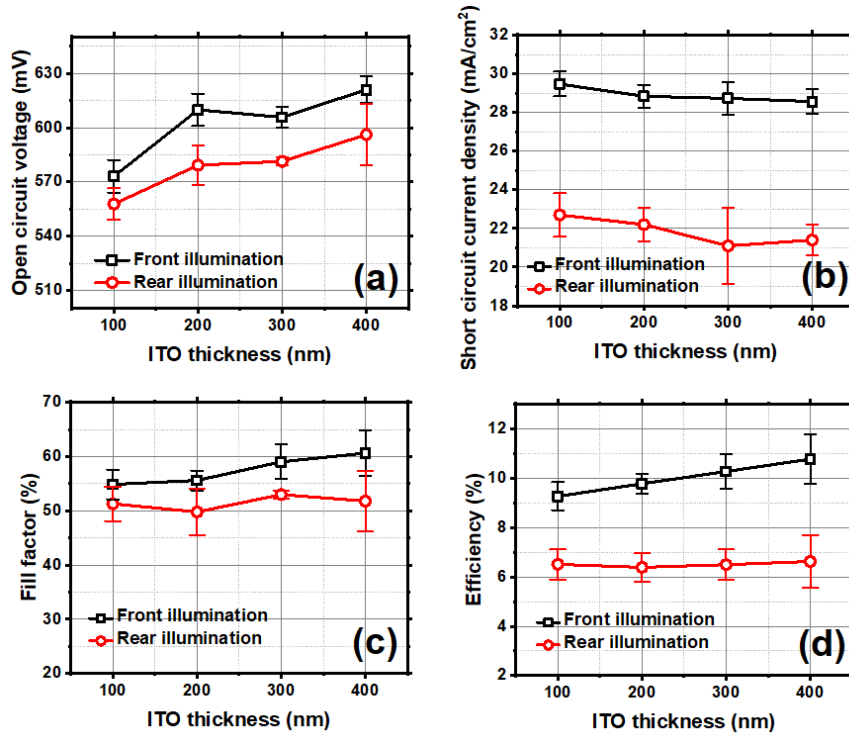


Figure 5-5. The front and rear PV parameters (a) open circuit voltage V_{oc} , (b) short circuit current density j_{sc} , (c) fill factor FF , and (d) efficiency of the solar cells on ITO-100 to ITO-400. Black squares refer to the front PV performance of the BSTUT CIGSe SCs and red circles to rear illumination. The error bar of the corresponding parameters includes at least 6 cells on each sample

We put the ITO/glass substrates with 100-400 nm ITO into the PVD together with 2 mg NaF to investigate the influences of ITO thickness on the front and rear PV performance of BSTUT CIGSe SCs. We use the first NaF PDT scenario to ensure ITO thickness is the only variation in the samples. The absorbers presented here have a thickness of 438 nm, CGI 0.85, and GGI 0.35.

Table 5-2 summarizes the front and rear PV performance of BSTUT CIGSe SCs on 100-400 nm ITO, along with the diode parameters of the corresponding devices. For better comparison, Figure 5-5 displays the front and rear PV parameters graphically. Under front illumination, V_{oc} demonstrates an increasing trend when the ITO thickness increases. Judging from the CV results, the width of the SCR shrinks continuously from 450 to 397 nm. N_A and V_D , however, fluctuate in the range from $5.6\text{-}8.5 \text{ E}15\text{cm}^{-3}$ and 0.77-0.95 V, respectively. In chapter 3, a higher N_A and V_D would be expected to lead to a higher V_{oc} . We cannot find a consistent trend between V_D , N_A and V_{oc} in the ITO thickness variation. It implies the V_{oc} enhancement of BSTUT CIGSe SCs on thicker ITO is not primarily determined by the CdS/CIGSe main junction but by the CIGSe/ITO back interface.

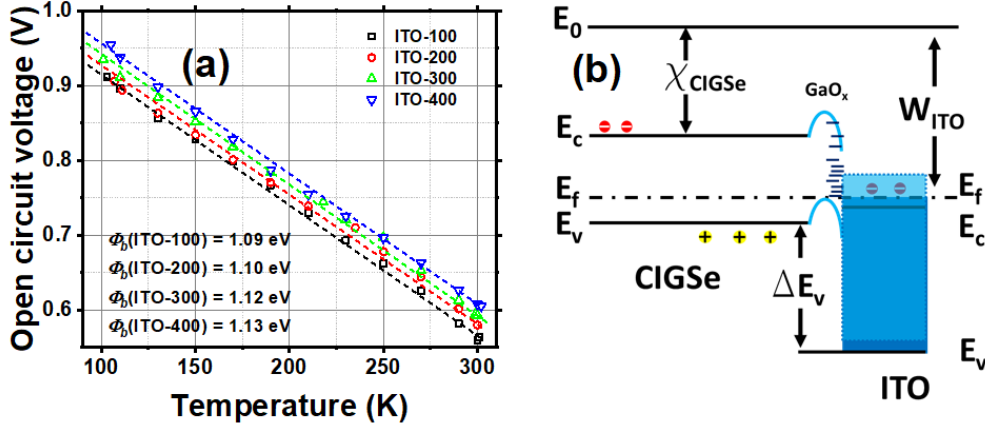


Figure 5-6. (a) The V_{oc} of ITO-100 to ITO-400 dependent on the temperature T , and the contact potential barrier height Φ_b in the corresponding diode (b) partial band diagram of the CIGSe solar cells at the CIGSe/ITO interface

To quantitatively estimate the back barrier height $E_{CIGSe/ITO}$ at CIGSe/ITO, we conduct IVT measurements to extract the barrier height Φ_b of the solar cells, as shown in Figure 5-6 (a). The Φ_b of the devices increases from 1.09 to 1.13 eV for sample ITO-100 to ITO-400. According to equation (1-11) $\Phi_b = E_g - E_{CIGSe/ITO}$. If we presume E_g equals 1.14 eV for all diodes (from the EQE results shown in Figure 5-7), $E_{CIGSe/ITO}$ decreases from 0.05 to 0.01 eV. According to the conclusion from chapter 4, those $E_{CIGSe/ITO}$ values are in the Ohmic contact range (< 0.17 eV). It is because we used $E_g = 1.14$ eV for calculation here. In reality, E_g of the CIGSe shall be higher than 1.14 eV, especially in the vicinity of the CIGSe/ITO interface, as the GGI ratio at the CIGSe/ITO interface side is higher than in the bulk of CIGSe. The diminished $E_{CIGSe/ITO}$ contributes 40 mV gain in the front V_{oc} of BSTUT CIGSe solar cells, which is close to the 48 mV V_{oc} difference between ITO-400 and ITO-100.

Figure 5-6 (b) shows the band diagram at the CIGSe/ITO interface to better illustrate how the B-M shift in the ITO layer influences the back barrier height $E_{CIGSe/ITO}$. The dark blue coloured box corresponds to ITO-100, while the light blue one with a dotted line border represents ITO-400. ΔE_v marks the valence band offset between ITO and CIGSe layers. Therefore, we have:

$$\Delta E_v = W_{ITO} + E_g(ITO) - \chi_{CIGSe} - E_g(CIGSe) \quad (5-4)$$

where W_{ITO} is the work function of ITO and χ_{CIGSe} is the electron affinity of CIGSe. Here we presume $E_g(CIGSe)$ and χ_{CIGSe} of CIGSe remain unchanged for all samples. On the ITO side, due to the B-M shift, a thicker ITO has a wider $E_g(ITO)$ but a lower W_{ITO} . According to Sato et al., “ W_{ITO} decrement is bigger than $E_g(ITO)$ increment, and the overall ΔE_v decreases for the thicker ITO” [139]. That explains the $E_g(ITO)$ increment is 0.14 eV in our experiments, while the $E_{CIGSe/ITO}$ decrement is only 0.04 eV. The reason is that ΔE_v decides the barrier height $E_{CIGSe/ITO}$ for holes at the CIGSe/ITO back interface.

From the material perspective, the mechanism of how $E_g(ITO)$ tunes ΔE_v is not confirmed yet. It might be the properties (like thickness and defect density) of the interfacial GaO_x are influenced by the morphology of ITO layer. As XRD measurements denote in Figure 5-4, the thicker ITO has a preferential orientation in the (222) direction. According to Kim et al., the

lattice constant of the thicker ITO is smaller [138]. That might also influence the formation of the GaO_x layer and affect $E_{\text{CIGSe/ITO}}$. Similarly, in organic solar cells and light-emitting devices, a thick ITO with a lower work function (originating from a larger E_g is beneficial for hole transport/collection as anode contacts due to the higher carrier density and wider bandgap in the ITO layer [138, 140, 141].

At this stage, the thicker ITO induces a lower W_{ITO} , which is beneficial for the front PV performance of BSTUT CIGSe solar cells. However, it is controversial with the conclusion in section 3.3.2 that the higher work function of the back contact W_{back} is beneficial for the solar cells. We need to further explain the two models behind to justify those two contradictory conclusions. In section 3.3.2, SCAPS treats the back contact as metal as default. Therefore, what we set as W_{back} is the metal work function W_m for the majority carriers. In this case, if W_s of the p-type semiconductor (CIGSe) is higher than W_m of the metal, the contact in between them is a blocking barrier. When $W_s < W_m$, the contact junction has an anti-blocking barrier, and the higher W_m benefits the solar cells. However, the ITO is a degenerated semiconductor, contacting with CIGSe in this chapter, which is different from the case of metal contact. SCAPS simulations cannot reproduce the band diagram of ITO-based solar cells because the n-type ITO contacts with the p-type CIGSe are supposed to form a heterojunction with an SCR, as predicted in reference [31]. In addition, we do not understand the properties of the interfacial layer GaO_x yet, so we cannot simulate them in SCAPS adequately. Given those two unavoidable difficulties, a reduced ΔE_V is just one of many models that can explain the beneficial effects of thicker ITO for the BSTUT CIGSe solar cells. Further theoretical research about the CIGSe/ITO contact is required to clear those doubts.

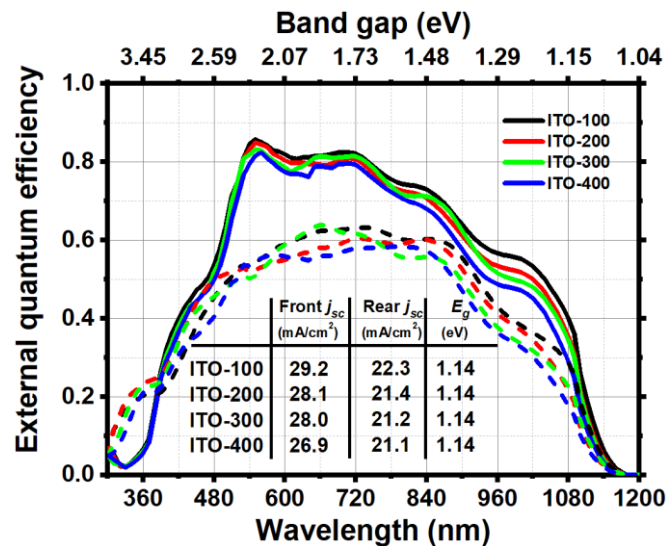


Figure 5-7. External quantum efficiency of bifacial semitransparent ultrathin (BSTUT) CIGSe solar cells on 100, 200, 300 and 400 nm thick ITO back contact (ITO-100 to ITO-400). Solid lines refer to the front, dashed lines to the rear illumination. The inserted table shows integrated current density and CIGSe bandgap E_g are extracted from the EQE derivative

For the BSTUT CIGSe SCs on thicker ITO, the front j_{sc} manifests a decreasing trend in Figure 5-5 (b). The EQE results in Figure 5-7 confirm this decreasing trend. Instinctively, two main reasons may cause the j_{sc} decrease:

(1) The parasitic absorption in the ITO layer. To quantitatively estimate the light loss in ITO by parasitic absorption, the equivalent absorption current density in the CIGSe layer is calculated on 100-400 nm ITO with the full stack solar cells in RefDex. The difference in equivalent current density is only 0.15-0.23 mA/cm² between ITO-100 and ITO-400. Compared to the j_{sc} decrement of 0.7-0.9 mA/cm², the parasitic absorption lost in the ITO layer is negligible.

(2) The recombination in bulk or at interfaces of the solar cells. Generally, we use the lifetime of the minority carriers to describe recombination in the CIGSe solar cells. Interface lifetime and bulk lifetime decide the overall lifetime of devices [79]. The bulk lifetime in ultrathin CIGSe is high as the SCR width is close to the CIGSe thickness. Therefore, interfacial recombination (or interface lifetime) mainly decides the j_{sc} of ultrathin CIGSe solar cells. In our case, the CIGSe/ITO interface is the only variation for different samples. For the solar cells with thicker ITO, the EQE is lower in the whole wavelength range (see Figure 5-7), which is attributed to the shorter lifetime in the ultrathin CIGSe solar cells.

In summary, judging from the EQE results, the lower j_{sc} for the samples with thicker ITO is mainly caused by higher electrical recombination in the solar cells. The optical parasitic absorption in the ITO layer is a trivial reason.

Now we move on to the front illumination FF . The V_{oc} -originated contribution can be estimated by equation [142]:

$$FF_0 = \frac{v_{oc} - \ln(v_{oc} + 0.72)}{v_{oc} + 1} \quad (5-5)$$

in which $v_{oc} = qV_{oc}/(nkT)$ is the normalized open circuit voltage. If the diode factor n took an average value of 1.5, the V_{oc} increases from 573 to 621 mV (ITO-100 to ITO-400), leading to a FF enhancement of 1.3% absolute. This part originating from the diminished $E_{CIGSe/ITO}$ is smaller than the observed FF increment of 5.8%. Because R_s and R_{sh} essentially influence FF , we use the following expression to estimate the impact of modified resistance values [142]:

$$FF = FF_0 \left\{ (1 - 1.1r_s) + \frac{r_s^2}{5.4} \right\} \left\{ 1 - \frac{v_{oc} + 0.7FF_0}{v_{oc} r_{sh}} \left((1 - 1.1r_s) + \frac{r_s^2}{5.4} \right) \right\} \quad (5-6)$$

in which FF_0 means the fill factor without shunt and series resistance, and r_s and r_{sh} stand for the normalized series and shunt resistance, respectively [142]. Comparing ITO-400 to ITO-100, R_s drops from 6.3 to 3.9 Ωcm² and R_{sh} from 498.5 to 477.2 Ωcm² (see Table 5-2). According to formula (5-6), the FF of ITO-400 increases by 8%, which is closer to the experimental FF gain of 5.8% than ITO-100. The change in FF may also include the decreased $E_{CIGSe/ITO}$, which correlates to a decreased R_s from the device point of view.

Under rear illumination, as manifested by the red lines in Figure 5-5, the V_{oc} and j_{sc} behave similar to their front performance. The increasing trend in V_{oc} is because of the diminished $E_{CIGSe/ITO}$ at the CIGSe/ITO interface. For the j_{sc} , however, the reduction in j_{sc} is mainly attributed to ITO parasitic absorption: compared to ITO-100, the j_{sc} loss observed

experimentally for ITO-400 is 1.3 mA/cm^2 , which almost equals the j_T difference (1.3 mA/cm^2) calculated from T/R measurements of 400 and 100 nm thick ITO. Interestingly, the j_{sc} of ITO-300 is 0.3 mA/cm^2 lower than ITO-400, close to the 0.4 mA/cm^2 difference in j_T , which again tells us the decisive importance of the ITO/glass transmission under rear illumination. The FF , however, shows a fluctuating change under rear illumination conditions. Under rear illumination light, the density of photogenerated carriers is higher at the back side of the device. As the neutral region is wider for thicker ITO, the collection efficiency will be lower in this case. The changes in V_{oc} and j_{sc} even each other. The overall efficiency varies in the range of 6.4-6.6%.

In conclusion, when the thickness of ITO increases in the ultrathin CIGSe solar cells:

- (1) The front and rear V_{oc} display an increasing trend due to the B-M shift in the ITO layer leading to a diminished $E_{CIGSe/ITO}$ at the CIGSe/ITO interface;
- (2) The front j_{sc} exhibits a decreasing trend due to the increased recombination at the CIGSe/ITO interface. The rear j_{sc} also manifests a decreasing trend due to the parasitic absorption in the ITO layer;
- (3) The front FF shows an increasing trend due to the V_{oc} increase combined with the R_{sh} and R_s change. Under rear illumination, the rear FF presents fluctuation because of the reversed distribution of photogenerated carriers in the solar cells;
- (4) Overall, on thicker ITO back contact, the front Eff of BSTUT CIGSe SCs shows a consistent increase, but the rear Eff is almost unchanged.

5.3 Impact of the NaF post-deposition treatment dose

The Na incorporation plays a critical role in controlling the CIGSe quality, as chapters 2 and 3 have demonstrated. Our previous study has verified that NaF PDT increases the carrier density N_A in the CIGSe absorber and decreases the back barrier for holes E_h at the CIGSe/ITO interface. This section will quantitatively correlate the front and rear PV performance with N_A and E_h .

For the NaF PDT process, the second scenario described in section 3.1 is employed here to minimized the differences in CGI, GGI, and CIGSe thickness between different samples. One batch of CIGSe absorbers is taken out of the PVD and separated into four groups. The CIGSe absorbers of each group are then separately put back into the PVD chamber along with 0, 2, 4 and 8 mg NaF powder, respectively, and subject to the PDT process. We refer to the corresponding samples as NaF_0, NaF_2, NaF_4 and NaF_8. In this section, the batch of CIGSe we analyse has a CGI of 0.87, GGI of 0.32, and a thickness of 491 nm. 300 nm ITO is used for NaF_0 to NaF_8, as ITO-300 has an adequate front and rear PV performance, but the overall thickness of BSTUT CIGSe solar cells is kept as thin as possible to ensure its transparency.

Table 5-3. The front and rear PV parameters, doping density N_A , space charge region width SCR at 0-volt bias, contact potential differences V_D , shunt resistance R_{sh} and series resistance R_s of the BSTUT CIGSe solar cells with 0-8 mg NaF PDT. The suffix '-R' means rear illumination PV performance of the solar cells

Sample name	NaF PDT dose (mg)	V_{oc} (mV)	j_{sc} (mA/cm ²)	FF (%)	Eff (%)	N_A (E15 cm ⁻³)	SCR width W_{SCR} (nm)	V_D (mV)	R_{sh} (Ω cm ²)	R_s (Ω cm ²)
NaF_0	0	517±9	29.2±1.0	57.3±3.0	8.7±0.9	2.19	588	530	1175	10.8
NaF_2	2	610±4	27.6±0.5	67.1±1.1	11.3±0.3	6.91	380	690	2973	5.9
NaF_4	4	621±2	28.2±0.8	67.1±1.4	11.8±0.5	7.95	369	720	329	5.7
NaF_8	8	630±4	28.2±0.3	62.8±4.1	11.2±0.7	11.63	318	750	411	4.4
NaF_0R	0	474±13	19.0±1.1	47.5±1.6	4.3±0.4					
NaF_2R	2	582±5	19.1±1.6	57.0±0.8	6.3±0.5					
NaF_4R	4	585±2	17.3±1.1	62.9±1.1	6.4±0.5					
NaF_8R	8	597±8	16.3±0.7	58.2±4.8	5.7±0.7					

Table 5-3 summarizes the front and rear PV parameters, carrier density N_A , space charge region width W_{SCR} at zero bias, contact potential difference V_D , shunt resistance R_{sh} , and series resistance R_s of the BSTUT CIGSe SCs with 0-8 mg NaF for PDT. Figure 5-8 visualizes the trends of the PV performance.

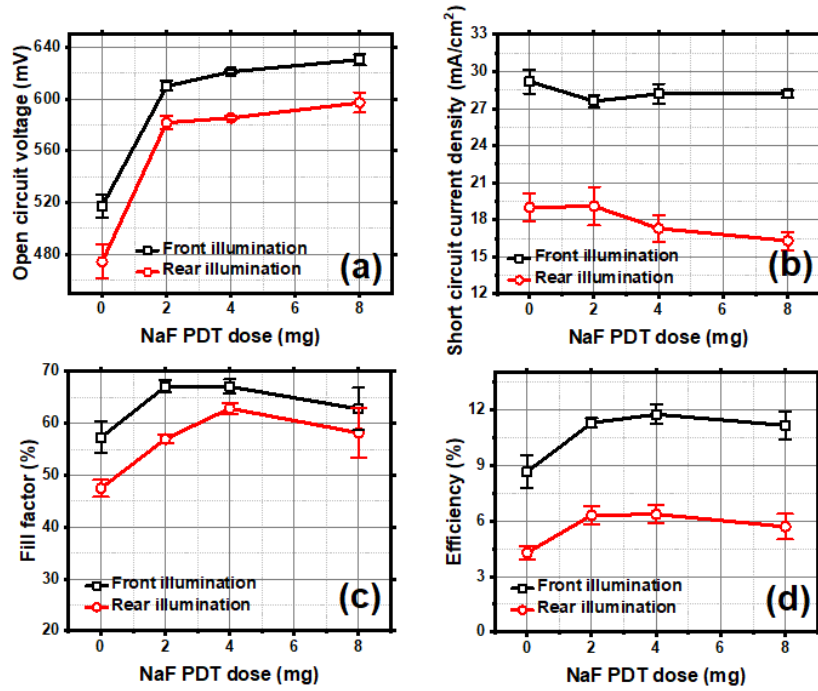


Figure 5-8. PV parameters (a) open circuit voltage V_{oc} , (b) short circuit current density j_{sc} , (c) fill factor FF , and (d) efficiency Eff for the samples with 0, 2, 4, or 8 mg NaF PDT (NaF_0, NaF_2, NaF_4 and NaF_8) in comparison. Black squares refer to front illumination and red circles to rear illumination

As the NaF PDT dose increases, the V_{oc} of the ultrathin CIGSe solar cells shows an increasing trend, consistent with the results obtained in chapter 3. We can use equation (2-2) to quantify the contribution of the increased N_A to the V_{oc} increase [111]. By setting $\Delta n = 1 \text{ E}14 \text{ cm}^{-3}$ and $n_i = 8.6 \text{ E}9 \text{ cm}^{-3}$, we vary N_A in the range from 2–12 $\text{E}15 \text{ cm}^{-3}$ which is derived from the CV measurements. The estimated V_{oc} increases from 559 to 604 mV, approaching the experimental V_{oc} summarized in Table 5-3 (517-630 mV). From the perspective of N_A increase, the V_{oc} of NaF_8 should be 45 mV higher than for NaF_0. In practical experiments, the V_{oc} of NaF_8 is 113 mV higher than for NaF_0. Therefore, the increased N_A is only partially responsible for the V_{oc} enhancement. The remaining V_{oc} gain originates from the decreased $E_{CIGSe/ITO}$ at the back interface.

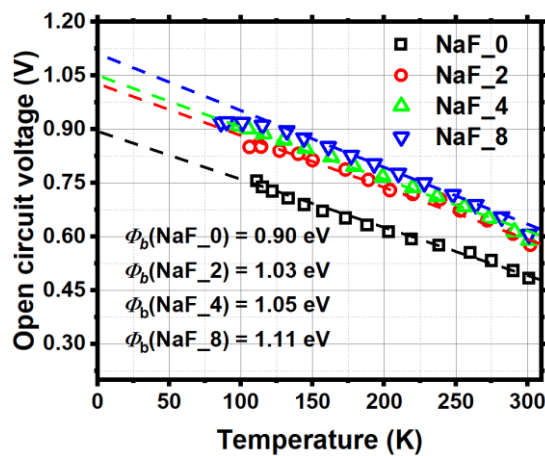


Figure 5-9. V_{oc} dependence on temperature of the BSTUT solar cells with 0, 2, 4 and 8 mg NaF PDT. Φ_b means the barrier height of the solar cell device

We extract $V_{oc}(T)$ from the IVT characteristics of the ultrathin CIGSe solar cells to quantify $E_{CIGSe/ITO}$ changes at the back interface, as illustrated in Figure 5-9. The insert shows linear fitting results of Φ_b . According to equation (1-11), E_g and E_h decide Φ_b . In reality, N_A mainly increases the contact potential difference at CIGSe/CdS, and $E_{CIGSe/ITO}$ relates to the barrier at the CIGSe/ITO interface. Therefore, the E_h decrease extracted from the Φ_b increase should have included the changes in $E_{CIGSe/ITO}$ and the contact potential difference at CIGSe/CdS. Compared to NaF_0, Φ_b of NaF_2 is 130 meV higher, higher to the observed V_{oc} gain of 92.7 mV. Compared to NaF_2, Φ_b of NaF_4 increases by 20 meV and for NaF_8 it increases by an additional 60 meV. Those Φ_b increases are higher than the measured V_{oc} gain of 11 and 20 mV, which is attributed to the V_{oc} deficit caused by recombination [143, 144]. Compared to NaF_0, NaF_8 shows 113 mV V_{oc} gain, in which 45 mV can be attributed to the N_A increase and 68 mV to the $E_{CIGSe/ITO}$ decrease.

In summary, the Φ_b increase implies that E_h decreases in the BSTUT CIGSe solar cells after NaF PDT. Quantitative analysis reveals two main reasons: increased N_A in the CIGSe layer and decreased barrier height $E_{CIGSe/ITO}$ at the CIGSe/ITO back interface.

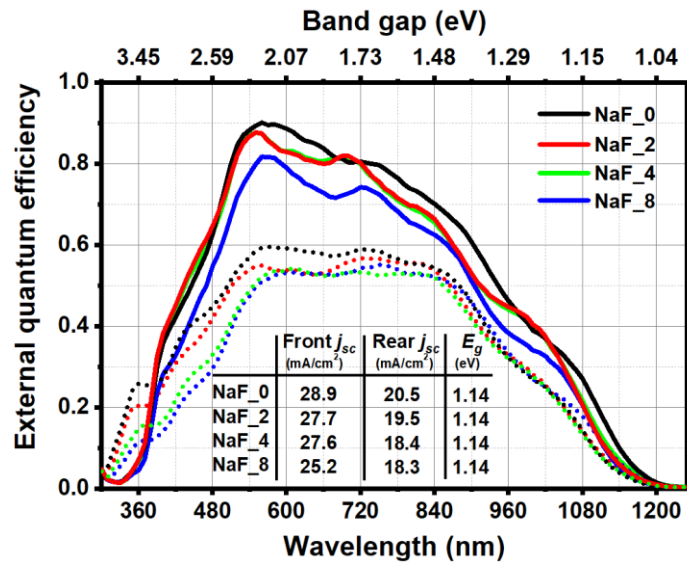


Figure 5-10. Front and rear EQE of NaF_0 to NaF_8. Solid lines refer to front illumination and dotted lines to rear illumination. The inserted table summarizes the current density j_{sc} integrated from EQE and the CIGSe bandgap E_g obtained from the EQE derivatives

In Figure 5-8 (b), the front j_{sc} of BSTUT CIGSe SCs presents a decreasing trend for higher NaF PDT doses. Generally, the anomaly of increased V_{oc} but reduced j_{sc} attributes to the high recombination of photo-generated minority carriers at the interfaces [100]. To explore recombination in the solar cells and cross-check the front j_{sc} trend, we conduct EQE measurements under front and rear illumination as plotted in Figure 5-10.

Usually, according to references [24, 129], recombination at the interfaces on the side of light incidence influences the EQE more in the short wavelength range, and a low diffusion length L_p keeps the EQE shape but lowers its overall level. In our case, the front EQE of NaF_0, NaF_2 and NaF_4 overlap in the wavelength range of 300-540 nm. It means the recombination at CIGSe/CdS is close for those three samples. However, in the 540-1200 nm wavelength range, the EQEs of NaF_2 and NaF_4 display a lower percentage than for NaF_0. The reason is that

compared to NaF_0, the NaF PDT process shortens the L_p in CIGSe: According to equation (1-6), the increase of N_A decreases the lifetime and diffusion length. The CIGSe bulk recombination increases and the j_{sc} of the solar cells drops with N_A increasing from $2 \text{ E}15 \text{ cm}^{-3}$ to $1.2 \text{ E}16 \text{ cm}^{-3}$. EQE of NaF_8 suffers an even more severe decrease over the whole wavelength range because it has the highest N_A and bulk recombination in the solar cells. The j_{sc} decrease is consistent with the conclusions in chapters 3 and 4 that the increased S_b at the CIGSe/ITO interfaces in the NaF PDT processed samples will decrease the front j_{sc} of BSTUT CIGSe solar cells.

When a solar cell is under rear illumination, the CIGSe/ITO interface is on the incident side. In the short wavelength range of 300-540 nm, the PDT processed samples manifest a consistent decrease in EQE. The reason is that the recombination increases at the CIGSe/ITO interface where the Na congregates. At 360 nm, we recognize a peak for all solar cells. Judging from the corresponding bandgap, it is because of the absence of CdS parasitic absorption. When the light comes from the front side, the CdS layer absorbs this part of solar light hence the light at those wavelengths contributes none quantum efficiency to the solar cells. When the light comes from the rear side, this part of the light can be absorbed and utilized by the CIGSe absorber. As a result, we can see the absorption peak in the rear EQE curves. In the wavelength range from 540-840 nm, the rear EQE is relatively flat because of a combination of two effects. In the case of rear illumination, the long wavelength light is generally absorbed closer to the SCR due to its higher penetration depth. So EQE should rise for longer wavelength in case of rear illumination. On the other hand, for ultrathin solar cells, long wavelength light is subject to transmission hence a reduction in EQE is also visible in the case of front illumination.

According to equation (5-5), when the front V_{oc} increases from 517 (NaF_0) to 610 mV (NaF_2), FF_0 increases by 2.7%, which is smaller than the experimental front FF difference of 9.8%. It implies that the R_s decrease (from 10.8 to 5.9 Ω) also contributes to the FF gain for NaF_2, which accounts for 18% in absolute according to formula (5-6). When the V_{oc} continues to increase from 610 to 621 mV (for NaF_4), the FF_0 increase according to equation (5-5) is only 0.3%, whereas (5-6) considering R_s and R_{sh} gives a 0.6% decrease. Overall, we expect the FF of NaF_4 to decrease by 0.3%, which is comparable to the stagnating measured value of 67.1%. For NaF_8, the trend of experimental FF reduction continues despite an increased V_{oc} due to the higher recombination in the devices.

Lastly, the rear efficiency Eff follows the trend of the rear FF . The Eff trend under rear illumination is also in parallel with the front efficiency, which means the light loss in the ITO/glass layers is almost the same for all NaF doses. NaF_4 reaches the highest efficiency of 11.8% under front and 6.4% under rear illumination.

In conclusion, when the NaF PDT dose increases, we find:

- (1) The front and rear V_{oc} increase due to an increased N_A and decreased $E_{CIGSe/ITO}$;
- (2) The front j_{sc} decreases because the recombination is increased both in the CIGSe bulk and at the CIGSe/ITO interface, as the front EQE decreases in the short and long wavelength range.

The rear j_{sc} decreases because of the increased back interface recombination, as the rear EQE mainly decrease in the short wavelength range;

(3) The overall Eff shows a parallel trend under front and rear illumination. The optimum NaF dose for this batch ultrathin CIGSe absorber (CGI is 0.87, GGI is 0.32, and thickness is 491 nm) shown here is 4 mg. The champion BSTUT CIGSe solar cells reveal 11.8% front efficiency and 6.4% rear illumination efficiency.

5.4 Summary and conclusion

In this chapter, the front and rear efficiency of ultrathin CIGSe solar cells was optimized for different glass types, ITO thicknesses, and NaF PDT doping doses. We find that:

(1) SLG-based solar cells show a higher front PV performance due to additional Na diffusion from SLG modifying the GGI gradient. The higher Ga grading effectively increase the front V_{oc} and FF of the BSTUT CIGSe solar cells on SLG. However, the pgo glass-based solar cells demonstrate a better rear efficiency because the pgo glass has higher transparency than SLG;

(2) Thicker ITO is beneficial for the front Eff due to the B-M shift in the ITO layer increases the V_{oc} of BSTUT CIGSe solar cells. The rear j_{sc} of the ultrathin CIGSe solar cells suffers from a drop on thicker ITO because thicker back contacts induce a more severe parasitic absorption. We propose a valence band off-set model to explain how the B-M shift leads to a lower $E_{CIGSe/ITO}$ at the CIGSe/ITO back interface;

(3) The NaF PDT process not only increases N_A in the SCR of the absorber but also diminishes $E_{CIGSe/ITO}$ at the CIGSe/ITO interface. According to EQE characterization, the front j_{sc} decreases for the higher NaF PDT processed samples because there is higher recombination in the CIGSe bulk and at the CIGSe/ITO interface. The rear PV parameters of the BSTUT CIGSe solar cells with 0-8 mg NaF PDT show a parallel trend with their front illumination performances.

Chapter 6 Light management

The j_{sc} of CIGSe solar cells degenerates the most among all the PV parameters when the absorber thickness decreases. In state-of-the-art CIGSe solar cells, the j_{sc} is 39.6 mA/cm² for general 2-3 μm thick CIGSe. The j_{sc} decreases to 26.4 mA/cm² for ultrathin (< 500 nm) CIGSe solar cells [15, 16]. The reason is that light absorption in the ultrathin CIGSe absorber is insufficient. The first-order light path shortens when the CIGSe thickness decreases. Part of the light is lost in transmission, especially in the long wavelength range. Light management can trap the light and enhance the j_{sc} of solar cells with ultrathin absorbers. Inserting nanoparticles (NPs) is an efficient light management method. The NPs can trap light incident from both front and rear side of the solar cells inside the absorber layer, which is the optimal choice for our bifacial semi-transparent ultrathin CIGSe solar cells (BSTUT CIGSe SCs).

This chapter explores the light trapping effects of SiO₂ NPs in BSTUT CIGSe solar cells. It is a cooperation work with the group of Prof. Albert Polman at AMOLF (Atomic and Molecular Physics, Science Park 104, Amsterdam, Netherlands). Dr. Stefan W. Tabernig fabricates the SiO₂ NPs at University of New South Wales (UNSW). The authors acknowledge the facilities and the scientific and technical assistance of Microscopy Australia at the Electron Microscope Unit (EMU) within the Mark Wainwright Analytical Centre (MWAC) at UNSW Sydney. Yong Li completes the other layers of the solar cells and conducts all characterization besides SEM. Here, we will first introduce the fabrication steps of SiO₂ NPs with the substrate conformal imprint lithography (SCIL) method. Then we characterize the light trapping effects of the NPs by comparing the PV performance of solar cells with/without SiO₂ NPs. We will also discuss the differences in the light trapping mechanism of the SiO₂ NPs under the front and rear illumination.

6.1 Fabrication of SiO₂ nanoparticles

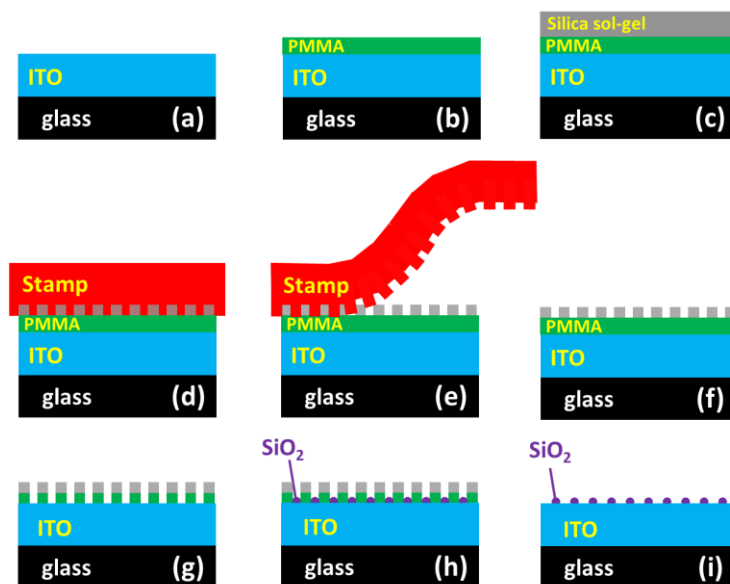


Figure 6-1. Fabrication steps of the SiO₂ nanoparticles by SCIL

Figure 6-1 shows the fabrication steps of SiO₂ nanoparticles with the SCIL method. (a) indicates the cleaning of ITO/glass substrates. The ITO/glass substrates are put into the supersonic bath with acetone for 15 minutes. In the same way, the substrates undergo a 15 minutes supersonic bath with isopropanol. The cleaning step finishes with deionized water bath and argon-gas blow. In order to fabricate a SiO₂ NPs mask, firstly, 280 nm PMMA are spin coated (b), followed by 70 nm silica sol-gel (c). Secondly, a flexible stamp with regular patterns imprints the samples (d). After lifting off (e), the samples are etched with CHF₃/Ar for residual sol-gel (f) and O₂ for PMMA (g). Now the substrates have a mask made of PMMA and silica. SiO₂ is evaporated into the patterned holes (h). By washing the PMMA and sol-gel away, we obtain ITO/glass substrates patterned with SiO₂ NPs (i).

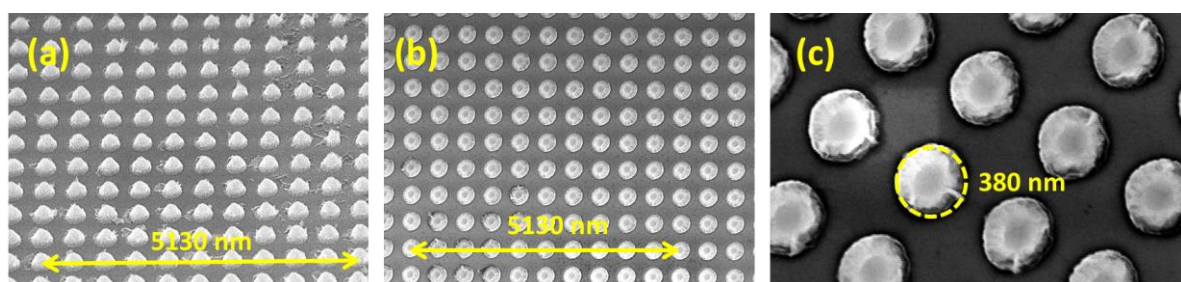


Figure 6-2. (a) Tilted-view and (b)-(c) top-view of SiO₂ NPs on ITO substrates

More fabrication details can be found in references [33] for SiO₂ NP SCIL. Figure 6-2 shows the top-view and tilted-view SEM pictures of the SiO₂ NPs. The SiO₂ NPs have a pitch of 513 nm and a diameter of 380 nm. This geometry follows an existing mask, which is not the optimum according to the simulations in reference [22]. The height of the SiO₂ NPs is 200 nm. This chapter intends to demonstrate the light trapping effects of the SiO₂ NPs under front and rear illumination.

6.2 Front illumination characteristics

Table 6-1. Front PV parameters, EQE-integrated equivalent current density j_{EQE} , diode parameters of the devices extracted from the dark IV characteristics, N_{CV} at 0 V bias, space charge region width W_{SCR} and contact potential difference V_D of the SCs with/without SiO_2 NPs

Sample name	j_{sc} (mA/cm ²)	j_{EQE} (mA/cm ²)	V_{oc} (mV)	FF (%)	Eff (%)	n	j_0 (E-8 A/cm ²)	R_s (Ω cm ²)	R_{sh} (Ω cm ²)	N_{cv} (E15 cm ⁻³)	W_{SCR} (nm)	V_D (mV)
ITO-100	26.7±0.5	26.4	579±34	57±4	8.8±1.0	1.9	10.0	4.5	837	6.1	509	710
ITO-100-SiO ₂	31.1±1.1	31.6	584±8	55±2	10.0±0.4	1.9	8.1	4.1	442	6.2	456	520
ITO-300	26.7±0.1	26.2	598±2	60±1	9.6±0.1	2.0	8.0	5.7	406	6.1	482	620
ITO-300-SiO ₂	30.8±0.3	31.0	608±12	61±2	11.4±0.7	1.9	3.9	3.2	325	6.2	468	530

Table 6-1 summarizes the front PV parameters of the BSTUT CIGSe solar cells without/with SiO_2 NPs. The absorbers in those solar cells come from one batch of 3-stage co-evaporation. The ultrathin CIGSe has a thickness of 468 nm, CGI of 0.83 and GGI of 0.33. The PDT process uses 2 mg NaF with the sequential doping scenario. Apart from this batch of CIGSe, we repeat the same experiment two more times with the same fabrication conditions. Figure 6-3 illustrates the PV parameter distributions of all three absorber batches to see the evolution trend after the SiO_2 NPs insertion. When measuring IV characteristics of the solar cells, we put black paper beneath the testing samples to avoid reflection from the sample holder. For simplicity, the abbreviation ITO-100 represents that 100 nm ITO is used as back contact. The suffix ' SiO_2 ' means that the ITO substrates have SiO_2 NPs for light trapping, and 'R' denotes the rear PV parameters of the solar cells.

The front j_{sc} of ITO-100-SiO₂ is 4.4 mA/cm² higher than for ITO-100, which is close to the prediction of 4.2 mA/cm² in reference [22]. From optical simulation perspective, the higher j_{sc} of ITO-100-SiO₂ is attributed to the SiO_2 light trapping effects. Similarly, ITO-300-SiO₂ shows a 4.1 mA/cm² j_{sc} gain over ITO-300, which is 0.1 mA/cm² lower than on 100 nm ITO substrates. The SiO_2 exhibits a higher j_{sc} gain on the thinner ITO substrates because a thinner back contact induces less parasitic absorption, so more light is reflected from ITO/Glass interfaces back into the CIGSe absorbers. For the front V_{oc} of BSTUT CIGSe solar cells, the SiO_2 NPs level it up by 5 mV on 100 nm ITO and by 20 mV on 300 nm ITO compared to the corresponding references. The enhanced V_{oc} is attributed to the j_{sc} gain according to the following relation between V_{oc} and j_{sc} [111, 145]:

$$V_{oc} = \frac{nkT}{q} \ln \left(\frac{j_{sc}}{j_0} + 1 \right) \quad (6-1)$$

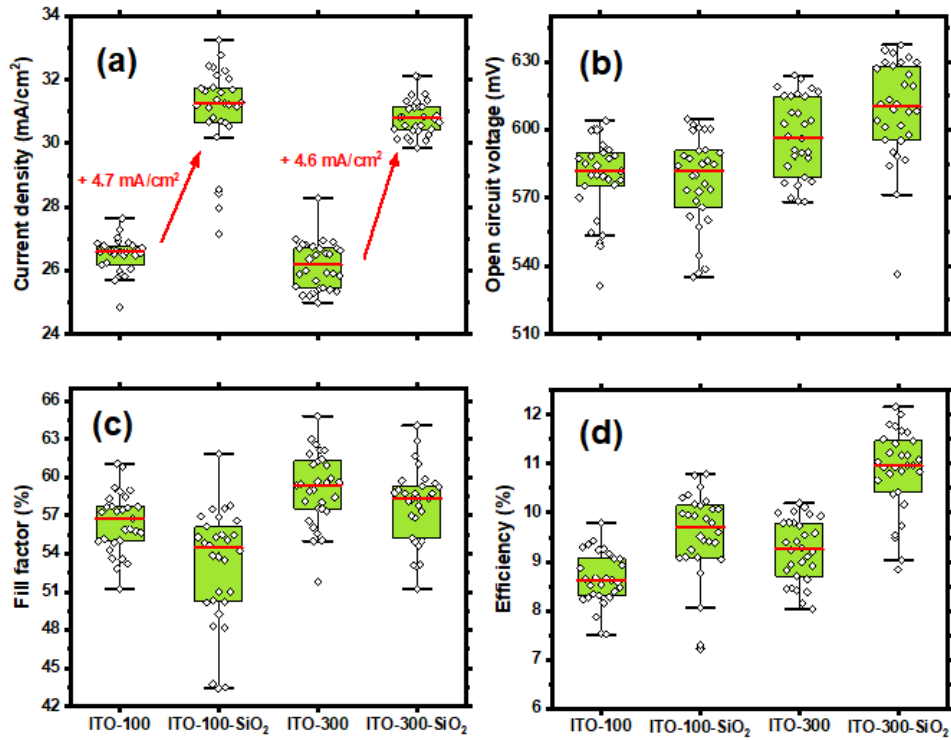


Figure 6-3. Statistic distribution (including three batches of samples) of the front PV performance

n is the ideality factor, kT/q is the thermal voltage, and j_0 is the dark saturation current density. We can estimate the front V_{oc} gain of ITO-100-SiO₂ that can be attributed to the j_{sc} increase of the solar cells in the following way: Set n to constant 2 (Table 6-1 shows that the extracted n is 1.9-2.0), kT/q equals 0.0259 V at room temperature, put j_{sc} of 26.7 mA/cm² into the formula (6-1), and adjusting j_0 until V_{oc} equals 579 mV we obtain $j_0 = 3.65 \text{ E-3 mA/cm}^2$ for ITO-100. To estimate the V_{oc} of ITO-100-SiO₂ that relates to the j_{sc} increase, presume j_0 is unchanged when the ITO thickness is the same. Using the obtained j_0 of 3.65 E-3 mA/cm² and j_{sc} of 31.1 mA/cm² on the right side of equation (6-1), the estimated V_{oc} is 587 mV for ITO-100-SiO₂. That is close to the experimental 584 mV of ITO-100-SiO₂. In the same way, on ITO-300, the fitted j_0 is 2.55 E-3 mA/cm², and the estimated V_{oc} for ITO-300-SiO₂ is 605 mV, also very close to the experimental 608 mV. From this rough estimation, the V_{oc} gain is fully attributed to the j_{sc} increase, and the deviation may come from the inaccuracy in the ideality factor n . Section 5.2 has discussed the V_{oc} difference between ITO-100 and ITO-300. ITO-300 has a higher V_{oc} than ITO-100 because of the B-M shift in the ITO layers. Here it needs to clarify why we do not use the j_0 values extracted in Table 6-1. These values come from one diode model. We calculate them by fitting the dark IV curves with the origin method. The fitting covers hundreds of data points to make the calculation IV curve align with the experiment IV curve by the regression method. But one diode model has limitations. It cannot be put into every estimation with a good fitting. Using those values in the V_{oc} calculation makes absurd results. But it does not mean the V_{oc} calculations are wrong. To link to specific physical meanings, a model needs to adapt to the specific circumstances. Here the V_{oc} estimation uses PV parameters extracted from light IV curves. The fitted j_0 are two orders of magnitude higher than the ones in Table 6-1. Because those j_0 values only fit one data point, linking j_{sc} and V_{oc} ,

there is no specific 'physical meaning' for those j_0 values. The fitting between experiment IV curves and theoretical IV curves that use those j_0 must be very poor. But when estimating just one data point of V_{oc} , those j_0 values give reasonable results.

The front fill factor FF exhibits a fluctuation according to Table 6-1. Compared to the corresponding reference solar cells, the FF of ITO-100-SiO₂ decreases by 2.1% while ITO-300-SiO₂ increases by 0.6%. Judging by the statistic distribution of the front PV performance in Figure 6-3, the front FF illustrates a decreasing trend for the BSTUT CIGSe solar cells with NPs. The front FF drops slightly after the SiO₂ insertion due to the reduction of R_{sh} . Overall, the NPs enhance the front Eff from 8.8% to 10.0% on 100 nm ITO and from 9.6% to 11.4% on 300 nm ITO, manifesting beneficial light trapping effects when the BSTUT CIGSe SCs are under front illumination.

Other than the optical light trapping effects, the electrical passivation effects of the NPs also need to be considered carefully. Table 6-1 summarizes the ideality factor n , dark saturation current density j_0 , series resistance R_s , shunt resistance R_{sh} , carrier density N_{cv} , width of space charge region W_{SCR} at 0 bias, and contact potential difference V_D of the diodes without/with SiO₂ NPs. After the SiO₂ insertion, n is almost unchanged on 100 nm ITO substrates while decreasing slightly on 300 nm ITO, which implies the recombination type/degree changes very little on both ITO thicknesses. However, the decrease of j_0 suggests that the recombination at the CIGSe/ITO interface decreases slightly. For unknown reason, the R_s and R_{sh} decrease after the SiO₂ insertion. That might imply that the one-diode model does not fit the SiO₂ passivated samples. N_{cv} , W_{SCR} , and V_D deduced from the CV characteristics imply a decreased built-in electric field in the devices, which is against the V_{oc} enhancement of the SiO₂ patterned solar cells. This contradiction again suggests the one-diode model cannot explain the enhanced PV performance here. Judging from those diode parameters and CV results, we cannot estimate the passivation effects of the SiO₂ correctly. According to conclusions obtained in chapter 4, passivating the CIGSe/ITO interface is detrimental to the PV performance of the solar cells. Here the SiO₂ NPs demonstrate beneficial effects for the solar cells, the reason might be that the 57% contact ratio between CIGSe and ITO is high (higher than all the tested ratios in chapter 4), so the passivation effects of SiO₂ NPs are trivial. The light trapping effects dominate the PV performance of the solar cells with SiO₂ NPs.

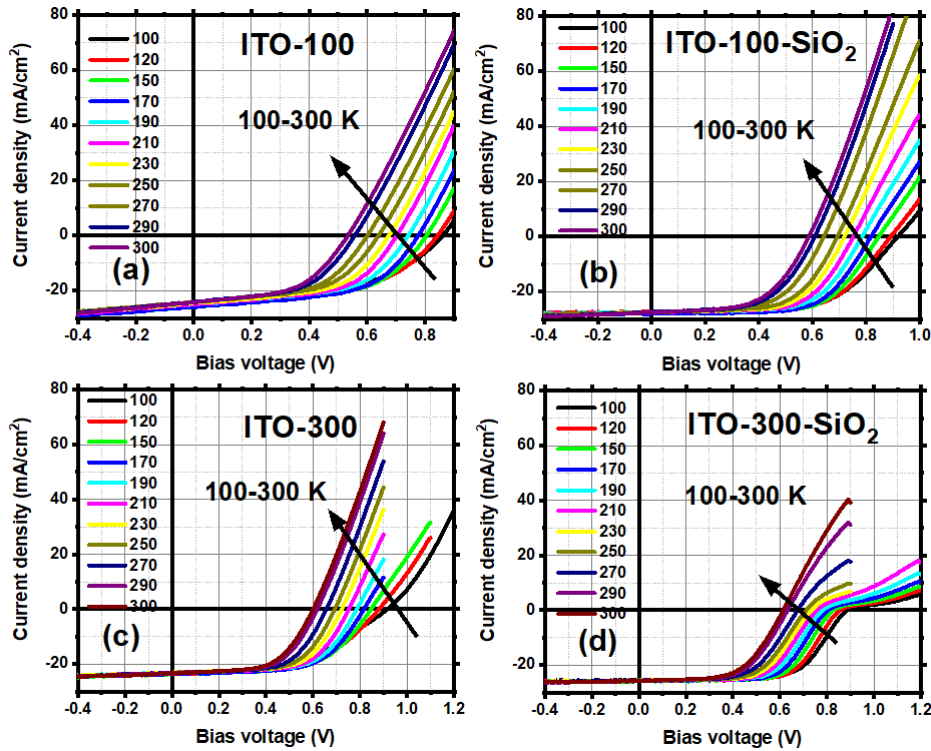


Figure 6-4. IVT characteristics of the BSTUT CIGSe solar cells without/with SiO_2 NPs

We carry out IVT characteristics of the solar cells to explore the E_h change at the CIGSe/ITO interface, as shown in Figure 6-4. Firstly, ITO-100 exhibits no roll-over effects of the IV curves under low temperatures. However, ITO-300 reveals a slight kink when the temperature is reduced to 110 K. Unlike the TD-ROE that bends the IV curves in the first quadrant, the kinked IV curves induce an S-shape in the fourth quadrant. According to reference [100], the kinked IV curve is attributed to a positive conduction band offset for photon current. In our case, the thicker ITO has a smaller W_{ITO} . When the temperature decreases, the Fermi level of CIGSe becomes lower and E_g widens, so the conduction band offset also increase, and then the kink in IV shows up.

Secondly, compared to ITO-100, Figure 6-4 (b) illustrates a slight TD-ROE for ITO-100- SiO_2 when the temperature is lower than 150 K. The low-temperature IV curves of ITO-100- SiO_2 show a good rectifying effect of the device, but we can still distinguish a slight bending in the first quadrant. That is consistent with the results observed in section 4.1.2, where a passivated back interface increases the T_r . The passivation effects can be seen more clearly on 300 nm ITO: compared to ITO-300, ITO-300- SiO_2 has a much higher T_r of 290 K. Comparing the T_r change before and after the SiO_2 NPs insertion, solar cells on 300 nm ITO are far more sensitive than on 100 nm ITO. Judging by the slight increase of T_r for the TD-ROE, the $E_{CIGSe/ITO}$ increases slightly with the SiO_2 NPs passivation. However, the increased $E_{CIGSe/ITO}$ is not significant to influence the collection process of photogenerated carriers and deteriorate the PV performance of the solar cells. The light trapping effects of the SiO_2 NPs dominate the PV performance of the solar cells.

In summary, we can observe a TD-ROE in IV curves of the SiO₂ patterned samples at low temperatures. The increasing T_r implies that the SiO₂ NPs passivate the CIGSe/ITO interface slightly, but the light trapping effects of the NPs dominate the solar cell performance.

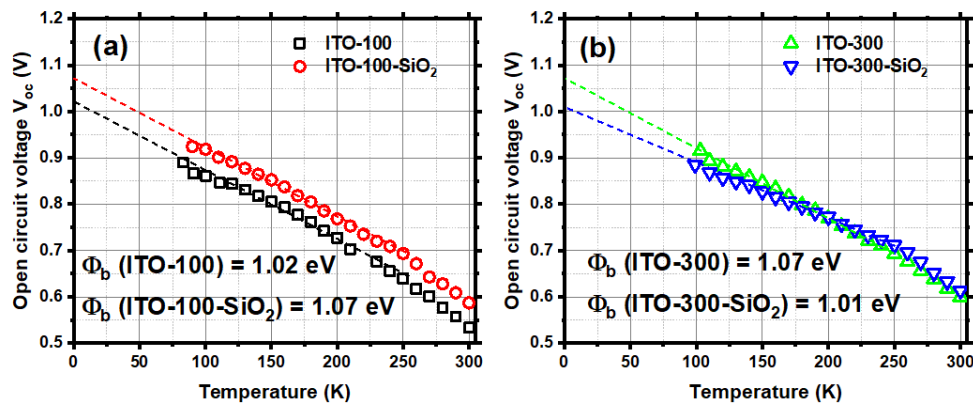


Figure 6-5. V_{oc} dependent on the temperature of the BSTUT CIGSe solar cells with/without SiO₂ NPs

As shown in Figure 6-5, we extract the V_{oc} dependent on temperature T ($V_{oc}-T$) to quantify the $E_{CIGSe/ITO}$ change at the CIGSe/ITO interface. Compared to ITO-300, the Φ_b of ITO-300-SiO₂ decreases from 1.07 to 1.01 eV. That is consistent with the results found in section 4.1.2: the passivation increases $E_{CIGSe/ITO}$ on 300 nm ITO and decreases Φ_b of the diodes. Interestingly, we can separate the linear fitting curve (blue dashes) of $V_{oc}-T$ on ITO-300-SiO₂ into two regions: 250-300 K and 150-250 K. In the 250-300 K region, the V_{oc} of ITO-300-SiO₂ is higher than for ITO-300, while in the 150-300 K region, the V_{oc} of ITO-300 exceeds ITO-300-SiO₂. According to Elanzeery et al., “a different slope of the $V_{oc}-T$ leads to different intercept with the y-axis which implies the recombination mechanisms are different. If the recombination mainly happens in the bulk, Φ_b is more likely to approach E_g of the CIGSe absorber. If the recombination mainly happens at the interfaces, Φ_b is more likely to deviate (smaller or bigger) from the E_g .” [146] In our case, the slope of $V_{oc}-T$ changes in the low-temperature range, which means the location (bulk or interface) where recombination mainly happens changes when the temperature decreases. Estimating from the EQE, the E_g is 1.14 eV for all samples. Therefore, the dominating recombination in ITO-300-SiO₂ is in the bulk when the temperature is 250-300 K ($\Phi_b = 1.15$ eV when $T = 0$ K), and the dominating recombination happens at the interfaces of the solar cell at 100-250 K ($\Phi_b = 1.01$ eV when $T = 0$ K).

For the solar cells on 100 nm ITO, Φ_b is 1.02 eV. This is smaller than 1.07 eV for ITO-300 due to the B-M shift in the thicker ITO layer, which is consistent with the conclusion in section 5.2.2. However, compared to ITO-100, ITO-100-SiO₂ has a higher Φ_b of 1.07 eV. It is against the results in section 4.1.2. According to SCAPS simulations in section 4.1.2, a reduced S_b at the CIGSe/ITO interface shall increase $E_{CIGSe/ITO}$ hence decrease Φ_b of the solar cells. For ITO-100-SiO₂, the j_{sc} increase is consistent with the SCAPS simulations, as a lower S_b leads to a j_{sc} increase for all E_h values. But why the SiO₂ NPs decrease the $E_{CIGSe/ITO}$ needs further investigations. One possible reason is that the optical light trapping effects of the SiO₂ NPs overwhelm their passivation effects, which electrical simulations cannot predict. The slope of ITO-100 and ITO-100-SiO₂ in the low-temperature range is the same, which might imply the interface recombination is only decreased slightly by the SiO₂ NPs.

In summary, on 300 nm ITO, the SiO₂ NPs passivate the CIGSe/ITO interface and increases the $E_{CIGSe/ITO}$ by 0.06 eV. So Φ_b of ITO-300-SiO₂ decreases from 1.07 to 1.01 eV. That is consistent with the SCAPS simulation in section 4.1.3. However, judging by the V_{oc} - T slope, the SiO₂ NPs might passivate the CIGSe/ITO interface slightly. Furthermore, $E_{CIGSe/ITO}$ on 100 nm ITO decreases with NP integration, which contradicts to our previous simulation. Because the front j_{sc} increase fits the front V_{oc} gain closely by equation (6-1), we deduce that the optical light trapping effects of SiO₂ NPs dominate the PV performance of ITO-100-SiO₂.

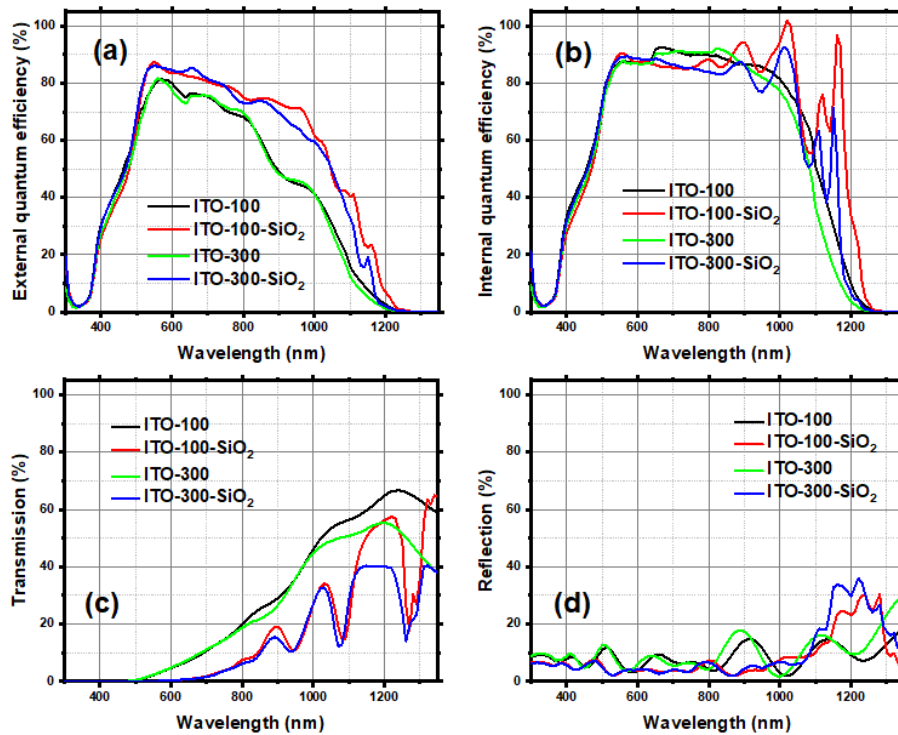


Figure 6-6. The front (a) external quantum efficiency (b) internal quantum efficiency (c) transmission and (d) reflection of the BSTUT CIGSe solar cells with/without SiO₂ NPs

We employ external quantum efficiency (EQE) and transmission/reflection (T/R) characterizations to help understand the optical light trapping effects of the SiO₂ NPs and the mechanism of the j_{sc} gain. Generally, EQE measurements are dimensionless, i.e., they do not count the area of the cells. So, the integrated current density j_{EQE} estimated by equation (1-24) is considered an independent method to cross-check the j_{sc} measured by IV. As denoted in Table 6-1, the enhancement of the j_{EQE} exhibits a consistent increase with the j_{sc} of the solar cells, which confirms the light trapping effects of SiO₂ NPs in the BSTUT CIGSe solar cells.

Firstly, we compare ITO-100 and ITO-100-SiO₂ to see the light trapping effects of SiO₂ NPs on 100 nm ITO. As illustrated in Figure 6-6 (a), ITO-100-SiO₂ shows an overall higher EQE than ITO-100 in the wavelength range of 500-1350 nm. That can be correlated to the lowered T/R of ITO-100-SiO₂, as Figure 6-6 (c) and (d) display in red. The T/R of ITO-100-SiO₂ is lower than for ITO-100 in the wavelength range of 500-1350 nm. At 1120 and 1180 nm wavelengths, we observe two pronounced EQE peaks. In Figure 6-6 (b), we can see those two peaks more clearly in the internal quantum efficiency (IQE) obtained from equation (1-25). Given the transparent properties of BSTUT CIGSe solar cells, we have to consider the transmitted light when calculating the IQE of the cells. According to Yin et al.'s simulation, those two peaks are

due to the waveguide modes of the SiO₂ NPs [22]. In transmission, we recognize two valleys at 1085 and 1280 nm wavelengths, which can be attributed to the scattering interferences (or Fabry-Perot interferences) induced by the NPs. In short, the SiO₂ NPs diminish the T/R and enhance the light absorption in the BSTUT SCs via waveguide modes.

Secondly, we compare ITO-100 (in black) with ITO-300 (in green) to see how the ITO thickness influences the EQE of the solar cells. In the wavelength range of 300-510 nm, the EQE curves overlap with tiny deviation. The reason is that the window layers ZnO: Al/i-ZnO and the passivation layer CdS absorb the light in this wavelength range and ITO-100 and ITO-300 have the same device structure. We observe a higher EQE deviation in the 510-990 nm wavelength range due to the Fabry-Perot interferences tuned by the ITO thickness. In the 990-1350 nm wavelength range, ITO-100 exhibits a higher EQE than ITO-300. According to section 5.2, the reason is that ITO-100 has lower recombination at the CIGSe/ITO interface and lower parasitic absorption in the ITO layer. Between ITO-100 and ITO-300, the difference in j_{EQE} here is smaller than in section 5.2.2. That is attributed to the difference between batch-to-batch ultrathin absorbers. The CGI, GGI, and thickness of the CIGSe here are 0.83, 0.33, and 468 nm, respectively. The absorbers in section 5.2.2 are 0.87, 0.32, and 500 nm, respectively. The overall trend of EQE in those two batches is the same. The cut-off wavelength of the EQE is the same for ITO-100 and ITO-300, confirming that the bandgap E_g of their absorbers is the same at 1.12 eV. In Figure 6-6 (c), ITO-100 (black) manifests higher T than ITO-300, especially in the long wavelength range. The reason is that ITO-100 has less severe parasitic absorption in the ITO layer.

Thirdly, compared to ITO-300, ITO-300-SiO₂ has an overall higher EQE and lower T/R . The EQE of ITO-300-SiO₂ is higher than for ITO-300 in the wavelength range of 510-1350 nm, where SiO₂ NPs reduced the T/R of the solar cells. When comparing ITO-100-SiO₂ and ITO-300-SiO₂ (red and blue lines), we notice their EQEs overlap in the 300-750 nm range. The reason is that their window/passivation layers are the same. In the 750-1350 nm wavelength range, ITO-100-SiO₂ shows higher EQE than ITO-300-SiO₂, implying the SiO₂ NPs work better on 100 nm ITO, especially in the long wavelength range. The waveguide mode-enhanced EQE manifests two peaks (1120 nm and 1180 nm) for ITO-100-SiO₂, whereas ITO-300-SiO₂ has only one. The stronger parasitic absorption of the thicker ITO can also be seen in the transmission, as the blue line is flatter in the long wavelength range in Figure 6-6 (c).

In conclusion, the SiO₂ NPs have improved the front PV performance of the BSTUT CIGSe solar cells via light trapping effects. The SiO₂ NPs decrease the T/R of the patterned solar cells through waveguide modes, and increase the light absorption in the devices, especially in the long wavelength range. In addition, the SiO₂ NPs reveal better light trapping effects on 100 nm ITO because thinner ITO has lower back recombination and weaker parasitic absorption.

6.3 Rear illumination characteristics

Table 6-2. Rear PV parameters, EQE-integrated equivalent current density j_{EQE} , diode parameters of the devices, N_{CV} at 0 bias, space charge region width W_{SCR} , and contact potential difference V_D of the SCs with/without SiO_2 NPs

Sample name	j_{sc} (mA/cm ²)	j_{EQE} (mA/cm ²)	V_{oc} (mV)	FF (%)	Eff (%)	n	j_0 (E-8 A/cm ²)	R_s (Ω cm ²)	R_{sh} (Ω cm ²)	N_{cv} (E15 cm ⁻³)	W_{SCR} (nm)	V_D (mV)
ITO-100R	21.3±0.1	20.5	555±22	37±1	4.4±0.3	1.9	10.0	4.5	837	6.1	509	710
ITO-100-SiO ₂ R	28.7±0.6	28.2	562±16	44±5	7.0±0.8	1.9	8.1	4.1	442	6.2	456	520
ITO-300R	19.8±0.7	20.2	564±119	37±5	4.1±1.3	2.0	8.0	5.7	406	6.1	482	620
ITO-300-SiO ₂ R	26.2±1.1	25.1	584±13	56±3	8.5±0.5	1.9	3.9	3.2	325	6.2	468	530

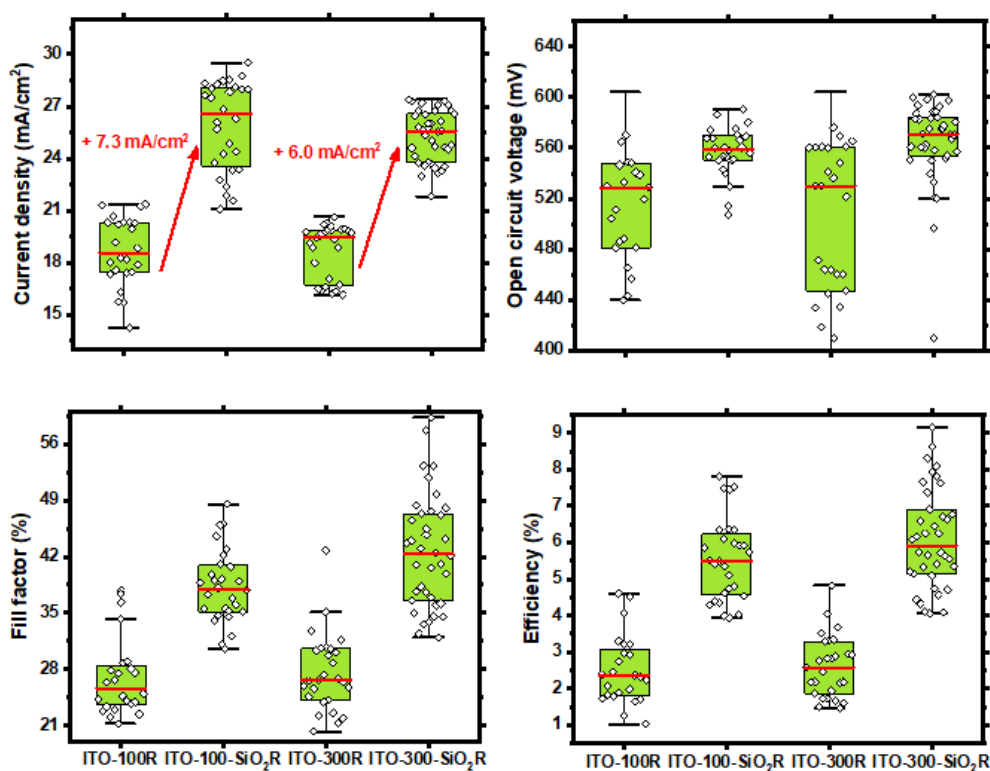


Figure 6-7. Statistic distribution (includes three batches of samples) of the PV parameters under rear illumination

Figure 6-7 indicates that the SiO_2 NPs level up all of the rear PV parameters of the BSTUT CIGSe solar cells. Compared to the corresponding references in Table 6-2, the rear j_{sc} of ITO-100- SiO_2 increases by 7.4 mA/cm², and for ITO-300- SiO_2 it increases by 6.4 mA/cm². That is higher than the maximum gain of 3.9 mA/cm² predicted in the optical simulation (with an Ag reflector on the AZO layer side). It implies that the SiO_2 NPs are not only beneficial for the solar cells in terms of optical light trapping but also contribute to the collection efficiency of the photogenerated carriers under rear illumination [22]. The increasing rear FF confirms that the SiO_2 NPs improve the collection efficiency of photogenerated carriers on both ITO thicknesses. Compared to the decreased front FF, the improved rear FF indicates that the light trapping mechanism of the SiO_2 NPs is different when the illumination direction changes.

For the rear V_{oc} of the SCs patterned with SiO_2 NPs, we also use equation (6-1) to estimate the V_{oc} gain resulting from the j_{sc} increase. For ITO-100R, j_0 is fitted to be $4.6 \text{ E-}3 \text{ mA/cm}^2$, and the V_{oc} of ITO-100- SiO_2R should be 571 mV, which is 9 mV higher than the experimental 562 mV. On ITO-300R, j_0 is fitted to be $3.6 \text{ E-}3 \text{ mA/cm}^2$, and the ITO-300- SiO_2R should be 579 mV, which is 5 mV lower than the experimental 584 mV. The deviation between calculated V_{oc} and experiment V_{oc} comes from the ideality factor n . n originates from dark IV curves, so there is no difference between front and rear illumination estimation here. When the rear illumination reverses the distribution of photogenerated carriers in the solar cells, n may deviate from 2 as the recombination also changes. Overall, the V_{oc} gain mainly originates from the light trapping effects of the SiO_2 NPs. Likewise, under rear illumination, ITO-300R illustrates higher V_{oc} than ITO-100R due to the B-M shift [147]. However, the rear j_{sc} of ITO-300R is slightly lower than ITO-100R, and ITO-300- SiO_2R is lower than ITO-100- SiO_2R . The reason is that thicker ITO induces higher parasitic absorption in the back contact layer. Overall, the rear conversion efficiency is boosted to 7.0% from 4.4% on 100 nm ITO and to 8.5% from 4.1% on 300 nm ITO, corresponding to 59% and 107% relative enhancement, respectively.

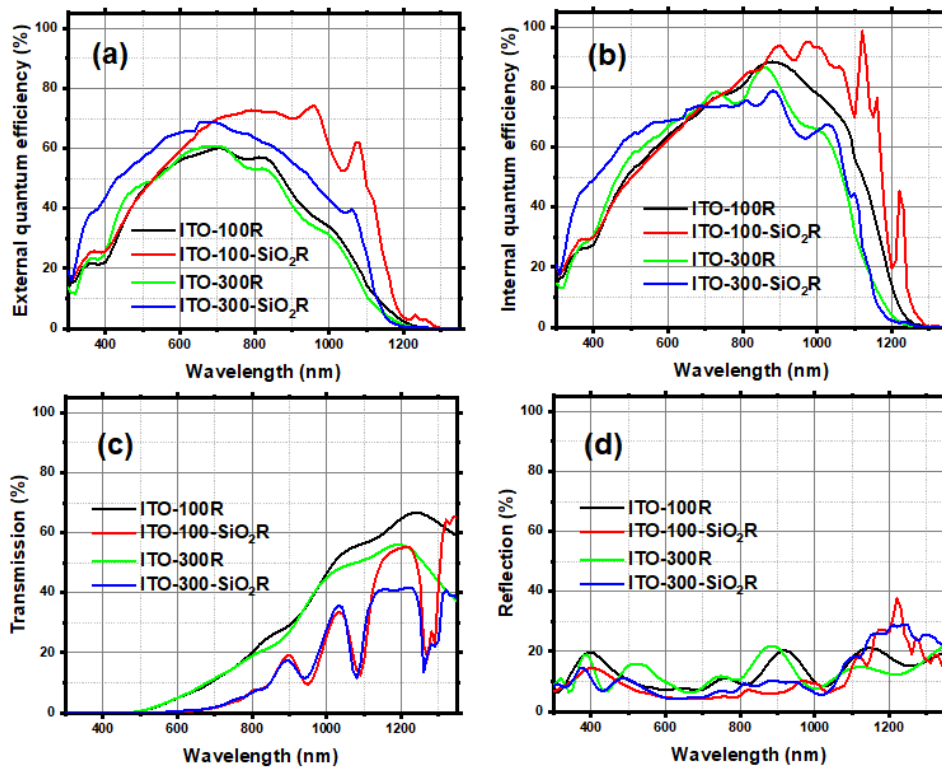


Figure 6-8. Comparison of the (a) EQE (external quantum efficiency), (b) IQE (internal quantum efficiency), (c) transmission and (d) reflection of the BSTUT CIGSe solar cells without/with NPs under rear illumination

As illustrated in Figure 6-8, we characterize the rear EQE, IQE, and T/R of the BSTUT CIGSe SCs to clarify the origin of the increased rear j_{sc} . In Figure 6-8 (a), compared to ITO-100R (black line), ITO-300R (green line) has a higher EQE in the wavelength range of 340-520 nm. The reason is that ITO-300R has a wider E_g than ITO-100R in the ITO layer due to the B-M shift. However, ITO-300R exhibits lower EQE in the wavelength range from 730-1260 nm. The reason is that thicker ITO induces stronger parasitic absorption, especially in the long wavelength range, as the lower T of ITO-300R illustrates in the wavelength range of 1050-

1350 nm (see Figure 6-8 (c)). We also observe Fabry-Perot interference peaks in the reflection curves (Figure 6-8 (d)).

Now we compare ITO-100-SiO₂R with ITO-100R to explore the light trapping effects of the SiO₂ NPs on 100 nm ITO substrates. ITO-100-SiO₂R demonstrates an overall higher EQE than ITO-100R. At 960 and 1080 nm wavelengths, two pronounced EQE peaks show up, corresponding to the waveguide modes of the SiO₂ NPs. The red lines in Figure 6-8 (c) and (d) illustrate that the SiO₂ NPs suppress the T/R of the solar cells. In Figure 6-8 (b), we can see that ITO-100-SiO₂R exhibits two peaks in the long wavelength range that are much higher than ITO-100, indicating the SiO₂ NPs improve the collection efficiency of photogenerated carriers. In the rear reflection (Figure 6-8 (d)), at around 400 nm wavelength, ITO-100R and ITO-100-SiO₂R both exhibit a peak of Fabry-Perot interference. They are aligned with each other because their ITO thickness is the same.

Comparing ITO-300-SiO₂R with ITO-300R, as displayed in Figure 6-8 (d), the rear reflection of the samples is tuned by the NPs in the short wavelength range. The Fabry-Perot interference peaks at 380 and 520 nm appear shifted. The T of the solar cells is suppressed by the NPs in ITO-300-SiO₂R, as illustrated in Figure 6-8 (c). Surprisingly, the IQE on 300 nm ITO is not increasing as on 100 nm ITO, see Figure 6-8 (b). It implies that the SiO₂ NPs do not improve the collection efficiency of photogenerated carriers on 300 nm ITO. Overall, the rear EQE on 300 nm ITO is enhanced by the light trapping effects of the SiO₂ NPs.

Compared to ITO-100-SiO₂R (red), ITO-300-SiO₂R (blue) exhibits higher EQE in the 300-630 nm wavelength range. The reason is that ITO-300-SiO₂ has a wider E_g in ITO due to the B-M shift. However, in the 670-1300 nm wavelength range, ITO-100-SiO₂R shows a much higher EQE because 300 nm ITO has a severer parasitic absorption in this wavelength range. The waveguide mode enhancement at 1080 nm is much higher on ITO-100-SiO₂R than on ITO-300-SiO₂R, as seen in Figure 6-8 (b). Overall, ITO-100-SiO₂R resulted in the highest j_{EQE} of 28.2 mA/cm². Besides, Fabry-Perot interferences dominate the reflection of the solar cells in the 300-750 nm wavelength range. While in the 600-1350 nm wavelength range, the transmission valleys of ITO-300-SiO₂R and ITO-100-SiO₂R align with each other. That is because their NPs having the same height, size and pitch.

In summary, SiO₂ NPs exhibit pronounced light trapping effects on both ITO thicknesses. After the SiO₂ NPs insertion, the rear j_{sc} of the solar cells increases by 6.4-7.4 mA/cm², which is higher than the front j_{sc} gain and even higher than the simulated expectation. It implies that the SiO₂ NPs can trap light in the solar cells and enhance the collection efficiency of the photogenerated carriers under rear illumination. Besides, the SiO₂ NPs exhibit better light trapping effects on thinner ITO back contacts because thinner ITO has less parasitic absorption.

6.3 Light trapping mechanism under front and rear illumination

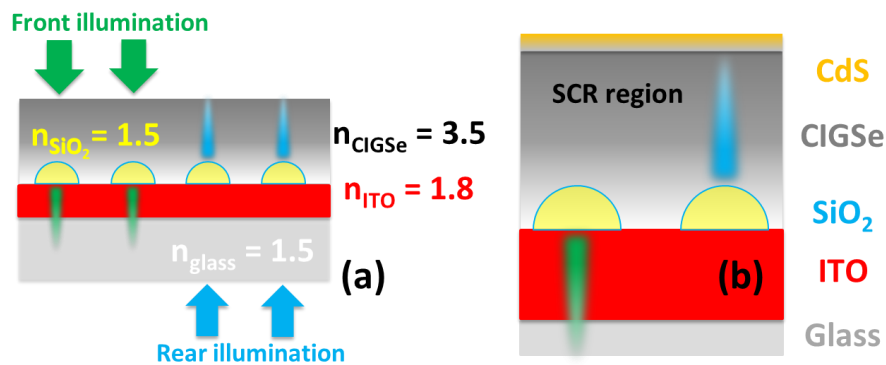


Figure 6-9. Jet-like distribution of the electric field induced by the forward scattering of the SiO_2 NPs in the BSTUT CIGSe solar cells under front and rear illumination

To better demonstrate why the rear j_{sc} gain is higher than the front j_{sc} increase in the same solar cell, we need to compare the light trapping mechanism under front and rear illumination. Apart from the waveguide modes, the NPs also induce a forward scattering whose electric field distribution is jet-like in front of the NPs [22]. For the front (green colour) and rear (blue colour) illumination, Figure 6-9 denotes the extension of the jet-like forward scattering.

Under front illumination, the jet-like tail guides the electric field into the ITO layer. However, as manifested in Figure 6-9 (b), the enhanced electric field under rear illumination is close to the SCR where the photogenerated carriers are more effectively separated. Therefore, the jet-like tail under rear light is more beneficial for the solar cells. The jet-like forward scattering improves the collection efficiency only under rear illumination. That is why the front FF decreases while the rear FF increases after the SiO_2 NPs insertion. Also because of this, the relative j_{sc} gain is higher under rear illumination.

6.4 Summary and conclusion

This chapter focused on inserting SiO₂ NPs to optimize the front and rear PV performance of BSTUT CIGSe solar cells. We find:

- (1) The front PV performance of the solar cells is enhanced by the waveguide modes of the NPs. The front j_{sc} increase (4.1-4.4 mA/cm²) fits the optical simulation (4.2 mA/cm²) well;
- (2) The rear PV performance of the BSTUT CIGSe is also enhanced by the SiO₂ NPs. The NPs increase the rear j_{sc} by 6.4-7.4 mA/cm². The j_{sc} gain under rear illumination is higher than the front j_{sc} increase and the simulated prediction.
- (3) Two reasons lead to a higher rear than front j_{sc} gain. Optically, more light is localized inside the absorber layer due to the scattering of the NPs. Electrically, the jet-like forward scattering of the SiO₂ NPs can be exploited for an improved collection of photogenerated carriers;
- (4) The passivation effects of the SiO₂ NPs at the CIGSe/ITO interface are trivial. The barrier $E_{CIGSe/ITO}$ is increased on ITO-300 but decreased slightly on ITO-100. Yet the front and rear PV performance of the solar cells is enhanced by the NPs on both ITO thicknesses. Based on the quantitative fitting between the j_{sc} increase and the V_{oc} gain, we deduce that the optical light trapping effects of the SiO₂ NPs dominate the electrical passivation effects in the BSTUT CIGSe solar cells.

Those experimental results verified the optical prediction of light trapping with SiO₂ NPs in BSTUT SCs. We proved the feasibility of nano-optical light management with NPs in bifacial semi-transparent solar cells.

Chapter 7 Summary and outlook

7.1 Summary

The ultimate goal of this work is to achieve bifacial semi-transparent ultrathin (BSTUT) CIGSe solar cells with comparable or even better performance than the Mo-based counterparts. This allows less raw material consumption in solar cell fabrication and high-efficiency light usage in solar panel installation. Co-evaporating the CIGSe with good quality and without deteriorating the conductivity of the transparent back-contact layer, extracting the photogenerated carriers effectively and increasing the insufficient light absorption are the main challenges hindering the achievement of high efficiency for BSTUT CIGSe solar cells. This thesis solves those challenges in sequence: chapters 2-3 focus on the first challenge by evaluating the front photovoltaic (PV) performance of the solar cells, chapter 4 is about the carrier transportation at the CIGSe/ITO interface, and chapter 5-6 evaluate both front and rear illumination PV parameters to solve the third challenge. The following will summarize what was achieved in experiments/simulations to provide profound insights into the BSTUT CIGSe solar cells.

The high quality of CIGSe absorbers is a basis for further performance optimization. During the CIGSe co-evaporation, the substrate temperature is lowered to 450 °C to avoid increasing the resistance of the back contact. Na incorporation is critical for the CIGSe quality, but the decreased substrate temperature limits the Na quantity/depth that can diffuse into the absorber. Therefore, chapter 2 optimizes the Na doping method for the ultrathin CIGSe absorbers. We compare the PV parameters of ultrathin CIGSe solar cells that use diffusion of Na from soda-lime glass (SLG), a NaF precursor, NaF post-deposition treatment (PDT) or a NaF precursor plus PDT Na-doping. It was revealed that the NaF precursor plus PDT method dopes the highest Na quantity into the CIGSe, but solar cells with NaF PDT doping show the best PV performance. Based on this, chapter 3 optimizes the NaF dose and characterizes the solar cells in detail to clear the mechanism of NaF PDT. Aided by multiple characterization methods, the working mechanism of the NaF PDT doping can be summarized in two aspects. (1) Increasing carrier density N_A hence levelling up the contact potential difference V_D at the CIGSe/CdS junction; (2) Increasing the back recombination velocity S_b at the CIGSe/ITO interface hence decreasing the back barrier height $E_{CIGSe/ITO}$ for holes. The simulations in SCAPS verify those two mechanisms consistently.

Effectively extracting the photogenerated carriers is another challenge for achieving high-performance BSTUT CIGSe solar cells. Passivation with SiO₂ point-contacts has been proven beneficial for the Mo-based CIGSe solar cells because it suppresses the recombination of the photogenerated carriers at the CIGSe/Mo interface. However, when chapter 4 utilizes SiO₂ point-contacts to modify the back interfaces on Mo and ITO substrates, the SiO₂ passivation reveals beneficial effects for Mo-based while detrimental ones for the ITO-based ultrathin CIGSe solar cells. The passivation at the CIGSe/ITO interface deteriorating the performance for the latter ones is consistent with the findings in chapter 1 that an increased S_b diminishes

the effective E_h at the CIGSe/ITO interface. Understanding the controversial role of passivation at the CIGSe/ITO and CIGSe/Mo interfaces requires further investigation. SCAPS simulations find that the E_h decides the role of S_b in the ultrathin CIGSe solar cells. If $E_h < 0.17$ eV (quasi-Ohmic contact), a higher S_b is detrimental for the solar cells, so the SiO_2 passivation increases the Eff of the solar cells. When $E_h > 0.17$ eV (Schottky contact), a higher S_b is desirable for the photogenerated carriers to go through the back barrier, so the passivation deteriorates the Eff of the solar cells. Therefore, passivation deteriorates the performance of the ITO-based ultrathin CIGSe solar cells because the CIGSe/ITO interface is a Schottky-like back contact.

The previous chapters evaluate the front PV performance of the ITO-based solar cells. However, the rear PV parameters are also critical for a high-performance BSTUT CIGSe solar cell. Under rear illumination, the distribution of the photogenerated carriers is reversed in the absorbers. A higher density of photogenerated carriers close to the CIGSe/ITO interface induces a different recombination behaviour in the devices, which poses extra challenges for the performance optimization of the solar cells. Chapter 5 optimizes the front and rear efficiency of ITO-based ultrathin CIGSe on different glass types, ITO thicknesses, and for various NaF PDT doses. The BSTUT solar cells on SLG show higher front Eff due to the extra incorporation of Na but lower rear Eff because of lower glass transmission. A thicker ITO is preferred for a higher V_{oc} under front and rear illumination due to the B-M shift in the ITO layer. 400 nm ITO has a 0.14 eV wider bandgap than 100 nm ITO and provides 50 mV higher front V_{oc} for the solar cells. On the other hand, the thicker ITO induces more severe parasitic absorption, thus decreasing the rear j_{sc} of the solar cells. For different NaF PDT doses, the front and rear PV performance show a parallel trend. Under the optimal conditions (300 nm ITO on alkali-free glass with 4 mg NaF for the CIGSe PDT), we achieved 11.8% front and 6.4% rear efficiency, which shows a promising future for BSTUT CIGSe solar cells.

Insufficient light absorption in the ultrathin CIGSe layer leaves much room for PV performance optimization by light trapping. According to Yin's optical simulations, inserting SiO_2 nanoparticles (NPs) at the CIGSe/ITO interface can increase the front j_{sc} by maximum 4.2 mA/cm^2 . Chapter 6 inserts SiO_2 NPs at the back interface to increase the light absorption in the ultrathin CIGSe. For the BSTUT CIGSe solar cells with SiO_2 NPs, the front j_{sc} shows a 4.1-4.4 mA/cm^2 increase due to emerging waveguide modes and light trapping in the absorber. This value is close to the 4.2 mA/cm^2 j_{sc} enhancement from simulations. Under rear illumination, however, the j_{sc} shows a 6.4-7.4 mA/cm^2 increase, which is higher than the front j_{sc} gain and the predicted values. It is because the SiO_2 NPs additionally enhance the light absorption via jet-like forward scattering towards the absorber layer, also leading to an improved collection efficiency of photogenerated carriers. Judging from the levelled-up front and rear PV performance, we proved that inserting SiO_2 NPs is a convenient light management strategy for BSTUT CIGSe solar cells.

7.2 Outlook for bifacial semi-transparent ultrathin Cu(In, Ga)Se₂ solar cells

In this thesis, the optimal efficiency of 12.9% shows a promising future for ITO-based BSTUT CIGSe solar cells. Compared to state-of-the-art ultrathin CIGSe on Mo substrates with 15.2% efficiency, there is still plenty room for improvement of ITO-based bifacial CIGSe solar cells.

To name a few, firstly, the ultrathin absorbers can incorporate other alkali elements. For the standard absorber thickness of 2-3 μm , potassium doping has been proven beneficial for the absorber quality and V_{oc} of the solar cells. Further investigations are required to clarify the working mechanism of different alkali elements in the CIGSe solar cells.

Secondly, we can try to replace ITO substrates with other types of TCOs. ITO cannot tolerate high temperatures exceeding 510 $^{\circ}\text{C}$, which limits the maximum temperature for CIGSe co-evaporation. Also, the doping type of ITO is n-type, which naturally forms a heterojunction at the CIGSe/ITO back-contact, as CIGSe is p-type. Therefore, p-type back-contacts are worth exploring to replace the ITO substrates.

Thirdly, this thesis has shown that the V_{oc} of the solar cells is very sensitive to the back potential barrier $E_{\text{CIGSe/ITO}}$ as a tiny modification at the interface influences the V_{oc} tremendously. From this perspective, we can try other surface modification techniques like plasma cleaning, annealing of the back-contact, or inserting an additional layer at the CIGSe/ITO interface to diminish $E_{\text{CIGSe/ITO}}$. As the back barrier is sensitive to the morphology of the ITO layer, we can improve the crystal structure and surface work function of the back-contact to improve the V_{oc} of BSTUT CIGSe solar cells. Surface cleaning has the same effects as the crystalline improvement, which can modify the surface work function of the back-contact. As for inserting interfacial layers, we can adopt certain materials that have selective influences on carriers' transport to improve the collection efficiency of holes at the CIGSe/ITO back-contacts. Ultrathin CIGSe absorbers on Mo have achieved 733 mV in V_{oc} , which shows the potential V_{oc} of the solar cells with a reduced absorber thickness. This encourages us to improve the V_{oc} of our BSTUT CIGSe (650 mV) via the aspects mentioned previously.

Fourthly, like Mo-based ultrathin CIGSe solar cell, we can improve the Ga grading by optimizing the 3-stage co-evaporation process. The optimal Ga grading can provide field passivation effects, which are beneficial for the V_{oc} of the solar cells. Also, NP integration can increase the light absorption by trapping the light. According to optical simulations, the pitch, size and height of the SiO₂ NPs can be further optimized to achieve a higher j_{sc} for the solar cells. In addition, light trapping via nanoparticles can exceed the Lambertian limit, thus there is also plenty of room for j_{sc} improvement in ultrathin CIGSe solar cells.

Last but not least, given the high transparency of BSTUT CIGSe solar cells, it may be interesting to combine ultrathin CIGSe with other wide bandgap semiconductors like perovskite or Ag/S doped CuInSe materials to form a tandem solar cell.

In summary, for the BSTUT CIGSe solar cells, the Eff still has plenty room to improve in many aspects and the fabrication cost can be further reduced. We believe that BSTUT CIGSe solar

cells with a higher *Eff* and a lower fabrication cost are promising to have a place in the tremendous green energy market.

Appendix A – Acknowledgement

Life is a journey, and we are all passengers. Looking back at the last five years, the life of a PhD candidate is also a journey with tears and laughter, the journey with setbacks and progress. Most importantly, I had the luck to have my supervisors, tutors, friends, colleagues and families around me. My heart fills with gratitude for them.

Firstly, I am grateful to my supervisor Martina Schmid. I would not be here if she didn't offer me the opportunity in the first place. I am thankful to Guanchao Yin for guiding me through the darkest moments when I had trouble in my study. I am grateful to Sara El-Molla. She helped me settle down when I started my life in Duisburg. I am grateful to Tristan Köhler. He is the best engineer I have ever known. He coached me in all the machines I used and taught me about cooking and repairing the setups for solar cell cooking. I am grateful to Klaus Pärschke. He taught me how to use a step profiler, optical measurements, lab-view and running to keep fit. He showed me the fun of setting up a machine by applying physics. I am grateful for Heidi. She printed my first name card, made me a beautiful stark statue, and helped me with all the procedures in summer school. I am grateful to Florian Beineke. He helped me fix the bug in the LLS program, which is the eye for absorbers fabrication. I am thankful to Jan Lucaßen. He helped me with the CV setup, lab view and Matlab learning. He is such a close friend that I feel like sharing everything in my life. I am grateful to Yao Gao, my senior and a good friend. He helped me with the PS deposition and many enlightening discussions. I am thankful to Dr Mario Bomers. He taught me how to schedule time slots and clear my head to focus only on my goals. I am grateful for Dr Setareh Sedaghat. She showed me the simulation in COMSOL and helped me with SCAPS. I am grateful to Ming Song. She showed me the PS deposition. I am grateful to Camillo Hinz. He taught me how to use the Perkin Elmer for angle resolution measuring. I am grateful to Julius Kruij. He taught me IV measurements with angle resolution.

I feel lucky and thankful to have reliable and friendly companions for cooperation. I appreciate professor Albert Polman from AMOLF Netherland for supervising me in light trapping experiments. My gratitude to Nikolai Bart from Bochum University for helping me with the PL mapping. I am thankful to Alexander Poßberg from Duisburg-Essen University. He helped me with the XRD measurements. I am thankful to Qingqing Fu from Duisburg-Essen University for teaching me the importance of fonts and the thickness of lines in a poster. My thanks to Cecile Marcelot and Sophie Meuret from CECMS France. They helped me with the TEM characterizations. I am grateful to Stefan Tabernig from AMOLF Netherland. He helped me with the SiO₂ NPs fabrications and SEM characterizations. I am thankful to Dr Spodig Detlef who coached me with the SEM. I am thankful to Christian Kaufmann from HZB. He taught me experiments on NaF PDT and phase changes in chalcogenide.

Most importantly, I am honoured to receive a scholarship from the CSC (China scholarship council). I will forever be thankful for their support. I also had the luck to receive financial

support from the Graduate Grand from Udo Rasum, Duisburg-Essen University. For the TEM characterizations, the research leading to these results has received funding from the European Union Horizon 2020 research and innovation programme under grant agreement No. 823717 – ESTEEM3.

Lastly, I want to express my most warm gratitude to my family. My grandparents brought me up and encouraged me to go after my dreams. I know they would be happy to see me today. May they rest in peace. I love my parents and my little sister, who had done nothing but support me. I love my wife, Chen Chen. Without her, I would have given up a thousand times on this work already. I love my daughter Mucheng Li who is a new light in my life. I love you until the end of my time.

Romain Rolland once said that nobody is an isolated island, we are all bound in one society, and only cooperation and love can lead us to a bright future. I did not mention every people that helped me, but my heart is always grateful for your kindness and friendship. I am willing to help the people I meet to pass on kindness and gratitude.

Appendix B – Curriculum vitae

Experience

2017.9-present. PhD candidate in MultiOptiX, Experimental Physics, Duisburg-Essen University. Mainly research in ultrathin CIGSe thin film solar cells on In_2O_3 : Sn substrates.

2014.9-2017.7. Master candidate in Solar R&D, Condensed matter physics, Academic of Science, Shanghai University. Majored working on passivation and characterization of Si-based heterojunction solar cells.

2010.9-2014.7. Bachelor candidate. Micro-electronics, Academic of Science, Physics department, Shanghai University. Mainly learned Theoretical Mechanics, Electron dynamic mechanics, Quantum mechanics, Thermodynamic and statistical physics. The major course also included Semi-conductor physics and devices, Integrated circuit electronics.

Publications and conferences

1. Yong Li, Stefan W. Tabernig, Guanchao Yin, Albert Polman, Martina Schmid. Beyond light trapping benefits: the effect of SiO_2 nanoparticles in bifacial semi-transparent ultrathin CIGSe solar cells. Solar RRL, Accepted

2. Yong Li, Guanchao Yin, Ye Tu, Setareh Sedaghat, Yao Gao, and Martina Schmid. Ultrathin $\text{Cu}(\text{In,Ga})\text{Se}_2$ solar cells with a passivated back interface: a comparative study between Mo and In_2O_3 :Sn back contacts. ACS Appl. Energy Mater 5 (2022), 7956–7964

2. Yong Li, Guanchao Yin, Martina Schmid. Bifacial semi-transparent ultra-thin $\text{Cu}(\text{In,Ga})\text{Se}_2$ solar cells on ITO substrate: How ITO thickness and Na doping influence the performance. Solar Energy Materials & Solar Cells 234 (2022) 111431

3. Yong Li, Guanchao Yin, Yao Gao, Tristan Köhler, Jan Lucaßen, Martina Schmid. Sodium control in Ultrathin $\text{Cu}(\text{In,Ga})\text{Se}_2$ solar cells on transparent back-contact for efficiencies beyond 12%. Solar Energy Materials & Solar Cells 223 (2021) 110969

4. Yong Li, Guanchao Yin, Nikolai Bart, Martina Schmid. Optimization of NaF doping for ultra-thin CIGSe solar cells. Poster presentation during 07-11 September 2020, Munich, Germany. EU PVSEC 2020.

5. Yong Li, Guanchao Yin, Martina Schmid. Optimization of Na doping for ultra-thin CIGSe on ITO back-contacts. Oral presentation during May 31-June 3 Virtual Conference, EMRS Spring Meeting 2021.

6. Li Y, Gao M, Wan Y Z, et al. The high-frequency tunnel capacitance overload phenomenon of semiconductor-insulator-semiconductor heterojunction caused by the ultra-thin interfacial layers (in Chinese). Chin Sci Bull, 2017, 62: 1–7, doi: 10.1360/N972016-00582

7. Y.Li, M. Gao, Y. Z. Wan, H. B. Chao, J. Yang, H. W. Du, Z.Q.Ma. A concise way to estimate the average density of interface states in an ITO– SiO_x /n-Si heterojunction solar cell. Applied Surface Science 416 (2017) 432–438

Appendix C – Abbreviations and symbols

α	Absorption co-efficient
δ	Thickness of the interfacial layer
ζ	Effective barrier of the interfacial layer
λ	Wavelength
Φ_b	Contact potential barrier of the diode
$\Phi_{\text{CIGSe/ITO}}$	Barrier height at CIGSe/ITO
$\Phi_{\text{CIGSe/Mo}}$	Barrier height at CIGSe/Mo
k	Boltzmann constant
ϵ_0	Dielectric constant of the vacuum
ϵ_r	Dielectric constant of the material
ΔE_v	Valance band offset
Δn	Excess carrier density
χ_{CIGSe}	Electron affinity of the CIGSe
A^*	Effective Richardson constant for thermionic emission
Ag	Silver
AM 1.5	Reference solar spectral irradiance under air mass 1.5
AZO	Al-doped ZnO (Al: ZnO)
ARC	Anti-reflection coating
Al	Aluminium
BSTUT	Bifacial semi-transparent ultrathin
B-M	Burstein-Moss
C_D	Capacitance of the depleted region
CBD	Chemical Bath Deposition
CdS	Cadmium sulphide
Cu	Copper
CIGSe	$\text{Cu}(\text{In}_{1-x}\text{Ga}_x)\text{Se}_2$

CV	Capacitance voltage spectroscopy
CGI	Cu ratio of Cu/(Ga+In)
d	Thickness of the film
d_{SCR}	Width of the space charge region
D	Diffusion coefficient
D_0	Maximum diffusion coefficient at infinite temperature
D_{it}	Interface traps density
E_A	Activation energy for diffusion
Eff	Conversion efficiency
E_g	bandgap
E_c	Conduction band minimum
E_v	Valance band maximum
E_f	Fermi level
E_h	Barrier heigh for holes
E_{h0}	Original barrier heigh for holes
$E_{h,e}$	Effective barrier heigh for holes
E_t	Trap state energy level
EQE	External quantum efficiency
e	Elemental electric charge
F	Optical path enhancement factor
FF	Fill factor
$FWHM$	Full width half maximum
G	Conductance of the diode
Ga	Gallium
GD-OES	Glow charge optical emission spectrometry
GGI	Ga ratio of Cu/(Ga+In)
HRTEM	High resolution transmission electron microscope
i-ZnO	Intrinsic ZnO
In	Indium

IQE	Internal quantum efficiency
ITO	Sn-doped In ₂ O ₃
<i>IV</i>	Current density-voltage
<i>IVT</i>	Temperature dependent current density-voltage
<i>j₀</i>	Dark saturation current density
<i>j_{sc}</i>	Short circuit current density
<i>j_{EQE}</i>	Equivalent current density integrated from EQE
<i>j_T</i>	Equivalent current density integrated from transmission
<i>j_{th}</i>	Current density originating from thermionic dynamics
<i>j_{diff}</i>	Current density originating from carrier diffusion
<i>j_{tunnel}</i>	Current density originating from tunnelling transport
<i>j_V</i>	Current density-voltage
<i>K</i>	Temperature unit
LLS	Laser-light scattering
Mo	Molybdenum
<i>n</i>	Diode ideal factor
<i>n_i</i>	Intrinsic carrier density of the semiconductor
<i>n</i>	Real part of the refractive index
Na	Sodium
NaF	Sodium fluoride
<i>N_A</i>	Acceptor doping density extracted from Mott-Schottky plot and in SCAPS simulation
<i>N_D</i>	Donor doping density extracted from Mott-Schottky plot
<i>N_{cv}</i>	Carrier density extracted from CV by Kimerling's model
<i>Ni</i>	Nickel
<i>NP</i>	Nano particle
<i>ODC</i>	Ordered defect compound layer
<i>PDT</i>	Post-deposition treatment
<i>PL</i>	Photoluminescence

<i>PV</i>	Photovoltaic
<i>PVD</i>	Physical vapour deposition
<i>q</i>	Elemental electric charge
<i>R</i>	Reflection
<i>R_s</i>	Series resistance of the diode
<i>R_{sh}</i>	Shunt resistance of the diode
<i>S_b</i>	Recombination velocity
<i>SC</i>	Solar cell
<i>SCIL</i>	Substrate conformal imprint lithography
<i>SCR</i>	Space charge region
<i>SEM</i>	Scanning electron microscopy
<i>Se</i>	Selenium
<i>SLG</i>	Soda-lime glass
<i>T</i>	Transmission
<i>T_r</i>	Inflection temperature point of roll-over IV characteristics
<i>TCO</i>	Transparent conductive oxide
<i>TEM</i>	Transmission electron microscope
<i>V_{oc}</i>	Open circuit voltage
<i>V_D</i>	Contact potential difference at CIGS/CdS
<i>W_{ITO}</i>	Work function of ITO
<i>W_D</i>	Space charge region width
<i>W_p</i>	Space charge region width in the p-type semiconductor
<i>W_n</i>	Space charge region width in the n-type semiconductor
<i>XRD</i>	X-Ray diffraction
<i>XRF</i>	X-Ray fluorescence

References

1. <https://www.bp.com/en/global/corporate/energy-economics/statistical-review-of-world-energy.html>. 2021.
2. Fraunhofer ISE: Photovoltaics Report, updated: 27 July 2021.
3. Green, M.A., et al., Solar cell efficiency tables (Version 58). *Progress in Photovoltaics: Research and Applications*, 2021. 29(7): p. 657-667.
4. Yin, G., P. Manley, and M. Schmid, Influence of substrate and its temperature on the optical constants of $\text{CuIn}_{1-x}\text{Ga}_x\text{Se}_2$ thin films. *Journal of Physics D: Applied Physics*, 2014. 47(13): p. 135101.
5. Yin, G., Preparation of Ultra-thin $\text{CuIn}_{1-x}\text{Ga}_x\text{Se}_2$ Solar Cells and Their Light Absorption Enhancement. 2015, der Technischen Universität Berlin: Berlin.
6. Scheer, R., A. Pérez-Rodríguez, and W.K. Metzger, Advanced diagnostic and control methods of processes and layers in CIGS solar cells and modules. *Progress in Photovoltaics: Research and Applications*, 2010. 18(6): p. 467-480.
7. Yin, G., et al., Enhanced performance of ultra-thin $\text{Cu}(\text{In,Ga})\text{Se}_2$ solar cells deposited at low process temperature. *Solar Energy Materials and Solar Cells*, 2015. 132: p. 142-147.
8. Herberholz, R., et al., Phase segregation, Cu migration and junction formation in $\text{Cu}(\text{In,Ga})\text{Se}_2$. *Eur. Phys. J. AP* 1999. 6: p. 131-139.
9. Caballero, R., et al., Effect of Cu excess on three-stage CuGaSe_2 thin films using in-situ process controls. *Thin Solid Films*, 2007. 515(15): p. 5862-5866.
10. Plummer, J.D., M.D. Deal, and P.B. Griffin, *Silicon VLSI technology-fundamentals, practice and modeling*. 2000, Upper Saddle River, New Jersey 07458: Prentice Hall.
11. Mollica, F., Optimization of ultra-thin $\text{Cu}(\text{In,Ga})\text{Se}_2$ based solar cells with alternative back-contacts, in *Chemical Physics 2016*, Université Pierre et Marie Curie Paris.
12. Kotipalli, R., et al., Addressing the impact of rear surface passivation mechanisms on ultra-thin $\text{Cu}(\text{In,Ga})\text{Se}_2$ solar cell performances using SCAPS 1-D model. *Solar Energy*, 2017. 157: p. 603-613.
13. Salomé, P.M.P., et al., Passivation of Interfaces in Thin Film Solar Cells: Understanding the Effects of a Nanostructured Rear Point Contact Layer. *Advanced Materials Interfaces*, 2018. 5(2).
14. Cunha, J.M.V., et al., High-Performance and Industrially Viable Nanostructured SiO_x Layers for Interface Passivation in Thin Film Solar Cells. *Solar RRL*, 2021.
15. Mansfield, L.M., et al., Efficiency increased to 15.2% for ultra-thin $\text{Cu}(\text{In,Ga})\text{Se}_2$ solar cells. *Progress in Photovoltaics: Research and Applications*, 2018: p. 1-6.
16. Nakamura, M., et al., Cd-Free $\text{Cu}(\text{In,Ga})(\text{Se,S})_2$ Thin-Film Solar Cell With Record Efficiency of 23.35%. *IEEE Journal of Photovoltaics*, 2019. 9(6): p. 1863-1867.
17. Schneider, T., et al., Ultrathin CIGSe Solar Cells with Integrated Structured Back Reflector. *Solar RRL*, 2020. 4(10).
18. Schneider, T., et al., Comparison of Mo and ITO back contacts in CIGSe solar cells: Vanishing of the main capacitance step. *Progress in Photovoltaics: Research and Applications*, 2022. 30(2): p. 191-202.
19. Gouillart, L., et al., Interface engineering of ultrathin $\text{Cu}(\text{In,Ga})\text{Se}_2$ solar cells on reflective back contacts. *Progress in Photovoltaics: Research and Applications*, 2020. 29: p. 212-221.

20. Schmid, M., Review on light management by nanostructures in chalcopyrite solar cells. *Semiconductor Science and Technology*, 2017. 32(4): p. 043003.
21. Klinkert, T., et al., New insights into the Mo/Cu(In,Ga)Se₂ interface in thin film solar cells: Formation and properties of the MoSe₂ interfacial layer. *J Chem Phys*, 2016. 145(15): p. 154702.
22. Yin, G., P. Manley, and M. Schmid, Light trapping in ultrathin CuIn_{1-x}Ga_xSe₂ solar cells by dielectric nanoparticles. *Solar Energy*, 2018. 163: p. 443-452.
23. Nakada, T., et al., Novel device structure for Cu(In,Ga)Se₂ thin film solar cells using transparent conducting oxide back and front contacts. *Solar Energy*, 2004. 77(6): p. 739-747.
24. Keller, J., et al., Bifacial Cu(In,Ga)Se₂ solar cells using hydrogen-doped In₂O₃ films as a transparent back contact. *Progress in Photovoltaics: Research and Applications*, 2018. 26(10): p. 846-858.
25. Gouillart, L., et al., Reflective Back Contacts for Ultrathin Cu(In,Ga)Se₂-Based Solar Cells. *IEEE Journal of Photovoltaics*, 2020. 10(1): p. 250-254.
26. Gouillart, L., et al., Development of reflective back contacts for high-efficiency ultrathin Cu(In,Ga)Se₂ solar cells. *Thin Solid Films*, 2019. 672: p. 1-6.
27. Mollica, F., et al., Light absorption enhancement in ultra-thin Cu(In,Ga)Se₂ solar cells by substituting the back-contact with a transparent conducting oxide based reflector. *Thin Solid Films*, 2017. 633: p. 202-207.
28. Saifullah, M., et al., Development of semitransparent CIGS thin-film solar cells modified with a sulfurized-AgGa layer for building applications. *Journal of Materials Chemistry A*, 2016. 4(27): p. 10542-10551.
29. Saifullah, M., et al., Performance and Uniformity Improvement in Ultrathin Cu(In,Ga)Se₂ Solar Cells with a WO_x Nano-Interlayer at the Absorber/Transparent Back-Contact Interface. *ACS Applied Materials and Interfaces*, 2019(11): p. 655-665.
30. Kim, D., et al., Flexible and semi-transparent ultra-thin CIGSe solar cells prepared on ultra-thin glass substrate: a key to flexible bifacial photovoltaic applications. *Adv. Funct. Mater.*, 2020: p. 2001775.
31. Kim, K. and W.N. Shafarman, Alternative device structures for CIGS-based solar cells with semi-transparent absorbers. *Nano Energy*, 2016. 30: p. 488-493.
32. Yin, G., M. Song, and M. Schmid, Rear point contact structures for performance enhancement of semi-transparent ultrathin Cu(In,Ga)Se₂ solar cells. *Solar Energy Materials and Solar Cells*, 2019. 195: p. 318-322.
33. Yin, G., et al., Optoelectronic Enhancement of Ultrathin CuIn_{1-x}Ga_xSe₂ Solar Cells by Nanophotonic Contacts. *Advanced Optical Materials*, 2017. 5(5): p. 1600637.
34. <https://www.ebay.de/i/223693957591>.
35. <https://www.bbc.com/news/science-environment-48910569>.
36. <https://www.advancedsciencenews.com/solar-trees-semitransparent-flexible-organic-solar-cells/>
37. <https://solaredition.com/the-dawn-of-solar-windows-in-building-semi-transparent-solar-panel/>.
38. J, H., et al. ZnO/CdS/Cu(In,Ga)Se₂ thin film solar cells with improved performance. . in *Proceedings of the 23rd IEEE Photovoltaic Specialists Conference*. 1993. Louisville, KY, USA.: The Institute of Electrical and Electronics Engineers.

39. Holz, J., F. Karg, and H.v. Philipsborn. The effect of substrate impurities on the electronic conductivity in CIS thin films. in 12th European Photovoltaic Solar Energy Conference. 1994. Amsterdam, Netherlands.
40. JE, G., et al. Quantitative incorporation of sodium in CuInSe_2 and Cu(In,Ga)Se_2 photovoltaic devices. in 26th IEEE Photovoltaic Specialists Conference. 1997. Anaheim, CA, USA: The Institute of Electrical and Electronics Engineers.
41. Rudmann, D., et al., Na incorporation into Cu(In,Ga)Se_2 for high-efficiency flexible solar cells on polymer foils. *Journal of Applied Physics*, 2005. 97(8).
42. Chirila, A., et al., Potassium-induced surface modification of Cu(In,Ga)Se_2 thin films for high-efficiency solar cells. *Nat Mater*, 2013. 12(12): p. 1107-11.
43. Carron, R., et al., Advanced Alkali Treatments for High-Efficiency Cu(In,Ga)Se_2 Solar Cells on Flexible Substrates. *Advanced Energy Materials*, 2019.
44. Sun, Y., et al., Review on Alkali Element Doping in Cu(In,Ga)Se_2 Thin Films and Solar Cells. *Engineering*, 2017. 3(4): p. 452-459.
45. Salomé, P.M.P., H. Rodriguez-Alvarez, and S. Sadewasser, Incorporation of alkali metals in chalcogenide solar cells. *Solar Energy Materials and Solar Cells*, 2015. 143: p. 9-20.
46. Shin, D., et al., Effects of the incorporation of alkali elements on Cu(In,Ga)Se_2 thin film solar cells. *Solar Energy Materials and Solar Cells*, 2016. 157: p. 695-702.
47. Abou-Ras, D., et al., Innovation highway: Breakthrough milestones and key developments in chalcopyrite photovoltaics from a retrospective viewpoint. *Thin Solid Films*, 2017. 633: p. 2-12.
48. Cho, D.-H., et al., Electronic effect of Na on Cu(In,Ga)Se_2 solar cells. *Applied Physics Letters*, 2012. 101: p. 023901.
49. Rudmann, D., et al., Effects of NaF coevaporation on structural properties of Cu(In,Ga)Se_2 thin films. *Thin Solid Films*, 2003. 431-432: p. 37-40.
50. Ishizuka, S., et al., Na-induced variations in the structural, optical, and electrical properties of Cu(In,Ga)Se_2 thin films. *Journal of Applied Physics*, 2009. 106: p. 034908.
51. Nicoara, N., et al., Direct evidence for grain boundary passivation in Cu(In,Ga)Se_2 solar cells through alkali-fluoride post-deposition treatments. *Nat Commun*, 2019. 10(1): p. 3980.
52. Abou-Ras, D., et al., No Evidence for Passivation Effects of Na and K at Grain Boundaries in Polycrystalline Cu(In,Ga)Se_2 Thin Films for Solar Cells. *Solar RRL*, 2019. 3(8).
53. Muzzillo, C.P., Review of grain interior, grain boundary, and interface effects of K in CIGS solar cells: Mechanisms for performance enhancement. *Solar Energy Materials and Solar Cells*, 2017. 172: p. 18-24.
54. Zhang, S.B., S.-H. Wei, and A. Zunger, Defect physics of the CuInSe_2 chalcopyrite semiconductor. *PHYSICAL REVIEW B*, 1998. 57(16): p. 9642.
55. Wei, S.-H., S.B. Zhang, and A. Zunger, Effects of Na on the electrical and structural properties of CuInSe_2 . *Journal of Applied Physics*, 1999. 85(10): p. 7214-7218.
56. Handick, E., et al., Formation of a K-In-Se Surface Species by NaF/KF Postdeposition Treatment of Cu(In,Ga)Se_2 Thin-Film Solar Cell Absorbers. *ACS Appl Mater Interfaces*, 2017. 9(4): p. 3581-3589.
57. Muzzillo, C.P., H.M. Tong, and T.J. Anderson, The effect of Na on Cu-K-In-Se thin film growth. *Journal of Crystal Growth*, 2018. 488: p. 36-42.

58. Abou-Ras, D., et al., Dependence of the MoSe₂ Formation on the Mo Orientation and the Na Concentration for Cu(In,Ga)Se₂ Thin-Film Solar Cells. *Mater. Res. Soc. Symp. Proc.*, 2005. 865.
59. Diffusion equation. https://en.wikipedia.org/wiki/Diffusion_equation.
60. Mass diffusivity of solids. https://en.wikipedia.org/wiki/Mass_diffusivity#Solids.
61. Kaufmann, C.A., et al., Depth profiling of Cu(In,Ga)Se₂ thin films grown at low temperatures. *Solar Energy Materials and Solar Cells*, 2009. 93(6-7): p. 859-863.
62. Vermang, B., et al., Employing Si solar cell technology to increase efficiency of ultrathin Cu(In,Ga)Se₂ solar cells. *Progress in photovoltaic research and application*, 2014. 22(10): p. 1023-1029.
63. Xiao, C., et al., Locating the electrical junctions in Cu(In,Ga)Se₂ and Cu₂ZnSnSe₄ solar cells by scanning capacitance spectroscopy. *Progress in Photovoltaics: Research and Applications*, 2017. 25(1): p. 33-40.
64. Stokes, A., et al., Nanoscale insight into the p-n junction of alkali-incorporated Cu(In,Ga)Se₂ solar cells. *Progress in Photovoltaics: Research and Applications*, 2017. 25(9): p. 764-772.
65. Hsiao, K.J., et al., Electrical impact of MoSe₂ on CIGS thin-film solar cells. *Phys Chem Chem Phys*, 2013. 15(41): p. 18174-8.
66. Bär, M., et al., Electronic level alignment at the deeply buried absorber/Mo interface in chalcopyrite-based thin film solar cells. *Applied Physics Letters*, 2008. 93(4).
67. Zhu, X., et al., Determining factor of MoSe₂ formation in Cu(In,Ga)Se₂ solar Cells. *Solar Energy Materials and Solar Cells*, 2012. 101: p. 57-61.
68. Abou-Ras, D., et al., Formation and characterisation of MoSe₂ for Cu(In,Ga)Se₂ based solar cells. *Thin Solid Films*, 2005. 480-481: p. 433-438.
69. Kohara, N., et al., Electrical properties of the Cu(In,Ga)Se₂/MoSe₂/Mo structure. *Solar Energy Materials and Solar Cells*, 2001. 67: p. 209-215.
70. Rostan, P.J., et al., Formation of transparent and ohmic ZnO:Al/MoSe₂ contacts for bifacial Cu(In,Ga)Se₂ solar cells and tandem structures. *Thin Solid Films*, 2005. 480-481: p. 67-70.
71. Nakada, T., Microstructural and diffusion properties of CIGS thin film solar cells fabricated using transparent conducting oxide back contacts. *Thin Solid Films*, 2005. 480-481: p. 419-425.
72. Heinemann, M.D., et al., Cu(In,Ga)Se₂ superstrate solar cells: prospects and limitations. *Progress in Photovoltaics: Research and Applications*, 2015. 23(10): p. 1228-1237.
73. Garud, S., et al., Surface Passivation of CIGS Solar Cells Using Gallium Oxide. *physica status solidi (a)*, 2018. 215(7).
74. Saifullah, M., et al., The role of NaF post-deposition treatment on the photovoltaic characteristics of semitransparent ultrathin Cu(In,Ga)Se₂ solar cells prepared on indium-tin-oxide back contacts: a comparative study. *Journal of Materials Chemistry A*, 2019. 7(38): p. 21843-21853.
75. Son, Y.-S., et al., Control of Structural and Electrical Properties of Indium Tin Oxide (ITO)/Cu(In,Ga)Se₂ Interface for Transparent Back-Contact Applications. *J. Phys. Chem. C*, 2019. 123: p. 1635-1644.
76. Heinemann, M.D., et al., The Importance of Sodium Control in CIGSe Superstrate Solar Cells. *IEEE Journal of Photovoltaics*, 2015. 5(1): p. 378-381.

77. Chantana, J., H. Arai, and T. Minemoto, Trap-assisted recombination for ohmic-like contact at p-type Cu(In,Ga)Se₂/back n-type TCO interface in superstrate-type solar cell. *Journal of Applied Physics*, 2016. 120(4): p. 045302.
78. Li, Y., et al., Sodium control in Ultrathin Cu(In,Ga)Se₂ solar cells on transparent back contact for efficiencies beyond 12%. *Solar Energy Materials and Solar Cells*, 2021. 223.
79. Sze, S.M. and K.K. Ng, *Physics of semiconductor devices*. 2007, Hoboken, New Jersey. Published simultaneously in Canada.: John Wiley & Sons.
80. Bose, S., et al., Optical Lithography Patterning of SiO₂ Layers for Interface Passivation of Thin Film Solar Cells. *Solar RRL*, 2018. 2(12).
81. Casper, P., et al., Optoelectrical improvement of ultra-thin Cu(In,Ga)Se₂ solar cells through microstructured MgF₂ and Al₂O₃ back contact passivation layer. *physica status solidi (RRL) - Rapid Research Letters*, 2016. 10(5): p. 376-380.
82. Hsu, W.W., et al., Surface passivation of Cu(In,Ga)Se₂ using atomic layer deposited Al₂O₃. *Applied Physics Letters*, 2012. 100(2).
83. Keller, J., et al., On the beneficial effect of Al₂O₃ front contact passivation in Cu(In,Ga)Se₂ solar cells. *Solar Energy Materials and Solar Cells*, 2017. 159: p. 189-196.
84. Kim, S.T., et al., Surface passivation and point defect control in Cu(In,Ga)Se₂ films with a Na₂S post deposition treatment for higher than 19% CIGS cell performance. *Sustainable Energy & Fuels*, 2019. 3(3): p. 709-716.
85. Ledinek, D., et al., Effect of different Na supply methods on thin Cu(In,Ga)Se₂ solar cells with Al₂O₃ rear passivation layers. *Solar Energy Materials and Solar Cells*, 2018. 187: p. 160-169.
86. Ledinek, D., et al., Rear Contact Passivation for High Bandgap Cu(In, Ga)Se₂ Solar Cells With a Flat Ga profile. *IEEE Journal of Photovoltaics*, 2018: p. 1-7.
87. Ohm, W., et al., Bifacial Cu(In,Ga)Se₂ solar cells with submicron absorber thickness: Back-contact passivation and light management, in *Photovoltaic Specialist Conference (PVSC)*. 2015. p. 1-5.
88. Vermang, B., et al., Highly reflective rear surface passivation design for ultra-thin Cu(In,Ga)Se₂ solar cells. *Thin Solid Films*, 2015. 582: p. 300-303.
89. Werner, F., et al., Oxidation as Key Mechanism for Efficient Interface Passivation in Cu(In,Ga)Se₂ Thin-Film Solar Cells. *Physical Review Applied*, 2020. 13(5).
90. Cunha, J.M.V., et al., Insulator Materials for Interface Passivation of Cu(In,Ga)Se₂ Thin Films. *IEEE Journal of Photovoltaics*, 2018. 8(5): p. 1313-1319.
91. Massiot, I., A. Cattoni, and S. Collin, Progress and prospects for ultrathin solar cells. *Nature Energy*, 2020. 5(12): p. 959-972.
92. Green, M.A., Lambertian light trapping in textured solar cells and light-emitting diodes: analytical solutions. *Progress in Photovoltaics: Research and Applications*, 2002. 10(4): p. 235-241.
93. Wang, K.X., Y. Guo, and S. Fan, Wave optics light-trapping theory: mathematical justification and ultimate limit on enhancement. *Journal of the Optical Society of America B*, 2019. 36(9).
94. Brongersma, M.L., Y. Cui, and S. Fan, Light management for photovoltaics using high-index nanostructures. *Nat Mater*, 2014. 13(5): p. 451-60.
95. Shin, M.J., et al., Semitransparent and bifacial ultrathin Cu(In,Ga)Se₂ solar cells via a single-stage process and light-management strategy. *Nano Energy*, 2021. 82.
96. Yin, G., et al., Integration of plasmonic Ag nanoparticles as a back reflector in ultra-thin Cu(In,Ga)Se₂ solar cells. *Applied Surface Science*, 2015. 355: p. 800-804.

97. Hegedus, S.S. and W.N. Shafarman, Thin-film solar cells: device measurements and analysis. *Progress in Photovoltaics: Research and Applications*, 2004. 12(23): p. 155-176.
98. Li, J.V. and G. Ferrari, *Capacitance Spectroscopy of Semiconductors*. 2018, Pan Stanford Publishing Pte. Ltd. Penthouse Level, Suntec Tower 38 Temasek Boulevard Singapore 038988.
99. Abou-Ras, D., T. Kirchartz, and U. Rau, *Advanced Characterization Techniques for Thin Film Solar Cells*. 2016.
100. Scheer, R. and H.-W. Schock, *Chalcogenide Photovoltaics Physics, Technologies, and Thin Film Devices*. 2011, Boschstr. 12, 69469 Weinheim, Germany: WILEY-VCH Verlag & Co. KGaA.
101. Kimerling, L.C., Influence of deep traps on the measurement of free-carrier distributions in semiconductors by junction capacitance techniques. *Journal of Applied Physics*, 1974. 45(4): p. 1839-1845.
102. Werner, F. and S. Siebentritt, Buffer Layers, Defects, and the Capacitance Step in the Admittance Spectrum of a Thin-Film Solar Cell. *Physical Review Applied*, 2018. 9(5).
103. Werner, F., et al., Can we see defects in capacitance measurements of thin-film solar cells? *Progress in Photovoltaics: Research and Applications*, 2019. 27(11): p. 1045-1058.
104. Niemegeers, A. and M. Burgelman. Numerical modelling of ac-characteristics of CdTe and CIS solar cells. in *25nd IEEE Photovoltaic Spec. Conf.* 1996. Washington DC, New York.
105. Manley, P., G. Yin, and M. Schmid, A method for calculating the complex refractive index of inhomogeneous thin films. *Journal of Physics D: Applied Physics*, 2014. 47(20).
106. Rudmann, D., et al., Efficiency enhancement of Cu(In,Ga)Se₂ solar cells due to post-deposition Na incorporation. *Applied Physics Letters*, 2004. 84(7): p. 1129-1131.
107. Salome, P.M.P., et al., Incorporation of Na in Cu(In,Ga)Se₂ Thin-Film Solar Cells: A Statistical Comparison Between Na From Soda-Lime Glass and From a Precursor Layer of NaF. *IEEE Journal of Photovoltaics*, 2014. 4(6): p. 1659-1664.
108. Dominik, R., Effects of sodium on growth and properties of Cu(In,Ga)Se₂ thin films and solar cells. 2004, ETH.
109. Rudmann, D., et al., Sodium incorporation strategies for CIGS growth at different temperatures. *Thin Solid Films*, 2005. 480-481: p. 55-60.
110. Niemegeers, A., et al., Model for Electronic Transport in Cu(In,Ga)Se₂ Solar Cells. *Progress in Photovoltaic: Research and Applications*, 1998. 6.
111. <https://www.pveducation.org/pvcdrom/solar-cell-operation/open-circuit-voltage>.
112. Yin, G., et al., Well-Controlled Dielectric Nanomeshes by Colloidal Nanosphere Lithography for Optoelectronic Enhancement of Ultrathin Cu(In,Ga)Se₂ Solar Cells. *ACS Appl Mater Interfaces*, 2016. 8(46): p. 31646-31652.
113. Rebecca, S., S-Shaped Current–Voltage Characteristics in Solar Cells: A Review. *IEEE Journal of Photovoltaics*, 2019. 9(6): p. 1477-1484.
114. Niemegeers, A. and M. Burgelman, Effects of the Au/CdTe back contact on IV and CV characteristics of Au/CdTe/CdS/TCO solar cells. *Journal of Applied Physics*, 1997. 81(6): p. 2881-2886.
115. Caballero, R., et al., Influence of Na on Cu(In,Ga)Se₂ solar cells grown on polyimide substrates at low temperature: Impact on the Cu(In,Ga)Se₂/Mo interface. *Applied Physics Letters*, 2010. 96(9).

116. Green, M.A., General temperature dependence of solar cell performance and implications for device modelling. *Progress in Photovoltaics: Research and Applications*, 2003. 11(5): p. 333-340.
117. Pianezzi, F., et al., Unveiling the effects of post-deposition treatment with different alkaline elements on the electronic properties of CIGS thin film solar cells. *Phys Chem Chem Phys*, 2014. 16(19): p. 8843-51.
118. Herberholz, R., M. Igalson, and H.W. Schock, Distinction between bulk and interface states in CuInSe₂/CdS/ZnO by space charge spectroscopy. *Journal of Applied Physics*, 1998. 83(1): p. 318-325.
119. Eisenbarth, T., et al., Interpretation of admittance, capacitance-voltage, and current-voltage signatures in Cu(In,Ga)Se₂ thin film solar cells. *Journal of Applied Physics*, 2010. 107(3).
120. Lee, H., et al., Passivation of Deep-Level Defects by Cesium Fluoride Post-Deposition Treatment for Improved Device Performance of Cu(In,Ga)Se₂ Solar Cells. *ACS Appl Mater Interfaces*, 2019. 11(39): p. 35653-35660.
121. Ledinek, D., et al., Effect of NaF pre-cursor on alumina and hafnia rear contact passivation layers in ultra-thin Cu(In,Ga)Se₂ solar cells. *Thin Solid Films*, 2019. 683: p. 156-164.
122. Colombara, D., et al., Sodium enhances indium-gallium interdiffusion in copper indium gallium diselenide photovoltaic absorbers. *Nat Commun*, 2018. 9(1): p. 826.
123. Simchi, H., et al., Structure and interface chemistry of MoO₃ back contacts in Cu(In,Ga)Se₂ thin film solar cells. *Journal of Applied Physics*, 2014. 115(3): p. 033514.
124. Burgelman, M., P. Nollet, and S. Degraeve, Modelling polycrystalline semiconductor solar cells. *Thin Solid Films*, 2000. 361-362: p. 527-532.
125. Decock, K., S. Khelifi, and M. Burgelman, Modelling multivalent defects in thin film solar cells. *Thin Solid Films*, 2011. 519(21): p. 7481-7484.
126. Burgelman, M., et al., Advanced electrical simulation of thin film solar cells. *Thin Solid Films*, 2013. 535: p. 296-301.
127. Park, Y., et al., Work function of indium tin oxide transparent conductor measured by photoelectron spectroscopy. *Applied Physics Letters*, 1996. 68(19): p. 2699-2701.
128. Tu, Y., et al., Is a passivated back contact always beneficial for Cu (In,Ga)Se₂ solar cells. *Progress in Photovoltaics: Research and Applications*, 2021.
129. Klenk, R. and H.-W. Schock. Photocurrent collection in thin film solar cells-calculation and characterization for CuGaSe₂/(Zn,Cd)S. in 12th European Photovoltaic Solar Energy Conference. 1994. Amsterdam.
130. Li, Y., et al., Ultrathin Cu(In,Ga)Se₂ Solar Cells with a Passivated Back Interface: A Comparative Study between Mo and In₂O₃:Sn Back Contacts. *ACS Applied Energy Materials*, 2022.
131. Kato, T., et al., Record Efficiency for Thin-Film Polycrystalline Solar Cells Up to 22.9% Achieved by Cs-Treated Cu(In,Ga)(Se,S)₂. *IEEE Journal of Photovoltaics*, 2018: p. 1-6.
132. Ishizuka, S., et al., Progress in the Efficiency of Wide-Gap Cu(In_{1-x}Ga_x)Se₂ Solar Cells Using CIGSe Layers Grown in Water Vapor. *Japanese Journal of Applied Physics*, 2005. 44(No. 22): p. L679-L682.
133. Yang, S.C., et al., Influence of Ga back grading on voltage loss in low-temperature co-evaporated Cu(In,Ga)Se₂ thin film solar cells. *Progress in Photovoltaics: Research and Applications*, 2021.

134. Kim, S., et al., Effect of Crystal Orientation and Conduction Band Grading of Absorber on Efficiency of Cu(In,Ga)Se₂ Solar Cells Grown on Flexible Polyimide Foil at Low Temperature. *Advanced Energy Materials*, 2018.
135. Ando, Y., et al., Relationship between bandgap grading and carrier recombination for Cu(In,Ga)Se₂-based solar cells. *Japanese Journal of Applied Physics*, 2018. 57(8S3).
136. Kotipalli, R., et al., Influence of Ga/(Ga+In) grading on deep-defect states of Cu(In,Ga)Se₂ solar cells. *physica status solidi (RRL) - Rapid Research Letters*, 2015. 9(3): p. 157-160.
137. Gloeckler, M. and J.R. Sites, Band-gap grading in Cu(In,Ga)Se₂ solar cells. *Journal of Physics and Chemistry of Solids*, 2005. 66(11): p. 1891-1894.
138. Kim, H., et al., Effect of film thickness on the properties of indium tin oxide thin films. *Journal of Applied Physics*, 2000. 88(10): p. 6021-6025.
139. Sato, Y., et al., Carrier Density Dependence of Optical Band Gap and Work Function in Sn-Doped In₂O₃ Films. *Applied Physics Express*, 2010. 3(6).
140. Kim, H., et al., Electrical, optical, and structural properties of indium–tin–oxide thin films for organic light-emitting devices. *Journal of Applied Physics*, 1999. 86(11): p. 6451-6461.
141. Zhang, C., et al., Plasma treatment of ITO cathode to fabricate free electron selective layer in inverted polymer solar cells. *J. Mater. Chem. C*, 2014. 2(41): p. 8715-8722.
142. <https://www.pveducation.org/pvcdrom/solar-cell-operation/fill-factor>.
143. Krause, M., et al., Microscopic origins of performance losses in highly efficient Cu(In,Ga)Se₂ thin-film solar cells. *Nat Commun*, 2020. 11(1): p. 4189.
144. Abou-Ras, D., et al., Optoelectronic Inactivity of Dislocations in Cu(In,Ga)Se₂ Thin Films. *physica status solidi (RRL) – Rapid Research Letters*, 2021.
145. Schroder, D.K., *Semiconductor Material and Device Characterization*. 2006: IEEE.
146. Elanzeery, H., The cause of interface recombination in Cu-rich CIS thin film solar cells. 2019.
147. Li, Y., G. Yin, and M. Schmid, Bifacial semi-transparent ultra-thin Cu(In,Ga)Se₂ solar cells on ITO substrate: How ITO thickness and Na doping influence the performance. *Solar Energy Materials and Solar Cells*, 2022. 234.

DuEPublico

Duisburg-Essen Publications online

UNIVERSITÄT
DUISBURG
ESSEN

Offen im Denken

ub | universitäts
bibliothek

Diese Dissertation wird via DuEPublico, dem Dokumenten- und Publikationsserver der Universität Duisburg-Essen, zur Verfügung gestellt und liegt auch als Print-Version vor.

DOI: 10.17185/duepublico/78269

URN: urn:nbn:de:hbz:465-20230420-082324-4



Dieses Werk kann unter einer Creative Commons Namensnennung 4.0 Lizenz (CC BY 4.0) genutzt werden.